2015

Aero-Thermal Characterization Of Silicon Carbide Flexible Tps Using A 30kw Icp Torch

Walten Owens
University of Vermont

AERO-THERMAL CHARACTERIZATION OF SILICON CARBIDE FLEXIBLE TPS USING A 30KW ICP TORCH

A Dissertation Presented

by

Walten Owens

to

The Faculty of the Graduate College

of

The University of Vermont

In Partial Fulfillment of the Requirements
for the Degree of Doctor of Philosophy
Specializing in Mechanical Engineering

May, 2015

Defense Date: March 27, 2015
Dissertation Examination Committee:

Douglas Fletcher, Ph.D., Advisor
Christopher Landry, Ph.D., Chairperson
Frederic Sansoz, Ph.D.
Walter Varhue, Ph.D.
Tariq Quadir, Ph.D.
Cynthia J. Forehand, Ph.D., Dean of the Graduate College

ABSTRACT

Flexible thermal protection systems are of interest due to their necessity for the success of future atmospheric entry vehicles. Current non-ablative flexible designs incorporate a two-dimensional woven fabric on the leading surface of the vehicle. The focus of this research investigation was to characterize the aerothermal performance of silicon carbide fabric using the 30 kW Inductively Coupled Plasma Torch located at the University of Vermont. Experimental results have shown that SiC fabric test coupons achieving surface temperatures between 1000°C and 1500°C formed an amorphous silicon dioxide layer within seconds after insertion into air plasmas. The transient morphological changes that occurred during oxidation caused a time dependence in the gas / surface interactions which may detrimentally affect the in-flight performance. Room temperature tensile tests of the SiC coupons have shown a rapid strength loss for durations less than 240 seconds due to oxidation. Catastrophic failure and temperature spikes were observed on almost all SiC coupons when exposed to air plasmas at heat fluxes above 80 W/cm^2. Interestingly, simulation of entry into the Mars atmosphere using a carbon dioxide plasma caused a material response that was vastly different than the predictable silica layer observed during air plasma exposure.

ACKNOWLEDGEMENTS

My name may be on the title page of this dissertation and may someday be on the last diploma I will ever receive but in no way could I have done this on my own. It is the tools that I have been given from my family, friends, co-workers, and advisor that have allowed me to make it this far on my journey through life…

and right now I am just leaving the shire.

Special Thanks to

Doug Fletcher
Dan Merkel
Jason Meyers
Frederic Sansoz
Corey Tillson
Luke Allen
Corinna Thompson
Nick Vachon
Silas Smith
Max Dougherty
Andrew Lutz
Jürgen Uhl
Emily Parulis
Mom & Dad
Ryan Crocker
Doug Gomez
Floyd Vilmont
Joseph Del Corso
Stephen Hughes
F. McNeil Cheatwood
Scott Splinter
Anthony Calomino

Thanks to My Funding Sources

NASA Grant
NNX11AR69G &
NNX14AN20A

NASA EPSCoR / Vermont
Space Grant Consortium

AFOSR Grant
FA9550-11-1-0201

Provost Office

TABLE OF CONTENTS

Page

LIST OF TABLES

Table Page

LIST OF FIGURES

Figure Page

CHAPTER 1: INTRODUCTION

1.1. Flexible TPS

Many qualified entry decent and landing (EDL) systems have been pushed to their limits. Future missions with heavier payloads and higher entry velocities will induce greater heat loads that may exceed the qualifications of these systems. Inflatable aerodynamic decelerator (IAD) technology is a promising EDL advancement with potential game changing benefits. By overcoming the mechanical constraints of the launch vehicle shroud, IADs can achieve lower ballistic coefficients by dramatically increasing the entry vehicle drag area. A decreased ballistic coefficient will effectively reduce the peak heating rate and allow greater deceleration higher in the atmosphere. This increased deceleration will provide additional time between the atmospheric interface and landing, thus enabling previously unobtainable planet surface access and increasing the probability of success [1].

IADs are exposed to extremely harsh conditions during atmospheric entry due to a rapid temperature rise and subsequent dissociation and possible ionization of gases across the bow shock, whereas the degree of dissociation changes with the flight trajectory. Success of this technology requires maturation of a new type of thermal protection system (TPS) that must be flexible in order to deploy from a tightly packed configuration. Continuous advancements are implemented as new materials and designs are tested. The current IAD design and flexible TPS lay-up are visually displayed in Figure 1. The thermal energy balance on the surface of the TPS is also illustrated.

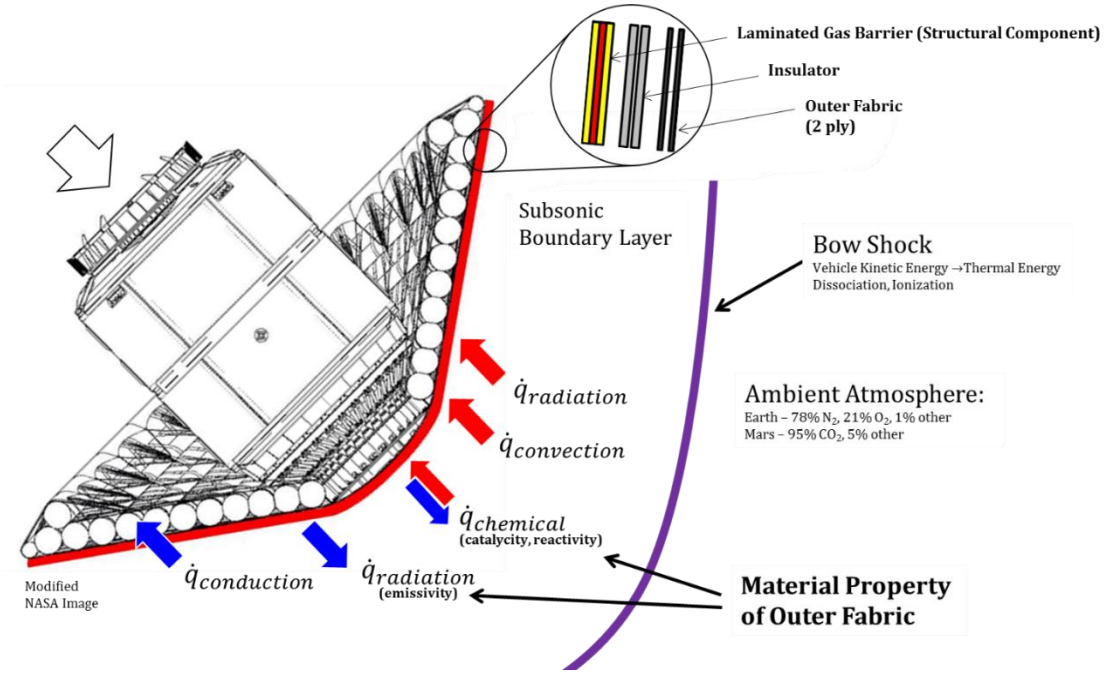

Figure 1: Thermal energy flux diagram for the IAD surface [modified NASA image]. The layered TPS design is also illustrated.

Flexible non-ablative designs use a 2-D woven outer fabric that is mechanically attached to an underlying insulator and a Kapton-Kevlar gas barrier through a stitching pattern. The insulator impedes the propagation of the integrated thermal load while a laminated gas barrier serves as both an impermeable membrane and a structural component [2]. The flexible outer fabric is exposed directly to the harsh aerodynamic environment. Therefore it must withstand the intense radiative, convective and chemical heating while minimizing hot gas impingement on the consecutive plies. An additional ply of the outer fabric material is used to assure structural integrity [1].

A properly selected outer fabric can significantly reduce the peak heat rate and the total heat load experienced by the entry vehicle. Therefore thermal analysis of the

interactions between the gas phase and TPS surface is critical in the design of any EDL sequence. Understanding the maximum survivable conditions is also important to assess the viability of candidate outer fabric materials. Whereas the failure mechanisms of the outer fabric may include; a weakening tensile strength, or rapid material removal due to excessively high heating.

Qualification of outer fabrics presents a substantial challenge. Before any in-fight testing is performed, candidate flexible materials must first be screened using ground based testing methods. Gas chemistry, shear, heat load, peak heat flux, surface pressure, and duration of exposure must all be addressed in order to accurately predict the in-flight performance of woven outer fabrics. It is desirable to test the outer fabric under the exact flight profile with constantly varying conditions as experienced in flight. This has a direct influence on the gas surface interactions due to the changing surface temperature and pressure throughout atmospheric entry. However, no known ground test facility can match all conditions of the flight profile, therefore cooperation between facilities is essential. Numerical analysis can enable simulation of the entire flight trajectory, but the results still rely on experimental ground testing for validation [3].

Currently, 2-D woven silicon carbide (SiC) fibers appear to be the most promising potential outer fabric material for trajectories inducing peak heat fluxes below 100 W/cm^2 [2]. In order to aid in the qualification process, this research effort investigates the aerothermal performance of the woven SiC fibers by;

- Exposing candidate flexible outer fabric coupons to high enthalpy flows typical of atmospheric entry using a 30 kW Inductively Coupled Plasma (ICP) Torch Facility
- Outlining the theories and findings of high temperature tests performed on SiC by other researchers
- Characterizing the thermal energy balance and the dynamic feed-back loop occurring on the SiC surface
- Performing tensile strength tests on the post-test SiC coupons
- Documenting the microstructural evolution and operating conditions leading to catastrophic failure of the 2-D woven SiC fibers
- Assessing the influence of the Martian atmospheric gas chemistry on the SiC coupon performance

CHAPTER 2: SILICON CARBIDE FIBERS

2.1. Hi-Nicalon

Along with a performance evaluation, the outer fabric selection criteria includes material consistency, supplier viability, and cost of development for full scale manufacturing [4]. Original SiC fibers were prepared through a chemical vapor deposition process but their high manufacturing cost discouraged high volume applications and the large 100-150 μm diameters were too stiff to weave [5]. Fortunately innovative technologies overcame these drawbacks allowing cheaper, smaller diameter flexible fibers. Silicon carbide-type fibers are now produced commercially by a variety of manufactures and are commonly incorporated into ceramic matrix composites for a number of high temperature applications.

Hi-Nicalon^{TM} SiC fiber has been chosen for this investigation. COI Ceramics is the exclusive North American distributer for the Hi-Nicalon SiC fibers which is trade marked by the Nippon Carbon Company based out of Japan [6]. Hi-Nicalon is a multifilament fiber derived from polycarbosilane which is synthesized from a dimethyldichlorosilane base material to provide the silicon carbon silicon backbone. The pre-ceramic polymer is put in a solution of organic solvents, melt spun, cured and pyrolized to achieve the resulting fiber [7]. The following table presents the fiber technical data provided by the distributer.

Table 1: COI Ceramics technical data for Hi-Nicalon SiC fibers [6]

Material	SiC (Hi-Nicalon)
Filaments per Tow	500
Filament Diameter (μm)	14
Density (g/cc)	2.74
Fiber Denier	1800
C/Si Atomic Ratio	1.39
Composition, wt. % Si:C:O	62:37:0.5
Sizing	PVA

The fiber is comprised of β-SiC nanocrystals that are separated by intergranular free carbon and a silicon oxycarbide phase [5]. The heterogeneous fiber has a Si:C:O weight % ratio of 62:37:0.5 respectively with less than 0.3% hydrogen remaining from the organosilicon precursor [5]. The low oxygen content is achieved using a near oxygen free electron beam curing process. For most applications, Hi-Nicalon fibers provide superior performance over the standard Nicalon fibers owing to the severe thermal instability of the SiC_xO_y phase [5]. However, purely stoichiometric, Hi-Nicalon Type S fibers are more expensive [8] and not flexible enough to meet the bend requirements.

2.2. Woven Outer Fabric

Hi-Nicalon is a textile grade material commercially available as spools of untwisted fibers that can be woven together to form a large variety of woven fabrics, tubes and braids. [6]. Unlike yarn that is typically made of twisted filaments of a finite length, the fibers are in the form of a tow which is a bundle of continuous parallel filaments. The outer filaments of each tow are coated with polyvinyl alcohol (PVA)

sizing to limit fiber to fiber abrasion [5]. Different techniques can be used to prepare the surface and standardize testing but no attempts were made to remove any of the surface impurities for this study.

For use as an inflatable heat shield, the SiC outer fabric must have high drape, high packability and be able to survive hard creases of near zero bend radii. An optimized outer fabric weave must also have a low areal weight and low permeability while still being flexible. A 5 harness satin 26x26 (warp x weft) weave type was determined to be advantageous due to its limited permeability and its ability to conform to complex curves. This weave type has 26 fibers per inch in both the warp and weft direction. Whereas, each fiber overlaps 4 cross fibers before being woven under 1 cross fiber. The permeability was measured between 38 and 43 standard cubic feet per square foot [2]. Whereas, permeability is highly dependent on the weave architecture, filament diameter and filaments per tows [2]. Harness satin weaves also provide an advantage compared to plain and twill weaves due to the limited number of crimp locations. Images of the Hi-Nicalon fabric architecture that is used in this study are depicted in Figure 2.

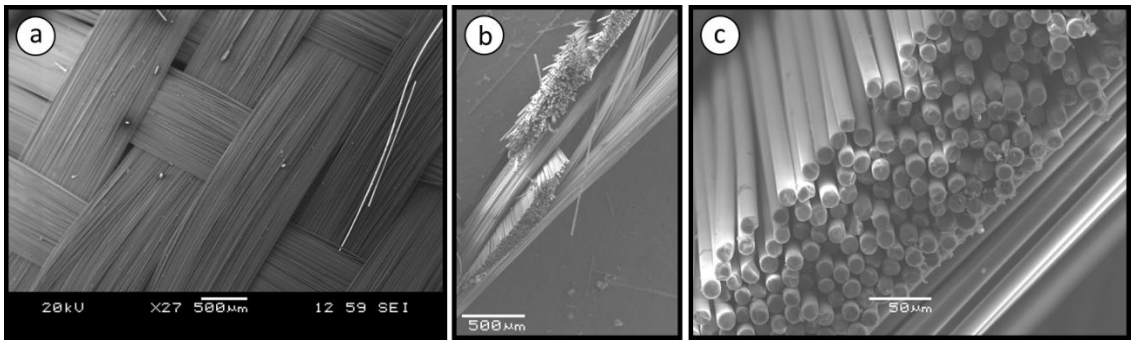

Figure 2: SEM image of the weave architecture a) top view b,c) cross cut at increasing magnifications

It can be seen that the tows consisting of 500 filaments conform to a lenticular shape due to the crimp of the fabric. Unlike rigid SiC or ceramic matrix composites, there is a drastically increased exposed macroscopic surface area which allows solid-gas phase interaction around the circumference of each fiber.

CHAPTER 3: 30 KW INDUCTIVELY COUPLED PLASMA TORCH

3.1. Introduction

A 30 kW Inductively Coupled Plasma Torch has been developed for the Plasma Test and Diagnostics Laboratory at the University of Vermont to assess the performance of new, advanced aerospace materials. The relatively small-scale ICP Torch was designed with sufficient power to provide a high enthalpy flow that can replicate the post shock heating experienced during planetary entry for a certain range of trajectories. The Torch is comprised of three major components for plasma testing which include; power supply, gas injection system, and vacuum chamber. Supplementary systems are used to actively cool the torch and control the test conditions. Various intrusive probes and non-intrusive diagnostic techniques are used to characterize the experimental conditions allowing material performance results to be extrapolated to actual flight environments. This chapter provides an overview of the ICP Torch and the diagnostic equipment.

3.2. ICP Torch Design

3.2.1. Vacuum Chamber

Aerothermal tests are performed within a 40 cm i.d. x 70 cm tall actively cooled stainless steel vacuum chamber in order to control the static pressure of the testing environment. The 3.6 cm o.d. plasma jet enters the test chamber vertically to promote uniformity in the plasma. The vacuum chamber diameter was chosen as a compromise between ease of optical access and fluid dynamic stability. Downstream from the test location, the plasma flow passes through a dual stage copper finned heat exchanger

before exiting to an elevated vacuum pump, which exhausts into a ventilated duct aided by a rooftop blower. The vacuum pump continuously operates using non-reactive fomblin oil and provides the full range of desirable pressures for start-up and test conditions. Remotely mounted compressed gas tanks and stainless steel tubing supply the induction region with variable gas mixtures.

Chamber locations with the highest heat loads are actively cooled through a closed loop water system operating in parallel at 4 liters per minute. A rooftop chiller circulates glycol to the lab which provides cooling to the power supply and to a glycol/water heat exchanger. A schematic of the ICP Torch can be seen in Figure 3.

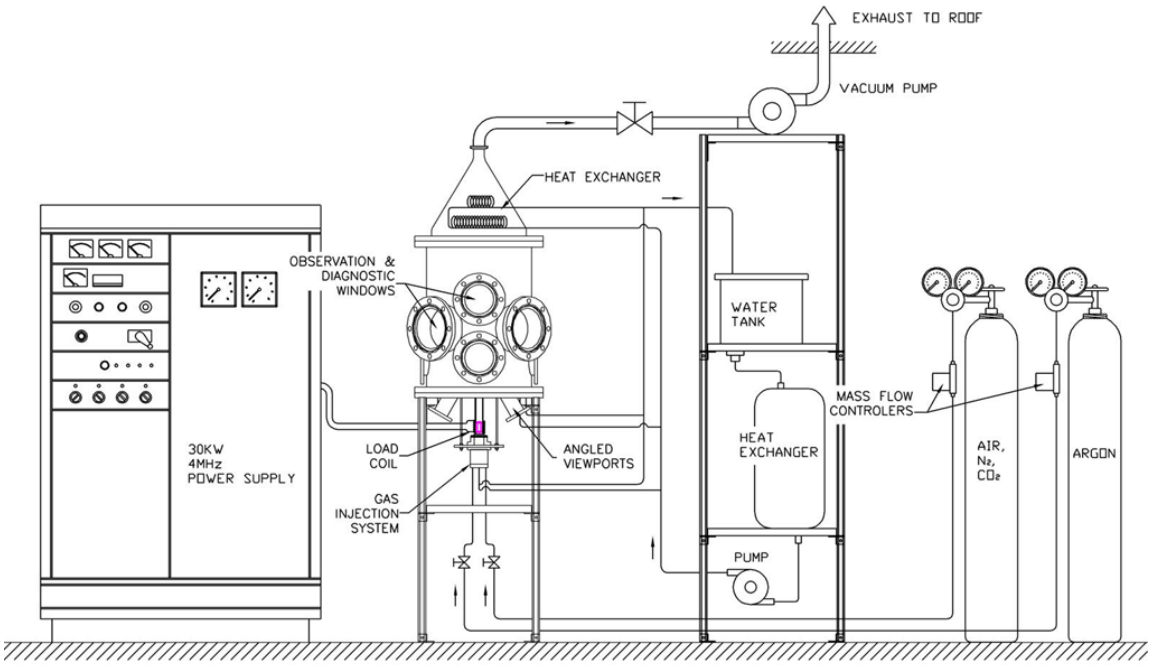

Figure 3: Scale drawing of the major components of the ICP Torch. Rooftop chiller, computer controls and diagnostic equipment are missing from the drawing

3.2.2. Power Supply

A Lepel solid state induction heating generator delivers up to 30kW at frequencies between 2.5-5Mhz. The power supply contains a primary saturable reactor control with silicon diode rectifier stacks which converts 3 phase AC current to a very high DC voltage. Power is controlled by varying this DC voltage level. A grid tuned oscillator converts the high voltage DC into a time varying AC current that is fed to the tank circuit. The parallel tank circuit and grid tuned oscillator provide the flexibility required for matching a wide variety of plasma conditions to the generator output [9].

3.2.3. Tank Circuit

Plasma generation requires massive currents to dissociate and ionize the test gas. However switching large currents at radio frequencies can be damaging and inefficient, therefore a tank circuit is needed. The parallel tank circuit transfers energy between electric and magnetic fields, where only the power transmitted into the plasma is replenished with each oscillation. The circuit consists of a capacitor bank and a water-cooled, variable air inductor. A wiring diagram containing the principal features of the power supply and tank circuit can be seen in Figure 4.

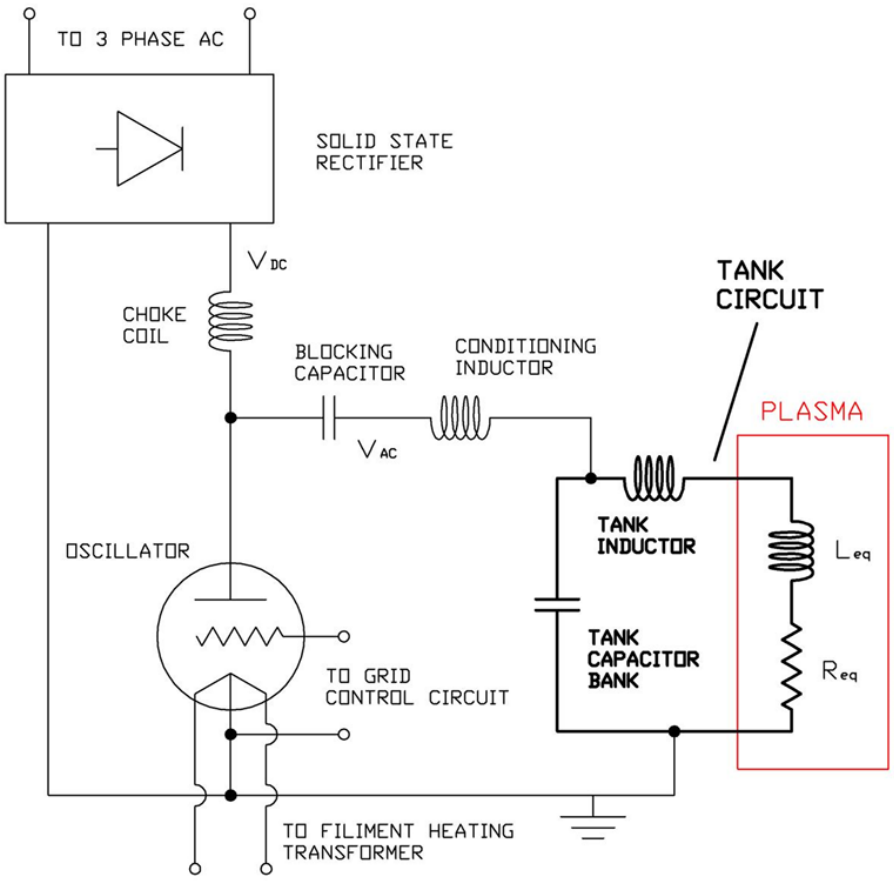

Figure 4: Wiring diagram of the RF power supply and tank circuit

The parallel tank circuit was experimentally tuned by following the trends expressed in equations 1 and 2 [10].

$$Frequency = \frac{1}{2\pi\sqrt{LC}} \quad \text{eq. 1}$$

$$Impedance = \frac{L}{RC} \quad \text{eq. 2}$$

The product of the total inductance *L*, and capacitance *C*, determines the operating frequency which must remain within the limits of the load resonant power

supply. Inversely tuning these parameters allows efficient energy transfer which occurs when the impedance of the tank circuit matches the operating impedance of the power supply. Where *R* is the tank circuit resistance.

3.2.4. Induction Region

The core components of the plasma creation include the coil, confinement tube, and the gas injection system. The assembly is based on a VKI design and can be seen in Figure 5.

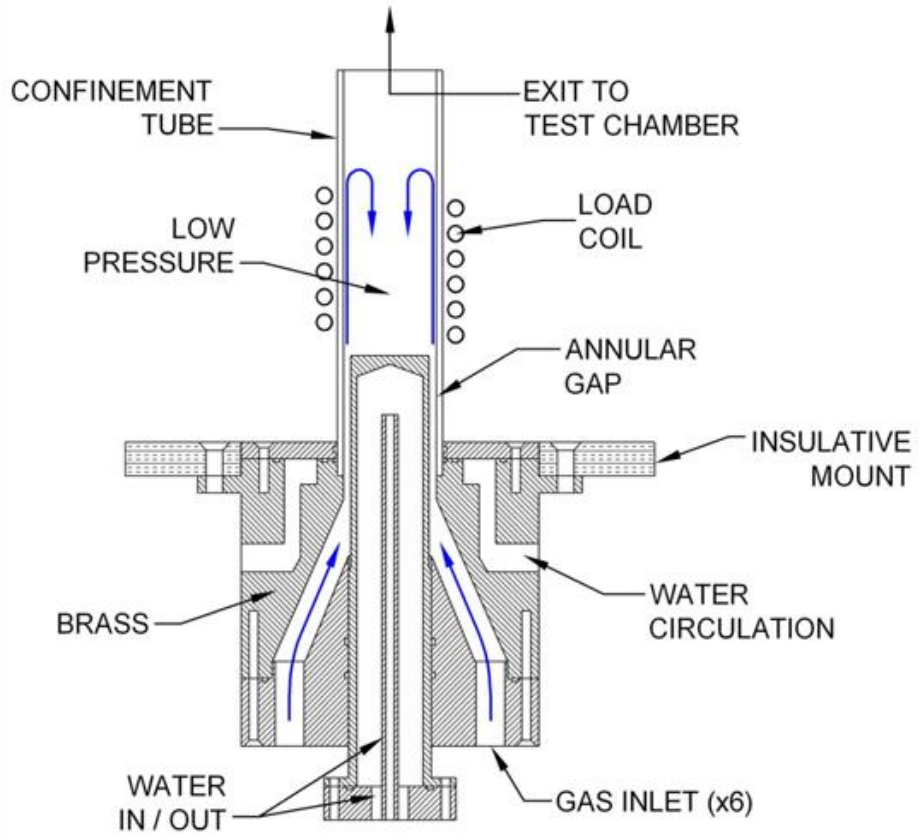

Figure 5: Plasma generation components

A tightly wound 6 turn helical coil provides a concentrated oscillating magnetic field within a 3.6 cm i.d. x 4.0 cm o.d. quartz tube. Quartz is used due to its high temperature capabilities and good electrical insulating properties. Annular gas injection creates a low pressure recirculation zone which sustains the plasma within the coil. This also provides a protective sheath gas that keeps the hot plasma from touching the quartz confinement tube. All brass components in the injection system are water cooled.

3.2.5. Control System

Operation of the small scale ICP torch can be carried out by one or two personnel using manual controls as well as a computer based system. Power and grid tuning takes place on the front panel of the power supply. Input power is calculated using the power supply gage display of the plate voltage and current. Gas composition, flow rate and static pressure are all monitored, controlled, and recorded during each test. The volumetric gas flow rate is reliably held at the desired rate using individual mass flow controllers. Each mass flow controller is externally driven using the computer interface and digitally displayed. Pressure is held steady at the desired condition using a PID controlled bypass valve at the inlet of the vacuum pump to assure consistency.

3.3. ICP Torch Operation

3.3.1. Start-up Procedure

To achieve the desired test conditions a simple but strict start-up procedure is required. The ignition of the plasma must be started at low pressures and a low flow rate

of argon before converting to the desired operating conditions. Argon is a monatomic gas that can be capacitively ionized by the high and low leads of the induction coil. This creates an electrically conductive glow discharge where power is then electro-dynamically transferred into the plasma within a specific skin depth depending on the operating conditions [11]. To prevent damage to the confinement tube, the gas flow rate is quickly increased forcing the plasma downstream into the re-circulation zone. This transition from the glow discharge to the proper coupling can be seen in Figure 6.

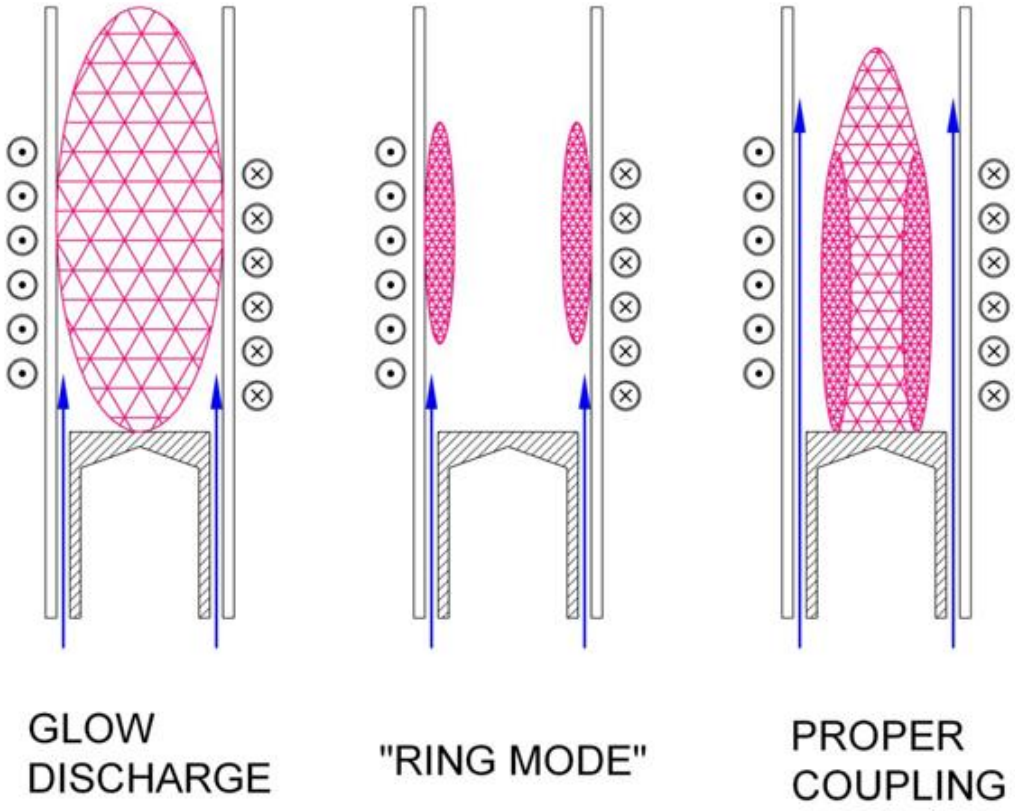

Figure 6: Argon plasma transition during start-up

The pressure is allowed to rise causing the plasma to constrict and move away from the walls of the confinement tube. Power can then be increased above the minimum sustaining power as the test gas is slowly added and argon is slowly removed. This procedure is graphically represented in Figure 7.

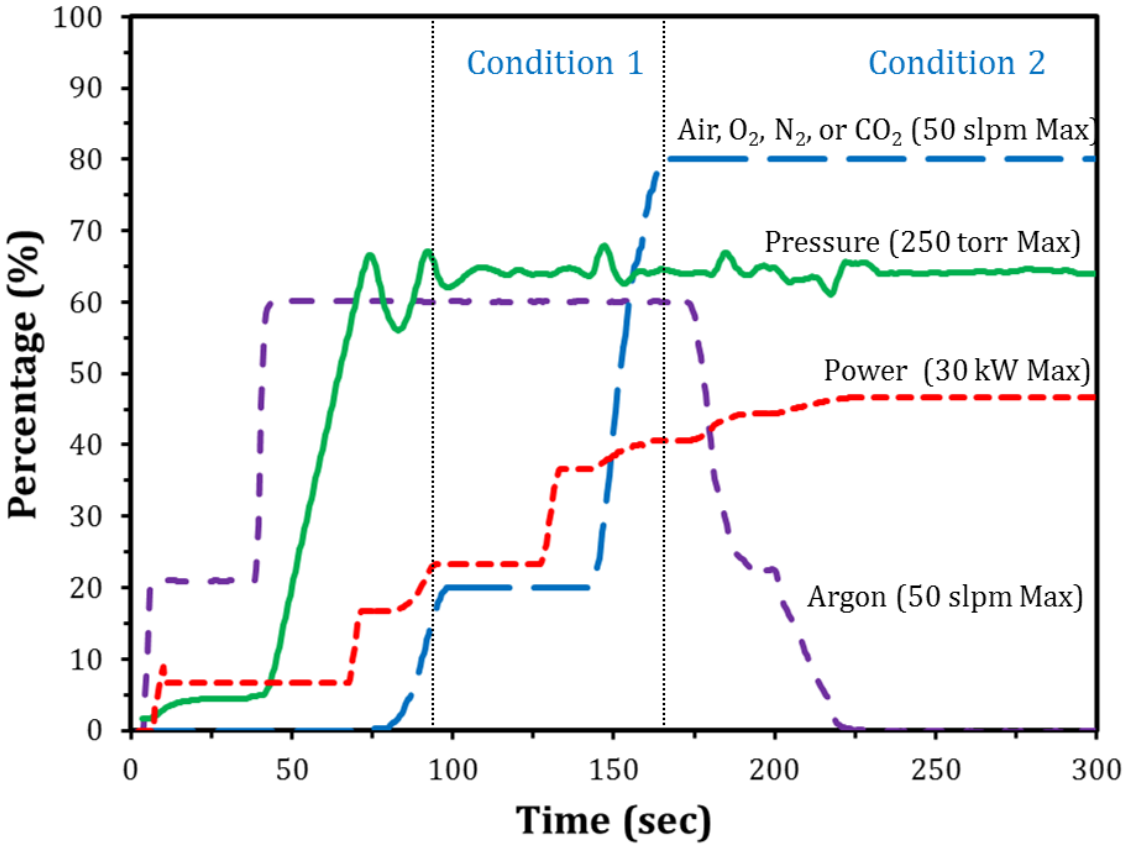

Figure 7: ICP Torch start-up sequence

Once 100% of the test gas is reached, the pressure, flow rate, and power can be adjusted to achieve the desired conditions. Within the stable operating envelope, the torch can run continuously with no further inputs. The uniform steady flow can then be used for all experiments requiring spectroscopic measurements.

The current configuration of the ICP Torch can provide long duration, contaminant free plasma flows using multiple test gases. A certain range of relevant post-shock conditions of Mars and Earth hypersonic entry trajectories can already be replicated but its operating capabilities are continuously improving; including peak heat flux, test gas composition and static pressure range. The operating gas compositions that have already been tested are nitrogen, air, oxygen, carbon dioxide or admixtures depending on the reaction and species of interest. Despite the fact that the ICP Torch can run on pure gas plasmas, a high sustaining power is required which can lead to very harsh conditions. Some test gas mixtures are diluted with argon, in turn lowering the minimum sustaining power and thereby allowing softer plasma conditions. Argon can also be used to decrease the partial pressure of a desired test gas if needed. This has proven useful for oxidation analysis.

3.3.2. Operating Envelope

Characterization of the material performance as well as the plasma conditions that the material is exposed to are essential to extrapolate the ground test results to flight conditions. Pressure, gas flow rate, and operating frequency are all measured directly in order to quantify the experimental conditions. A combination of experimental measurements and computational analysis allows the remaining plasma conditions to be determined. The tested operating conditions can be seen in in Table 2.

Table 2: ICP Torch Operating Envelope

Run Duration	0 – 90 *min.*
Heat Flux	10 - 150 $W\ cm^{-2}$
Free Stream Temperature	1000 – 8000 $°C$
Static Pressure	80 – 250 *torr*
Dynamic Pressure	2.5±.5 *torr (sub sonic configuration)*
Gas Composition	N_2, Air, CO_2, O_2, Ar *(or add mixtures)*
Inlet Gas Flow Rate	25 – 50 *slpm*
Flow Velocity	>130 $m\ s^{-1}$
Mach Range	.2 – 1.5
Operating Frequency	2.5 *Mhz*
Peak Power	30 *kW*
Plasma Jet Diameter	3.6 *cm*

Heat flux and velocity were calculated using equations 3 and 4, respectively. The Mach number was determined numerically [12] and laser induced florescence was used to determine the free stream temperature. These diagnostic techniques are described in further detail in later sections.

3.4. Plasma Characterization

3.4.1. Intrusive Probes

Manually controlled sting arms are designed to hold interchangeable diagnostic equipment and test samples in stagnation point configuration. This configuration is used to provide the thermophysical and chemical environment rather than the aerodynamic shear component of hypersonic flight.

A machined brass sting arm can quickly insert the test samples into an already established stable plasma stream. The brass sting arm holding a sample in stagnation point configuration can be seen in Figure 12 of Chapter 4. Three concentric tubes provide water cooling throughout the sting and probe head. This allows material surfaces that require water cooling to sustain long durations in the plasma flow. This sting uses o-ring seals and is bolted together making it easy to interchange individual mounting configurations between test campaigns. An adjustable external support permits radial and axial movement during operation. The axial degree of freedom of the brass probe allows the heat flux on the material surface to be easily adjusted by raising or lowering the sample. Samples are carefully centered, as a 20% heat flux reduction is possible if the sample is misaligned. The brass sting arm holds the sample at a floating potential by electrically insulating it from the rest of the test chamber.

A simple copper sting was also designed and built to allow multiple experiments to take place throughout continuous ICP Torch operation. A central vacuum-sealed tube easily allows external access to the head of the probe therefore most experiments requiring back face temperatures also use this probe. Its gooseneck design allows the probe to be tucked out of the way while not in use. The sting is constructed of copper tubing with internal plumbing providing water cooling throughout. The semi-permanent sweat copper joints limit its versatility but it has still proven valuable for mounting heat flux calorimeters while the brass probe typically holds the material samples.

3.4.2. Pressure Measurements

The static pressure was measured through a pressure tap located in a lower port on the test chamber. An ambient temperature capacitance manometer and digital meter provide a continuous display of the static pressure for a full scale pressure range of 1000 torr.

The dynamic pressure is measured in the plasma flow with a pitot tube mounted in a stagnation point configuration. 6mm diameter internal routing within the sting arm connects the pitot probe to the pressure transducer. For subsonic conditions, a differential pressure transducer rated for ±10 torr is used. Total pressure is then determined using the dynamic and chamber static pressures. For Mach numbers less than 0.3, velocity measurements were calculated using the following equation.

$$v = \frac{\sqrt{2(P_{total} - P_{static})}}{\rho_{gas}} \qquad \text{eq. 3}$$

where v is the velocity, P is the pressure and ρ_{gas} is the density of the gas. Even though the ICP can provide supersonic flows [12], all test cases in this study were performed in the subsonic flow regime which can still provide the boundary layer conditions typical of a supersonic flow [185]. Although, the dynamic pressure was less than 2% of the total surface pressure [12], hence the chamber static pressure is used to control the material surface pressure.

3.4.3. Heat Flux

In reentry conditions, heat flux plays an important role in material behavior. Owing to the efficiency losses of the oscillator tube, water, and transmission lines, the power supply input power does not linearly correlate to the power into the plasma. Therefore intrusive calorimeters held in the plasma flow provide the stagnation point heat transfer rate at the same location as material testing. Besides quantifying the test conditions, heat flux measurements can also be used to assure consistency throughout the duration of a single test, between different experiments and as a way to make comparisons between different facilities. For this test campaign a thermal capacitance calorimeter is used to measure the cold wall heat flux. The design uses a copper slug with a thermocouple fixed to the back side. The calorimeter works with the assumption of one-dimensional heat conduction into a cylindrical piece of material (slug) with known physical properties. The current design minimizes radial conduction loss although it does still exist; thus the slug calorimeter inevitably gives conservative results. Using the temperature-time curve recorded by a back-face thermocouple, and knowing the slug's dimensions and material properties, the heat flux q, can be calculated using the following equation [13]:

$$q = l\rho_{slug}c_p\frac{dT}{dt} \qquad \text{eq. 4}$$

Where l is the length of the slug, ρ_{slug} is the density of copper, c_p is the specific heat of copper and $\frac{dT}{dt}$ is the change in temperature vs time taken from the thermocouple

measurement. The calorimeter reliability has been established through repeatability and with comparisons to a gardon gage and water cooled designs.

Even though all samples and calorimeters have the same outer diameter and edge radius, it is imperative to note that the measured heat flux by the copper slug does not accurately predict the heat transfer to the coupon surface due to the difference in gas / surface interactions [14].

3.4.4. Spectroscopic Techniques

Abundant optical access of the material surface allows in-situ characterization of the experimental conditions within the reacting boundary layer. Five viewports provide direct line of sight of the test material for non-intrusive diagnostic measurements. Three 15 cm round fused silica windows located on the chamber are arranged orthogonally enabling multiple spectroscopic techniques to be implemented simultaneously. Due to the fact that the facility can operate at steady conditions for long durations an extensive set of measurements can be performed for each test. The vacuum chamber and diagnostic configuration can be seen in Figure 8.

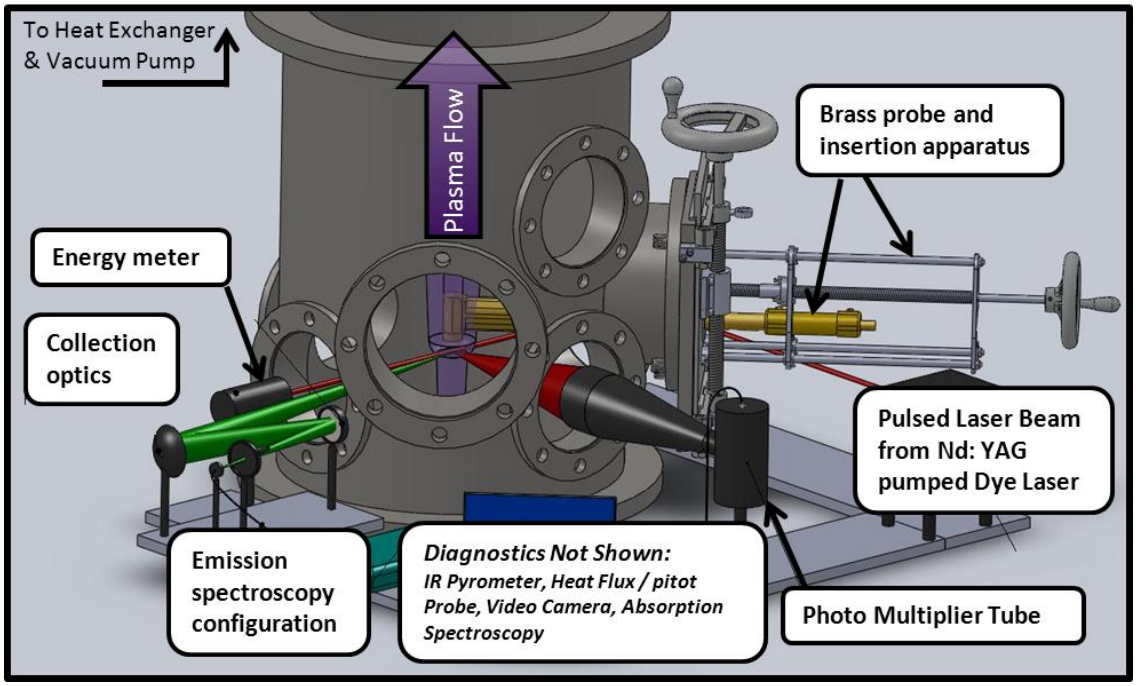

Figure 8: Optical access for spectroscopic measurements. Angled viewports with direct view of the surface are not shown [courtesy J. Uhl]

Two angled viewports located on the base plate provide a direct view to the leading edge of the test sample. If needed, the congruent angles of each viewport allow for any diagnostics requiring reflection off the surface. Currently an infrared pyrometer utilizes one of these ports to perform continuous material surface temperature measurements, while the other can simultaneously be used for surface imaging.

An arsenal of spectroscopic techniques with high spatial resolution can be used to detect a wide range of atoms and molecules within the reacting boundary layer. The chemical composition of the plasma and the species of interest will determine the diagnostic technique used. For all spectroscopic measurements, translation stages allow for scanning in the axial and radial directions.

For some tests, an Ocean Optics HR-4000 series spectrometer was used to make temporally resolved measurements in the boundary layer. This emission spectrometer allowed assessment of the material integrity by monitoring volatilizing species coming from the sample within the detection range of 200 – 1100 nm with a spectral resolution of 0.27 nm. This wavelength range allows detection of N atom, O atom, CN, NO and N_2 as well as silicon carbide oxidation products such as Si, SiO and SiO_2. Mirrors located approximately 60 cm from the plasma axis form the conical collection envelope across the entire material surface and reflect the emission into an Ocean Optics P400-2-UV-VIS fiber optic cable that is attached to the spectrometer. The fiber optic cable is 2 meter long, 400 μm in diameter and rated for wavelengths between 300 nm and 1100 nm. The optical configuration can be seen in the Figure 8.

Spatially resolved measurements were performed using a Nd:YAG laser system which has proven the ability to detect O atom, N atom and CO through two photon absorption laser induced florescence (LIF) [15][16]. Single photon LIF has also been shown to detect the presence of NO. A schematic representation of the experimental configuration for the laser measurements is shown below in Figure 9.

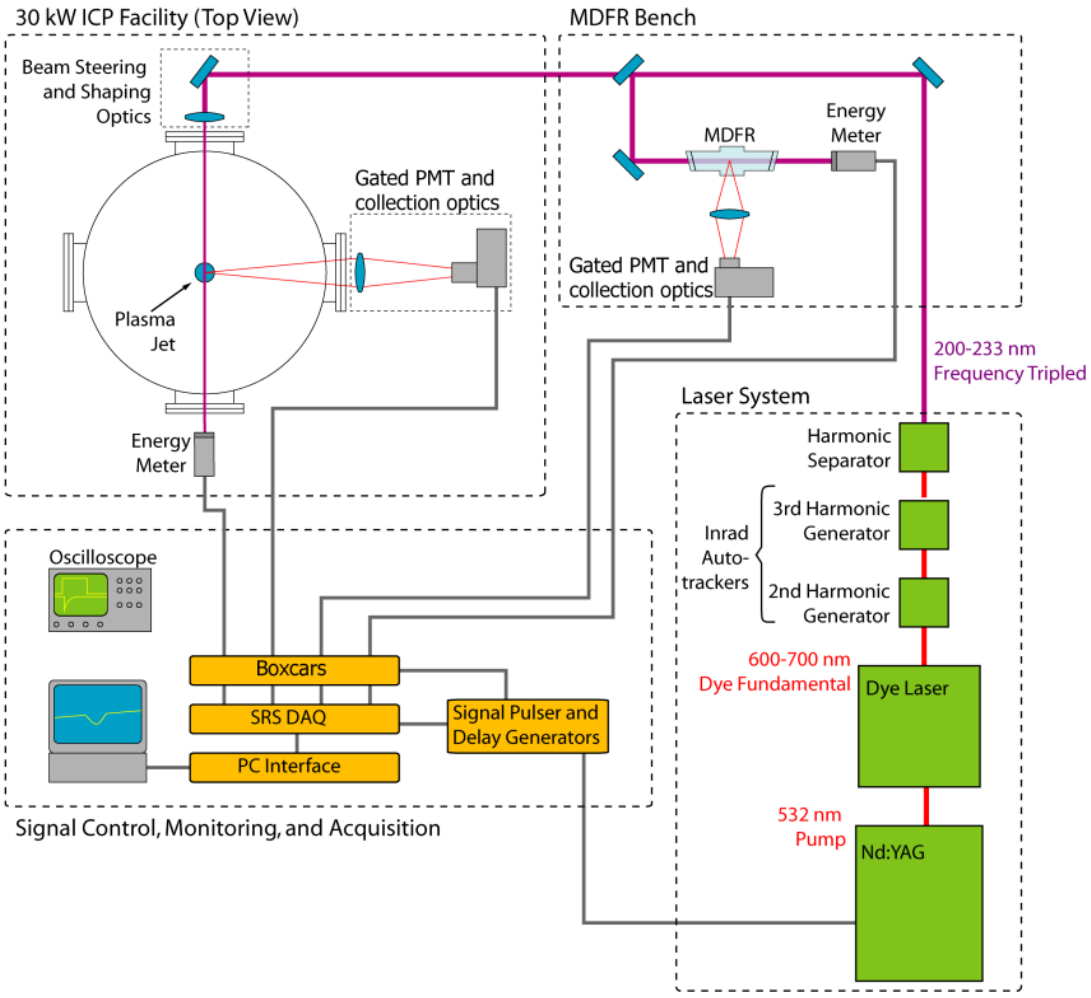

Figure 9: Schematic of the approximate laser beam path configuration. Additional steering optics and beam dumps are not shown. [courtesy J. Meyers].

A frequency-doubled Nd:YAG pumped dye laser emits visible light that is then frequency tripled through a series of nonlinear optical crystals to generate ultraviolet light at wavelengths from 207 to 232 nm. The UV output of the laser system is split into two paths; one traveling to the ICP Torch and the second to a microwave discharge flow reactor. The flow reactor provides a simultaneous population of the target atoms or molecules at a known temperature (293 K) and pressure (0.5 torr). Laser scans are

performed over the desired transition wavelength and the fluorescence is collected perpendicular to the laser beam path using a photomultiplier tube at each location. A delay generator correctly synchronizes the data acquisition system with the laser pulse. Using the measured laser line widths and the known conditions in the flow reactor, the gas temperature within the ICP torch can be calculated.

3.4.5. Computational Analysis

The input power is adjusted in order to control the heat flux, although many influential plasma flow characteristics also change including; gas dissociation fraction, flow dynamics, electrical potential and radiation intensity. Whereas, the degree of dissociation of molecular species increases with increasing temperature until relatively high temperatures at which atomic species begin to ionize. Assuming local thermodynamic equilibrium at these conditions, the MUTATION code can be used to show this temperature dependence [17]. The species mole fractions are plotted for an air plasma at 160 torr from 600 to 10,000 K.

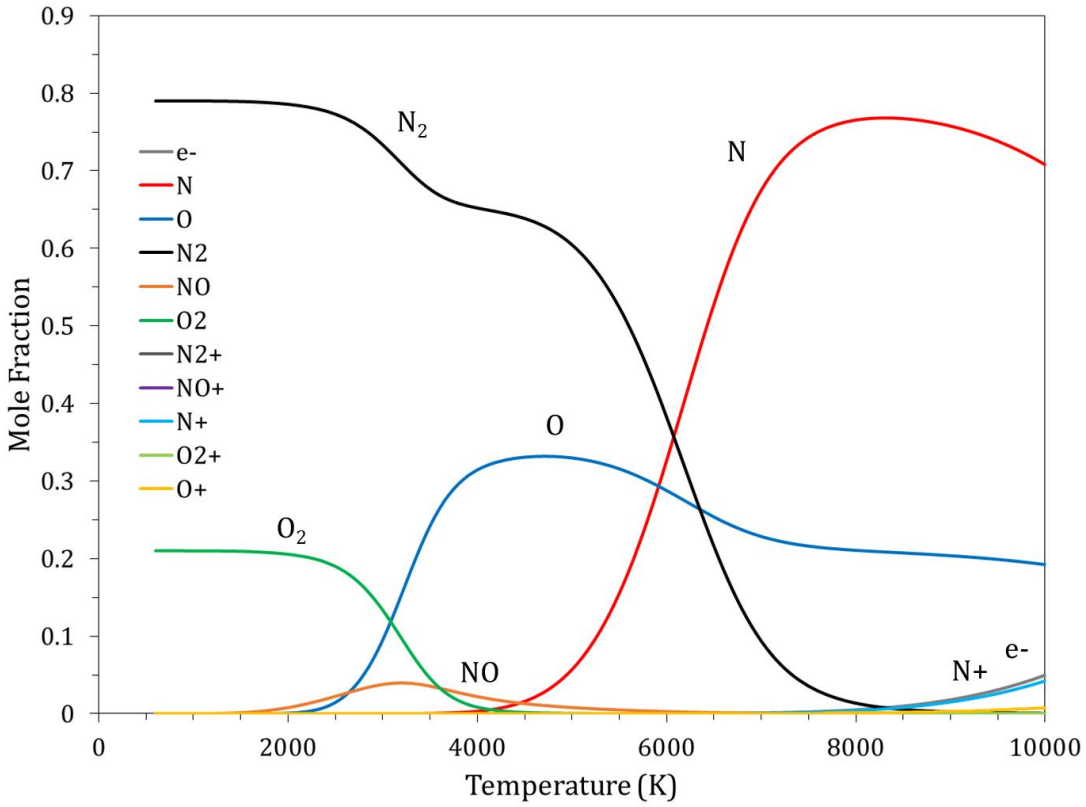

Figure 10: MUTATION Mole Fraction vs Temperature plot at 160 torr [Courtesy A. Lutz]

Free stream temperatures derived from LIF measurements of nitrogen and oxygen atoms at similar conditions to those used in this study ranged around 6500 K [18]. Figure 10 shows that in air plasmas for this temperature range, nitrogen exists in both atomic and molecular states. Whereas, oxygen is almost completely dissociated and was experimentally confirmed as seen in appendix A.

CHAPTER 4: AEROTHERMAL SCREENING OF CANDIDATE FLEXIBLE THERMAL PROTECTION MATERIALS

4.1. Introduction

Flight testing of TPS materials can be very expensive, therefore ground testing facilities are used to first screen and qualify candidate materials. With this in mind, the 30 kW ICP Torch was configured specifically to expose candidate woven outer fabrics to aerothermal heating conditions relevant to atmospheric entry. Different analysis techniques can be carried out to quantitatively and qualitatively characterize the aerothermal performance of the material. This chapter describes the experimental configuration and diagnostic equipment used throughout this study. The high temperature screening results for different 2-D woven materials is also presented.

4.2. Experimental Set-up

4.2.1. 2-D Woven Materials

The search for candidate materials to be used as a flexible outer fabric began in 2007 through analytical and experimental screening of off the shelf materials [2]. Besides being flexible, candidate outer fabrics must have high continuous use temperatures, high emissivity, low catalycity, and produce limited particulate [2]. Investigations by several test facilities are ongoing to evaluate the performance of individual materials as well as different layup configurations. Numerous possible outer fabrics have been eliminated while other materials have been deemed viable and require further evaluation [2]. To date, SiC fabric has shown great promise and has been

proposed as the second generation flexible outer fabric material [2]. To convey the superior performance, 2-D woven Hi-Nicalon SiC fabric was compared against Nextel BF-20, Kevlar and carbon fiber. A brief overview of each material is presented;

- Nextel BF-20 fabric is woven from Nextel 440 ceramic fibers with a 5 harness satin weave. These aluminoborosilicate fibers are used for high temperature industrial applications and can withstand temperatures up to 1370°C [19]. This material is considered the first generation material and has been successfully flight tested as an outer fabric for the Inflatable Re-entry Vehicle Experiment [20].

- Kevlar is a H-C-N-O fiber that is known for its high tensile strength. Due to this strength, current TPS designs use Kevlar as a structural TPS layer and to stitch the outer fabric to the rest of the TPS [1]. Kevlar was tested with a braided weave type and had the largest bulk thickness and largest diameter tows.

- Carbon materials have many beneficial properties making them suitable for high temperature applications. Carbon felts are currently being tested as a flexible thermal insulation that is placed behind the outer fabric. Even though the oxidation of carbon can be very damaging, the performance reported for graphite at extremely high heating conditions has actually been shown to far exceed those reported for SiC [21]. In-turn, impregnated 3-D carbon weaves are being investigated for

heating conditions beyond the survivable limits of SiC fabric [22]. The carbon fiber material used in this campaign was tested as a 2-D plain weave.

The following table shows the material properties of the tested fabrics.

Table 3: Tested coupon properties

Material Properties	Carbon Fiber	Kevlar	Nextel BF-20	Silicon Carbide
Composition	C	H-N-C-O	Al-B-Si-O	Si-C
Weave	Plain	Braid	5 Harness Satin	5 Harness Satin
Bulk Thickness (cm)	0.02	0.06	0.05	0.05
Coupon Mass (g)	0.05	0.15	0.17	0.13

An image of each as-received weave type can be seen in the following figure. The increments along the scale are in mm.

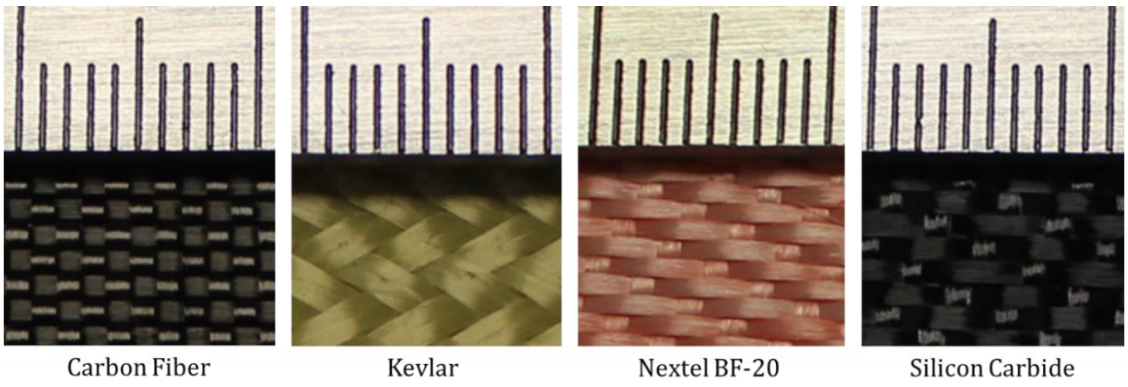

Figure 11: Surface image of the fiber weave types.

4.2.2. Material Test Configuration

In order to test the candidate flexible outer fabric materials, most 2-D weaves were mechanically punched into 20 mm diameter circular coupons. The braided Kevlar fibers could not be mechanically punched into coupons, therefore circular pieces had to be manually cut to fit within the coupon holder. The coupon holder was developed in collaboration with NASA Langley Research Center and modeled after the design for HYMETS. The mounting apparatus uses a clasp design that holds the coupon in the center of a 25 mm outer diameter sintered SiC sleeve. The secured outer edges of the coupon limit the actual exposed diameter to 18 mm while providing a standardized edge chamfer with a radius of 3.2 mm. The standardized sample holder geometry assures boundary layer uniformity between the sample and calorimeters which can significantly affect the surface heating. An original sample holder sleeve was made from two phase, reaction cured SiC but pores through the fragile 0.2 mm thick SiC coating allowed carbon to leach out and interfere with the material performance. A sintered SiC backing piece sits behind the fabric coupons and is contoured to provide a semi-flush leading surface between the coupon and the sleeve edge. Care is taken to assure consistency in the assembly, although seating of the outer fabric coupon can cause a fabric/sleeve offset of approximately ±0.5 mm.

Two outer fabric coupons were tested simultaneously with a leading and sub layer. The leading ply is exposed directly to the plasma flow while the sub ply is mildly protected between the leading ply and the SiC backing piece. To limit conduction losses

and maximize heating a ZIRCAR RSLE-57 refractory insulator thermally isolates the coupon from the copper stem. A view of the component assembly used in the nitrogen plasma campaign is shown below. A central hole through the holder components not shown in the photo allows thermocouple access to the lead ply.

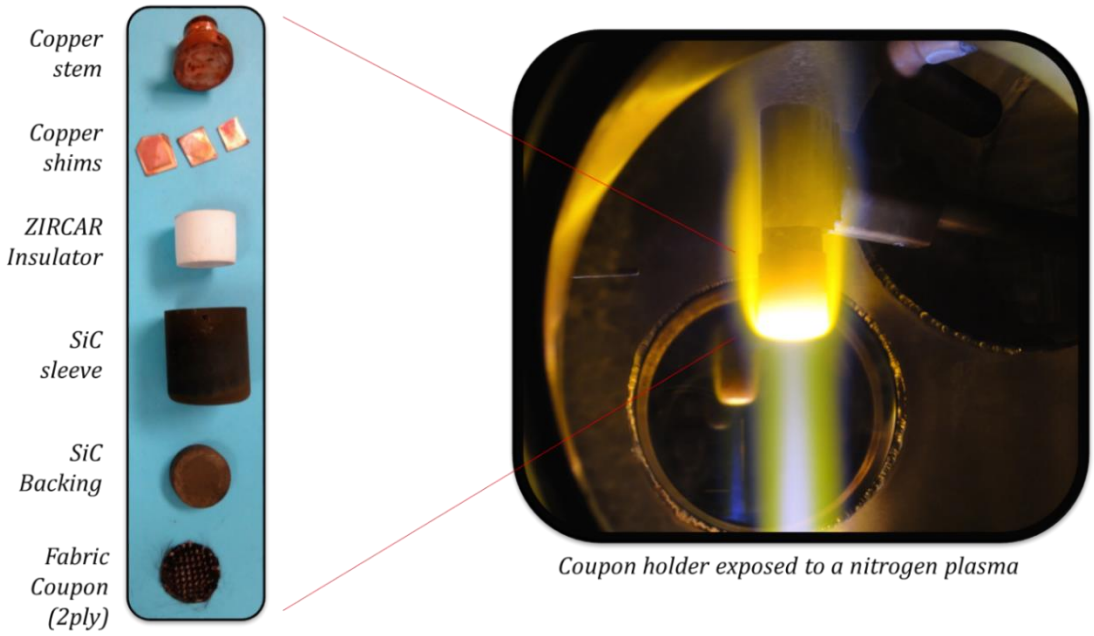

Figure 12: Exploded view of the two phase β-SiC coupon holder after exposure to 80 minutes of nitrogen plasma.

Each layer of the coupon holder within the outer SiC sleeve is not hermetically sealed and potential contamination from the copper shims, zircar insulator or other components cannot be ruled out.

4.2.3. Test Procedure

The performance of the 2-D woven fabrics was assessed for re-entry conditions through exposure to the high enthalpy air plasma. The flow rate and chamber pressure were held constant, for the entire duration of the plasma test. The following table shows the exposure conditions for the air plasma tests.

Table 4: Air plasma test conditions

Test Gas	Air (bottled)
Operating Power (kW)	14
Plasma Composition	N_2, N, O_2, O
Mass Flow Rate (g/min)	49
Static Pressure (torr)	160
Dynamic Pressure (torr)	2.5±.5
Heat flux (W/cm^2)	80

Samples were radially inserted into the steady plasma flow column and were stored in a cooler recirculation zone before and after each test. This insertion procedure led to a large thermal shock and an extremely rapid temperature rise. Figure 13 shows the radial temperature profile of the plasma column and re-circulation zone.

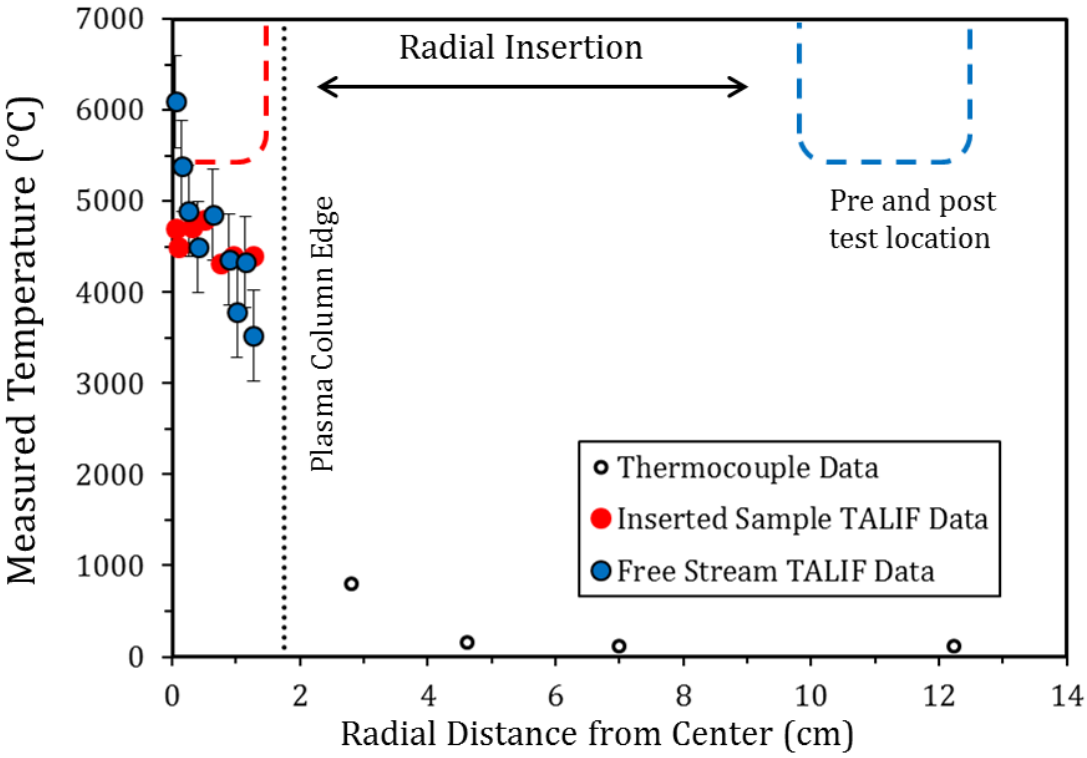

Figure 13: Diagram showing the sample exposure temperature during the insertion/removal procedure.

Gas temperature measurements in the plasma flow and chamber recirculation zone were made using two different diagnostic techniques. Thermocouples were used to determine the gas temperature outside the plasma flow column. Within the plasma, laser induced fluorescence was used. The gas temperature measurements with the inserted sample were taken within the thermal boundary layer over a quartz surface in an oxygen/argon environment. Free stream measurements were taken at the same axial height after the sample was removed from the same oxygen/argon plasma.

4.3. Material Performance Characterization

4.3.1. Video Recording

A Canon VIXIA HF M300 records 2.99 megapixel, high definition video of the fabric leading surface or sample profile during operation at 30 frames per second. For surface imaging, the camera is located 30-40 cm from the surface of the material at an angle of 23° to 30° off normal depending on the axial positioning of the sample. The diagnostic equipment configuration is presented in Figure 14.

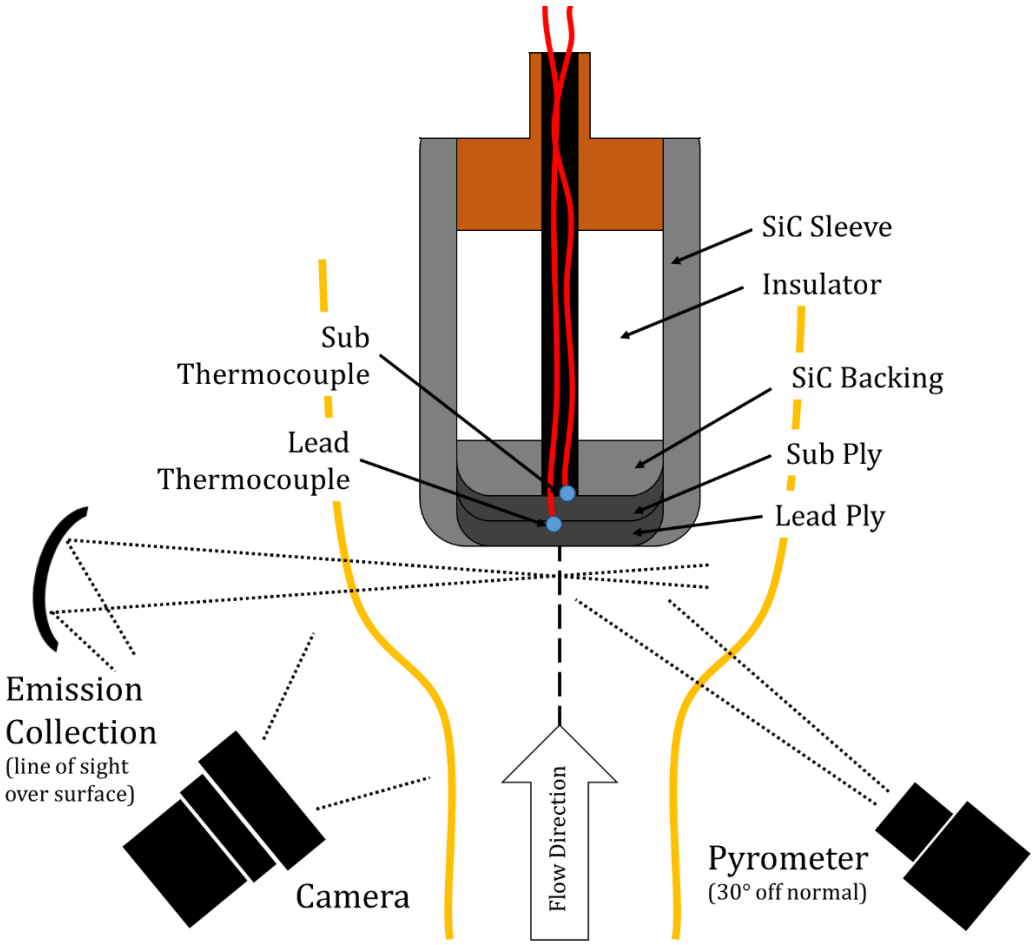

Figure 14: A not to scale schematic of the diagnostics techniques that can be used to make direct assessment of the coupon performance.

Significant features of the material evolution are easily observable on the surface of the fabric during operation. Manual focus and automatic light intensity adjustment allows for continually sharp images for the duration of the test. Profile videos taken perpendicular to the plasma axis can also be useful for ablative or sublimating materials. A computer code is used to detect the surface profile from video footage frame by frame and calculate recession rates. This data combined with spectroscopic measurements can be useful to determine basic material evolution analysis.

4.3.2. Infrared Pyrometry

Determining the surface temperature is critical for evaluating the material performance as well as assuring consistency between tests. However, due to the harsh heating environment, confidence with surface temperature measurements is always a concern. Physical constraints and the relatively low temperature capabilities of thermocouples makes them not suitable for this type of application. In order to measure the surface temperature of the fabric coupons at higher temperatures a remotely located optical pyrometer is used. Care must be taken when selecting a pyrometer as they are not universal and must be chosen for specific applications. The pyrometers used in this study are a Marathon Series MR1SACF (600°C-1400°C) and MR1SCCF (1000°C-3000°C). Measurements are recorded from the linear analog output of the pyrometer. The pyrometer has a high sampling time of 10 milliseconds but the recorded data is limited to 2 hz by the ICP Torch data acquisition system. The long transition lines from the pyrometer to the DAQ adds noise to the system averaging around ±5°C but depends on the operating conditions. The pyrometer has direct view of the surface through an optical window which has over a 90% transmittance for the entire pyrometer operating wavelength. The pyrometer has a focusing range from 30-60 cm and is located at the same distance and angle as the camcorder. The pyrometer is aligned using through-the-lens sighting. 95% of the energy is collected within a measurement spot size of approximately 3 mm for the high temperature pyrometer and 7 mm for the low temperature pyrometer at the distance tested [23]. For all the experiments in this study, the entire coupon is within the sighting reticle.

Both pyrometers used can perform measurements in 1 or 2 color mode. Each mode has its advantages and disadvantages. The single wavelength band measurement is made from the absolute radiated energy within the wavelength band of 0.75 to 1.1 μm. Whereas the radiation collected by the pyrometer can be comprised of a complex mix of reflected, transmitted and re-radiated emission in addition to the emitted radiation from the material as seen in the following figure.

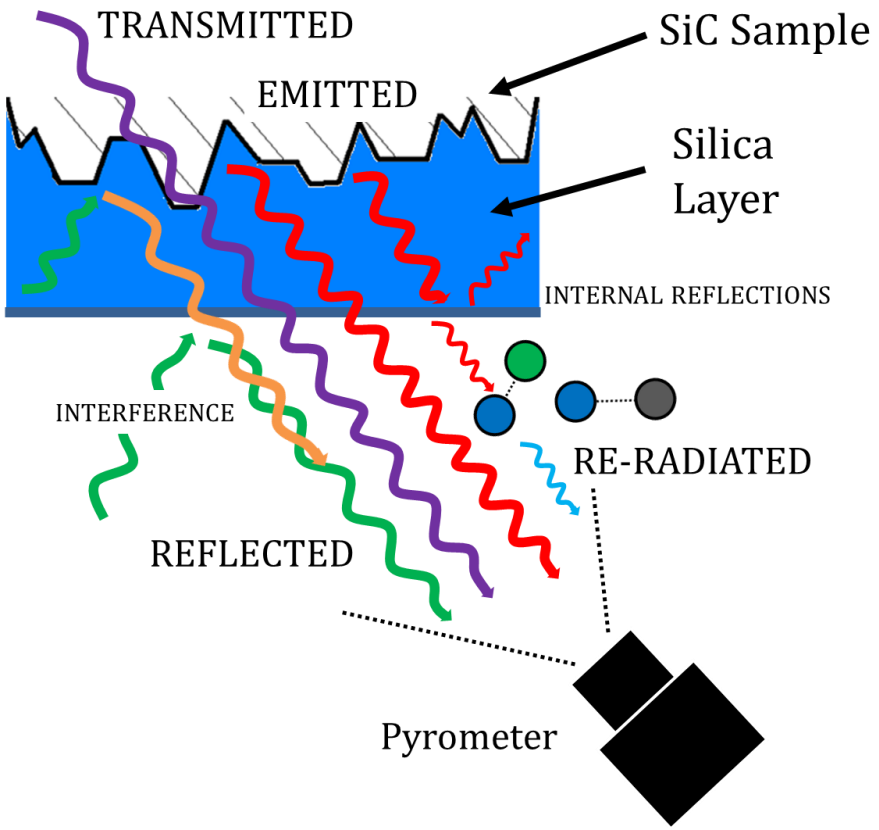

Figure 15: Image showing the emission collected by the pyrometer over an oxidized SiC surface.

Ideally the object being measured should be opaque, however the transmittance of the weave is dependent on the sample viewing angle [24]. Therefore the presence of a sub ply can affect the pyrometer measurement when the measurements are made off normal to the surface.

The single band measurement can give reliable results as long as the emissivity of the material is known for the desired operating conditions. However, the emissivity can change with time as the material surface evolves making it difficult to determine. Any energy transmission reduction through dirty windows or lenses will inevitably lead to lower measured temperatures. The 1 color mode will provide an average temperature within the sighting reticle and has limited use for objects that do not completely fill the optical collection envelope.

The 2 color mode uses dual wavelength bands to determine the temperature. The pyrometer electronics automatically converts the temperature into an analog signal using the energy ratio between 0.75 to 1.1 μm and the coinciding 0.95 to 1.1 μm wavelength band. This allows reliable measurements to be taken if the emissivity is not known and therefore is most commonly used in the lab due to its ease of use. Unlike the 1 color mode, the 2 color mode detects peak temperatures within a measured region providing better results when the surrounding environment is much cooler than the target [23]. Another advantage of this setting is that it can still make quality measurements up to 45 degrees off normal where 1 color losses reliability over 30 degrees.

The accuracy of the pyrometers and the consistency of the facility has been checked by comparing results of the high and low temperature pyrometers for their overlapping temperature range from 1000°C to 1400°C. Although, surface temperature measurements on low emissivity materials such as Nextel BF-20 or during oxidation of SiC have shown unrealistic results when compared to thermocouple measurements. Due to the 2 color modes high sensitivity to optical interference effects observed on SiC oxidized coupons, all SiC surface temperatures below 1200°C are measured using 1 color mode. However, uncertainty in the 1 color results does still arise due to the temporally changing emissivity during oxidation.

4.3.3. Thermocouple Measurements

Thermocouples are known to be very reliable for most test cases and can be used to determine the conduction through the SiC fabric. In addition, thermocouples can assess the accuracy of the pyrometer measurements through back face temperatures on the lead and sub ply. A rough estimate of the material surface temperature can be made using the temperature drop across the sub ply with the assumption that there is a similar temperature drop across the lead ply. Although, the conduction coefficient is expected to change with temperature, gas composition, exposure time, oxidation state, pressure and thermocouple placement. Thermocouple placement can be seen in Figure 14. A central hole through the holder components allows thermocouple access to the SiC coupons.

For test conditions below 1000°C, Omega 5TC Series, type E thermocouples with glass braid insulation were used and data was recorded using a National Instruments DAQ. Type E thermocouples provide the largest EMF per degree [25], in turn minimizing the influence of electronic noise produced from the plasma. At higher temperatures, type K thermocouples were used. Except for the initial melting of the glass braid sheathing at temperatures above 482°C [25] and when the coupons undergo catastrophic failure, the thermocouples provided smooth consistent data with very little noise.

4.3.4. Mass Change

Quantitative mass measurement results between the pre and post-test samples were not reliable or repeatable for fabric samples. Component fusing due to chemical reactions during plasma exposure made the cross contamination of particulate upon disassembly almost impossible to avoid. This caused a large scatter in mass measurements of the fabric coupons. Therefore mass change results were not used in the material analysis.

4.3.5. Microscopic Analysis

Qualitative analysis through surface imaging was used to provide clues of the microstructural and morphological evolution of the material. Digital photographs

allowed side by side comparisons of pre and post samples after high temperature exposure.

A scanning electron microscope (SEM) was also utilized in order to analyze the transient morphology of the fabrics. The JEOL 6060 microscope used in this study is a high-performance, compact, scanning electron microscope that has excellent secondary electron and back scattering electron resolution. High definition microscopic imaging of the fibers was possible without any treatment or coating although the low electric conductivity of highly oxidized SiC samples caused some electrostatic charging. The SEM is equipped with an energy dispersive x-ray microanalysis system (EDS) from Oxford Instruments. EDS is a valuable tool that allows semi quantitative elemental characterization of the sample.

A Keyence VHX digital microscope is also a highly valuable tool for characterization of the surface morphology due to its ability to take high resolution microscopic color photographs with optimal contrast. The Keyence microscope uses optical lenses and digitally stitched frames to create fully focused images through the entire depth of field.

4.4. Material Screening Results

Figure 16 shows the temperature vs time profile for carbon fiber, Kevlar, Nextel BF-20, and Hi-Nicalon SiC fabric for the first 120 seconds.

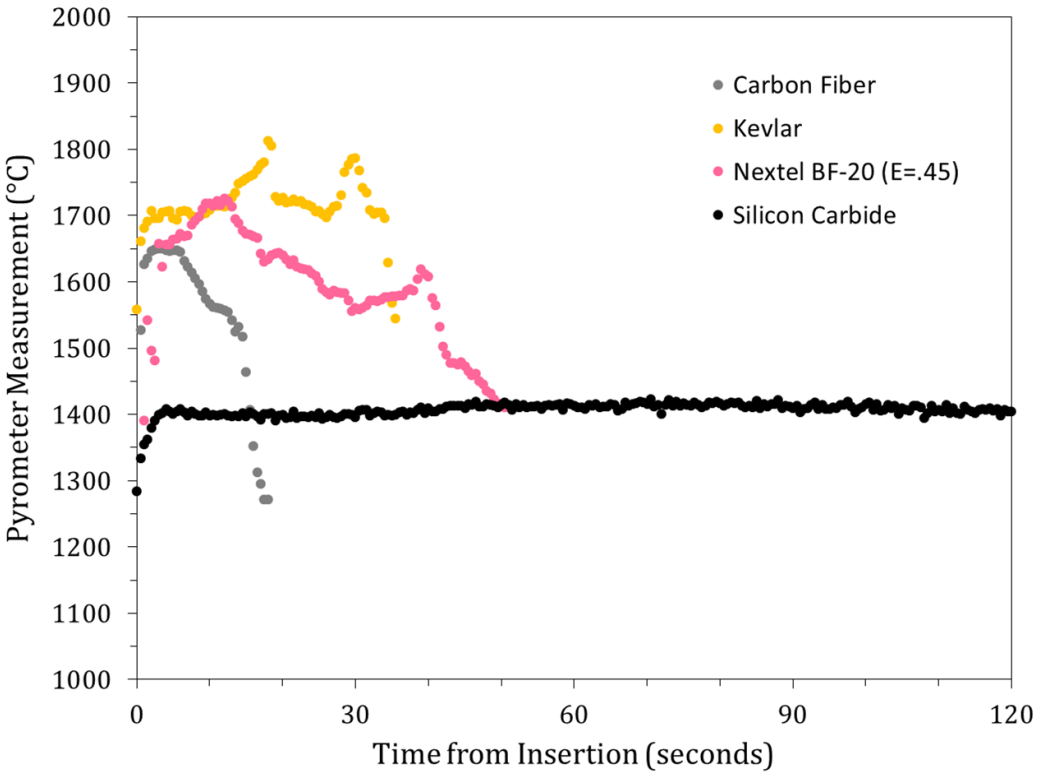

Figure 16: Surface temperature vs time plot of candidate fabric materials exposed to an air plasma

The Nextel BF-20 surface temperature was measured using 1 color mode with a set emissivity of 0.45 [26]. Surface temperatures for the other materials were measured using the pyrometer in 2 color mode. Large fluctuations in the pyrometer measurements were observed for all destroyed coupons due to the rapidly changing surface morphology and material removal during failure of the woven materials. The end of the pyrometer measurement occurred when the material was completely destroyed and the cooler SiC backing piece was exposed.

Even though all materials were tested at the exact same conditions, different surface temperatures are achieved due to thermal properties specific to each material including, emissivity, catalycity and reactivity. Figure 17 shows profile and surface images for carbon fiber, Kevlar, Nextel BF-20, and Hi-Nicalon SiC fabric at varying exposure times.

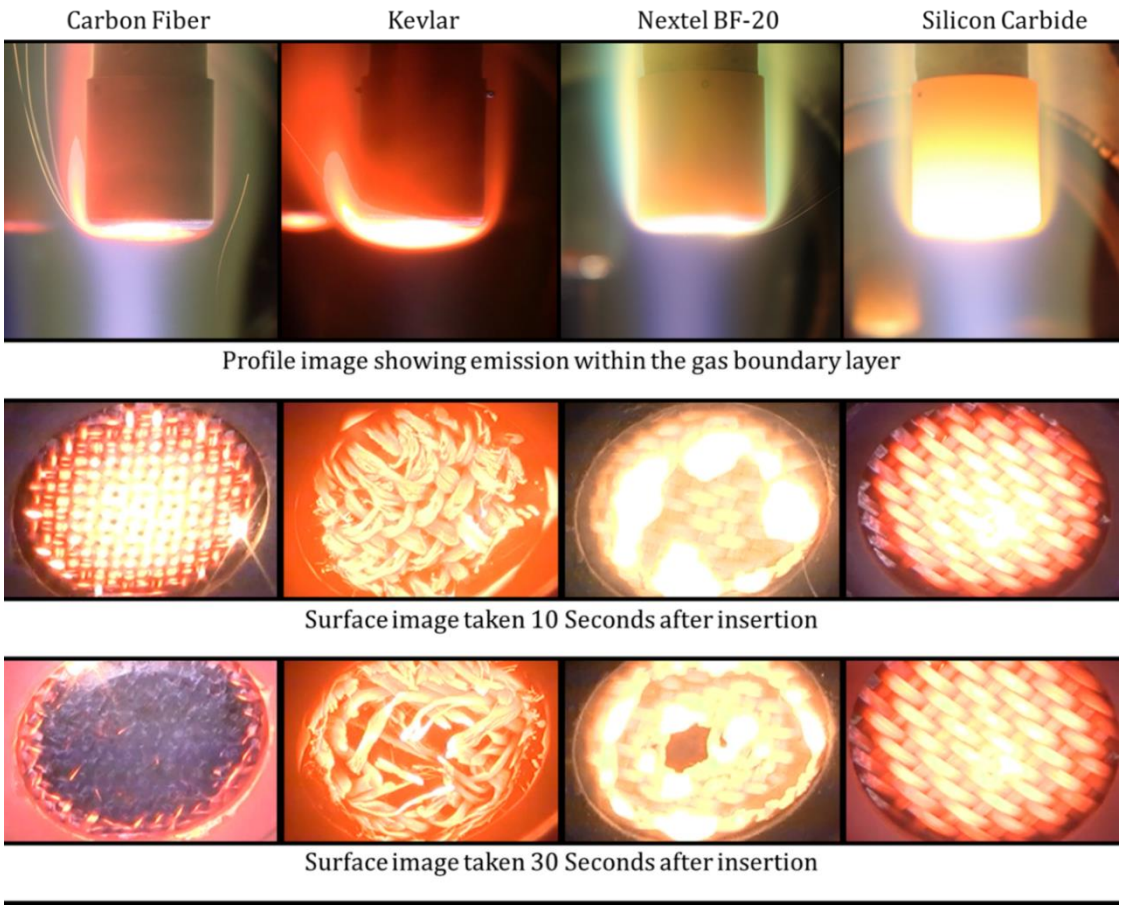

Figure 17: Profile and surface images taken during plasma testing

Profile images were taken immediately after insertion except for the silicon carbide sample which was taken when the sample reached a stable surface temperature.

SiC fabric achieved a surface temperature over 1400°C and was the only material to withstand more than 30 seconds in the 80 W/cm^2 air plasma. A few SiC samples had propagating flares that consumed individual tows, although the iridescence caused by oxidation and an increase in coupon stiffness were typically the only easily observable changes in the post test sample. All other materials displayed signs of spallation and decomposition immediately after insertion. Carbon was the thinnest coupon tested and was expected to experience significant oxidation. Flares on the surface were easily observable along with severe spallation. No carbon fiber coupon remains were observable after 60 seconds of exposure. Kevlar decomposition was visually observable through shortening and shrinking of fiber diameters along with a strong light emission. The Kevlar coupon took slightly longer to decompose but was also 3 times the thickness and weight of the carbon weave. A strong green boron dioxide emission was easily observable instantly after Nextel BF-20 insertion. Nextel coupons quickly melted into viscous pools that flowed on the surface, eventually leading to complete disappearance of the coupon.

CHAPTER 5: THEORETICAL AND EXPERIMENTAL ANALYSIS OF WOVEN SIC OXIDATION IN AN AEROTHERMAL ENVIRONMENT

5.1. Introduction

Despite the higher temperature capabilities of SiC fabric compared to Nextel BF-20, extensive testing performed by others in static heating environments has proven long duration exposure to oxidizing gas mixtures as a limiting factor in the versatility of SiC fibers [27]. Although, tests using room air or flowing molecular gases are far from the actual conditions of flight. In order to more accurately examine the oxidation performance of woven outer fabrics for atmospheric entry applications, SiC coupons were tested using the 30 kW ICP Torch which provides the radiative, convective and chemical heating more typical of hypersonic flight.

5.2. Silica Detection

SiC fabrics exposed to oxygen containing plasmas underwent a dramatic morphology evolution that was not uniform throughout the weave architecture. Microscopic analysis of post-test samples displayed a rapid silicon dioxide growth in the form of thick scales, bubbles and even hairs leading to an increase in fabric stiffness and brittleness. The SEM equipped with EDS was used to verify the formation of a thick silicon-oxygen layer. Just like decorative anodized components, the presence of the vitreous oxide layer was visually observable through a colorful iridescence pattern due to the thin film interference. These visible signs of oxidation occurred after exposure times on the order of seconds for temperatures above 1000°C. This is typical of many

investigators that have tested SiC based materials in high enthalpy oxidizing plasmas [28-46] including samples with positive erosion rates [30]. The following photos show the post test samples for the different test gases and EDS results of the oxidized sample.

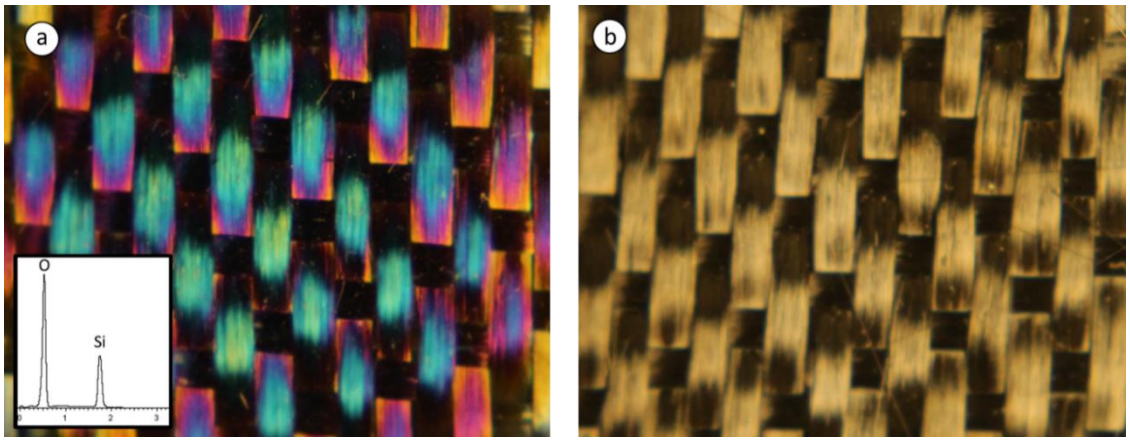

Figure 18: Photograph comparisons between a) an oxidized SiC sample (test condition: 30 slpm Argon / 10 slpm O_2, 160 torr, 1250°C) b) and a SiC sample exposed only to a nitrogen plasma (test condition: 40 slpm N_2, 160 torr, 1400°C). EDS analysis of the oxidized sample is also shown.

It can be seen that any SiC fabrics exposed to atomic oxygen bearing plasmas will lead to a surface that is significantly different in visual appearance and elemental composition than the virgin material or samples tested in pure nitrogen plasmas.

For exposure durations over 10 minutes at surface temperatures above 1400°C, thicker oxide layers form causing the surface to look glassy and black. Commonly observed protective oxide layers are amorphous SiO_2, cristobalite or a mixture. Although the clear glassy nature is typical of amorphous SiO_2 whereas cristobalite usually has a milky white appearance. For many high temperature applications of SiC, this formation of an oxide layer is considered as a beneficial phenomenon leading to lower SiC recession

rates; however it can have detrimental effects on the fine diameter, high surface area fabrics.

These observations of surface evolution are not unexpected seeing that the topic of oxidation on silica formers (Si, Si_3N_4 and SiC) has been studied since the early 19th century and continues today. Although, the many different techniques used in experimental studies have displayed drastically different results due to the immense number of oxidation complexities. Variations of flow rates, gas composition, heating methods, internal or external impurities [47], SiC microstructure [48], oxygen partial pressure, total pressure [49], and electrical potential [50] can all lead to contradictions throughout literature. In addition, the presence of atomic species in the oxidizing environment can also significantly affect the resulting surface structure or reaction rates [21, 51-55]. Therefore, it is imperative that candidate flexible TPS materials are analyzed in ground test facilities that can simulate the high enthalpy plasma flow experienced during flight. To date, reports of aerothermal testing of SiC materials in high temperature oxidizing environments have been focused on rigid ceramic matrix composites. However, some of the conclusions may not be applicable to flexible materials.

5.3. Idealized Oxidation Stages

Upon atmospheric entry there is a highly complex variation in gas composition, pressure, shear, temperature and other transient influences of flight. At high altitudes, the low density may limit the availability of oxygen atoms [40] but low oxygen partial

pressures can be damaging [57]. The intermediate range is the location of the anticipated peak heat flux followed by the peak surface pressure. Finally the high density of low altitudes can drive the reacting flow towards chemical equilibrium at the surface where molecular gases are the predominant impinging species [40]. Depending on the entry trajectory, oxidation stages could potentially reverse directions leading to hysteresis effects through the changing temperatures and pressures [47].

Even though the real world complexities exist, a highly simplified model was created to help decipher the basics of the oxidation phenomena during aerothermal testing of SiC fibers. The following figure illustrates this idealized dynamic evolution of the sample mass when exposed to plasma heating conditions at high temperatures above the silica softening point.

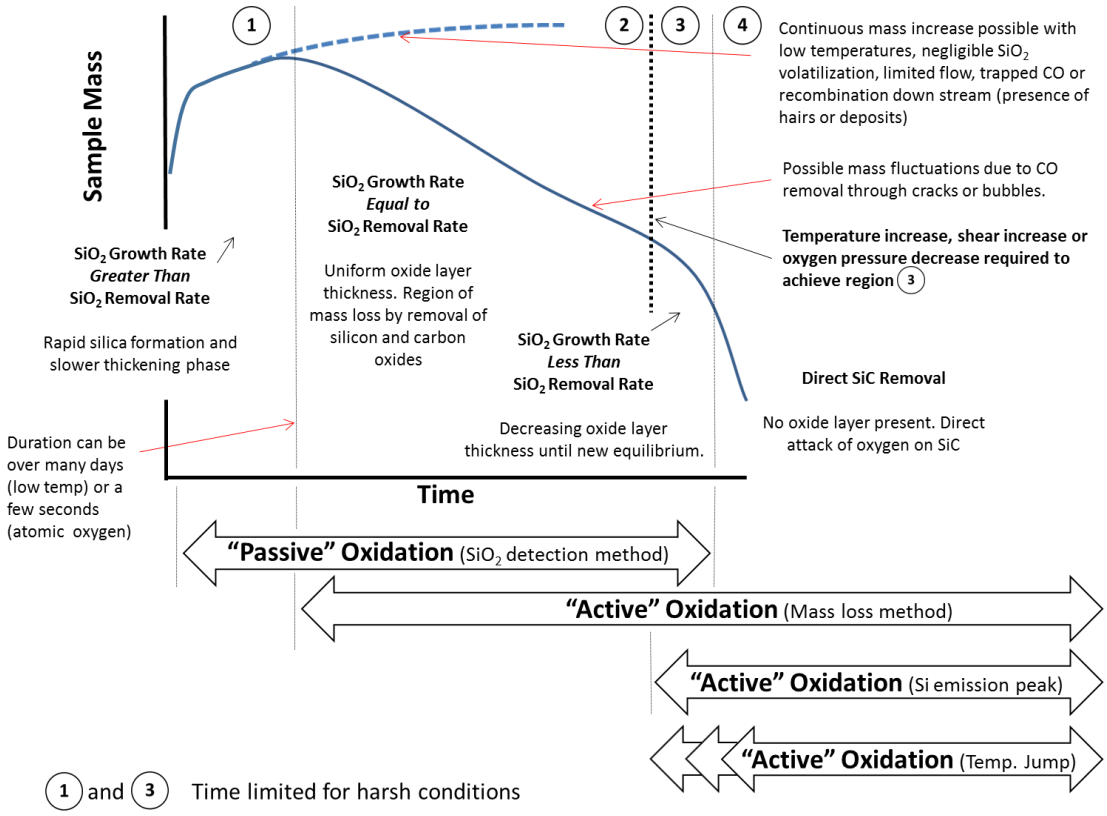

Figure 19: Illustration of an idealized sample mass vs time plot showing the oxidation stages and the inconsistency between different transition detection methods

The illustration shows the macro-scale mass evolution of a SiC coupon that is first passively oxidized until the conditions are changed to a harsher environment by either a temperature increase, shear increase, pressure decrease or transition in the gas chemistry. Investigation at the micro-scale or molecular level of the actual oxidation phenomena within the weave architecture is much more complex. This schematic does not show a burning off phase where high erosion occurs [32] directly after insertion or oxidation without the initial formation of a silica layer.

5.4. Passive and Active Oxidation

Extensive research in conventional ovens has been carried out on the oxidation of SiC fibers but it is important to understand that the theories, models and experiments are not universal and typically apply to only a small region of the entire oxidation spectrum.

It is very useful for authors to split up the oxidation processes into a mass increase regime due to the development of a passive SiO_2 layer or a mass loss regime due to the active removal of SiC. Wagner used the oxidation of silicon to develop a model for the transition between these significantly different oxidation regimes [57]. However large discrepancies arise throughout literature on the definition and location of this transition. The two processes that lie on either side of the transition are called "passive" and "active" oxidation but are typically oversimplified [37] into the following molecular reactions [58];

Passive Oxidation: $$SiC + \frac{3}{2}O_2 \leftrightarrow SiO_2 + CO$$ eq. 5

Active Oxidation: $$SiC + O_2 \leftrightarrow SiO + CO$$ eq. 6

The passive regime depicts the inherent mass gain on the material surface by the loss of carbon and the addition of two oxygen atoms. The active regime shows the direct

removal of SiC into the gas phase leading to a total mass loss as the gaseous species propagate away from the surface.

Some regard the transition between these two regimes as a hard line while others believe passive and active reactions can occur simultaneously [47]. The different experimental procedures for inducing the transition also plays a significant role in the location of the transition [47]. It has been shown by Morino that the active to passive boundary can be very different between plasma and static testing and even between two different plasma facilities [36]. Reactant dissociation has also been shown to limit the pressure dependence of the transition [21] and enlarge the pressure-temperature domain that is characteristic of a steady state semi-protective oxide film [48] [21]. Whereas the degree of dissociation of both oxygen as well as nitrogen in the reactive boundary layer will influence the resulting surface [35].

Using thermogravmetric analysis, some determine the active/passive transition point by the total mass change [47] while others use the rate of the mass change [49]. Using visual inspection, some authors label the transition to active oxidation as the location of a bare SiC surface [21] [59], while others use the detection of silica. Although, the silica layer can be discontinuous, poorly adherent to the SiC substrate and non-uniform in thickness [49]. Therefore, regions where both silica and a bare SiC surface exist can cause controversy depending on the definition of the transition. The degree of protection the surface provides has even been considered as the transition criteria [58].

Using spectroscopic techniques, the transition from passive to active has also been identified as a rapid increase in SiO production [34] or Si emission [58].

Whatever the definition or method used, the separation into only the active and passive regime is inadequate for hypersonic flight [31]. For aerothermal testing of SiC it is insufficient to assume that a mass loss occurs only in the active regime and is a direct indication of a bare SiC surface [31]. It is not uncommon to observe a condensed reaction product on the surface while accompanied by a net mass loss or total thickness decrease [21]. In order to apply the results of many authors and more accurately represent the phenomena observed during aerothermal testing of woven SiC fibers, the oxidation reactions were split into 4 separate stages; silica formation (deposition and thickening), equilibrium, intermediate, and direct SiC removal.

5.5. Stage 1 – Silica Formation

On high purity SiC materials, silica formation through a solitary thickening phase at the SiC/SiO_2 interface is commonly reported in conventional ovens. If no changes to the test environment were made it would be expected that the mass would keep asymptotically increasing and stages 1 would continue indefinitely. Theories matching a parabolic mass increase predict a diffusion controlled process [60] while a more linear mass change may be due to a kinetically controlled system [61] but these models are inherently oversimplified for ballistic entry due to the dissociation of gases causing parallel diffusion of atomic and molecular species [62]. Models that incorporate the

potential influence of atomic species have been shown to better predict the high initial oxidation rates [63]. For thin oxide layers, the oxide thickness on silicon in the presence of O-atoms was shown by Vora to be up to 20 times that with only molecular oxygen at similar operating conditions. Whereas, the oxide layer growth was shown to be directly proportional to the O-atom concentration [56]. In order to more accurately represent the observed plasma oxidation phenomena, a much more representative model splits the formation stage into a rapid silica deposition phase and a slower thickening phase.

5.5.1. Initial Deposition

For a certain range of conditions within the ICP Torch, the plasma free stream is comprised of both atomic and molecular oxygen that can react with the SiC surface. Based on the oxidation theory of Hilfer and Auweter-Kurtz, atomic oxygen which is also characteristic of hypersonic flight is unlikely to collide simultaneously with more than one other species and also have enough energy to initiate a reaction. This leads to the assumption that many concatenated reactions control the overall oxidation phenomenon [30]. The initial reaction step would be:

$$SiC + O \leftrightarrow SiO + C \qquad \text{eq. 7}$$

Whereas atomic oxygen is the active species and the reaction products are temporarily stable in the gas phase. This is then followed by the sequential oxidation of SiO and C as seen in the following reaction.

$$C + O \leftrightarrow CO \quad \text{eq. 8}$$

$$SiO + O \leftrightarrow SiO_2 \quad \text{eq. 9}$$

This continuous SiO reaction could take place while SiO is still adsorbed on the surface or in the gas phase creating a barrier within the thermal boundary layer, consisting of SiO, SiO_2 smoke and CO [64] [65]. Reactions between CO and O to form CO_2 have not been detected but if present would be expected to remain in the gas phase. Inevitably, any of these reactions would result in an unavoidable decrease in oxygen partial pressure towards the surface [65].

By definition, oxidation by a highly dissociated plasma flow would inherently be considered to occur within the active oxidation regime if the formation of SiO gas was the deciding criteria. This silica deposition phase is illustrated in Figure 20.

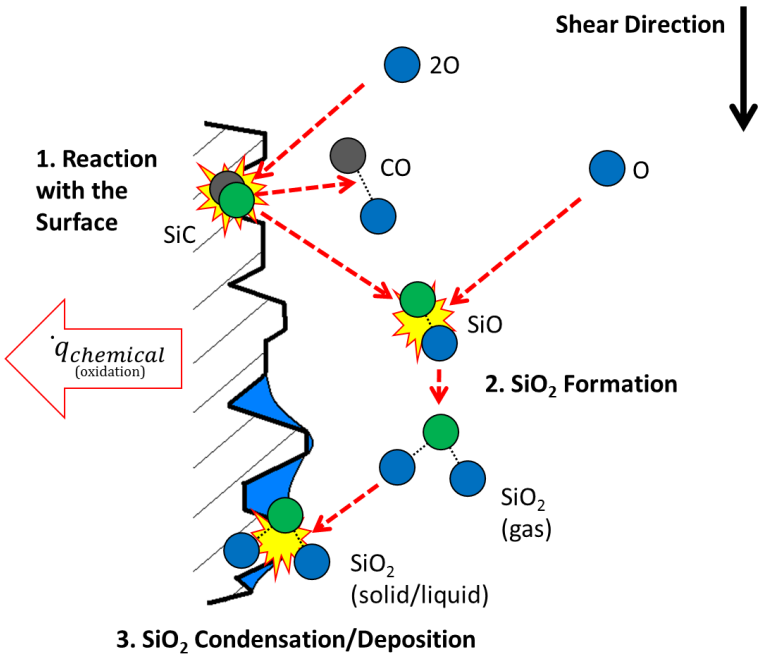

Figure 30: Illustration showing the rapid silica formation phase

High velocities could cause the gaseous intermediate reaction products to be swept downstream due to the relative timescale of the process before undergoing additional reactions. In turn, this can lead to deposition of evaporated SiO_2 or further oxidation of SiO gas at locations of lower temperature or higher oxygen pressure [30].

Depending on the gas composition and ICP Torch power setting, virgin SiC fabric samples followed the same temperature profile (±25°C) with a rapid temperature rise of over 1000°C/sec upon insertion into the plasma. Due to the extreme heating method, the initial silica formation phase was expected to occur concurrently with thermal decomposition and the removal of impurities. At temperatures above 1000°C, emission spectroscopy has captured the impurity removal process by an initial spike in carbon

containing reaction products. Emission spectra results captured directly after insertion into a pure nitrogen plasma is compared to SPECAIR data [66] in the following figure.

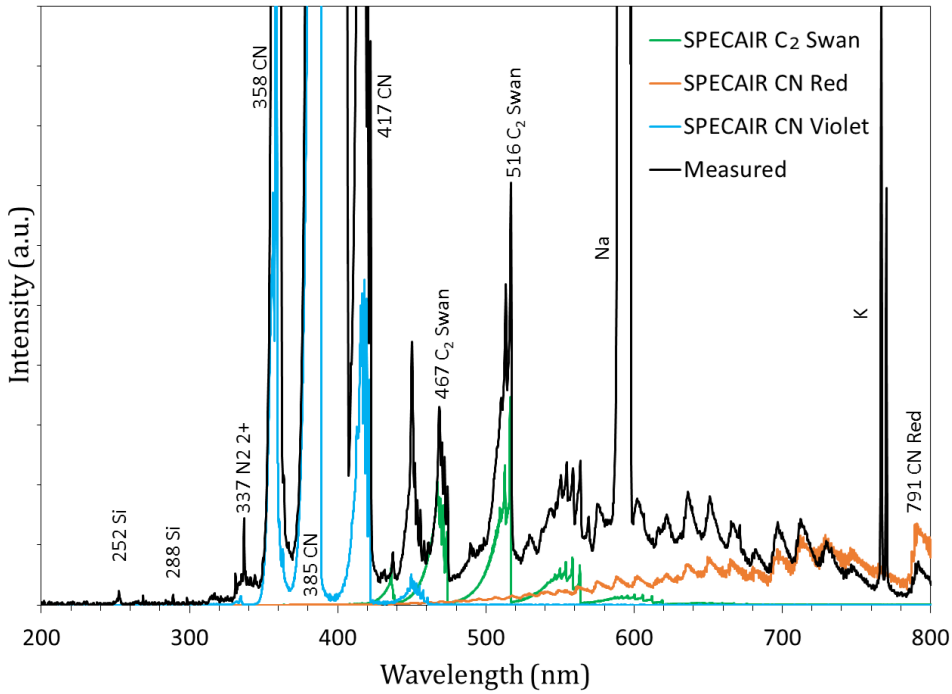

Figure 41: Emission upon SiC coupon insertion into a pure nitrogen plasma within the thermal boundary layer using an integration time of 10 seconds [66]

Hirsch described this visually observable process during aerothermal testing of SiC CMCs as a burn off phase which lasted for times ranging from 0.3 to 15 seconds depending on the temperature. [32]. This burn off phase is only observable on virgin materials and is most easily seen in pure nitrogen plasmas. CN violet, CN red, and diatomic carbon emission are easily distinguishable using the emission spectrometer. Si has been detected upon insertion at 252 and 288nm but it is easily drown out when capturing the strong CN emission. In addition, the fiber optic cable used with the

emission collection optics loses sensitivity below 300nm which is the location of Si and SiO features.

For virgin samples directly inserted into oxidizing plasmas, it has been reported that a visual blurring effect only observable immediately after virgin sample insertion is due to this silicon-oxygen fog and rapid silica formation [32]. Although, the blurring front is not unique to oxidizing environments or silica forming materials suggesting that it is the result of a high volume of material ejected into the boundary layer creating a superimposed emission with a broad wavelength range. Never the less, significant silica formation is expected to occur within the timespan of this blurring front. The blurring effect can be seen in the following figure when comparing the insertion of a virgin and oxidized SiC coupon into a nitrogen plasma flow.

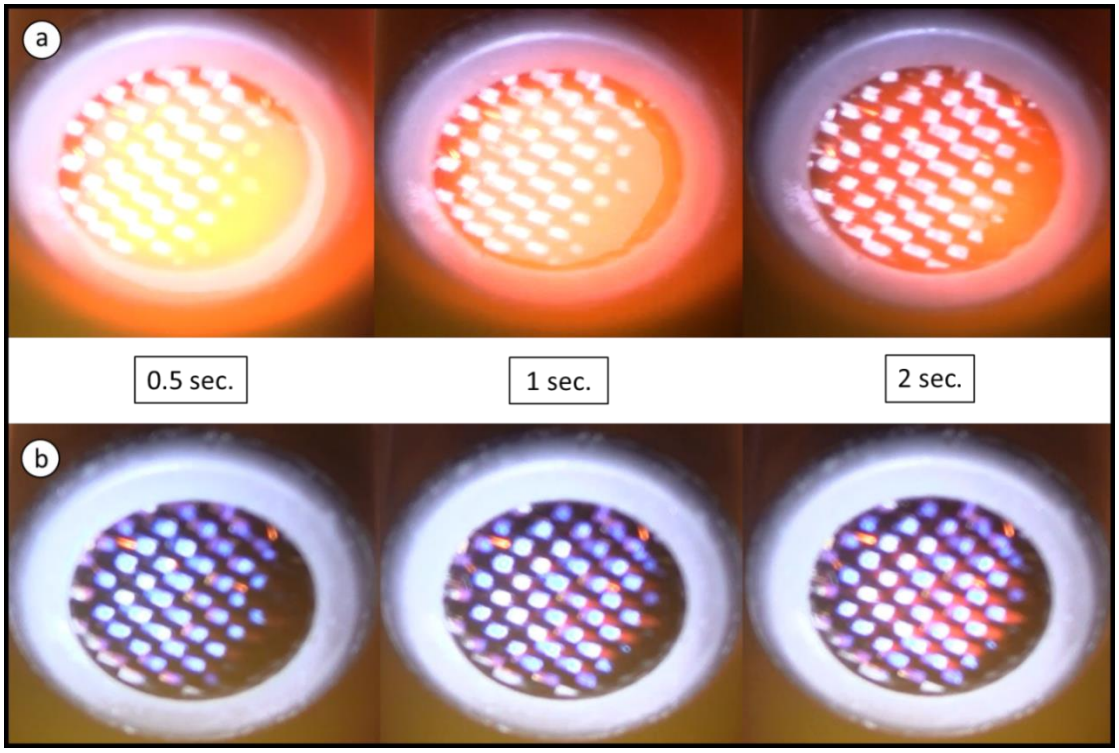

Figure 52: Surface images taken during insertion into a nitrogen plasma for a) a virgin SiC coupon and b) a previously oxidized coupon

For tests at 1200°C using two plies of SiC fabric, two waves of the blurring front were observed within 3 seconds after insertion. For any plasma condition, no blurring front has been observed at surface temperatures below 1000°C. In addition, samples tested at 926°C in oxygen containing plasmas were exposed to very low dissociation fractions and took much longer to display any signs of oxidation.

For SiC coupons that were directly inserted into a nitrogen plasma, the simultaneous burn off of impurities can last over 20 seconds which is much longer than the blurring front. Although this is not the case in oxidizing plasmas. The visually observable impurity removal phase is much more suppressed when oxygen is present.

The blurring front in air occurs for only a fraction of a second and the duration is even shorter for pure oxygen plasmas. In a 100% oxygen plasma the development and disappearance of the blurring front occurs so rapidly it is sometimes difficult to distinguish from the sustained silica coating on the surface.

The following plot shows the absence of emission from carbon containing species that is captured by the spectrometer upon insertion into an air plasma.

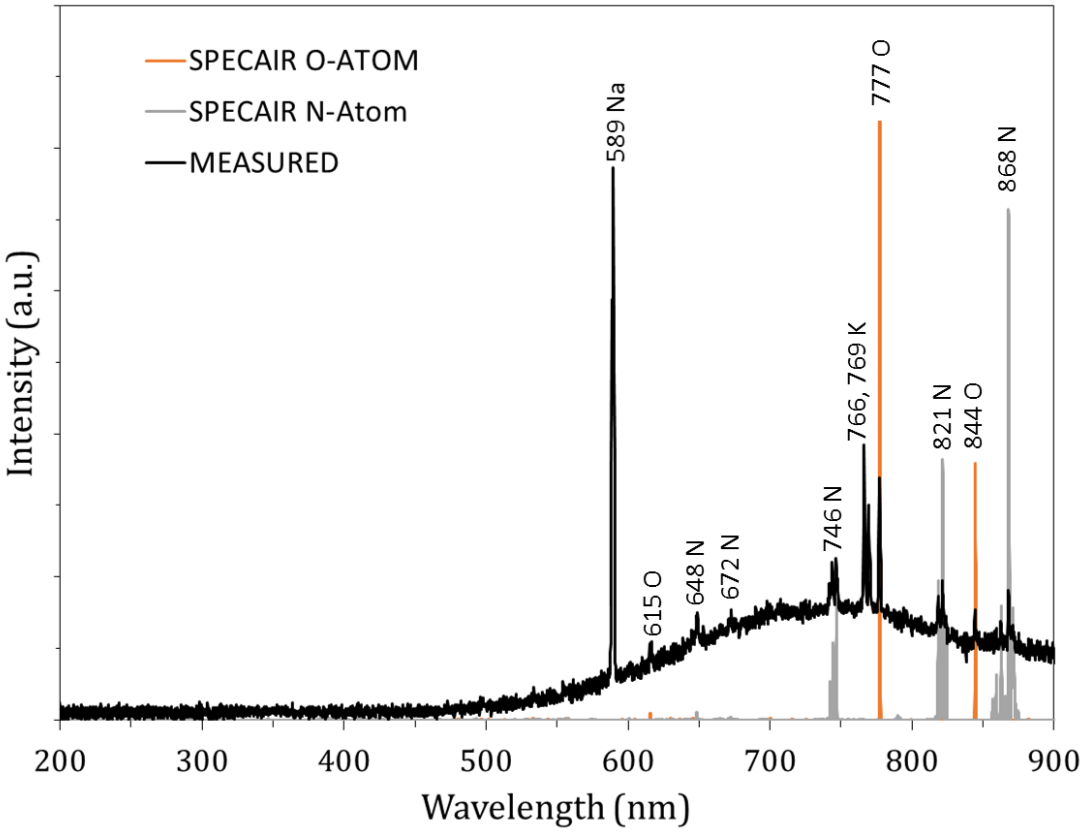

Figure 63: Emission upon SiC coupon insertion into an air plasma within the thermal boundary layer using an integration time of 10 seconds [66] (test condition: 32 slpm N_2 / 8 slpm O_2, 160 torr, 1400°C)

The emission was collected at the same spatial location, with the same spectrometer collection configuration, and 10 second integration time as used in the pure nitrogen case. Even though the impurity removal phase occurs at temperatures below the temperature range of silica formation, the rapid temperature rise after direct insertion may allow the newly deposited silica coating to suppress the removal of free carbon. In-turn, unreacted carbon will be trapped underneath or within the silica layer. The lack of Si or SiO features, could suggest that silica formation occurs while the atoms are bonded to the SiC surface. Although, the intensity of the feature, the limited sensitivity of the collection optics below 300nm and the rapid timescale of the blurring front in oxidizing plasmas could also lead to the absence of a detectable feature.

For the aerothermal conditions tested and a surface temperature of 1400°C, the continued deposition of SiO_2 eventually covered the entire fiber surface creating a passive silica coating. This oxide layer formed in a matter of seconds and could be seen within the weave architecture using the SEM. Figure 24 was taken after a tensile test at 1200x for a 1 minute exposure time and 430x for the 4 minute case.

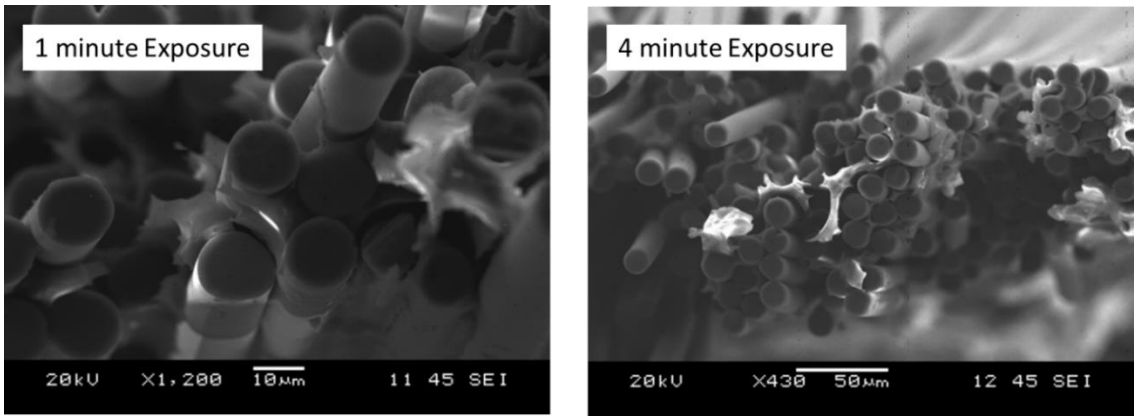

Figure 74: SEM images of the coupon cross-sections after a 1 and 4 minute exposures to an air plasma. (test condition: 32 slpm N_2 / 8 slpm O_2, 160 torr, 1400°C)

It is obvious that the SiO_2 formation occurred primarily in the hypocycloids and other irregular shaped vacancies between the fibers. EDS was used to confirm the silicon-oxide elemental composition. The SEM image and EDS analysis does not show any type of oxygen diffusion transition region but depicts an abrupt interface between the SiO_2 layer and the SiC fiber. The distinct boundary can be seen where the silica has detached from the fiber which also suggests low adhesion and the probable condensation of a silicon-oxygen fog. Once the silica was formed no substantial change in the thickness was observed within the limitations of the SEM between 1 and 4 minutes. SiC filament diameter reduction between the different locations throughout the weave was also not distinguishable.

5.5.2. Thickening

A relatively slower thickening of the SiO_2 layer following the rapid deposition phase is expected to cause catalytic recombination to be the dominating oxygen atom

consumption path. This transition occurs due to the diffusion limitations of oxygen through the newly formed passive silica layer [32]. The oxide growth rate can be controlled by boundary layer transport, adsorption onto the oxide surface, diffusion mass transfer of the oxidant through the SiO_2 layer, kinetic oxidation of SiC from free oxygen, and outward diffusion of the reaction products [67]. Whereas the limiting process can vary with time, temperature and pressure. Diffusion of silicon through the passive SiO_2 network was ruled out by Pretorius who used radioactive ^{31}Si to determine that the continued silicon dioxide formation occurs at the Si-SiO_2 interface which implies that and oxygen is the diffusing species. [68] Although, this conclusion does not include deposition of SiO_2 from the rapid formation phase. This, thickening stage is illustrated in Figure 25.

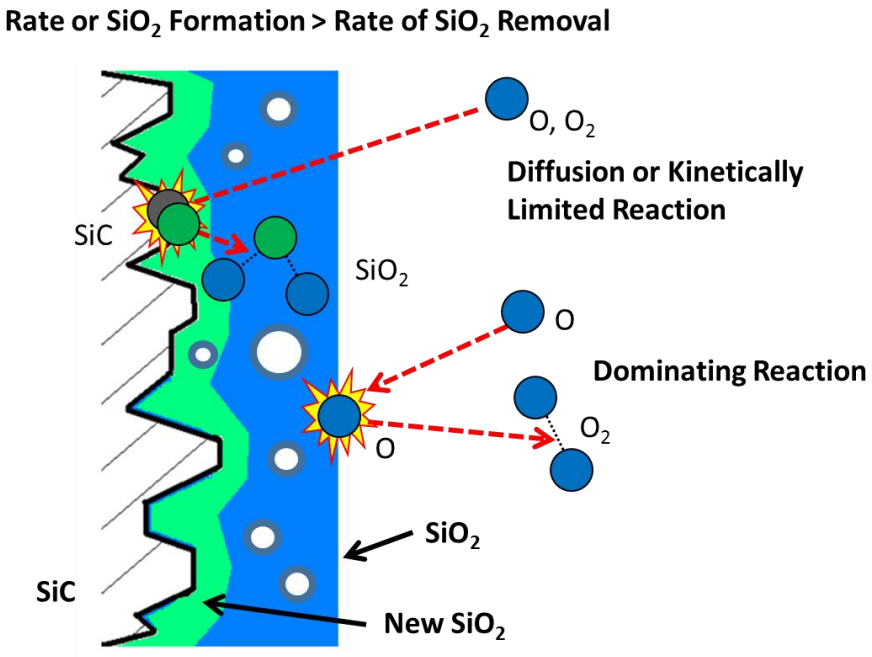

Figure 85: Illustration showing the slower thickening phase

The thickening stage is more similar to established molecular oxidation models. Whereas the limiting factors of the oxidation process act in series causing the overall rate to be controlled by the slowest process. Although, the presence of atomic and molecular species can potentially accelerate the oxidation process through parallel reaction pathways [62]. Experiments performed by others have shown the differences between these two reactive oxygen states. ^{18}O tracers were used to discover how exposure to atomic oxygen gradually disorders and modifies an existing SiO_2 network as it diffuses inward toward the substrate interface. Meanwhile, under exposure to molecular oxygen, no oxygen exchange in the bulk SiO_2 was observed [51] [55]. Furthermore, during plasma oxidation, the concentration of molecular oxygen was found to play an insignificant role until the oxide layer thickens and the reaction with O_2 becomes the prevailing mechanism to supply the oxidant to the SiO_2/SiC interface [56].

For exposure times of only a few minutes, the influence of this thickening phase is expected to be much more pronounced on the leading side of the fabric rather than within the weave due to the relatively thin silica film on the surface. Oxygen diffusion through the weave architecture is expected to occur on a much longer time scale. This is unique to fabrics due to the fact that most rigid SiC or CMC materials are designed to be impermeable to oxygen. Visual signs of this thickening stage can be seen in the following photos. The different sample holder sleeves were reused between tests and could build-up thick silica layers over time. Attempts were made to sand off the leading surface between tests.

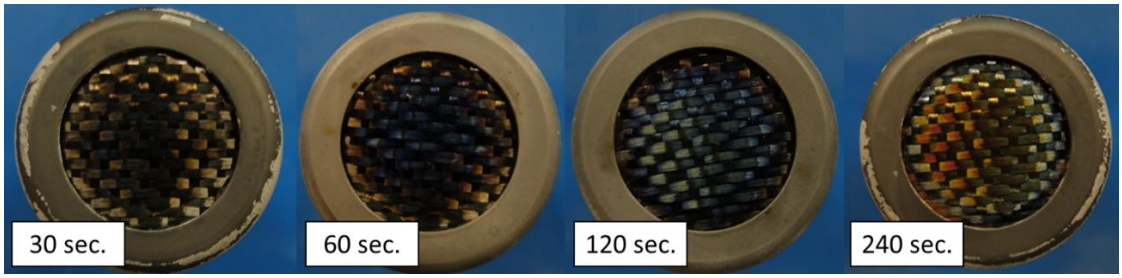

Figure 96: Illustration showing the slower thickening phase

The changing iridescence signifies that the thickness is changing on the order of angstroms [69] which is much too small to be detected using the SEM due to the electrostatic charging on the silica. It is important to note that the repeating interference colors change with inspection angle and only suggest a uniform thickness for each contiguous color instead of a visually quantifiable surface thickness. The highest plasma temperatures occur along the central axis of the plasma flow and is a possible reason for the strong iridescence in the center of the oxidized sample. Although the increased conduction path due to the crimp of the sleeve as well as the increased boundary layer velocity near the edge of the sample can also contribute.

5.6. Stage 2 - Equilibrium

SiO_2 is not stable at temperatures near or above its softening point [65]. In-situ video recording of the SiC fabrics exposed directly to high enthalpy oxygen containing plasmas at temperatures around 1400°C depict flowing liquid silica due to external aerodynamic forces which can be seen from 30 sec. to 1 min. after insertion in the form

of balls and streaks. This silica flow is also observable when oxygen is added to a pure nitrogen plasma.

Besides mechanical removal, continuous chemical reactions can cause both the removal of SiC as well as SiO_2. Aerothermal testing by others has shown a time independent SiO_2 erosion behavior that leads to an equilibrium oxide thicknesses and linear SiC recession rates in overall mass and thickness [31]. The evolving surface morphology observed on the SiC fibers provides evidence of ongoing chemical reactions beyond those described in stage 1. Accumulation of gaseous bi-products forming at the SiC/SiO_2 interface can lead to observable bubbles on the silica surface [65]. These bubbles and other silica features can be seen in the following figure.

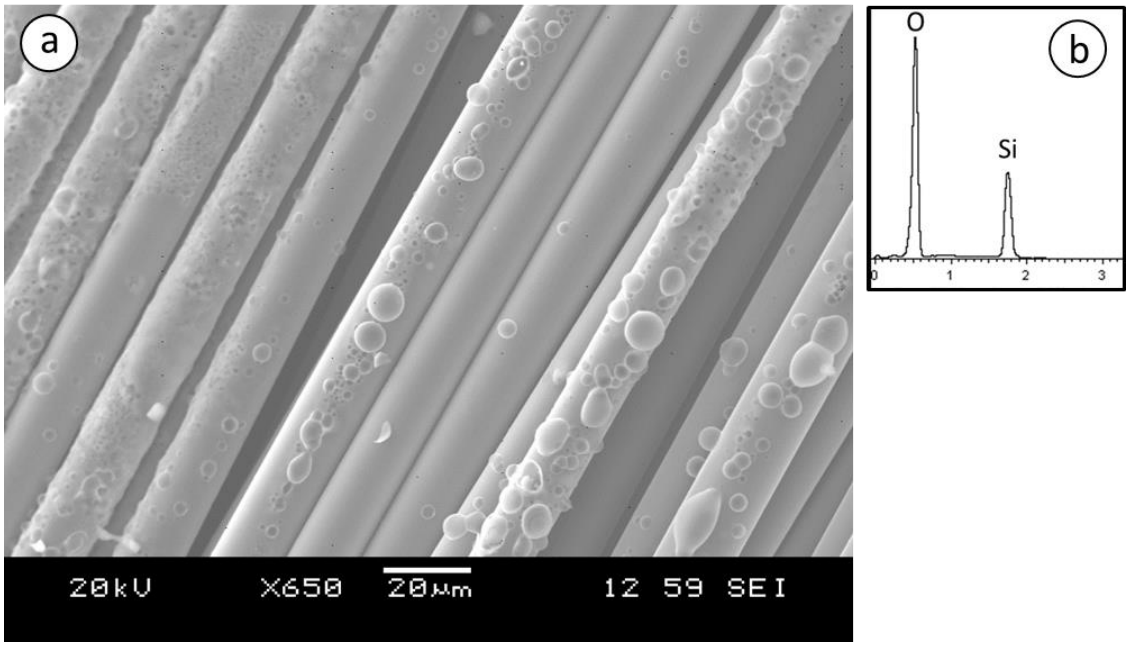

Figure 107: a) SEM image of silicon-oxide layer showing bubbles and pores and b) EDS results taken on the surface of an oxidized sample(test condition: 32 slpm N_2 / 8 slpm O_2, 160 torr, 1400°C)

In order for bubbles to form, the total pressure at the SiC/SiO_2 interface must be greater than the surface pressure at the SiO_2/gas boundary [49]. It is assumed that the large number and size of these bubbles is attributed to free carbon within the fibers, whereas the initial rapid deposition phase traps the carbon underneath or within the passive silica layer. The trapped carbon could react with oxygen atoms that diffuse through the silica and produce high CO pressures. These bubbles also suggests minimal gas escape through micro-cracks or pores that span the entire oxide thickness. Due to these potential micro-channels in thin films, a critical oxide layer thickness is required until bubbles will arise [70].

On SiC fabrics, the bubbles appear to be limited to the diameter of the fibers but will increase in volume as the gases diffuse outward through the passive film [102] typical of Oswald Rippening. They continue to grow until rupture from the buildup of internal pressure and shear forces from the flow environment [31]. Bubble formation is consistent with actual flight results on SiC coated ceramic matrix composites [37]. Although the bubble formation during flight has been observed to be much more damaging than predicted using aerothermal ground testing results [37].

Continued bursting of bubbles can accelerate erosion and oxidation rates [71], although outward diffusion of gaseous reaction products through bubbles does not necessarily represent silica removal or total mass loss. In order to counteract the mass increase due to the silica formation, SiO_2 reactions at the gas boundary [37], viscous

silica flow, or reactions between SiC and SiO_2 at the interface [65] must occur. Whereas, reactions at the gas boundary could include sublimation of SiO_2 or dissociative removal. Therefore, silicon may be removed in different oxidized states including; Si, SiO or SiO_2. Although if the oxide leaves the surface in molecular form, possible dissociation could occur in the high temperature boundary layer, even if oxygen is sufficiently available [58].

This depletion of silicon and silicon-oxides into the boundary layer is in agreement with many other researchers using different materials and spectroscopic techniques [34] [39]. The equilibrium stage resulting in this silicon and carbon removal is illustrated over SiC in Figure 28.

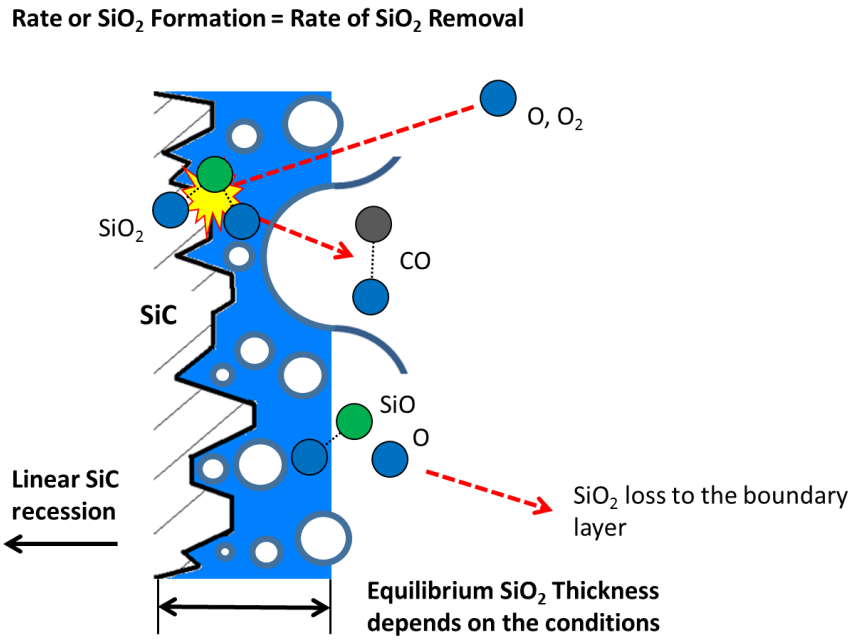

Figure 118: Illustration showing the equilibrium phase.

If the silica growth rate decreases with increasing thickness and the silica removal rate remains constant over all thicknesses, eventually an equilibrium thickness will be reached. This same equilibrium will occur in the case of viscous silica flow even if the removal rate increases with silica thickness. With increasing temperature, the equilibrium oxide layer thickness will decrease and shorter times will be required to reach the steady state thickness [72]. Due to the thickness dependence on viscosity and volatilization rates, the equilibrium oxide thickness will be expected to vary throughout the weave architecture with the local surface temperature, oxygen concentration, and total pressure [31].

Operating at a high total pressure, low temperature or low gas flow rate makes the oxide thickness large and linear mass loss may not be observed within the timeframe of the experiment [49]. Negligible SiO_2 volatilization at low temperatures or deposition of SiO_2 at other locations on the measured sample can all cause an asymptotic mass increase. For the small diameter fibers, the steady state thickness may actually be larger than the fiber radius and complete consumption may ensue before an equilibrium thickness is achieved [73]. However, stage 2 is likely to occur during exposure to the extreme conditions of aerothermal testing and it is thought to be reached in just a few seconds for high enthalpy operating conditions [39].

The continual removal of SiO_2 and SiC of stage 2 is independent of time and will only stop until complete consumption of the SiC substrate if allowed to continue long

enough. Thus, SiO_2 removal cannot be ignored either in interpretation of short term oxidation results [72] or in predicting the life of reusable materials [31].

5.7. Stage 3 - Intermediate

During atmospheric entry, a change in the plasma enthalpy or pressure can throw the oxidation mechanisms off balance. A small change in conditions can lead to a new steady state oxide layer thickness and new removal rate. Unique to plasma environments, a change in surface catalycity, emissivity or reactivity may also throw the thermal equilibrium off balance. A large enough shift in the equilibrium conditions can lead to complete removal of the silica layer. Any preexisting oxide layer over the SiC surface requires a transitional time period that must exist between stages 2 and the bare SiC surface of stage 4. This stage was designated by Gulbersun as an "intermediate" phase which doesn't exist in the reverse direction [65].

A change in shear can also change the silica equilibrium thickness. Therefore different locations of similar temperatures on a hypervelocity vehicle would be expected to have different silica thicknesses depending on the aerodynamics. Some authors arrived at the conclusion that increasing flow velocity increases the silica formation rate by increasing the amount of oxygen available [48]. However this theory only holds true for small velocities which are mostly irrelevant to ballistic entries [30]. Under high shear, the gaseous oxidation products may be continuously carried downstream which could greatly enhance erosion mechanisms [37].

Depending on the environment, the removal of the oxide layer progresses similar to the combination of reactions of stage 2. This non equilibrium region is illustrated in Figure 29.

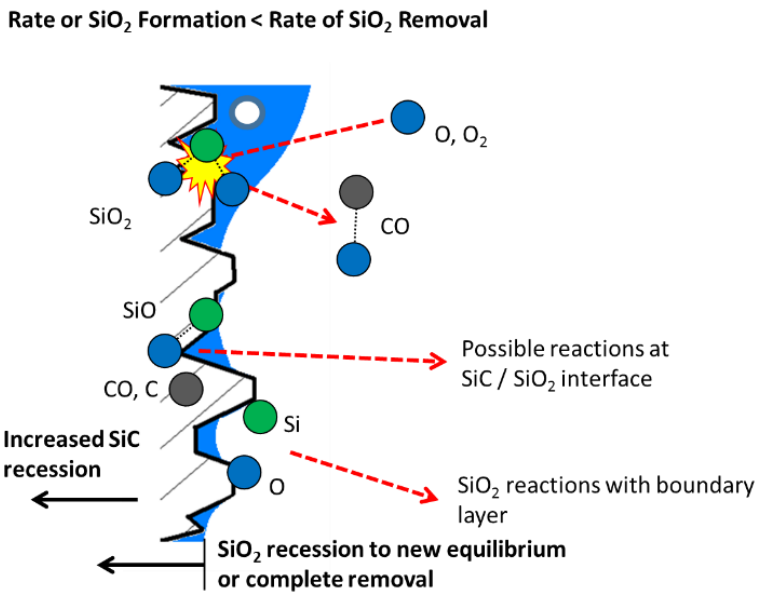

Figure 129: Illustration showing the intermediate phase

An increase in the silicon removal rate due to a transition in the thermal energy balance has been observed in the ICP torch facility using emission spectroscopy. Spikes of silicon containing species have been detected within the thermal boundary layer over SiC and SiO_2 materials at temperatures above 1400°C. The Si emission lines were commonly seen at 251-253 and 288 [74] in oxidizing and non-oxidizing environments. Silicon-oxide features were observed for all oxidizing environments tested, although the features were much more elusive compared to Si emission. The following figure shows

SiO $A^1\Pi$-$X^1\Sigma^+$ [74], SiO $^3\Sigma$-$^3\Pi$ [75], and weak SiO_2 -? [75] features that have been captured in the ICP torch over SiC fibers.

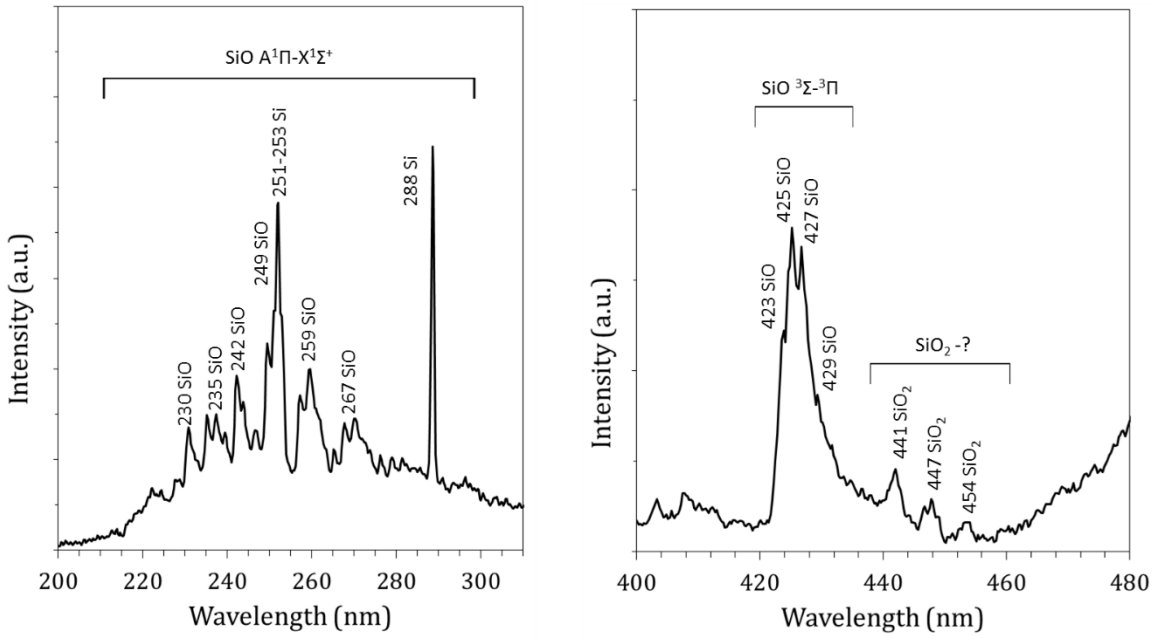

Figure 30: Emission over a SiC coupons in oxidizing environments showing the best capture of SiO and SiO_2 [76][74][75]

The highest signal to noise data collected for SiO was seen in an air plasma, whereas the presented SiO_2 feature was captured at 1400°C in a CO_2 plasma. Both features were also captured in pure oxygen plasmas but the features were much less well defined.

The duration of Stage 3 is dependent on the silica removal rate and initial oxide thickness. By increasing the heat flux in a step wise fashion to a constant condition, the transition to a bare surface has been shown to be delayed as long as 180 seconds [46]

where the time is shorter for larger power increases or thinner initial films [77]. For the irregular surfaces of SiC fabrics it is unlikely that the silica layer will be removed uniformly. Therefore, there is a possibility to observe a heterogeneous SiC / silica surface.

5.8. Stage 4 – Direct SiC Removal

After complete consumption of the silica layer a new thermodynamic equilibrium can be reached on the bare SiC surface with different oxidation/volatization rates [77]. Initial exposures to extremely high temperatures or low pressures can lead to direct removal of SiC without the formation of an oxide layer. At these harsh conditions stages 1-3 may not exist and the material will start directly in stage 4. This stage is defined as the absence of SiO_2 on the surface allowing unhindered oxygen attack of the SiC. At these new conditions all reaction products are gaseous and no condensed phase exists. Possible reactions on the bare SiC surface are illustrated in Figure 31.

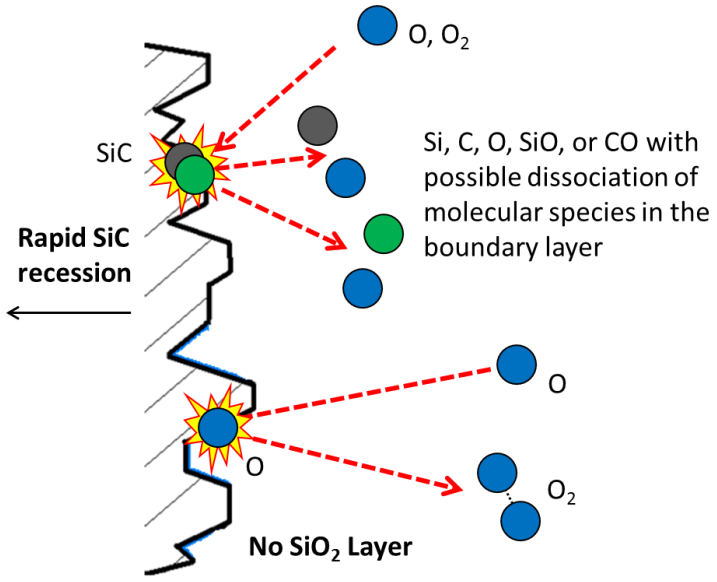

Figure 31: Illustration showing direct SiC removal

The rate of mass loss during stage 4 is dependent on the operating conditions. No data has shown an increase in mass loss rates during the combined removal of silica and SiC of stage 3. Although, operating at oxygen partial pressures near the transition to the bare surface have shown maximum erosion rates at constant temperatures [36] due the high concentration of unhindered reactive species.

5.9. Additional Stages

Stage 1 is almost unanimously referred to as the "passive" regime, meanwhile stage 4 is usually referred to as the "active" regime. "Bubble formation" has also been classified as a separate regime [71]. The existence of stage 2 during oxidation testing at temperatures above the stable point of silica is the common culprit of confusion between aerothermal testing and conventional ovens. However, an additional phenomena

described by a sharp temperature jump at extremely high temperatures has led to further discussion about the transition between active and passive. This temperature jump has been referred to as the active oxidation regime [45]. Although according to others a jump in temperature is a unique phenomenon separate from active oxidation [78] and has actually been observed during this investigation in pure nitrogen plasmas. Subsequently it has also been split into 3 cases, active, passive and temperature jump [78]. With this in mind, it is proposed that oxidation during aerothermal testing should inevitably be described by more than just 2 stages. Formation, equilibrium, intermediate, direct SiC removal and temperature jump are better suited when trying to specifically define the individual oxidation stages.

CHAPTER 6: TRANSIENT THERMAL PROPERTIES OF SIC FABRICS CAUSED BY OXIDATION

6.1. Introduction

Analysis of the interactions between the gas phase and TPS surface can be modeled using the thermal energy balance illustrated in Figure 1 of Chapter 1. It can be seen that the net heat flux on the surface is comprised of both heating and cooling components that are dependent on the surface properties of the TPS. Where $\vec{q}_{radiation\ in}$ is an artifact of the irradiance acting on the surface that originates in the shock layer and $\vec{q}_{convection}$ is the heat transfer to the surface from the impinging gas species.

Not including potential pyrolysis from the insulators, the cooling effects of ablative mass transfer $\vec{q}_{mass\ transfer}$ are assumed to be negligible on the SiC outer fabric for the temperature range of this investigation. This leaves outward radiative cooling $\vec{q}_{radiation\ out}$ and conduction $\vec{q}_{conduction}$ into the entry vehicle as the dominating heat removal mechanism on non-pyrolyzing materials. Minimal conduction into the entry vehicle is essential therefore attempts are made to maximize the radiative cooling through high emissivity materials.

6.1.1. Emissivity

The radiative cooling is dominated by the surface temperature and the efficiency at which the material radiates. Whereas an increase in surface temperature will increase the total radiative heat flux from the surface. This temperature dependence is described by the following equation:

$$\vec{q}_{radiation\ out} = \sigma \epsilon T^4 \qquad \text{eq. 10}$$

where T is the surface temperature, σ is the Stefan-Boltzmann constant and ϵ is the total emissivity value. This emissivity value is defined as the ratio between 0 and 1 of the radiated energy reduction compared to a perfect black body and is typically reported for a flat smooth surface. A black body has an emissivity of 1 and the radiation from the surface follows Planks distribution. A graybody is a material that exhibits a constant emissivity over all temperatures and wavelengths.

6.1.2. Catalycity

The rapid temperature rise across the bow shock can cause dissociation and possible ionization of the atmospheric gases leading to extremely harsh conditions and an additional heating mechanism. Thermodynamic non-equilibrium flow close to the entry vehicle allows highly reactive atomic species to reach the TPS surface [40]. The chemical component $\vec{q}_{chemical}$ of the thermal energy balance incorporates the additional energy released from exothermic chemical reactions occurring on or with the surface. The catalycity of the material describes the efficiency at which dissociated species recombine on the surface. In the case of re-entry, N_2, N-atom, O_2, O-atom and traces of NO are expected to be the predominant gas species after the bow shock. The three competing catalytic reactions during re-entry are presented in the following equations.

$$N + N + s \rightarrow N_2 + s \qquad \text{eq. 11}$$

$$O + O + s \rightarrow O_2 + s \quad \text{eq. 12}$$

$$N + O + s \rightarrow NO + s \quad \text{eq. 13}$$

Where N is atomic nitrogen, O is atomic oxygen and s represents a surface reaction site. Evidence of all three reactions occurring in the thermal boundary layer has been observed using laser induced fluorescence during aerothermal testing.

Catalycity is a macroscopic surface property that can be calculated as the ratio of reacting atoms to the number of atoms impinging on the surface. Gamma is typically used as the catalytic recombination coefficient and can be seen in the following equation [79]:

$$\gamma_i = \frac{\dot{N}_{i\,recom}}{\dot{N}_{i\,total}} \quad \text{eq. 14}$$

Where i is the gas species, $\dot{N}_{i\,total}$ is the arriving flux and $\dot{N}_{i\,recom}$ is the recombined flux. This ratio inevitably leads to a gamma value between 0 (non-catalytic) and 1 (fully catalytic). Although, in actuality it is expected that all materials have varying degrees of partial catalycity. Surface morphology, microstructure, and elemental composition can all affect the overall catalycity of the material [80]. Environmental factors such as the impinging reactant species, surface temperature, and total and partial pressure can also contribute [80]. Whereas, diffusion of reactants in the boundary layer, surface reaction

kinetics, and diffusion of the products from the surface will influence to the overall reaction time and effective catalycity.

6.1.3. Reactivity

The reactivity of the material describes chemical reactions between the gas phase and the surface of the material. In the case for SiC fabrics, the following reactions have been detected using energy-dispersive spectroscopy on the surface and emission spectroscopy in the boundary layer:

$$SiC + O \rightarrow SiO + C \quad \text{eq. 15}$$

$$SiO + O \rightarrow SiO_2 \quad \text{eq. 16}$$

$$C + N \rightarrow CN \quad \text{eq. 17}$$

$$C + O \rightarrow CO \quad \text{eq. 18}$$

$$SiC + xO + yN \rightarrow SiO_xN_y + C \quad \text{eq. 19}$$

More reactions are expected than the ones listed but have not been experimentally observed to date. Surface temperature and partial pressure can directly affect the existence and rates of these reactions. Whereas, operating at surface temperatures below 1000°C significantly slows the SiO_2 formation in oxidizing environments and the reaction to form a silicon oxynitride is only observed when operating with extremely low oxygen partial pressures.

Each of these reaction pathways will simultaneously compete with the consumption of gas species through catalytic recombination. The following relationship is used to describe the number of impinging gas species that are consumed by reactions with the surface.

$$\psi_i = \frac{\dot{N}_{i\,react}}{\dot{N}_{i\,total}} \qquad \text{eq. 20}$$

Where $\dot{N}_{i\,react}$ is the reacted flux. The catalycity and the reactivity can then be combined to account for all the impinging gas species;

$$\gamma_i + \psi_i = 1 - \frac{\dot{N}_{i\,unreacted}}{\dot{N}_{i\,total}} \qquad \text{eq. 21}$$

Where $\dot{N}_{i\,unreacted}$ is the flux of impinging gas species that bounce off the surface chemically unmodified. Even with this seemingly simple equation, significant complexity arises when analyzing the heat transfer as each potential consumption pathway has its own reaction rate, activation energy, exothermicity, and accommodation coefficient. Even further complexities arise when accounting for the transient influences of material surface evolution on catalycity, reactivity and emissivity.

6.1.4. Feed-back Loop

Many authors report the properties of non-ablating thermal protection materials with the assumption that the surface properties do not change with time. Although,

scanning electron microscope images of the SiC fabric surface show a dramatic morphology evolution after exposure to oxidizing plasmas. Whereas, exposure to pure nitrogen plasmas leads to relatively minor observable changes. Therefore any thermal analysis for SiC fabrics in atomic oxygen bearing plasmas will be made on a material that is significantly different in surface area and elemental composition than the virgin material.

The inherent permeability of the outer fabrics also makes them unique compared to other SiC materials due to the ability for gas surface reactions to occur within the weave. Whereas, silica formation can seal the cracks between the fibers as seen in Figure 4 in Chapter 5 and would be expected to significantly slow in depth reactions. This silica formation within the weave architecture would also have direct influence on the conduction into the material.

The overall aerothermal performance of outer fabric can be modeled by a dynamic feed-back loop that will dictate the thermal equilibrium of the material. Catalycity, emissivity and reactivity are all functions of the material surface as well as the exposed environment. Their combined influence is reflected in the resulting surface temperature. A visually interpreted energy balance similar in concept to the diagram presented by Herdrich [81] can be seen in Figure 32.

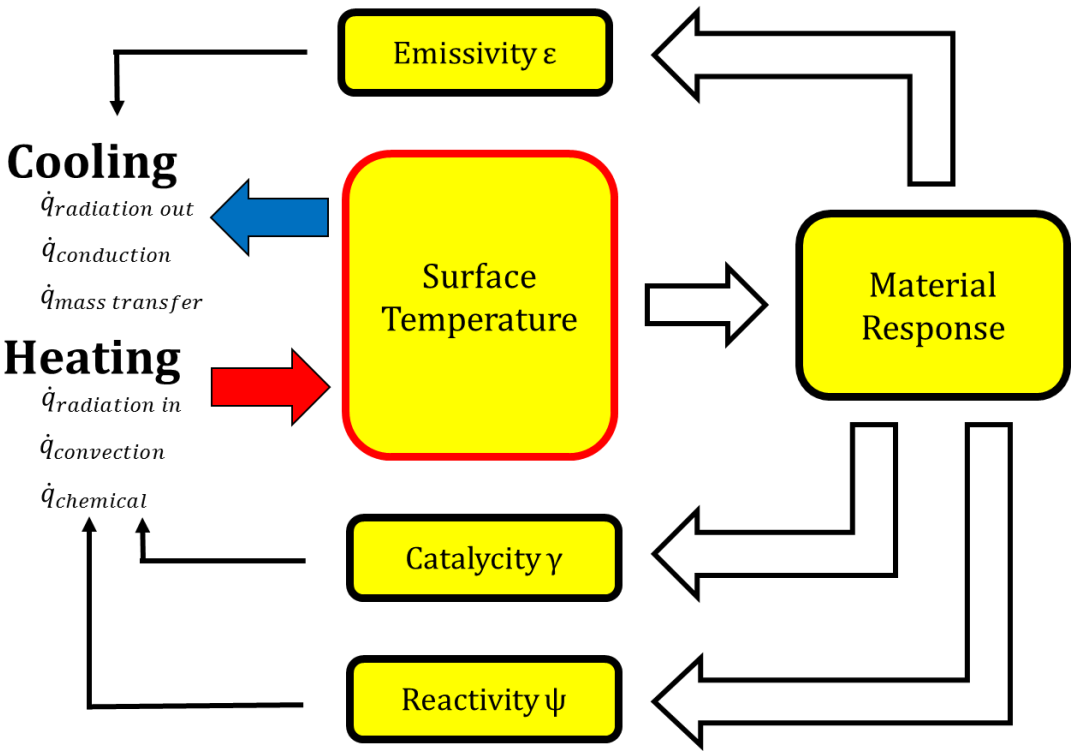

Figure 32: Illustration showing the influence of SiC surface dependent properties

The feed-back loop shows the direct influence of the material response on the catalycity, reactivity and emissivity. This in-turn leads back into the energy balance on the surface. Even though radiative and convective heating as well as conductive cooling can be effected by transient changes in the material and comprise part of the coupon energy balance, this research is focused on the catalycity, reactivity and emissivity and their dependence on the material response.

6.2. Experimental Conditions

Experiments were carried out in the same manner as described in chapter 3 except different gas compositions were used. It is desirable to test the TPS under the exact flight

profile with constantly varying conditions due to its direct influence on the gas surface interactions. Although, for this test campaign, steady state conditions were used to simplify the experiments. Whereas, priority was focused on reproducing the aerothermal and chemical environment during peak heating rather than the aerodynamic characteristics of flight.

Hypersonic flight within earth's atmosphere is the focus of this chapter, therefore experiments were carried out in variable O_2/N_2 gas mixtures at steady temperatures up to 1500°C for applicable trajectory durations. Pure nitrogen plasmas and admixtures with argon were used to provide insight on the coupling effects between multiple gas species and the influence of oxidation reactions. The operating conditions used in the test campaign of this chapter are presented in the following table.

Table 5: Operating flow rates, chamber pressure and powers for the thermal evolution tests. *calculated for specific coupon exposure diameter

Material	Compressed Gas	Test Chamber		Oxygen	Power Supply	
		Gas Flow slpm (±1)	Pressure torr (±5)	Mass Flow* g/min (±.5)	Power kW (±2)	Heat Flux W/cm^2 (±10)
Hi-Nicalon SiC Fabric (2ply)	Nitrogen	40	160	0	14	62
	Air	40	160	3	14	80
	Air : Nitrogen	15:30	160	1	14	73
	Oxygen : Argon	10:30	160	3.5	6.6 (low)	57
	Oxygen : Argon	10:30	160	3.5	7.5 (high)	78

The oxygen mass flow rate was calculated from the measured volumetric flow rate and scaled according to the cross sectional area of the 36 mm diameter plasma column and the 18 mm diameter coupon exposure diameter.

6.3. Direct Coupon Insertion

Experiments were performed comparing surface temperatures in oxidizing plasmas and pure nitrogen plasmas. Results have shown very different virgin sample temperature profiles depending on the presence of oxygen even if similar steady state temperatures are achieved. The temperature profile for the N_2 and O_2/N_2 test case can be seen in Figure 33.

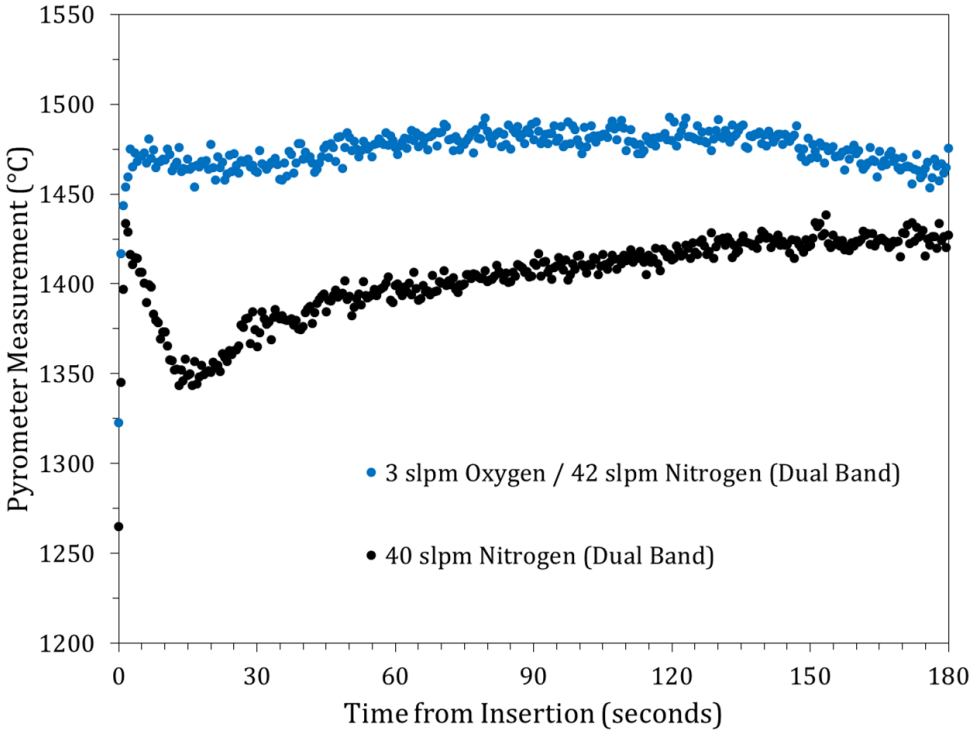

Figure 33: Temperature profile for the air : nitrogen plasma test compared to the pure nitrogen plasma test

It can be seen that the addition of a small amount of oxygen into the plasma significantly increases the initial surface temperature profile of virgin coupons. This increased heating phenomena that occurred while operating at the same torch operating power is associated with a higher chemical reactivity during the initial formation time of the silica layer [32] and confirmed by others using a heat flux probe with a SiC surface [40] [82] [39]. The secondary hump on the O_2/N_2 case after 30 seconds is believed to be associated with a subsequent increase in nitrogen catalycity on the oxidized surface which is described in further detail at the end of this chapter. It is interesting to note that at the conditions tested, the copper slug heat flux measurement was approximately 10 W/cm^2 higher in the O_2/N_2 test case even though the resulting temperatures are similar.

Reinsertion of a previously oxidized sample will not display the initial temperature hump. Differences between the first and second insertion have also been observed by others on temporally changing materials [38][191]. Experiments were performed by exposing samples to 2 minutes of nitrogen or O_2/argon plasmas, then allowed to cool down to room temperature and reinserted into the same conditions. Figure 34 shows the temperature profile on virgin and reinserted samples.

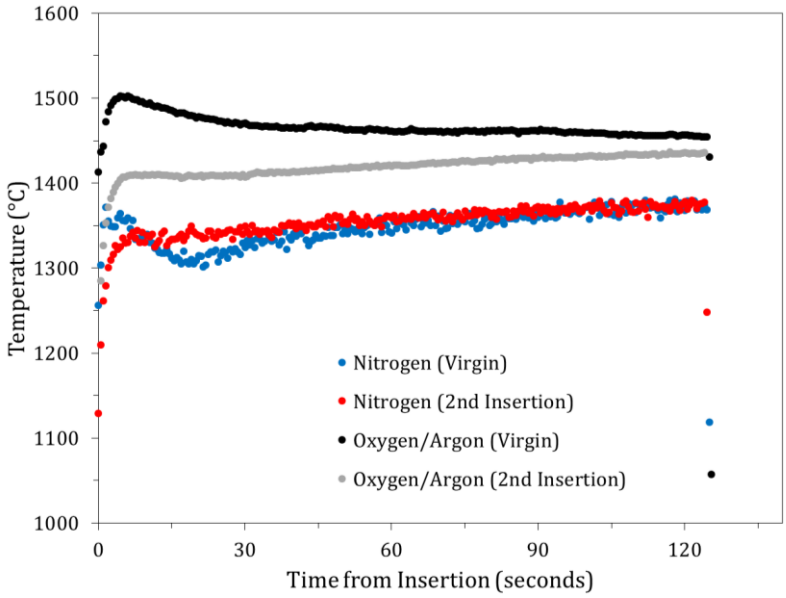

Figure 34: Temperature profiles of virgin and re-inserted SiC coupons for the high power oxygen : argon plasma test compared the pure nitrogen plasma test

Oxygen/argon was used to remove the complexity of oxygen/nitrogen coupling effects which has been shown by Rosner to decrease the total reactivity [83]. These coupling effects can be seen when comparing the shape of the virgin insertion temperature profiles for oxidizing environments presented in Figures 33 and 34. A

secondary hump is almost always observable when nitrogen is present but disappears for oxygen/argon tests. Comparing the first and second insertion of the O_2/argon case, the temperature profile does not show as high of an initial temperature in the second insertion even though they settle at a similar steady state temperature. The almost 100°C temperature differential between the virgin and oxidized SiC coupon would relate to a significantly higher heat load experienced by the entry vehicle. This disappearance of the temperature overshoot on SiC after reinsertion in an oxidizing plasma was confirmed by Gulhan using a spectral pyrometer and a 2 color pyrometer for first and second insertion [38]. It can also be seen that the surface temperature for the oxidized sample almost parallels the nitrogen case exactly. Except for the disappearance of the initial temperature spike, the reinserted nitrogen case follows the same slow temperature rise seen on the virgin sample. The initial flare correlates the increased CN red emission that appears within the pyrometer collection band immediately after insertion. The CN feature and potassium emission line can be seen using the emission spectrometer in the following figure. The dip centered around 945 nm is an absorption feature of the fiber optic cable not seen by the pyrometer.

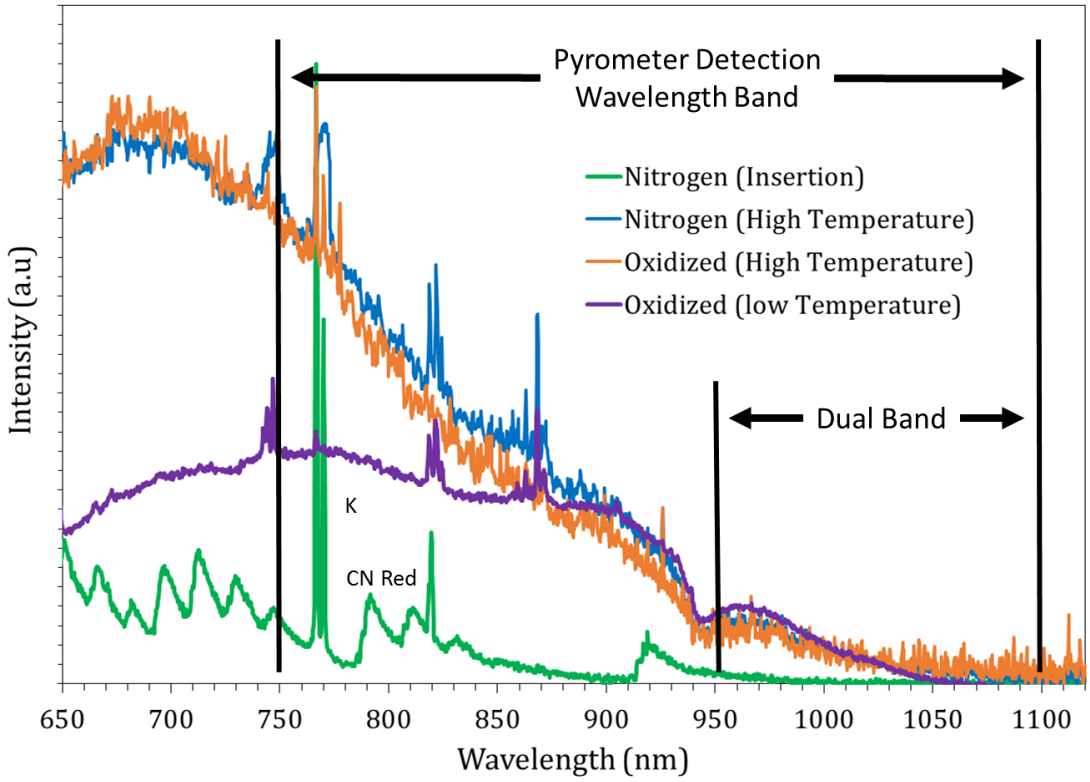

Figure 35: Emission features and graybody emission that occurs within the wavelength band of the pyrometer

The strong CN red and potassium emission can be seen upon insertion into a nitrogen plasma. The high carbon content on the surface of the SiC fibers and thermal decomposition of the inherent silicon-oxycarbide phase is expected to be the cause of the very high CN signal upon insertion into a N_2 plasma. Within the first few seconds, CN emission decreases and the sample temperature increases causing the graybody emission to dominate the spectrum within the pyrometer wavelength band.

SiC is a selective emitter, therefore further error in the pyrometer measurements can exist if the wavelength dependent sample emission intensity is not accounted for.

Compared to the planks distribution of a perfect blackbody, the non-ideal wavelength dependent emission can be seen on the low temperature emission profile. This error can be accentuated when using 2 color mode which uses the energy ratio of two coinciding wavelength bands. Confidence in the temperature measurement can be gained if a similar temperature is measured in both pyrometer modes. The results of this error are shown in appendix D. Fortunately, more ideal graybody emission profiles exist at the higher temperatures used in this study and are shown on an oxidized and un-oxidized surface at 1400°C.

In addition to the non-ideal graybody profile, the oxide film can also bring about considerable difficulties with the pyrometer measurements. Interference effects that arise within the wavelength of the pyrometer from the oxide layer that forms can cause measurement errors as much as 100°C if the 2 color mode is used [84]. These unrealistic measurements using 2 color mode are easily observable in the form of oscillations at temperatures below 1200°C on rigid smooth surfaces. A plot of these oscillations that occur as the silica layer thickens are presented in appendix D.

6.4. Emissivity Calculations

All the components of the dynamic feed-back loop are directly dependent on the surface elemental composition and morphology, including the emissivity. In order to calculate the potential emissivity change in the material, comparisons were made from data collected using 1 and 2 color mode on the same pyrometer.

If the target material acts as a graybody within the measured wavelength, the dual wavelength band measurement can give a reliable temperature without knowing the emissivity value. Due to this ability to provide temperatures independent of surface emissivity it would be expected that any emissivity change in time would still lead to reliable results using the 2 color mode. Although, this is only the case if the material is not a selective emitter and the emissivity changes equally within both wavelength bands maintaining the same ratio of energies.

If the material behaves as a graybody and an accurate emissivity value is entered into the pyrometer, the single wavelength band measurement can also provide a highly reliable measurement. However, a perfect graybody doesn't exist in nature, therefore an effective emissivity value must be selected on the pyrometer in order to account for any anomalies. This effective emissivity value must not only account for the material properties including temperature, object geometry, microstructure, surface morphology and transmittance but it also must account for the experimental configuration. The effective emissivity value used to make the pyrometer measurements is an artifact of the angle of measurement, spectral range of the pyrometer and other attenuation factors that are specific to the ICP Torch. This leaves the potential for the environment and surface characteristics to have greater influence over the resulting effective emissivity value than the actual elemental composition. Many of these surface characteristics drastically change with time during exposure to oxidizing plasmas. However, the emissivity value

selected on the pyrometer will remain constant until manually adjusted. Therefore time dependent emissivity corrections must be made in post processing to compensate for the surface temperature and oxidation state of silicon carbide. The following figures show the time dependent measurement error during oxidation in an O_2/N_2 plasma. Comparisons to a pure nitrogen exposure are also made.

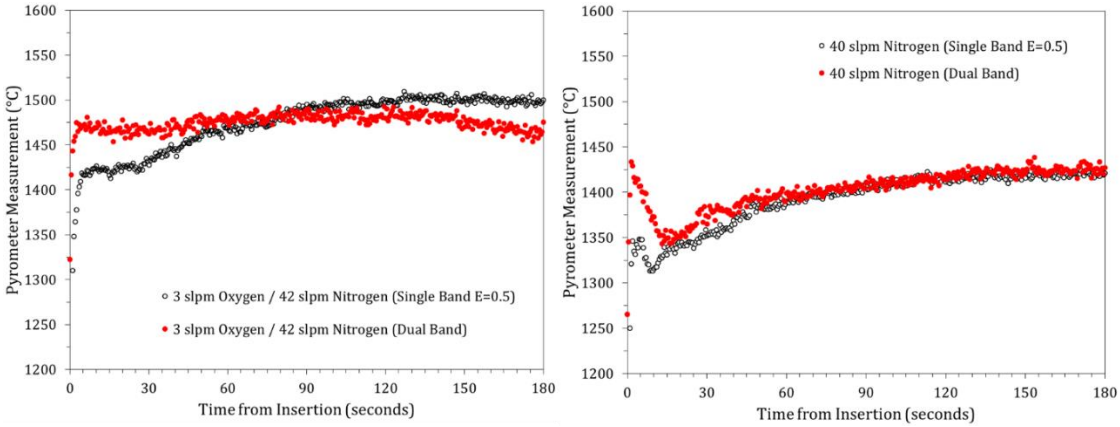

Figure 36: Pyrometer measurements made in 1 and 2 color mode for the air : nitrogen (left) and the pure nitrogen (right) plasma tests

Besides the accentuated error of the initial flare in 2 color mode which is an artifact of surface impurity removal, the nitrogen plasma test provides similar trends and temperatures using a 1 color mode emissivity value of 0.5. If both temperatures parallel each other, a constant spectral emissivity would be calculated and the material could be represented as a gray body as seen in nitrogen plasma case. For the air plasma test, it is obvious that the surface selected pyrometer emissivity used in 1 color mode does not track the exact temperature measured in 2 color mode. This divergence signifies a time dependence on the emissivity.

Assuming confidence in the measurements made using 2 color mode and knowing the inputted emissivity used in 1 color mode, the spectral emissivity ϵ_{2c} can be numerically determined using the following relationship:

$$\sigma\epsilon_{1c}T_{1c}^4 = \sigma\epsilon_{2c}T_{2c}^4 \qquad \text{eq. 22}$$

Where ϵ_{1c} is the emissivity value manually inputted into the pyrometer, T_{1c} is temperature measured in 1 color mode, and T_{2c} is temperature measured in 2 color mode.

Although this effective emissivity value will only be relevant to the experimental configuration due to the specific pyrometer wavelength range, orientation, and line of sight into the ICP torch. Due to the rough coupon surface this effective emissivity value is not expected to match reported values for a smooth flat surface. Also, the effective emissivity value does not represent the total emissivity which includes all wavelengths and angles, not just the 30° and 0.75 to 1.1 μm of the pyrometer. Whereas, the total emissivity determines the radiative cooling of the surface. Fortunately, even if the total emissivity value is unknown, the extraction of the emissivity time dependence is still distinguishable.

Calculated emissivity for two different gas compositions can be seen in Figure 37.

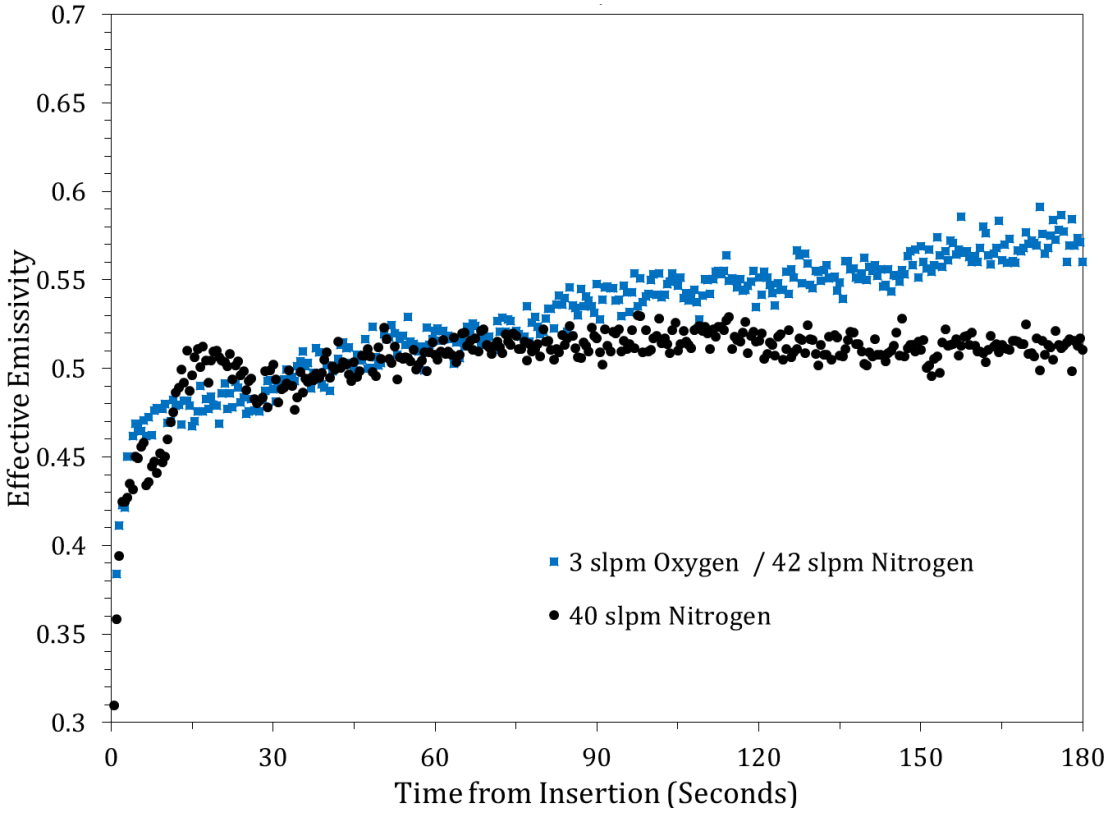

Figure 37: Emissivity values calculated from temperature vs time data for the air : nitrogen and the pure nitrogen plasma tests

This increasing effective emissivity with time can be seen for all virgin samples exposed to oxygen containing plasmas. Although differences in magnitude exist due to the different surface temperatures. For the angle and spectral range of the pyrometer, the non-oxidized samples ranged around 0.5 whereas the oxidized samples increased from 0.45 up to 0.6 within 3 minutes, although the confidence lies in the change with time and not the actual emissivity value. It is interesting to note that this change in emissivity is on the order of minutes like the observed silica thickening phase. This change in emissivity is in agreement with others that have shown that the emissivity on SiC surfaces can change with temperature, roughness and oxidation state [43].

6.5. Oxygen Addition Testing

6.5.1. Influence of Oxidation on Emissivity

Due to the many transient phenomena occurring directly after insertion into the plasma, a different method was used to extract the effects of oxygen on the surface temperature. By exposing the samples initially to pure nitrogen plasmas, the influence of potential impurities and the thermal inertia of the sample holder could be minimized. Once a steady state temperature was achieved in nitrogen, air was added into the plasma. This addition of oxygen at constant ICP torch power supply conditions led to a temporal change in equilibrium temperature. The manual changes made in the operating conditions can be seen in the top section of Figure 38. The flow rate is shown on the left while the copper slug heat flux is labeled on the right. The heat flux measurements were taken before and after the test at the known steady state conditions. The bottom section of the figure shows the resulting temperature and scaled graybody peak emission vs time for a virgin sample. A re-insertion test was also performed following the same procedure.

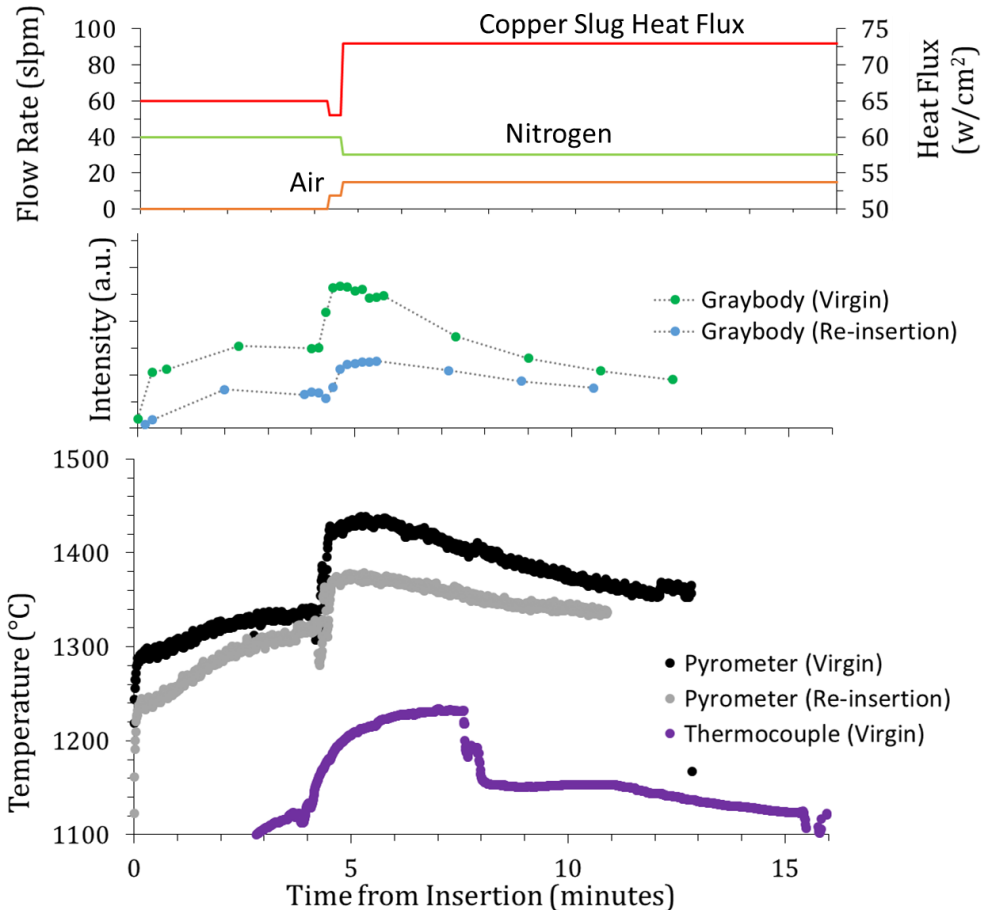

Figure 38: Plot showing the oxygen addition procedure and the resulting temperature response

In order to maintain a stable plasma jet, the nitrogen flow rate was decreased in a stepwise fashion when the air was added. Once oxygen was present in the plasma flow a large jump in surface temperature was observable followed by a slow asymptotic decrease of almost 100°C. This is unique for a virgin SiC material as an oxidized sample will not show as significant of a temperature increase suggesting that it is not specific to the increased heat flux when air is added but actually material dependent. The peak graybody signal and thermocouples were used to confirm the existence of a temperature hill. Although the thermocouple measurements were affected by the silica formation

within the weave and had to be performed at a lower heating condition due to the increased potential of catastrophic failure when thermocouples are placed within the weave. These results are consistent with the direct insertion tests whereas a lower temperature was observed on the re-inserted sample.

There are many possible contributions to this interesting phenomena. Due to the fact that the rapid increase then decrease in temperature occurred at constant operating conditions, the phenomena must be due to a change in the feed-back loop. In order to determine the emissivity of the fabric, additional tests were performed using the pyrometer in 1 and 2 color mode. These measurements can be seen in the following plot where the oxygen was added and then removed twice in the same stepwise manner as seen Figure 39.

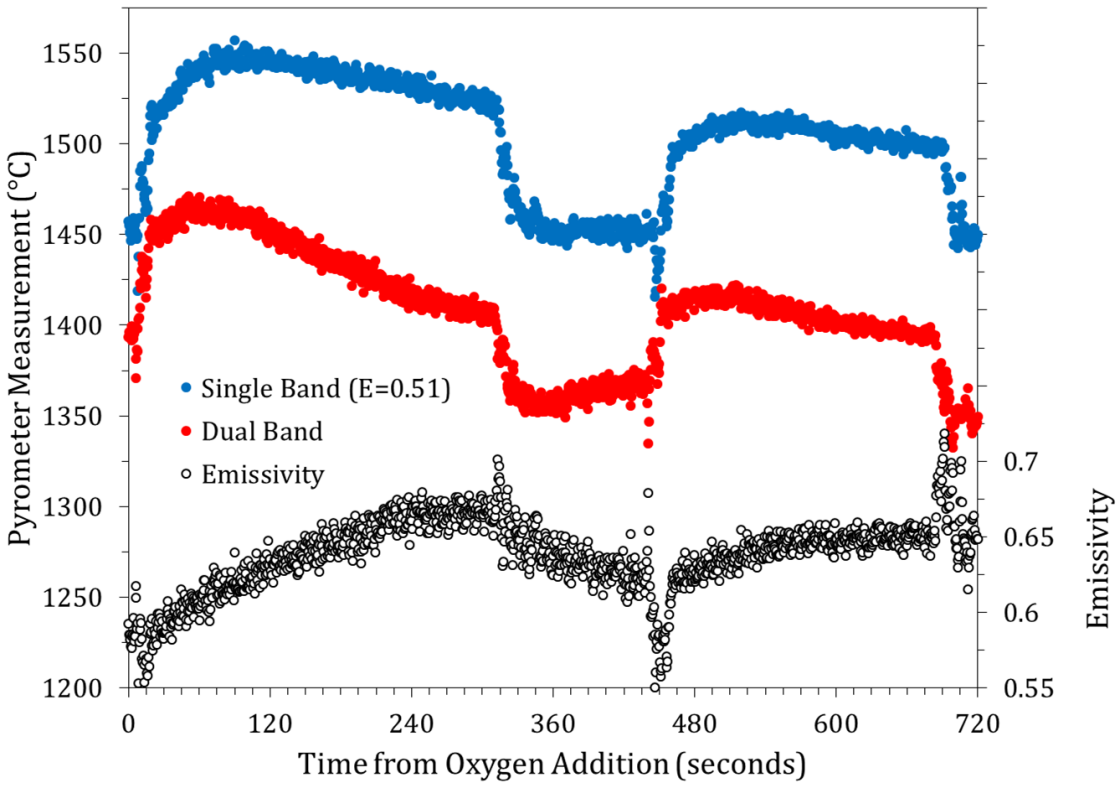

Figure 39: Plot of an oxygen addition test showing the emissivity calculated from pyrometer measurements made in 1 and 2 color mode

It can be seen that the emissivity increases similar to the direct insertion into an oxidizing plasma and then decreases when the oxygen is removed. This suggests the removal of silica during nitrogen exposure which is in agreement with the O-atom emission that can be observed on an oxidized coupon surface in a nitrogen plasma. Although the rate at which the nitrogen plasma removes the silica is much slower than the initial formation stage, therefore no significant visual change has been observed. It can be seen that a relatively constant emissivity is achieved after 6 to 8 minutes of oxygen exposure suggesting a more steady state silica thickness. This is in agreement with other authors that have reported an equilibrium thickness in aerothermal heating facilities [30].

Even though strong quantitative statements can't be made about the influence of emissivity on the radiative heat flux due to a lack of the total emissivity value and the complexity of the feed-back loop, an increase in emissivity would naturally lead to lower surface temperatures due to the increased radiative cooling. Preliminary estimations using equation 1 suggests that a temperature decrease of this magnitude is possible purely by an emissivity change. This can be seen in the following plot of temperature vs emissivity for the first and second oxygen addition. Comparisons to the theoretical calculations are also shown.

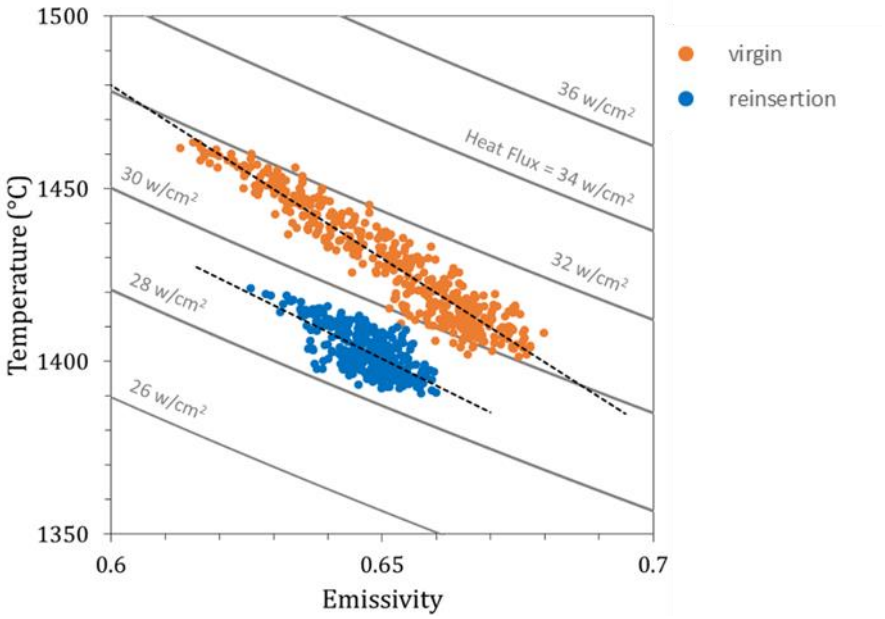

Figure 40: Plotted temperature vs emissivity comparing experimental and theoretical data

It can be seen that the measured surface temperature falls faster than is predicted by the theoretical calculations. If the measured temperature followed the calculated slope

it would be strong evidence that the temperature decrease is purely a function of the emissivity change. Never the less, the plot shows that a 60°C temperature drop is plausible within the margin of error for the relevant surface temperature and emissivity range. Although the difference in slopes between the theoretical and the measured suggest that there is a decrease in the heating mechanism and/or an increase in the cooling mechanism simultaneous to the emissivity change. Comparisons between the first and second addition of oxygen show higher temperatures for the virgin coupon which also suggests that there is further changes occurring in the feedback loop. This could arise from an increase in the conduction through the coupon as well as a decrease in reactivity or catalycity. This includes a change in both nitrogen and or oxygen catalysis. It is unlikely that the variance in temperatures is purely an artifact of the thermal inertia of the sample holder because the temperature drops faster than predicted by the emissivity increase.

6.5.2. Influence of Oxidation on Reactivity

In addition to the emissivity increase during oxidation, a change in atom consumption can be observed during oxidation of SiC materials. For relatively short durations, the rapidly changing surface morphology on the SiC fibers provides evidence of ongoing chemical reactions besides catalytic recombination. This includes the formation of the silica layer as well as bubbles that originate below the silica surface. Whereas, a viscous silica layer on the surface is expected to be reached on the order of seconds at 1400°C in aerothermal environments.

The catalytic efficiency is expected to be purely an artifact of the surface structural nature and only occur on the SiO_2/gas boundary. In contrast, oxidation reactions can occur below the oxide surface at the SiC/SiO_2 boundary and the reaction rate will decrease as the silica layer thickens due to diffusion limitations [60]. Conveniently, the transient reaction rates of oxidation can help to distinguish between catalytic and reactive pathways. The time dependence of the gas surface interactions is illustrated in Figure 41.

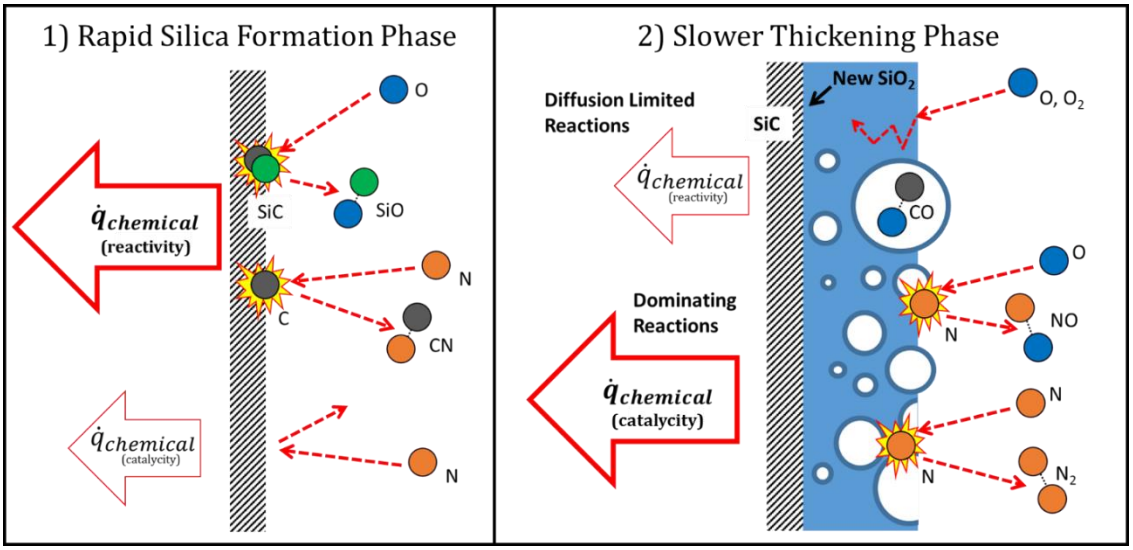

Figure 41: Illustration showing chemical reactions that have been detected during oxidation in the ICP Torch

The illustration depicts a few of the different exothermic reaction pathways that have been detected in an air plasma on an evolving surface. Additional reactions are expected to occur that are not illustrated including homogeneous oxygen recombination.

Endothermic reactions can also occur and remove heat from the surface by ejecting atoms and molecules into the boundary layer [85] but were not included.

In order to show the time dependence in the atomic species consumption through the different pathways, emission spectroscopy was used in the boundary layer in front of the sample. However emission data of SiC fabric coupons had very low signal to noise. Therefore, a rigid SiC disk replaced the fabric coupons due to the ability to better track the gas features from both molecular and atomic species just off the material surface. The following figure shows the emission spectra for the fabric and rigid SiC material at the exact same operating conditions and experimental configuration using a 10 second integration time. Within the free stream most gas species cannot be detected for the integration time used but once the sample is inserted, the cooler, higher density boundary layer near the surface allows molecular and atom species to be tracked. The wavelengths for the dominant features are labeled.

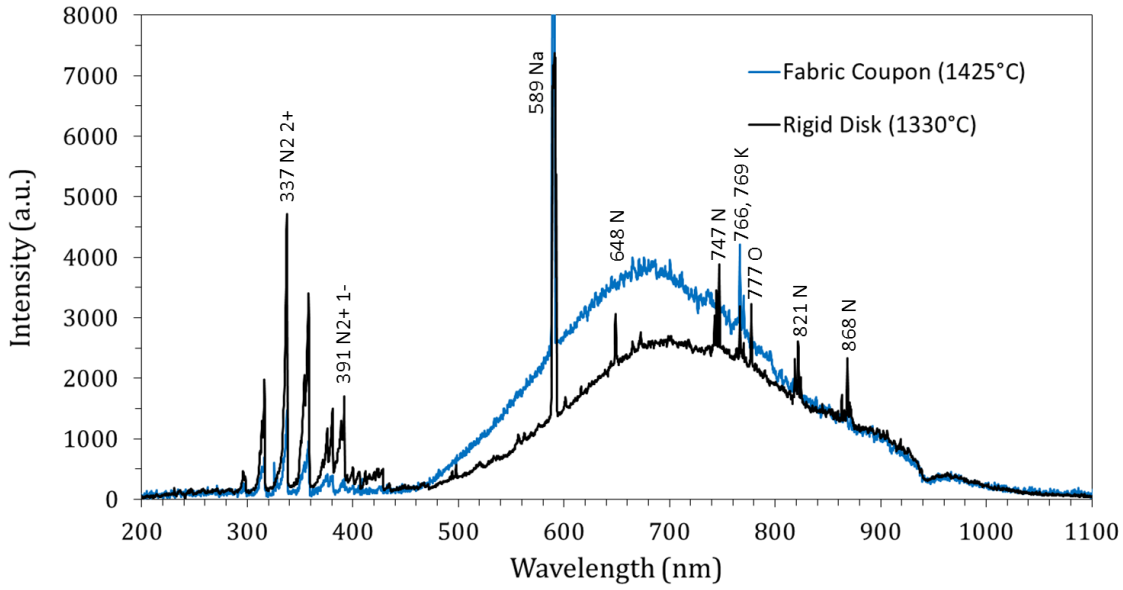

Figure 42: Emission spectra within the boundary layer for two different SiC materials at equivalent ICP Torch operating conditions [66][76]

The difference in graybody emission is due to the higher steady state temperature of the fabrics. The high surface area and the thermal contact resistance between the fibers of the weaves is expected to be the reason for the higher temperature and lower atomic species emission. The non-ideal wavelength dependent emission on the rigid sample can also be seen.

An oxygen addition experiment was performed on the rigid sample in the same stepwise manner as described in Figure 38. The results of the species intensity vs time data is displayed in the following figure. The wavelengths of the features tracked are labeled. The lines between the data points are visual guides to help interpret the data and do not represent physical values.

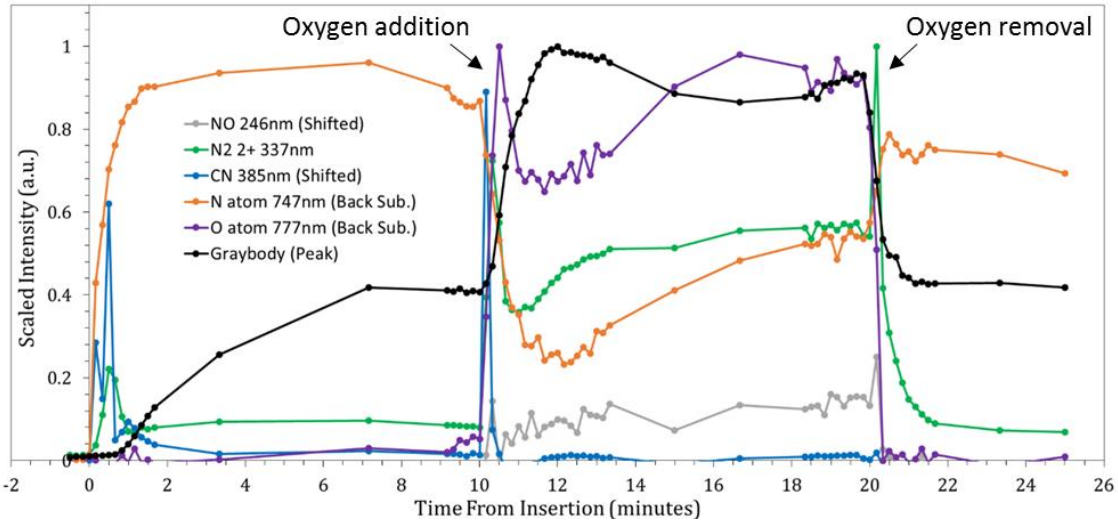

Figure 43: Scaled emission intensities within the boundary layer of a rigid sample

The emission signal intensities were collected with a 10 second integration time and individually scaled to 1. Background subtraction was performed for tracked emission lines that overlapped additional features including the graybody emission. CN and NO features where manually shifted to zero when no signal was observable.

After the initial flare of N_2 2+ and CN, N-atom is easily detectable. Once the surface temperature reached a more steady state, a small flow of air was added to the plasma flow at 10 minutes. During this transition of flow rates, the sample temperature jumped from 1260°C to a peak of 1330°C. O-atom and NO also became detectable using the emission spectrometer. High concentrations of other species are expected in the thermal boundary layer during oxygen addition including CO and O_2. However the spectrometer could only detect strong emitters within the 200 to 1100nm wavelength range. After 20 minutes the conditions were returned to a pure nitrogen plasma.

As the surface morphology evolves due to oxidation, the energy balance described in Figure 32 is not in equilibrium, even if the operating conditions are kept constant. This is also true during exposure to relatively inert gas mixtures including nitrogen, where the transient surface temperature may lead to microstructural changes in the material that can cause a time dependence in the gas-surface interactions.

CN violet is a very strong emitter at 385nm and was observed during the oxygen addition procedure. Within this time frame, it is plausible that a form of active oxidation occurs initially at the low oxygen partial pressures. Whereas the CN spike is due to the formation of free carbon after oxygen reacts with the silicon carbide surface to form SiO. Once the desired oxygen partial pressure was achieved, the surface temperature continues to rise along with a high consumption of atomic species. The initial decrease in N_2 2+ and lower NO signal suggests that other reactions are occurring besides catalytic recombination. After the temperature hump the atomic and molecular gas species increase with time. This is expected to be due to the transfer from oxidation reactions to a predominately catalytic consumption pathway.

6.5.2. Influence of Oxidation on Catalycity

After relatively long durations where a thick silica layer is formed, it would be expected that most impinging gas species will either recombine through catalytic reactions or return to the boundary layer chemically unmodified [21]. Whereas

heterogeneous and homogeneous catalytic recombination is usually predicted to be the dominant atom loss mechanism within the boundary layer. At this point, oxidation reactions would most likely comprise only a small percentage of the chemical component of the heat flux [39][77]. This conclusion is in agreement with experimental results by Hirsch [32] and the kinetic theory calculations carried out by Kimura where only 0.2% of the incident oxygen species contributed to the oxide layer in plasma oxidation [51].

Temporal surface modifications by oxidation have been shown to change the recombination coefficient after exposure times of less than 140 seconds [86]. Whereas, the SiO_2 formed on the surface of SiC in oxidizing environments has also been predicted to be less catalytic than the underlying SiC surface [81]. This change in catalycity leads back into the feed-back loop in turn creating a new equilibrium temperature and continued surface evolution and potential change in emissivity, catalycity or reactivity.

Besides the temporally changing oxidation reactions, Figure 43 also provides additional insight into the N-atom consumption on an un-oxidized and oxidized SiC surface. After 20 minutes, oxygen was removed and the flow rates were returned to the original pure nitrogen plasma. When comparing temperatures before and after oxygen addition, the sample temperature dropped from 1260°C down to 1240°C. It is interesting to note that after the sample was oxidized, the N-atom emission intensity is lower in magnitude when comparing the intensity to the virgin material in the pure nitrogen plasma. This temperature drop and lower N-atom emission intensity is typical for SiC

fabrics as well. It is also interesting that a peak in the O-atom signal occurs at 17 minutes and the graybody emission begins another slow increase. These results suggest that the catalycity of the material may still be changing due to the formation of bubbles leading to a silica surface that may actually have a higher catalytic efficiency. Another possibility for the decrease in N-atom signal is the N + Si or N + O reaction that may occur between the gas phase and the SiO_2 surface. This is in contradiction to results by others that have shown a decrease in catalytic efficiency on SiO_2 surfaces compared to SiC. Although, the oxidation in dissociated gases at these high heating conditions can lead to a rough, porous and viscous silica surface, as seen in Figure 27 of Chapter 5. Therefore, the net drop in temperature may be due to the higher emissivity and a decrease in the oxidation reaction rate.

CHAPTER 7: FRACTURE BEHAVIOR OF TWO-DIMENSIONAL WOVEN SILICON CARBIDE FIBERS EXPOSED TO HIGH-TEMPERATURE NITROGEN AND OXYGEN PLASMAS

7.1. Introduction

Outer fabrics must withstand intense post shock heating while remaining strong and pliable to accommodate the associated stresses of flight. However oxidation of the fine diameter SiC fibers has raised questions about the possibility of heat shield failure due to a weakening tensile strength of the outer fabric. Many authors have reported a change in the tensile strength of SiC fibers after exposure to static heating environments or with flowing molecular gases in more conventional furnaces [5, 8, 27, 87-103] but these test configurations are far from the actual conditions of flight. Flowing dissociated gases along with combined radiative and convective heating, which is more representative of hypersonic flight aerothermodynamics, can significantly enhance chemical reactions with the SiC surface [53]. To examine the performance of woven outer fabrics in an environment that better replicates atmospheric trajectory aeroheating, tests were conducted in the 30 kW ICP Torch Facility. These tests involved exposing fabric samples to different plasma heating conditions for varying lengths of time. Additional tests were carried out using different plasma gases to better understand the plasma chemistry influence on fabric strength. The following sections describe the SiC material properties, the high temperature test environment, and the results of tensile tests on the woven fiber coupons.

7.2. Experimental Conditions

Re-entry conditions were of interest, therefore experiments were performed with 100% nitrogen, dilute air, normal air, and 100% oxygen plasmas to elucidate the effects of oxidation reactions while maintaining a constant chamber static pressure of 160 torr. The operating conditions for each test case of this chapter can be seen in Table 6.

Table 6: Operating flow rates, chamber pressure and powers for the fracture strength tests. *calculated for specific coupon exposure diameter

Material	Compressed Gas	Test Chamber		Oxygen	Power Supply	
		Gas Flow slpm (±1)	Pressure torr (±5)	Mass Flow* gpm (±.5)	Power kW (±2)	Heat Flux W/cm^2 (±10)
SiC Fabric (Hi-Nicalon) (2 Ply)	Nitrogen	40	160	0	14	62
	Air : Nitrogen	15:30	160	1	14	73
	Air	40	160	3	14	80
	Oxygen	40	160	14	12	79

For all of the different test durations, the fabric samples exhibit the same temperature profile within ±25°C for each unique gas composition and power setting. The temporal variation of surface temperature for the four-minute tests in the different plasma mixtures can be seen in the following plot.

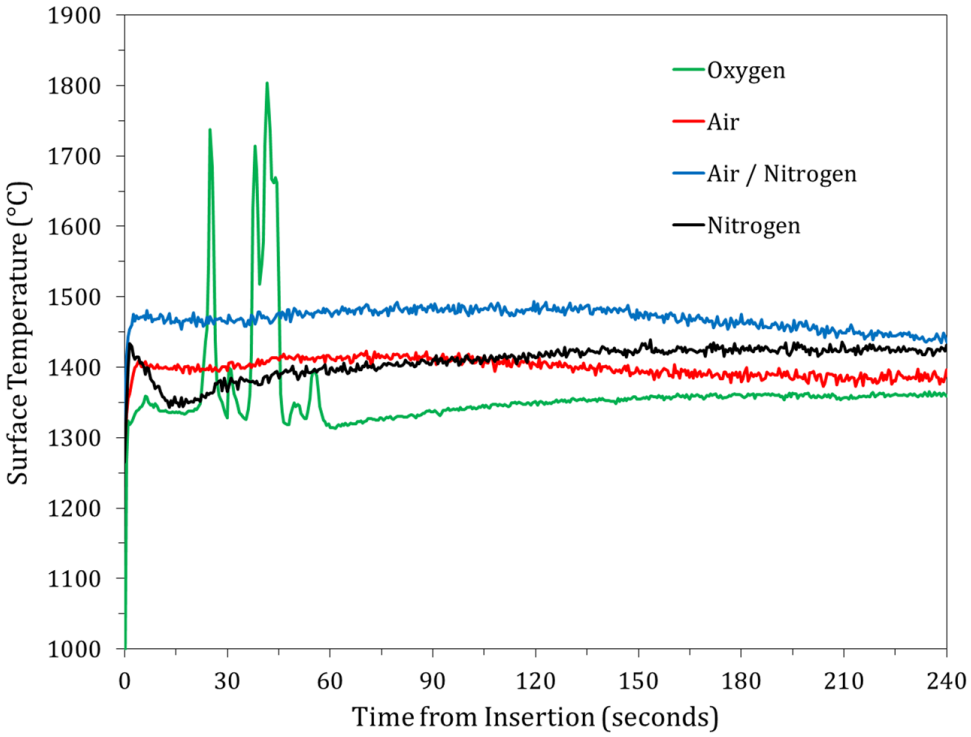

Figure 44: Two-color pyrometer measurements of the coupon surface for the duration of a plasma test for different plasma gases

The heating conditions were chosen to provide similar steady state temperature levels for all test gases. However, it was not possible to exactly match the temperature evolution for each gas composition due to the different gas-surface interactions occurring for different plasmas. One example is shown by the high-temperature excursions, which appear as surface flares in video records, for the pure oxygen test case.

7.3. Tensile Testing

7.3.1. Coupon Test Configuration

To characterize the fiber strength change for flight applications, hot sample tensile tests would be ideal. However, due to experimental limitations to date, room

temperature tensile tests were performed on the circular woven fabric coupons after plasma exposure. To execute the strength tests, a Test Resources 1000M single column tensile machine equipped with a 5kN maximum capacity force transducer was used. Owing to the circular shape of the coupons, no ASTM standard for testing textiles could be carried out. Metal pipe strapping was attached at opposite ends of the coupon using a two-part adhesive to securely mount the specimen in the knurled grips. Tests were performed at a constant extension rate of 1mm/min and samples were pulled to elongation at fracture. A schematic of the loading configuration is shown in Figure 45.

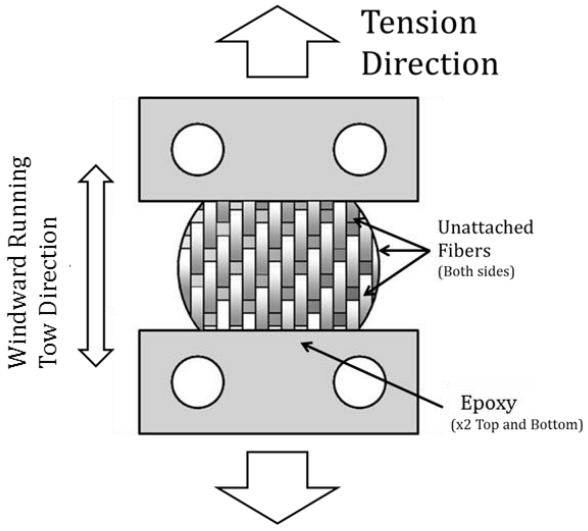

Figure 45: Mounting configuration used to test the 2 cm circular coupons

A custom jig was used to carefully mount the coupons to provide a consistent gage length of 6mm and to limit any off-axis loading to ±5°. Due to the asymmetry of the satin weave, the fibers on one face of the fabric visually run in one direction. Even though fabric tensile strengths can differ between warp and weft directions [27], it was

nearly impossible to distinguish the weave direction from the circular coupons; therefore the load direction was always oriented in the run direction on the windward side. For each test, there was an average of 18 loaded tows, leaving approximately 4-6 tows unattached for the specified gage length due to the circular shape of the coupons.

7.3.2. Fracture Strength Calculation

To present all results as tensile break strength, calculations were made from the load and head displacement output data. Given that the conversion to tensile stress depends on the coupon cross-sectional geometry, the number of filaments and specific diameter of each filament must be known. The following equation was used to convert fabric breaking loads to tensile strength.

$$\sigma_{fracture} = \frac{F_{max}}{\pi f \left(\frac{D}{2}\right)^2} \qquad \text{eq. 23}$$

Where $\sigma_{fracture}$ is the fracture strength, F_{max} is the peak load taken from the load vs strain plot, f is the number of filaments, and D is the filament diameter. The number filaments were determined using the filaments per tow data provided by the distributor and the counted number of broken tows, t, as seen in the following equation.

$$f = \frac{f}{t} \times t \qquad \text{eq. 24}$$

The manufacturer's data for the individual fiber diameter of 14 μm and 500 filaments per tow were used to make the strength calculations. These quantities were validated with the use of SEM imaging of the fibers and tows. Any fiber diameter reduction due to the conservation of mass during the transition from SiC to SiO_2 was deemed negligible within the limits of the SEM for the short exposure times. Therefore the same filament diameter of 14 μm was used for all calculations, which causes this method to provide conservative results. Any micro-composite calculation complexities that arise from the two component SiO_2/SiC oxidized samples were ignored due to the much smaller tensile strength of silica. The attached number of tows were counted before and after each tensile test as some tows de-bonded from the adhesive and slipped from the vice grips. Error bars are presented to show these stress calculation uncertainties.

Caution should be used when making direct comparisons between the results of the coupon strength and the strengths reported for single filaments. Fibers to fiber abrasion and weaving damage can counteract the potential increase in strength due to the fabric assistance provided by the weave [104]. Beside the influence of the weave, tensile strength comparisons between single tow tests and the single filament tests performed by others, as seen in appendix E, depict an approximate 40% loss in strength when multiple filaments are tested simultaneously which is in agreement with the bundle theory [92]. Whereas the bundle theory states that the individual filaments don't fracture uniformly and fracture propagation can be initiated by the weakest filament leading to a failure strength that is much lower than expected [92].

7.4. Fracture Strength Results

7.4.1. Nitrogen Plasma Strength

Tensile tests were performed on the samples following exposure times of 30, 60, 120, and 240 seconds. Results showing the strength reduction in a pure nitrogen plasma can be seen in Figure 46. It is important to note that all dotted lines between the data points in every plot are visual guides and do not actually represent physical measurements.

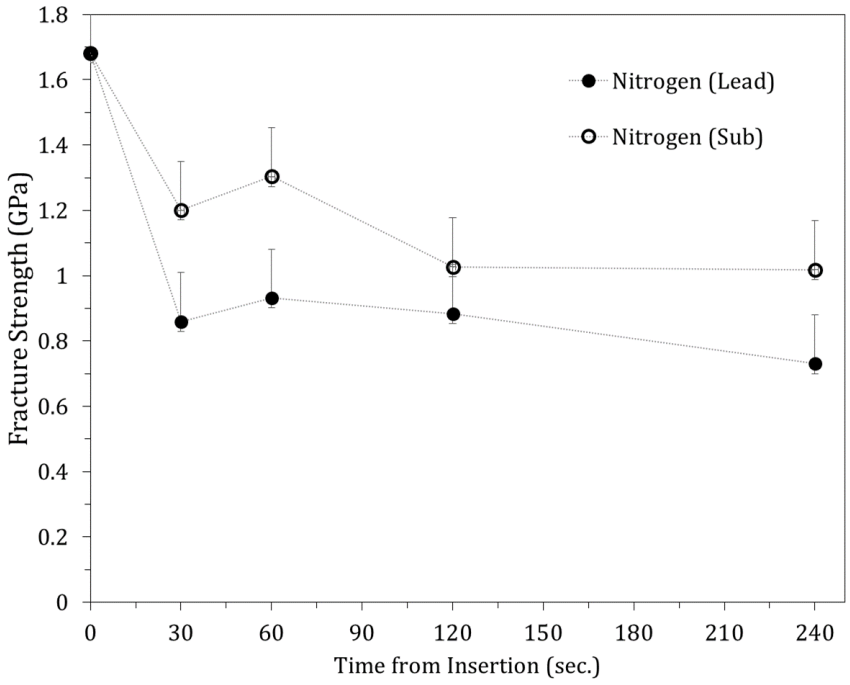

Figure 46: Fracture strength of the lead and sub ply after exposure to a nitrogen plasma

An exposure time of zero is represented by the 3 test average virgin coupon fracture strength. For both lead and sub ply there is a drastic strength loss after seconds

of exposure to the partially dissociated nitrogen plasma. The fracture strength of samples appears to level off at approximately 50% strength reduction for durations between 30 and 240 seconds and have retained their structural integrity after exposures of over 40 minutes. This limited time dependence for longer durations has also been shown to occur in molecular nitrogen for times between 1 and 400hrs at temperatures below 1500°C [91]. After any rapid transient effects that occur within 30 seconds, a relatively steady state strength offset between plies was observed in nitrogen plasma tests. The greater strength retention of the sub ply may arise from the naturally lower temperatures behind the leading surface. Although, the lead ply is also expected to attenuate the influences of damaging gas-surface interactions or possible radiation emitted from excited species transitions within the plasma.

7.4.2. Oxygen Plasma Strength

A distinct difference was observed when comparing the surface morphology and tensile strengths between the oxidized Hi-Nicalon samples and samples that were only exposed to pure nitrogen plasmas. Results showing the strength reduction in oxidizing plasmas can be seen in Figure 47.

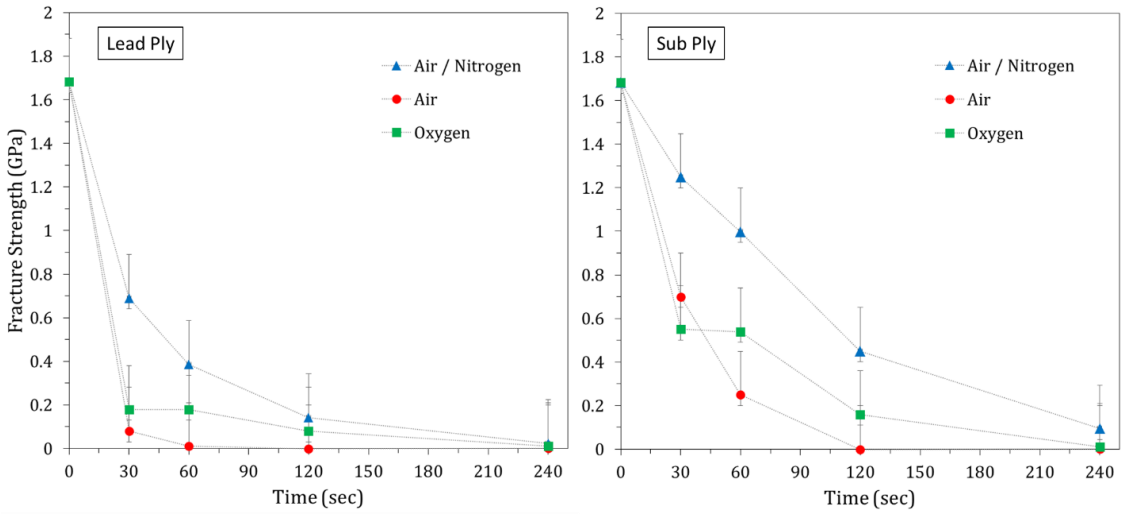

Figure 47: Fracture strength of the lead (left) and sub ply (right) after exposure to different oxidizing conditions

Compared to pure nitrogen plasmas, the strength decrease in oxygen containing plasmas displayed a greater magnitude and longer time dependence. The incredibly brittle nature of the SiC fiber after exposure to an oxidizing plasma bound the maximum testable duration to 240 seconds at the experimental temperatures. The strength reduction for the sub ply occurs at an initially slower rate compared to the leading ply. Suppression of damaging gas surface interactions deeper within the intricacies of the weave most likely contribute to the time delayed strength reduction of the sub ply. Whereas, boundary layer effects such as aerodynamic shear and dissociation fraction may decrease within the weave architecture. Not until after 240 seconds does the fracture strength of the lead and sub ply converge to an equivalent value within the margin of error.

7.5. Material Response

7.5.1. Nitrogen Plasma Morphology

Removal of any protective coatings including PVA and surface carbon is expected to occur at temperatures between 400-600°C [88], and such temperatures are achieved within the first few seconds for all test cases. The initial surface carbon removal could participate in the strength reduction due to its ability to ameliorate strength controlling surface flaws [100]. This removal of surface carbon was observed in a pure nitrogen plasma and can be seen in Figure 23 of Chapter 5.

Removal of carbon from the leading material surface can be seen immediately after insertion in pure nitrogen plasmas by the appearance of diatomic carbon and CN emission. Whereas, CN violet and CN red emission easily dominate the emission spectra. Atomic nitrogen features come from the plasma itself and the strong 589 nm sodium line is present during all tests, but it is not mentioned in the manufacturer's data. Removal of silicon can be also seen after insertion in pure nitrogen plasmas by the appearance of atomic Si emission. Note that the atomic Si emission is weaker than that of the strongly emitting polar molecule CN, and so it appears barely detectable when capturing the strong CN emission without saturating the detector. In contrast, impurity and free carbon removal is suppressed in an oxidizing atmosphere.

After a microscopic investigation using the SEM, most coupons exposed to nitrogen plasmas had a continuously smooth SiC fiber surface like the virgin coupons. A

few fibers did display signs of surface damage in the form of large pits and thinning fiber diameter. A SEM image of a damaged area can be seen in Figure 48. At these rare damaged locations on the surface, EDS has detected nitrogen incorporation on the fiber surface which has also been observed by Shimoo [105]. It is uncertain if the nucleation of damage is due to manufacturing imperfections or contamination by particulates within the weave architecture.

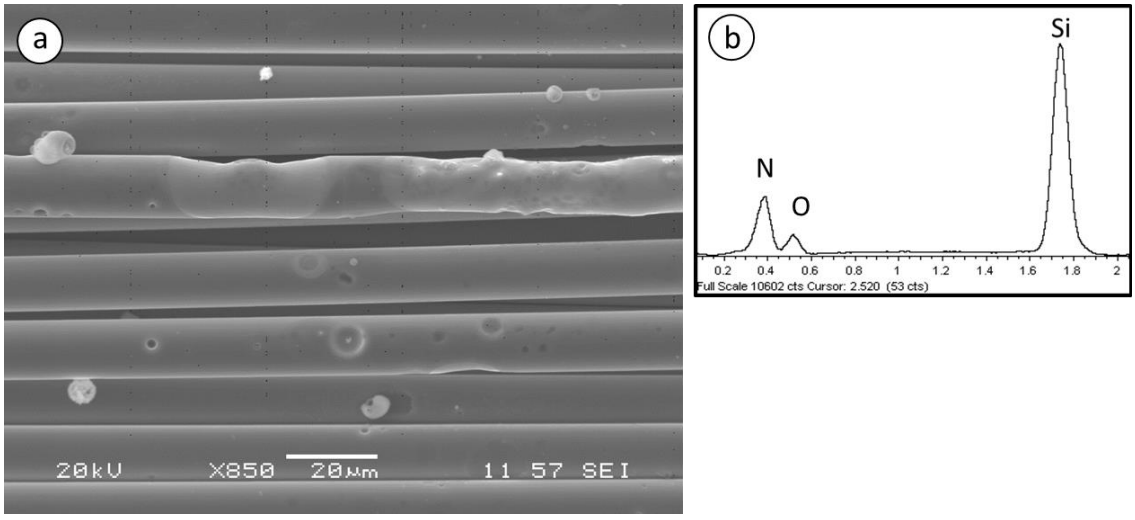

Figure 48: a) SEM image of the sample post pure nitrogen plasma exposure and b) EDS results on the surface showing signs of oxy-nitridation

Besides the gas/surface interactions leading to rare locations of fiber damage and removal of surface coatings, microstructural changes within the fibers from the high temperatures and radiation from excited gas species is another possible reason for the 50% fiber strength reduction in a 100% nitrogen plasma. Thermal decomposition of the amorphous silicon oxycarbide phase is commonly reported to significantly weaken non-stoichiometric SiC fibers [106]. Strength loss due to thermal decomposition can occur

through the coalescence and coarsening of the fine β-SiC grains [106], leading to structural defects such as dislocation and stacking faults [102]. Silicon depletion observable in Figure 23 of Chapter 5 could also render the fibers porous [98] leading to fiber strength losses of up to 20% [8].

7.5.2. Oxygen Plasma Morphology

As described in Chapter 5, SiC fabrics exposed to oxygen containing plasmas undergo a dramatic morphology evolution that is not uniform throughout the weave architecture. The combination of abundant atomic oxygen and high surface area for the SiC fabrics was determined to be the cause of the rapid silica formation. Any potential gain in strength due the sealing of flaws by the silica coating on the surface [102] appears to be negligible.

The newly formed silicon dioxide layer led to an increase in fabric stiffness and brittleness that increased with temperature and duration of exposure. This decrease in fabric flexibility has also been observed by Sawko at temperatures above 500°C in a static heating condition [27]. Significant stiffness is caused by inter-filament adhesion within the tows by the formation of silica. A SEM image of the broken cross sections for a post nitrogen plasma test sample compared to the post air plasma test sample can be seen in Figure 49.

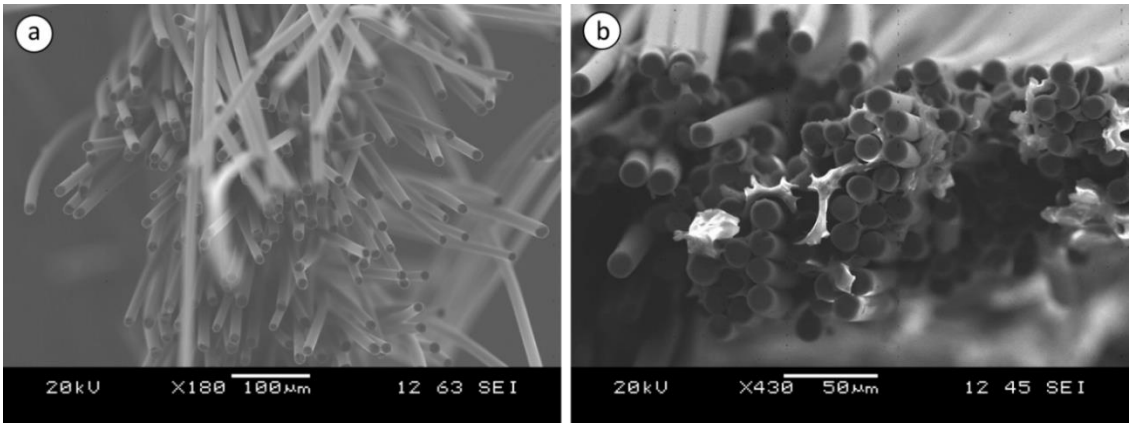

Figure 49: Post tensile test cross sections after exposure to a) a pure nitrogen plasma b) and an air plasma

No signs of fracture origin could be distinguished after plasma exposure. Significant SiO_2 formation can be seen in Figure 49 for the air case at an exposure time of 240 seconds. After the initial formation phase there is very little variation in the observable silica volume within the weave architecture for the plasma test durations of this investigation. Although, macroscopic observations of the continuous surface iridescence change, increasing stiffness, and coupon removal difficulty suggest further fusion of warp and weave tows by the viscous flow of silica.

Under tensile stress, fiber break after oxidation is typically due to brittle fracture arising from the rapid propagation of a critical flaw [103]. Therefore, it is expected that microstructural defects in the oxide layer act as nucleation points leading to a greater strength reduction in oxidizing plasmas. Figure 50 shows the flawed nature of the oxide layer at the location of a ruptured bubble. This bubble formation increases with temperature and time which demonstrates the limited protective nature of the silica.

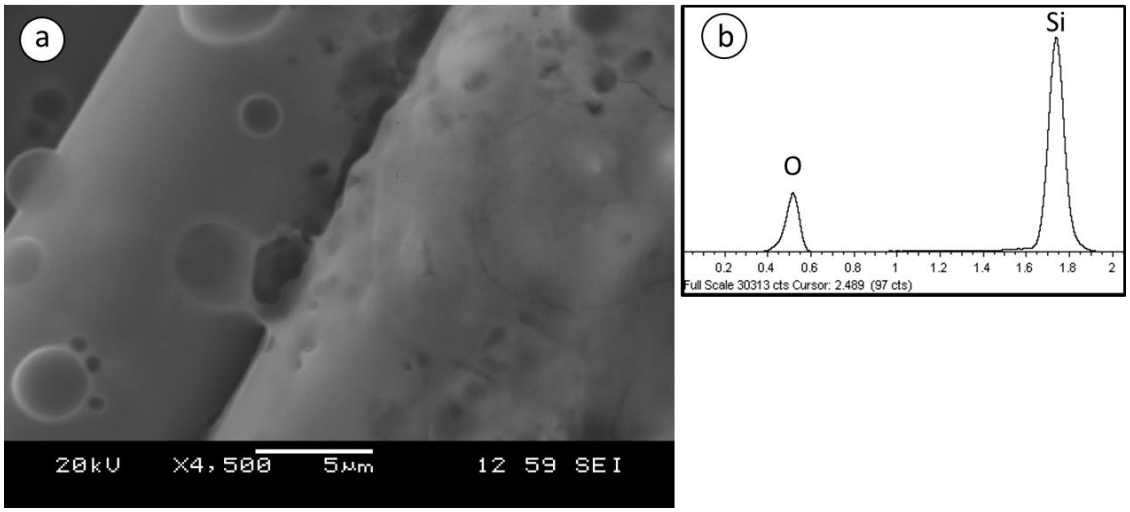

Figure 50: a) SEM image of the oxidized surface morphology and b) EDS results on the oxidized surface

Isolated cracks in the highly oxidized sample can also be observed. The cause of the cracks is uncertain, and it is possible that they may arise following plasma exposure during sample removal. They can also result during cool-down from a thermal expansion coefficient mismatch between SiO_2 and SiC, or between different SiO_2 crystalline structures [98].

It is important to note that the strength controlling effects caused by the brittleness of the silica and fabric stiffness displayed by the cooled samples may not be relevant to flight applications when the silica is viscous. The influence of the cooled silica layer was measured by Shimoo [98], after comparisons between oxidized samples with and without the silica layer [98]. It was shown that critical flaws within the silica layer act

detrimentally on the strength of the fiber [98]. However, the continued strength reduction for relatively constant oxide layer thicknesses after 30 seconds suggests microstructural changes are still taking place within the fiber. Thermal decomposition and continuous bubble formation caused by the continuous attack of oxygen on the SiC fiber would still be expected during flight.

7.6. Influence of Oxygen Concentration

Oxygen partial pressure has been shown to be one of the dominating factors in the oxidative strength reduction of Hi-Nicalon fibers [106]. The relationship between fracture strength and the ICP torch oxygen flow rate can be seen in Figure 51.

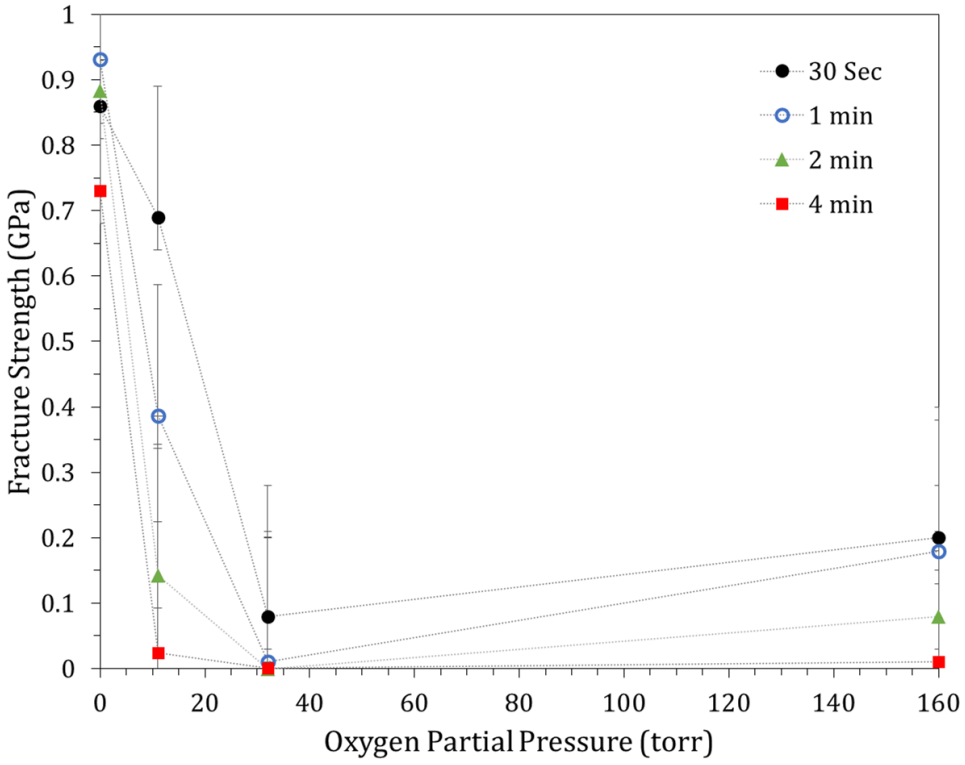

Figure 51: Fracture strength vs oxygen partial pressure for varying exposure times

To better understand the influence of oxygen concentration on fracture strength, the data are presented for each plasma condition at constant exposure times. The initial strength decrease at an oxygen partial pressure of 11 torr suggests a limited oxygen availability due to the strong time dependence. The strength continues to decrease with increasing oxygen concentration until the full air condition of 32 torr where the strength then increases for the full oxygen case. Even though there is no significant difference between the air case and the full oxygen case within the margin of error, a slightly stronger trend is still observable in the full oxygen case. It is believed that the cause of the inflection is due to the maximized combination of thermal decomposition and strength reducing flaws. The higher availability of oxygen atoms in the pure oxygen test

case may provide a more protective SiO_2 film that better restricts the removal of species that originate from the unstable silicon oxycarbide phase [98]. This phenomena can be seen in Figure 23 of Chapter 5 by the lack of carbon and silicon bearing species emission above the sample surface in an oxidizing plasma. Although, it is also possible that the 50°C lower steady state surface temperature recorded by the 2 color pyrometer on the pure oxygen sample could be the cause for this increase in tensile strength.

One significant strength controlling feature that was not observed in the dissociated plasma flow was a highly destructive "active oxidation" regime at extremely low oxygen partial pressures. This regime has commonly been obtained using molecular oxygen at oxygen concentrations too low to form a protective silica layer [106]. In the ICP torch, the probability of temperature flares leading to visually observable failure locations actually increases with oxygen concentration. It is probable that a minimum oxygen partial pressure for silica formation exists but none was detected at the operating conditions used in this test campaign. Any attempt to add oxygen to a steady nitrogen plasma always led to a passive silica coating or a form of oxy-nitridation.

7.7. Influence of Temperature

Along with oxygen concentration, temperature has been shown to be another dominating factor in the strength reduction Hi-Nicalon fibers [97]. ICP tests were performed at an oxygen volume flow rate of 10 slpm for two minutes. Admixtures with argon were used instead of nitrogen to broaden the achievable surface temperatures while

maintaining a similar oxygen gas flow rate as an air plasma. The heat flux ranged from 26 to 107 W/cm^2 which is coupled with a change in gas chemistry. Whereas, the degree of dissociation of O_2 increases with heat flux until relatively high plasma temperatures when the molecular oxygen is fully dissociated at the test location. The complete operating conditions for the strength vs temperature tests can be seen in Table 7.

Table 7: Operating flow rates, chamber pressure and powers for the strength vs temperature tests. *calculated for specific coupon exposure diameter

		Test Chamber		Oxygen	Power Supply	
Material	**Compressed Gas**	Gas Flow slpm (±1)	Pressure torr (±5)	Mass Flow* gpm (±.5)	Power kW (±2)	Heat Flux W/cm2 (±10)
SiC Fabric (Hi-Nicalon) (2 Ply)	Oxygen : Argon	10:30	160	3.5	3.7	26
	Oxygen : Argon	10:30	160	3.5	6.6	57
	Oxygen : Argon	10:30	160	3.5	7.5	78
	Oxygen : Argon	10:30	160	3.5	10.3	107

The achievable surface temperatures were bounded by the minimum sustaining power of the ICP torch and the high probability of catastrophic failure at higher heat fluxes. Therefore, no analysis on the trends at lower or higher temperatures could made.

The sub ply peak temperature for the softest condition test was anchored at 726°C using thermocouple data placed between the leading and sub ply. The sub ply data for conditions above the usable limits of the thermocouples were plotted at an estimated temperature of 110°C below the lead ply pyrometer measurement at 120 sec. Due to the inability to accurately measure the SiC surface temperatures below 1200°C using the pyrometer in 2 color mode, 1 color mode was used with an emissivity set at 0.6. Larger

error bars are presented to compensate for the limited reliability of the combined thermocouple and pyrometer data techniques.

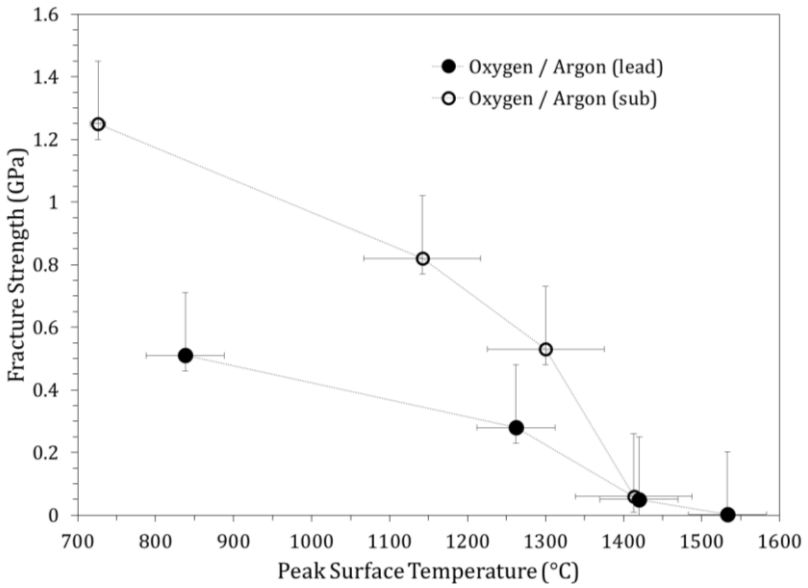

Figure 52: Fracture strength vs temperature plot showing results for both the lead and sub ply

Incorporating the coupled increase in dissociation fraction with temperature, Figure 52 shows the significant influence of temperature on the strength reduction of Hi-Nicalon coupons after 120 second exposure times. Samples show a continuous fracture strength decrease until a lead ply maximum peak temperature of 1533°C. Significant differences are observable in the tensile strength for different ply locations depending on the temperature. The offset between the lead and sub plies for similar temperatures confirms the existence of strength controlling gas-surface interactions. Whereas less atomic species are expected to penetrate deeper within the weave architecture. Therefore, the strength decrease of the coupons is not purely temperature dependent. Aerodynamic

shear, pressure and diffusion limitations are all expected to play a role in the greater strength reduction on the lead ply. These strength differences between ply locations exist until temperatures above 1400°C, whereas the tensile strengths overlap for similar coupon temperatures. At these extreme temperatures, any signs of protection of the sub ply provided by the leading ply are not observable.

CHAPTER 8: PROPAGATION OF EXOTHERMIC OXIDATION REACTIONS LEADING TO CATASTROPHIC FAILURE OF SIC FLEXIBLE TPS

8.1. Introduction

Oxidation has been shown to be damaging to the rough, high surface area SiC fabrics. The duration of flight is limited by the complete consumption of the SiC fibers whereas the rate of consumption will increase with increasing surface area [73][107]. Mechanical loads are limited by the brittle transition of the fibers when exposed to oxidizing environments which could also cause failure of the fabric. Another failure mechanism was observed when the fibers were pushed beyond their maximum survivable conditions leading to catastrophic destruction which occurred rapidly without warning. Further investigation into this phenomena was carried out in order to determine the cause and quantify the conditions that led to this catastrophic failure.

8.2. Experimental Conditions

The experimental conditions were mapped at varying heat fluxes which ranged from 44 to 80 W/cm^2. Different gas compositions were used in order to isolate specific chemical reaction pathways and analyze their influence on the failure mechanisms. Throughout the duration of each test, input power, flow rates and pressure of 160 torr all remained constant. The operating conditions used in this test campaign are presented in the following table.

Table 8: Operating flow rates, chamber pressure and powers for the failure tests.

***calculated for specific coupon exposure diameter**

Material	Compressed Gas	Test Chamber		Oxygen	Power Supply	
		Gas Flow slpm (±1)	Pressure torr (±5)	Mass Flow* g/min (±.5)	Power kW (±2)	Heat Flux W/cm^2 (±10)
Hi-Nicalon SiC Fabric (2ply)	Nitrogen	40	160	0	14	62
	Air	40	160	2.6	14	80
	Oxygen	40	160	14.3	12	79
	Nitrogen : Argon	10:30	160	0	7	44
	Air : Argon	10:30	160	0.6	7	49
	Oxygen : Argon	10:30	160	3.5	7	57

8.3. Catastrophic Failure in Oxidizing Plasmas

8.3.1. Temperature Flares

During aerothermal tests between 60 W/cm^2 and 80 W/cm^2 small fiber flares were occasionally observed on the coupon surface which sometimes led to catastrophic failure of the entire coupon. This rapid destruction was easily identifiable by the presence of strong emission flares within the visible range or as sharp spikes in the temperature measurements. The following plot displays the pyrometer measurement of failed samples.

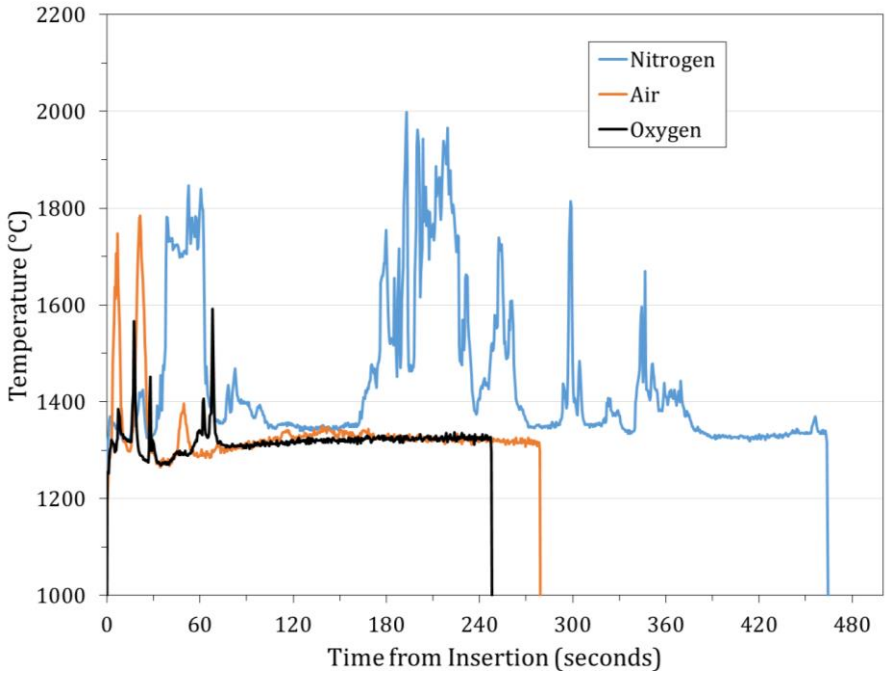

Figure 53: Pyrometer measurement of the SiC surface for different gas compositions

The temperature spikes were observed in pure oxygen plasmas, pure nitrogen plasmas and variable gas mixtures. Low probabilities of failure have been observed at surface temperatures as low as 1250°C in pure nitrogen and oxygen plasmas. Although, the probability of failure increased with increasing temperature or increasing oxygen concentration. Coupon exposure to heat fluxes above 80 W/cm^2 almost always led to a catastrophic failure for any test gas composition.

The existence of a large transitional regime where not all samples survived suggests inconsistency between the test samples. Even though, nucleation points leading to the catastrophic failure are extremely hard to predict, possible initiation could arise from manufacturing imperfections or by contamination from particulates within the

weave architecture. Gashes in the weave architecture can also act as nucleation points. Furthermore, SiC fabrics were not hermetically sealed from the insulators located on the backside therefore pyrolyzing gases could propagate out through the leading surface and interfere with the gas surface interactions.

The temperature spikes were easily detectable using the pyrometer in 1 and 2 color mode. Although, the drastically changing morphology and the very short duration at which the flare crosses within the pyrometer collection envelope, creates uncertainty in the temperature measurement. In order to strengthen confidence of the increase in temperature during the flare, two type K thermocouples were placed in the fabric weave. The following plot shows the thermocouple and pyrometer data during a nitrogen flare.

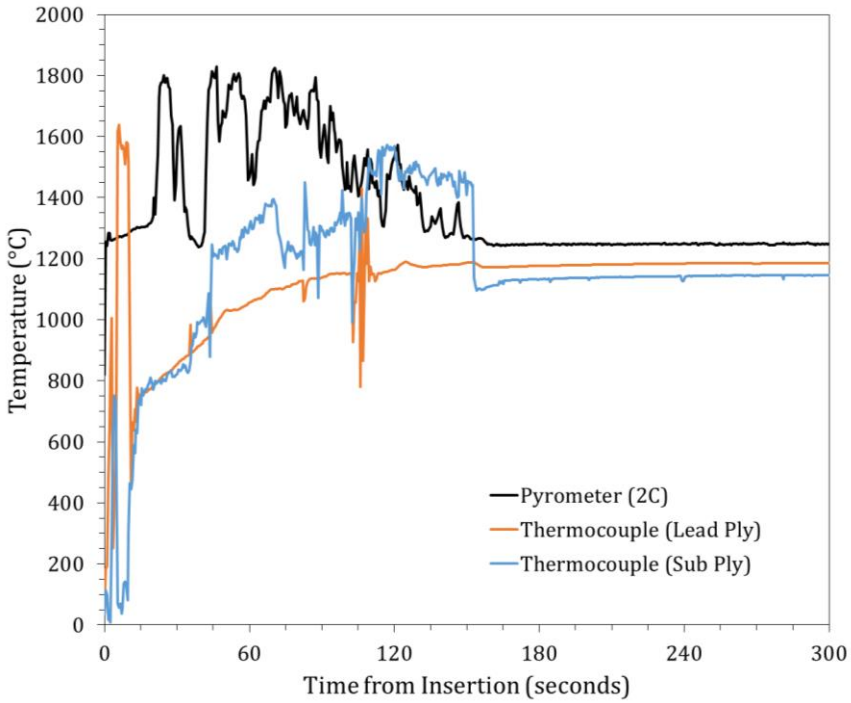

Figure 54: Plot of simultaneous pyrometer and thermocouple measurements during a flare in a nitrogen plasma

It can be seen that the thermocouple was able to detect the temperature rise due to the flare. One thing to notice is the localized failure was detected more significantly with the thermocouple located between the sub ply and the SiC backing piece. This agrees with the post-test analysis showing that the major signs of failure occurred over that thermocouple.

It is interesting to note that the failure probabilities are increased when thermocouples are placed within the weave. Additional impurities due to the braided fiber glass sheathing and the potentially higher catalycity of the metal thermocouples could also act as nucleating points within the weave [26]. Although the higher probability of

failure is most likely due to the grounding of the probe used to make thermocouple measurements which helps to limit noise in the thermocouple data for certain materials. Therefore, the material performance could have been severely altered due to the electrical conduction path through the sting arm which can enhance charged particle reactions by cathodization [54].

8.3.2. Propagation of Flares

Video recordings of the coupon surface allowed visual analysis of the failure mechanism. In the case of oxidizing plasmas, the surface flares propagated in straight lines along the tows of the fabric weave, in both the warp and weft directions. The following figure is a photo of the flare.

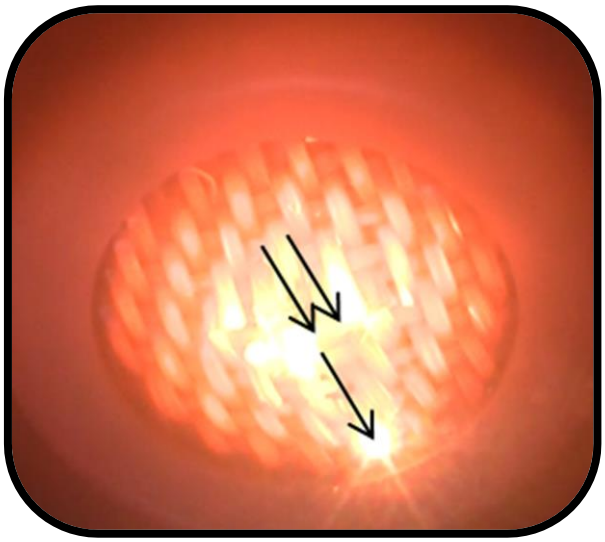

Figure 55: Propagation of a surface flare during air plasma testing

Three flares occurring simultaneously can be seen by the small localized bright white spots. The black arrows represent the propagation directions. The white area around the flare signifies a thick silica layer on the surface. The average velocity of propagating flares in oxygen containing plasmas was approximately 1 mm/s.

The existence of the flare could also be seen after visual inspection of the post-test coupon surface by the destruction paths. The following photo shows the leading surface of a sample that displayed the temperature spike in an air plasma.

Figure 56: Coupon image of failed sample after less than 10 minutes of air plasma exposure

It can be seen that the propagation of the flare was typically constricted to the individual tow and continued along the fiber direction in agreement with the in-situ imaging. Occasional jogs in the propagation direction occurred, but no preferred direction between the warp and weft was observed when comparing multiple failed samples.

During this catastrophic failure, entire coupon tows of 500 filaments were consumed in matters of seconds. This is orders of magnitude higher than the oxidation consumption rate at similar conditions that did not undergo catastrophic failure. Oxidation in conventional ovens leading to direct SiC removal without the formation of a silica layer has been shown to lead to high material removal rates but nothing to the degree seen during catastrophic failure in an aerothermal environment.

Even though pure oxygen plasmas lead to a higher probability of failure, the existence of surface flares didn't lead to as severe destruction compared to air tests at similar heat fluxes. The following photo is a post 100% oxygen plasma test sample.

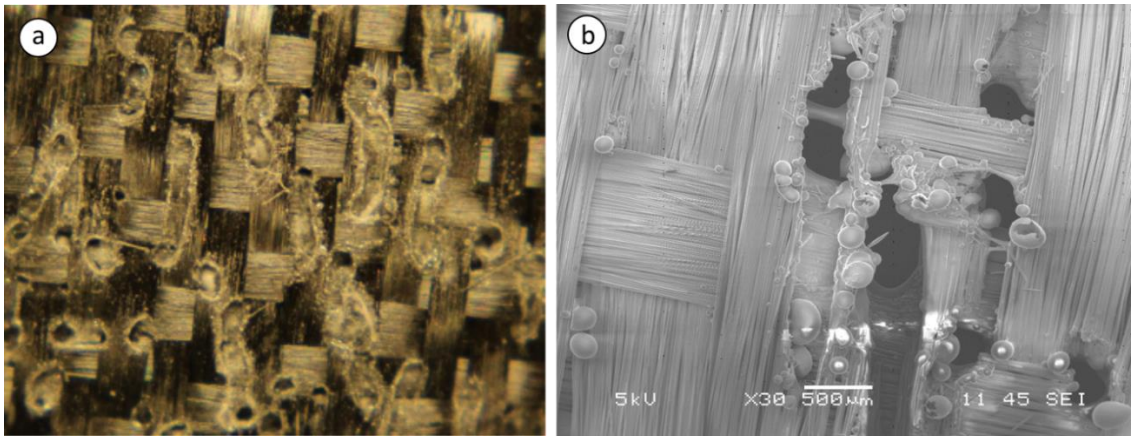

Figure 57: a) Photo and b) SEM image of a SiC coupon after failure in a pure oxygen plasma

It can be seen that the longer flares were only the width of a few tows, therefore the destructive nature of the flares was much less intense. It is expected that the high availability of oxygen in pure plasmas leads to a more rapid formation of SiO_2, whereas a silica film could provide protection from the impinging gas species [98].

8.3.3. Failure Surface Morphology

The catastrophic failure phenomena appears to be unique to aerothermal testing but is not unique to SiC fibers with its high surface area and inherent silicon oxycarbide phase. No reports of temperature spikes, extremely high erosion rates, or visually evident light emission have been found after conventional furnace testing at similar temperatures. Although, similar observations have been documented during aerothermal testing of bulk SiC, CMCs and other ultra-high temperature ceramics with SiC additives. [28, 30, 34, 37, 39, 77, 44-46]. Whereas, the only major difference being the duration of the observed

temperature jump, which is much shorter for fabrics due to fact that the thin fibers are completely consumed as the flare propagates.

Uncertainties exist over the necessity of silica removal in order to observe the temperature jump. Other researchers typically initiate the temperature jump by operating at conditions well above the stable point of silica, leaving a bare SiC surface after the test. In contrast, during this study, the flares were observed at the same operating conditions that led to a thick silica layer. These results show that the silica can suppress the damage of the flares but the removal of the silica layer is not necessarily a prerequisite to the temperature spike. Therefore the temperature spike can actually accelerate the silica removal process [77] while depositing more silica in other locations. The following photo was taken with a Keyence digital microscope and shows the viscous nature of the oxide layer that coats the entire SiC surface.

Figure 58: Post air plasma test surface image taken near a flare showing a thick amorphous silica layer

The Keyence microscope allows large bubbles to be observed due to the clear glassy nature of the amorphous silica layer. The presence of a thick silica layer was observable after failure in all oxygen containing plasmas and did not appear to depend strongly on the oxygen partial pressure. Besides bubbles, locations of irregular structures could be seen inside the silica layer. Mixtures consisting of amorphous SiO_2 and cristobalite are not uncommon and have been seen by Feigl during aerothermal testing [34]. Therefore these irregularities are expected to be crystallization of the silica layer although the possibility of N-atom or impurity incorporation into the oxide cannot be

ruled out without further analysis. Figure 59 is another photo at a different location around the flare path where this likely crystallization is more obvious.

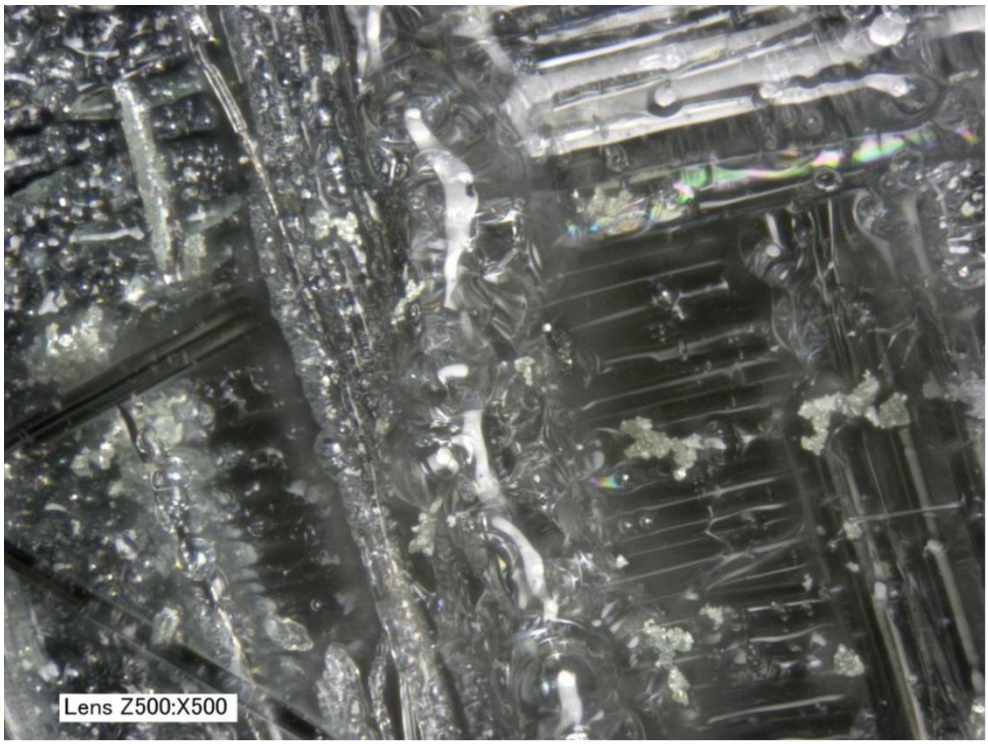

Figure 59: Keyence microscope image taken near a flare after air plasma testing showing possible crystalline features

Due to the suspected formation of cristobalite at relatively higher temperatures in oxygen containing atmospheres [5], it is expected to be a product of the flare and not a nucleation point. Although severe cracks and irregularities due to the formation of cristobalite, have been reported to provide higher permeability than amorphous silica [98].

8.3.4. Failure In-Depth Morphology

Even though most flares propagated along the surface tow of the weave architecture, flares also tended to stop in one location and burrow into the surface. The following digital microscope photo shows the thick silica on the lead side and the consumed fiber ends within the weave.

Figure 60: Keyence image of a location of catastrophic failure showing worm holes typical of failure in oxidizing plasmas

The highly viscous nature of the silica at the tested conditions can be seen around the surface of the hole. One very interesting feature is the ability to see pointed fibers

through the silica layer coating which confirms that the flare incorporates a gas-surface interaction.

The existence of these worm holes into the weave is interesting because the local temperature, oxygen concentration, and flow velocity are expected to decrease into the weave architecture. Therefore, if all of the SiC fabric heating occurs on the leading surface, another mechanism must be operating in parallel with the plasma heating in order for the flare to penetrate straight into the surface.

It is believed that the decreasing oxygen concentration gradient into the weave architecture is the reason for the burrowing of the flare. Simultaneously to a diffusion limited oxygen infiltration, CO generation from oxidation reactions with SiC may also contribute to lowering the oxygen partial pressure [106] deeper within the weave architecture. Further analysis within the weave provides evidence of a low oxygen pressure which may subsequently cause SiO gas to be the dominant oxide phase and limit the formation of a protective SiO_2 layer.

The back side of the oxidized lead ply coupons displayed a white discoloration around the holes through the weave. A SEM image of this region can be seen in the following figure.

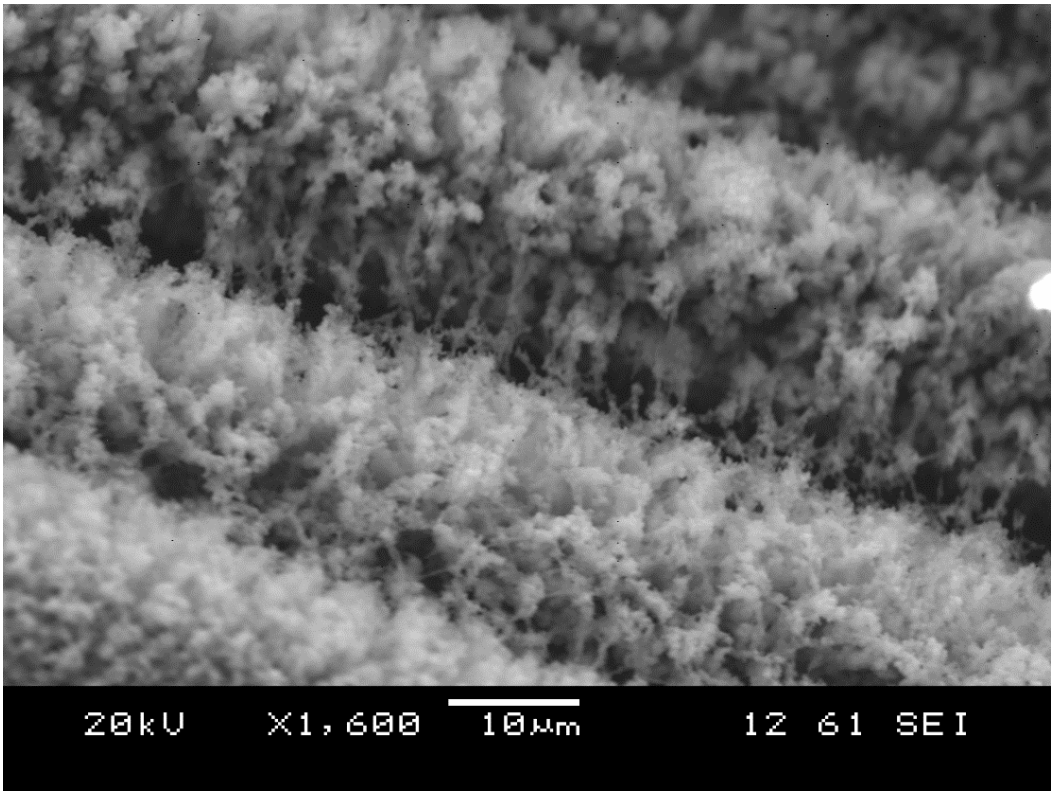

Figure 61: SEM image of hairs observed on the SiC coupon back side near a worm hole

The surface morphology is in the form of hairs which have only been observed in protected locations on the sample back side. EDS analysis results taken on the hairs is consistent with a silica composition. The formation of this non-passive oxide morphology comprised of long hairs has been seen others in static heating facilities [108] and most likely forms through the same phenomena. This is due to the protection from shear and direct gas phase bombardment within the thermal boundary layer that is provided by the leading weave architecture. The model used to describe the process leading to the hairs [108] is illustrated in Figure 62.

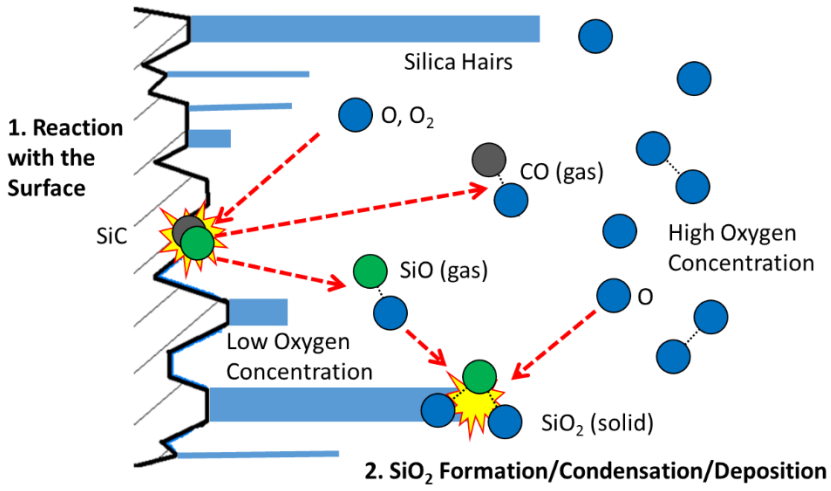

Figure 613: Illustration of hair formation [Hinze and Graham concept]

The low oxygen concentration within the weave causes SiO to be the major silicon-oxide phase near the fiber surface. The hairs are expected to grow from further oxidation of SiO gas and subsequent condensation at locations of higher oxygen concentrations. This would naturally cause the silica formation to occur at the silica/gas boundary not at the SiC/silica boundary. Any SiO that doesn't deposit as hairs would be swept thought the weave and be responsible for the thick amorphous silica layer around the flare location.

Besides the hairs, another very interesting surface was observed on the back side of the coupon around the flare location and is shown in the following figures.

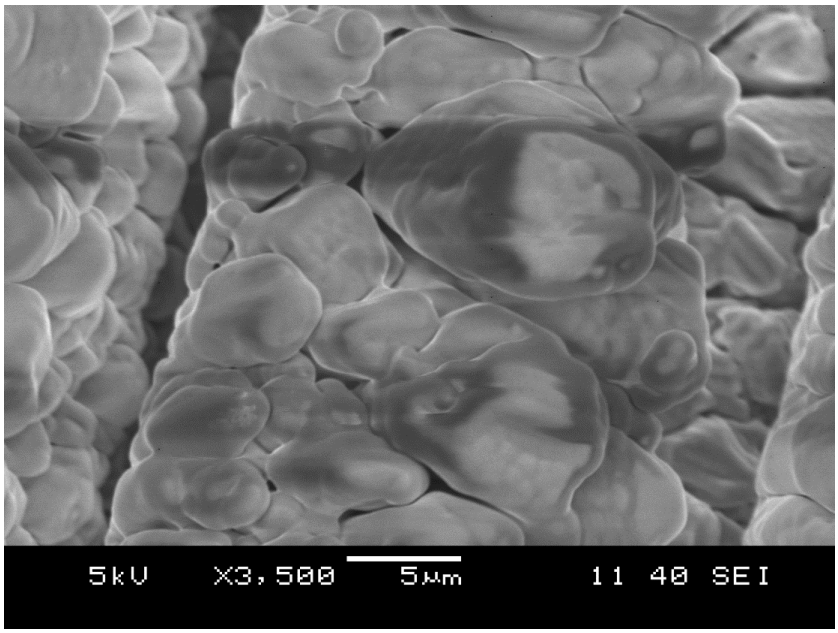

Figure 63: SEM images of interesting conglomerates observed on the SiC coupon back side

The fiber diameter almost doubled due to the oxide growth. EDS was used to determine the surface contained silicon, oxygen and carbon. Its close proximity to the silica hairs suggest that the unique surface morphology arises from consolidation of thickening hairs.

8.4. Oxidation Reaction Products

8.4.1. Emission Spectroscopy Measurements

It is expected that the majority of the SiC removal occurred either through species transport downstream in the gas phase or a rapid conversion into SiO_2. The emission spectrometer was used to monitor the gas phase within the thermal boundary layer. The recorded intensity vs wavelength during a flare for different oxygen concentrations can

be seen in Figure 64. For all cases the integration time was set at 10 seconds. All data was scaled and shifted to fit on the same plot.

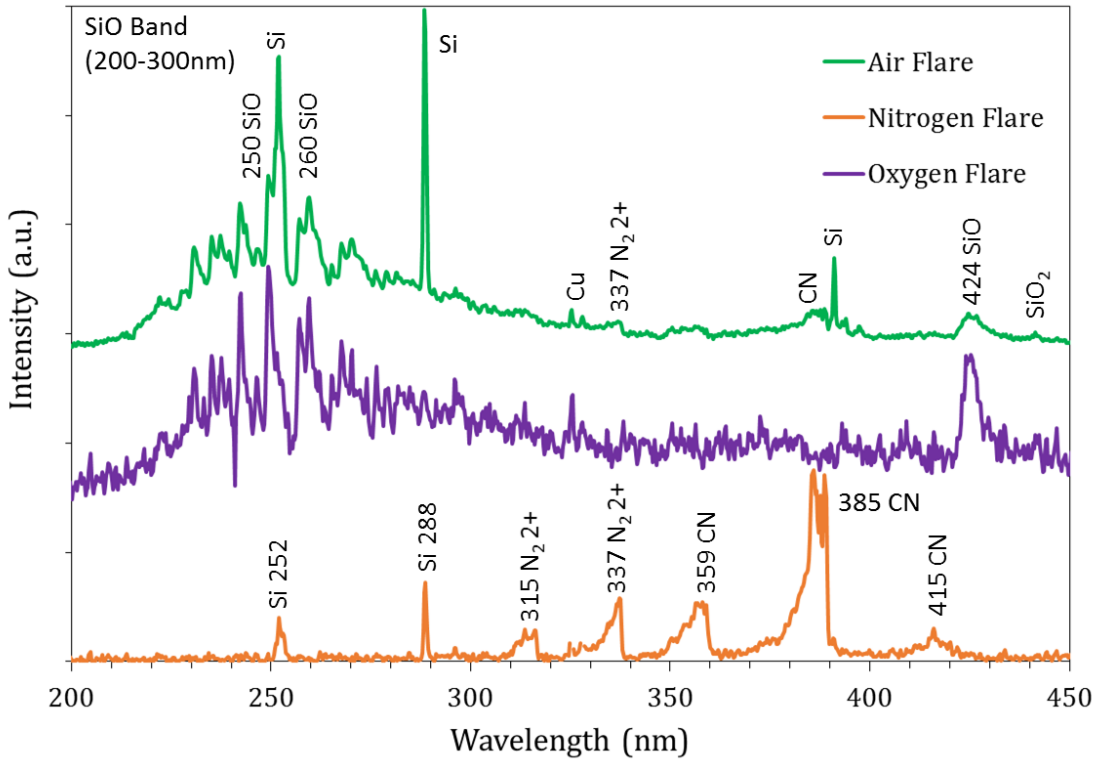

Figure 64: Scaled and shifted emission for different gas compositions

Flares for all oxygen containing plasmas show SiO and traces of SiO_2 but pure oxygen containing plasmas show no sign of Si. This is most likely due to the high availability of O-atoms. Even though carbon is expected to be transported away from the destroyed region, CO or C_2 was not observed during the flares in oxidizing plasmas. A small increase in emission at 385 nm can be seen in the air plasma and is suspected to be the broadened CN feature. Evidence of N_2 2+ can also be seen in the air plasma.

The trace SiO_2 observed in the gas phase could possibly be formed by the addition of oxygen to SiO gas or may be ejected from the surface. Subsequent dissociation of SiO_2 in the hot boundary layer into SiO and O is also possible.

8.4.2. Exothermic Reactions on the Gas / Surface Boundary

Many possible reasons for the temperature jump and extremely high material removal rate have been suggested by other authors. Due to the fact that the flares occur at constant conditions, most authors agree that a change in the catalycity, reactivity or emissivity is required to initiate the increase in the equilibrium temperature. A combination of changes to these material properties could lead to higher surface temperatures without an increase of free stream enthalpy.

Previous testing has shown that the emissivity change between an oxidized and an unoxidized surface could only account for a maximum of 100°C temperature change and occurred on a much longer time scale. Also, the emissivity increased during silica formation which led to lower measured temperatures. Therefore the cause of the temperature spike would be expected to be either an artifact of an increase in catalytic efficiency or reactions involving SiC and the high enthalpy dissociated gases within the thermal boundary layer.

Highly exothermic reactions that can completely consume the 500 filament tows in seconds is expected to be the leading cause of the higher thermal equilibriums in

oxidizing plasmas. Research on self-sustaining gas-solid combustion has shown that diffusion controlled combustion leading to steady state exothermic reaction propagation is possible. Whereas, a high surface area to volume ratio can significantly increase the combustion rate [109]. It has been shown that once the specific ignition temperature and conditions are reached, a heat wave will propagate at a constant rate but may still require an external addition of energy to sustain weakly exothermic reactions [109]. This type of self-sustaining reaction is very similar to the propagation of the flares observed on the video recording in oxidizing plasmas.

The removal of Si through sublimation out of the SiC lattice has been suggested to cause the rapid material removal [30]. This is in agreement with the fact that the rapid SiC consumption occurs in both oxygen and nitrogen plasmas and is independent of the oxidation state. Although if thermal decomposition of SiC was the only cause of the propagating failure, similar microstructural changes and failure mechanisms would be expected to occur in conventional ovens at similar temperatures. Whereas, the high O_2 reactivity, which has been shown to surpass the reactivity of O-atom around these temperatures [21], would be expected to lead to a just as rapid material degradation in molecular heating environments. No reports of mass loss at this magnitude and speed using more conventional furnaces have been found. Therefore, the reaction must still require the presence of highly reactive atomic species.

The existence of the reaction zone occurring at the gas surface boundary is confirmed by the incorporation of oxygen onto the surface as well as the points formed on the SiC fibers as seen in the following figure.

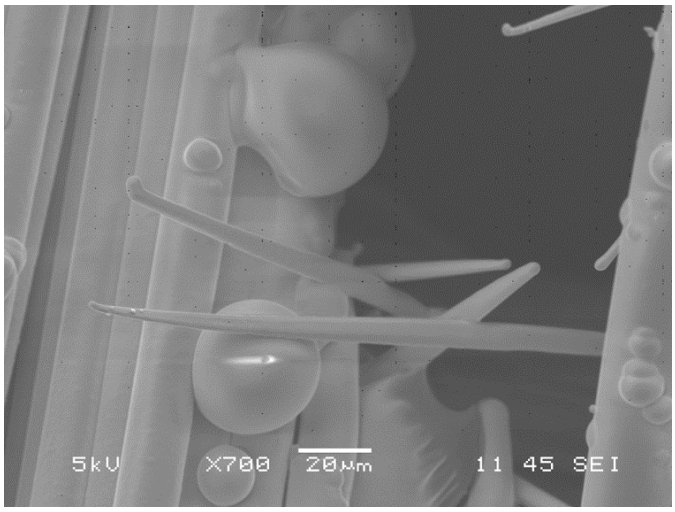

Figure 65: SEM image of fiber points that form after failure in an oxidizing plasma

This figure was taken near a destroyed hole through the weave. It shows both the points on the fibers and SiO_2 spheres which arise as a reaction product.

8.4.3. Reaction Product Tracking

Even if the higher equilibrium temperature during the flare is a result of highly exothermic chemical reactions that must occur between the gas phase and the SiC surface, the influence of each potential reaction pathway is still uncertain. These gas-surface interactions that occur only during the flare must either have a higher reaction rate, higher exothermicity, higher energy accommodation coefficient, or a combination.

In order to determine the potential changes in the gas-surface interactions, the emission spectrometer was used to track SiO within the gas phase. Figure 66 tracks the emission intensity vs time over the sample exposed to a pure oxygen plasma. The wavelengths of the features tracked are labeled on the plot. The slight offset between the flare features in the emission and pyrometer data is due to the 10 second integration time used to collect the emission. The pyrometer and spectrometer detection region are smaller than the exposed coupon area therefore the temperature and emission spikes represent the flares that propagated through the respective collection envelope. The dotted lines between each data point are visual guides only and don't signify actual values.

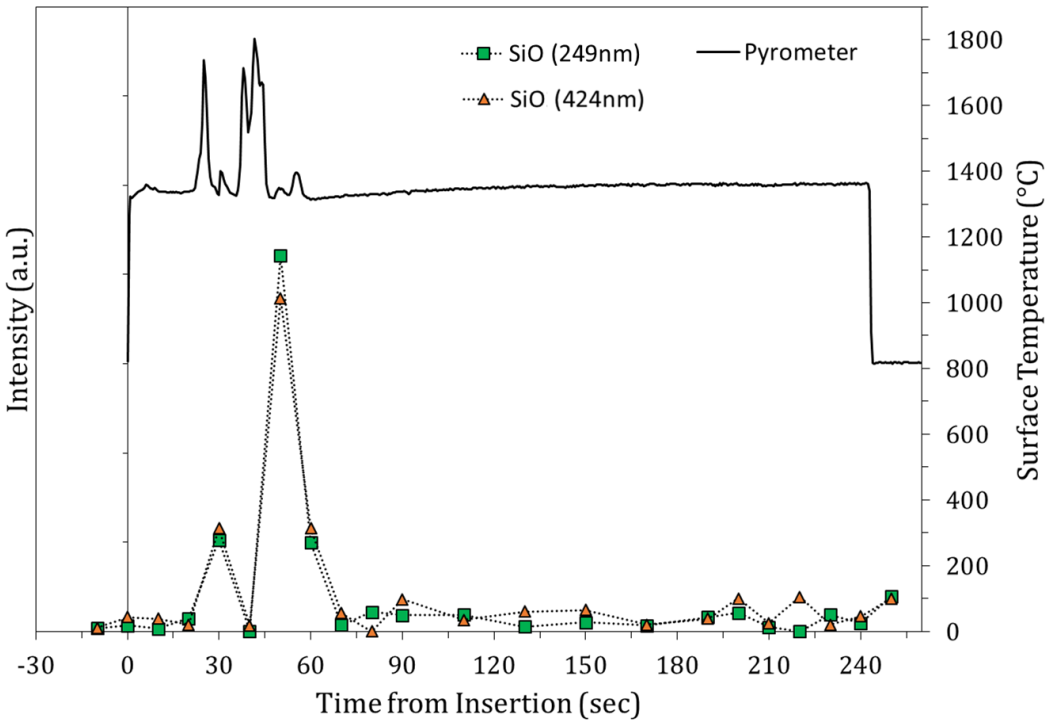

Figure 66: SiO tracking at two different wavelengths in an oxygen plasma

The emission signal for each SiO feature was scaled between 0 and 1. At these conditions the molecular oxygen is highly dissociated. The large spike in SiO can only be seen around the region of the temperature spike. These results suggest that a possible exothermic gas surface reaction pathway for the higher equilibrium temperature in pure oxygen plasmas includes;

$$SiC + 2O \leftrightarrow SiO + CO \qquad \text{eq. 25}$$

This reaction pathway is expected to occur throughout the duration of the plasma exposure but have a drastically increased reaction rate during the flare. It should be noted that the formation of SiO gas can occur in conditions leading to an oxide coating or a bare SiC surface. Therefore this is consistent with the findings of others that have observed temperature jumps resulting in a bare SiC surface.

Specific to the conditions tested in this study, the flare propagation in oxygen plasmas would also have the reaction requiring the removal of silica which could occur through dissociative removal or through the following equilibrium.

$$SiO_2(s) \leftrightarrow SiO_2(g) \qquad \text{eq. 26}$$

These endothermic reactions will suppress the temperature spike by both removing heat from the surface as well as limiting the diffusion of oxygen to the SiC surface.

Besides the oxidation reactions with SiC, an increase of the catalytic recombination efficiency may simultaneously be the culprit for the temperature jump [37, 39, 77, 78]. It is possible that a higher percentage of the total heat flux transferred to the surface could be dominated by gas-surface interactions with a higher reaction rate and not necessarily a greater accommodation coefficient or exothermicity. If the thermal spike was due to an increase in the catalytic efficiency, oxygen atoms will be consumed through the following equation.

$$O + O + s \leftrightarrow O_2 + s \qquad \text{eq. 27}$$

Where *s* is a surface reaction site. However the spectrometer couldn't detect any signs of catalytic production of O_2. O-atom was easily observable but no statistically significant change in the O-atom signal was observed over the surface for the duration of the test. Any O-atom tracking would be difficult to analyze due to the simultaneous complex reactions leading to consumption through catalysis and oxidation as well as production from decomposition of SiO_2. Although, whatever the reaction pathways are, the combined output of all gas surface reactions must have a net increase in energy deposition into the surface.

8.5. Catastrophic Failure in Nitrogen Plasmas

Pure nitrogen plasmas were used to investigate the necessity of oxygen on the catastrophic failure mechanism. Remarkably, obvious flares in nitrogen plasmas have shown that atomic oxygen originating from the plasma is not essential to observe a temperature spike. This shows how oxygen atoms and nitrogen atoms can attack the surface leading to highly detrimental consequences. Although, macroscopic observations depict a dramatic difference between the oxidized Hi-Nicalon samples and samples that were only exposed to pure nitrogen plasmas. Figure 64 compares the flares in oxygen plasmas to the emission spectra from flares in a nitrogen plasma and also shows a dramatic difference between the gaseous products during the flare. It can be seen that failure emission in nitrogen displays N_2, Si and CN.

Even though nitrogen plasmas are expected to have very different reaction pathways, SiC fabric fails above temperatures of 1200°C in oxygen and nitrogen. This suggests that the initiation of the flare has a similar activation energy independent of the reaction pathway with either nitrogen or oxygen. Comparing the temperature data presented previously in Figure 53, it can be seen that in oxygen containing plasmas the spike is usually very rapid and travels through the pyrometer view relatively quickly while the nitrogen flare is more sustained.

8.5.1. Failure Surface Morphology

In-situ visual analysis of nitrogen flares depicts both a larger flare area and a slower propagation speed. A macroscopic image of the coupon destroyed in the nitrogen plasma leads to a large surface area degradation.

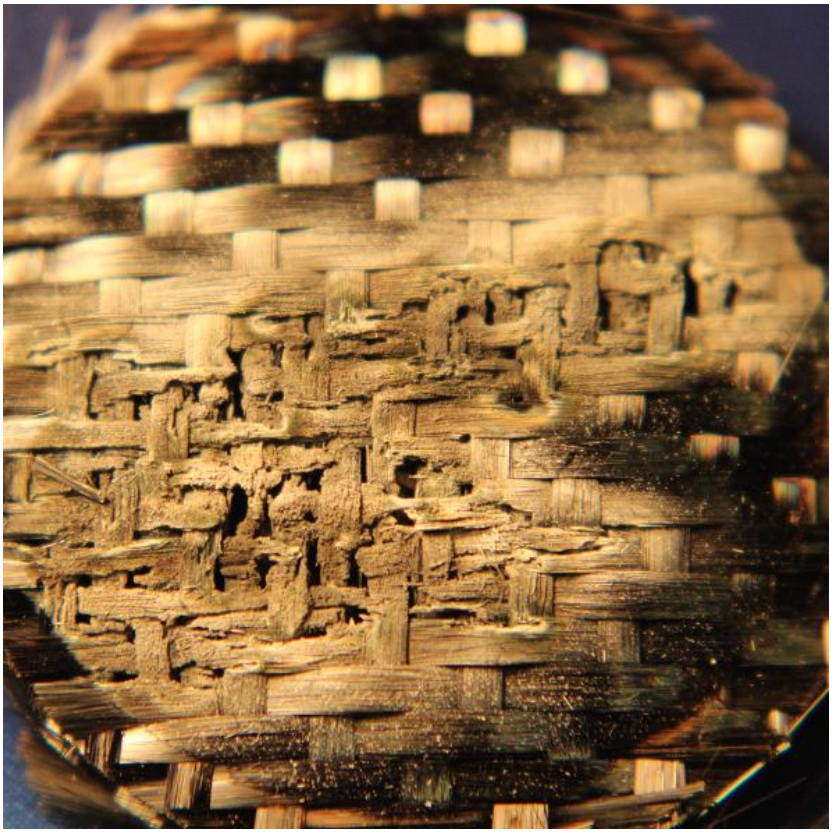

Figure 67: Photograph of destroyed coupon after less than 10 minutes of nitrogen plasma exposure

Even though the large destruction area is contiguous, this is much different than the oxygen case where the flares propagated along the fiber. The SEM was used to analyze the post failure surface. The following photos show the severely damaged fibers and a large area destruction.

Figure 68: SEM image of the SiC coupon surface after destruction in a nitrogen plasma taken at a) 30 X and b) 170 X

The destruction area is comprised of material build up in the form of tiny nodules causing the interlocking of individual fibers. The nodule conglomerates are larger than the 14 µm diameter of the fiber, suggesting the failure mechanism is not solely due to a thermochemical driven consumption of the SiC fibers. A more detailed image of these nodules can be seen in the following SEM images.

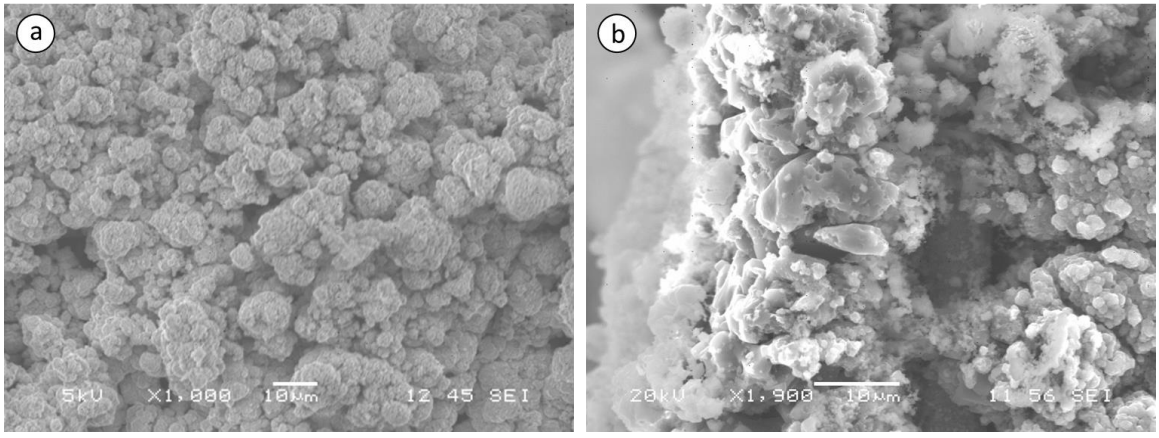

Figure 69: SEM image of nodules observed after failure in a nitrogen plasma

It can be seen that the nodules are not smooth at 1900x but appear jagged and sharp. A survived fiber underneath the nodules can also be seen. This surface morphology was only observed in pure nitrogen plasmas. EDS was used to determine the Si-O-N surface composition of the nodules which confirms the addition of nitrogen from the gas phase.

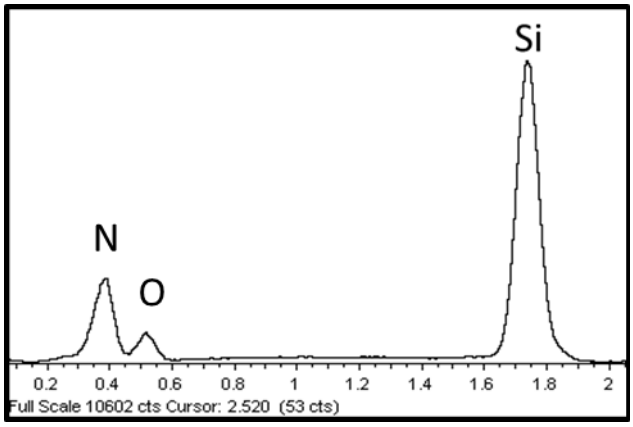

Figure 70: EDS results of the SiC coupon surface after catstrohic failure in a nitrogen plasma

The EDS analysis suggests oxynitridation reactions between existing SiC and nitrogen in the gas phase. It is possible that the release of oxygen from the silicon oxycarbide phase aids in the catastrophic failure. This thermal instability of the Si-O-C bonds can limit the maximum use temperature, whereas the relatively strong covalent bond between silicon and carbon requires a much higher temperature to decompose [5]. This has been confirmed Sacks using near stoichiometric fibers which can retain their strength up 1950°C in molecular nitrogen [95].

The presence of oxygen may not solely arise from the silicon oxycarbide phase but be an artifact of an oxygen impurity from the surrounding environment. Oxygen may also be available as a thin naturally occurring oxide film [47], whereas, the higher the fiber surface area to volume ratio, the higher the silica % per fabric mass. Any, residual silica layers clearly visible on the coupon holder after flares in oxygen containing plasmas may also contribute to the oxygen availability.

8.5.2. Exothermic Reactions in Nitrogen Plasmas

Just like the oxygen flares, species from the plasma flow were incorporated into the SiC surface as well as ejected from the surface into the boundary layer during flares in a nitrogen plasma. Therefore it is expected that heating occurs on the surface through the following reaction:

$$N + SiC \leftrightarrow Si + CN \qquad \text{eq. 28}$$

This reaction pathway is in agreement with the Si and CN emission observed with the emission spectrometer. Although, the ability to detect molecular nitrogen provides additional insight into the temperature spike. The following plot tracks the intensity of the N_2 2+ species with time in a nitrogen/argon plasma using a 0.5 second integration time.

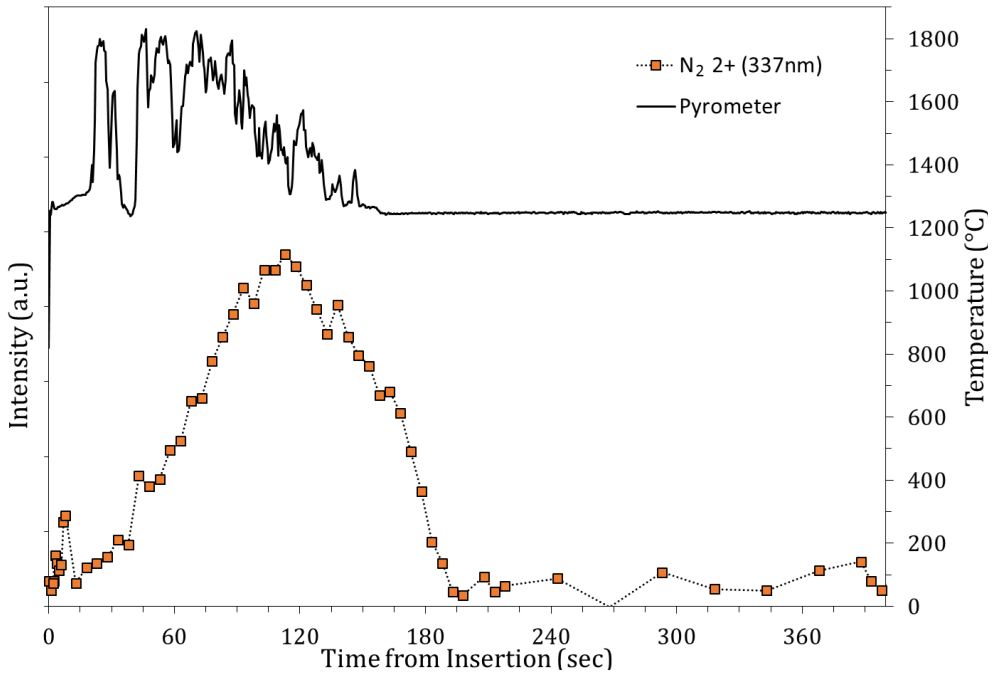

Figure 71: Plot of N_2 2+ production during a sustained flare

It can be seen that N_2 spiked during the flare and then trailed off. As described in the oxygen case, the increase in the equilibrium temperature may not solely be linked to the high material removal rate. The fact that N_2 increases during the flare suggests that there is a dramatic increase in the nitrogen catalytic efficiency which proceeds through the following reaction:

$$N + N + s \leftrightarrow N_2 + s \qquad \text{eq. 29}$$

It is interesting to note that the increase in N_2 production only occurs during failure but not after, suggesting that it is not purely the irregular post flare surface morphology. The increased N_2 production could possibly be an artifact of the higher

surface temperatures, or due to the transition from SiC to the Si-O-N surface. This conclusion of an increase in nitrogen catalytic efficiency and simultaneous oxidation reactions is in agreement with results from Herdrich who observed a 400°C temperature jump in air plasma but only a 200°C temperature jump in oxygen plasma [39].

CHAPTER 9: MATERIAL RESPONSE OF SILICON CARBIDE FLEXIBLE TPS DURING A SIMULATED MARS ENTRY

9.1. Introduction

Radical changes to the Mars Science Laboratory Entry Descent and Landing architecture are essential in order to carry out future human scale Mars missions due to the increased payload and safety requirements [110]. Besides the EDL challenges from the lower density and thinner atmosphere of Mars [111], the chemical composition of the atmosphere could be more damaging and limit the performance of the flexible thermal protection system.

Inflatable Aerodynamic Decelerators have proven to be an enabling technology through successful flight tests within the Earth's atmosphere [20]. Although, the viability of two-dimensional woven silicon carbide fabric when used as a flexible thermal protection material depends on the entry trajectory as well as the chemical composition of the atmosphere. Therefore, even if the heat rate, heat load, dynamic pressure and deceleration are all accounted for, uncertainties arise if flight results gained within the Earth's atmosphere are extrapolated to a Martian atmosphere. This chapter describes the material response of the SiC fabric when exposed to a CO_2 plasma.

9.2. Experimental Conditions

The majority of the Martian atmosphere is composed of carbon dioxide with small amounts of argon, nitrogen and other minor species [112]. Due to the dissociation of

gases across the bow shock of an entry vehicle, the gas species impinging on the TPS surface for Martian entry may include CO_2, CO, O, O_2, N_2, NO and traces of N, CN and C. Whereas the majority of the impinging gas species during hypersonic flight within earth atmosphere is expected to be N_2, N, O_2 and O.

Even though, the ICP torch can simulate the Martian atmosphere with a CO_2 – Ar - N_2 gas mixture, the gas composition was idealized in this study by using only compressed CO_2 gas. Any impurities and solid particulates typical of the mars atmosphere [111] were also ignored.

Images of the CO_2 and air testing are shown in the following figure along with a diagram of the coupon holder and diagnostic configuration.

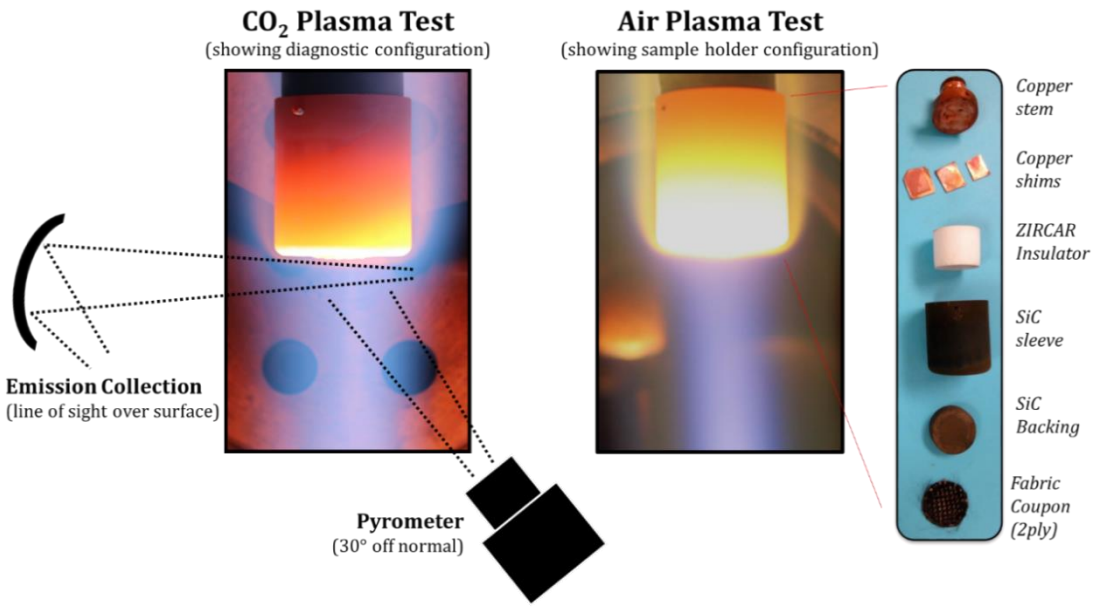

Figure 72: Photos of SiC coupon exposure to an air and CO_2 plasma. An illustration of the sample holder (right) and diagnostic configuration (left) are also shown

It can be seen that the experimental configuration is the same as used in the air plasma test. The following table shows the experimental conditions and operating parameters of the ICP torch during simulation of an Earth and Mars entry.

Table 9: Operating conditions for the three CO_2 test cases used in this study. The air plasma test condition is also summarized

CO_2 Plasma				Air Plasma
Test Gas	Carbon Dioxide			Air
Plasma Composition	CO_2, CO, O, C			N_2, N, O_2, O
Flow Velocity (m/s)	>130			>130
Static Pressure (torr)	160			160
Dynamic Pressure (torr)	2.5±.5			2.5±.5
Duration (s)	30 - 600			30 - 600
Operating Frequency (MHz)	2.5			2.5
Heat Flux (W/cm^2)	***50 ±5***	***60 ±5***	***70 ±5***	***80 ±5***
Plate Amperage (amps)	2.5	2.6	3	2.5
Power (kW)	13	14	17	14
Volume flow rate (slpm)	25	28	28	40

Experiments were performed at heat fluxes ranging from 50 to 70+ W/cm^2. Except for the specified emission tests, flow rates were held constant for the entire duration using individual mass flow controllers.

The following plot shows 4 minute temperature profiles for the samples exposed to air and CO_2 conditions that did not lead to catastrophic failure.

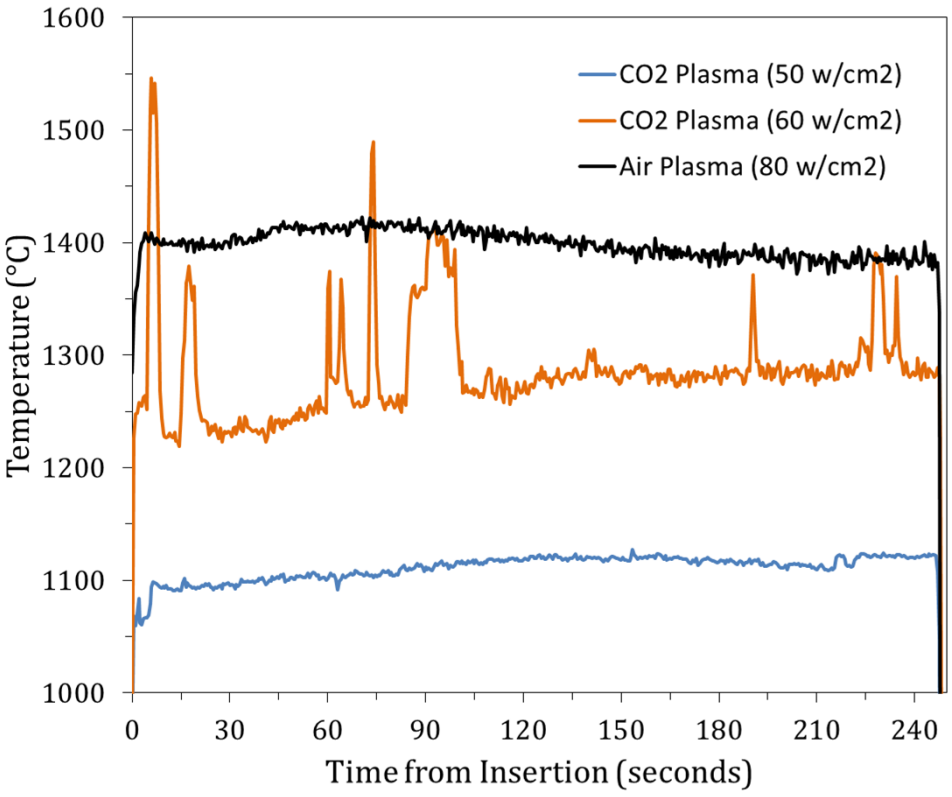

Figure 73: Temperature profiles for CO_2 plasma tests compared to a survived sample in an air plasma

The steady state surface temperatures achieved during this investigation ranged between 1100°C and 1500°C. At higher heating conditions within this temperature range, flares on the coupon surface were commonly observed in CO_2 plasmas, which are the source of the spikes in temperature.

For each CO_2 plasma conditions tested, many plasma flow characteristics also change when the heat flux is changed. A complex variation of convective and radiative heating, gas dissociation fraction and flow dynamics, all change with power, chamber pressure, and axial location of the sample in the plasma stream. Whereas, an increased

dissociation fraction of the test gas can lead to significantly enhanced oxidation rates [35].

Assuming local thermodynamic equilibrium within the CO_2 plasma free stream, the gas properties library called MUTATION was used to provide the species mole fraction expected during the ICP Torch operation [17]. Computational results for a temperature range between 600 and 10,000K at 160 torr can be seen in the following figure.

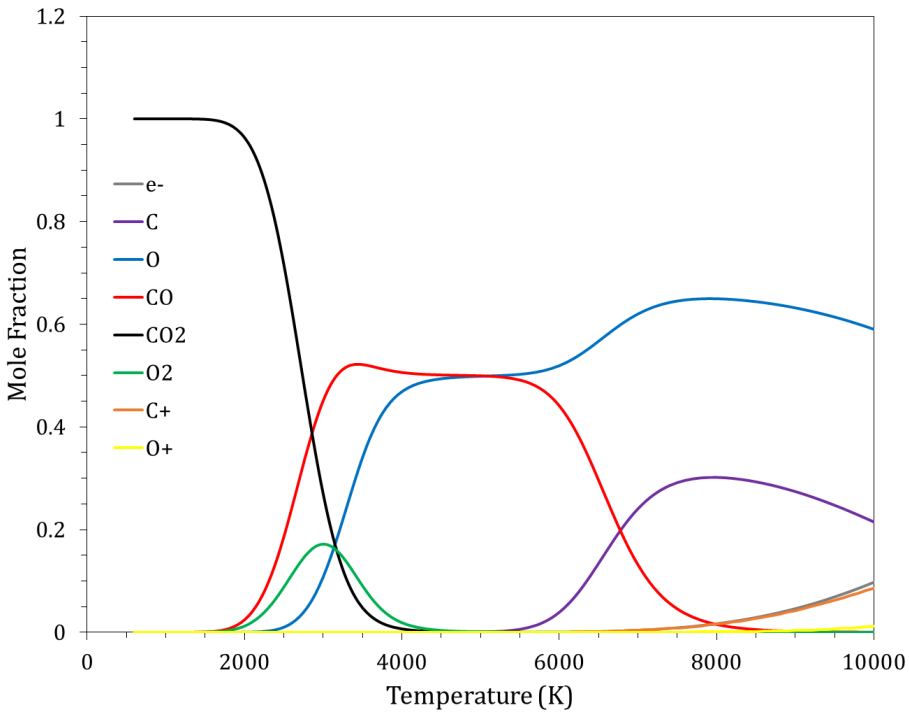

Figure 74: Plot of mole fraction vs temperature in a CO_2 plasma at 160 torr [courtesy A. Lutz]

As seen in Figure 74, the degree of dissociation of CO_2 increases with increasing temperature. For the operating conditions of this study, the free stream gas temperature was determined to range around 3500 to 6000°C using laser induced florescence [15]. For this temperature range, CO_2 is expected to be dissociated into O-atom and CO, leaving only trace amounts of CO_2 at the lower heat flux conditions. For the 50-60 W/cm^2 test cases, the dissociation of CO and further ionization is expected to be small, therefore the concentration of C-atom in the plasma free stream is assumed to be negligible.

9.3. Influence of CO_2 Plasma Environments on Oxidation

9.3.1. Silica Layer (50 W/cm^2)

Besides the low probability of flares, the material response was easily predictable for all air plasmas as well as any other tested N_2/O_2 gas ratio. This includes 100% oxygen tests. For relatively short durations at surface temperatures between 1000°C and 1400°C, all SiC coupons exposed to air plasmas displayed a colorful iridescence due to the silica layer that formed on the surface. Along with silica formation, the post test samples also underwent a significant decrease in flexibility. In contrast, coupon exposure to the CO_2 plasma for each heat flux tested led to a visually diverse range of macro and microscopic surfaces properties that were very sensitive to the operating conditions making them hard to predict. The morphologies of post test samples varied with time, temperature and location within the weave. For some CO_2 operating conditions, a colorful iridescence was easily observable on the samples similar to oxidation in an air plasma. Post 50 W/cm^2 CO_2 plasma tests samples can be seen in the following photos.

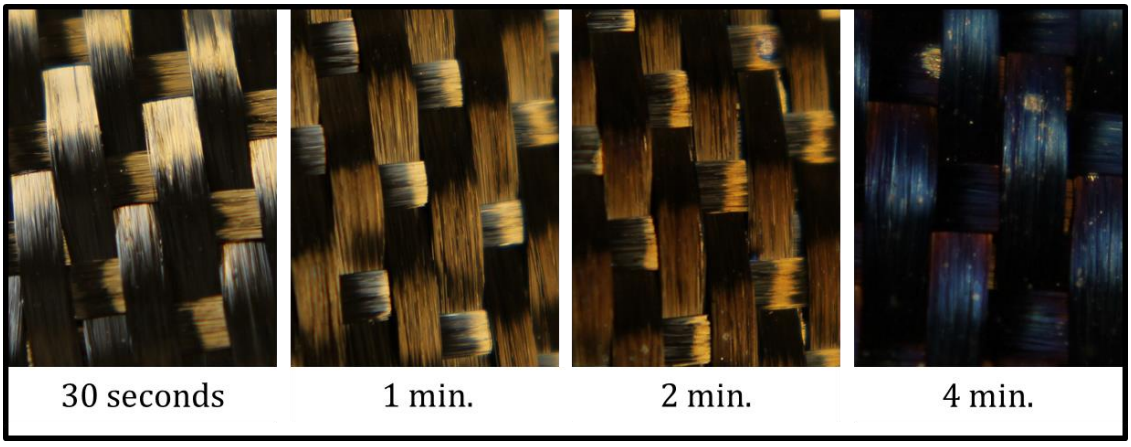

Figure 75: Photographs of the SiC coupon surface after a 50 W/cm^2 CO_2 plasma exposure for increasing durations

At these CO_2 plasmas conditions only slight differences were observable when comparisons were made to N_2/O_2 plasma results at similar temperatures. These minor differences could be seen using a low magnification optical microscope. Some CO_2 oxidized samples at test durations less than 2 minutes appeared to have silica particulates the size of grains of sand on the surface. Small spheres have also been reported by Balat using CO_2 [113]. At longer durations, thicker silica layers developed similar to air plasmas but discolored spots around 5 µm could be observed. These discolored spots are believed to be linked to the small spheres observed on the surface at shorter durations.

9.3.2. Flexible Carbon Layer (60 W/cm^2)

Higher heat fluxes were obtained by slightly increasing the power and decreasing the gas flow rate. At these new conditions a dramatic structural, elemental and

morphological changed occurred in the surface layer. Some of these differences can be seen in the following figure using a standard camera.

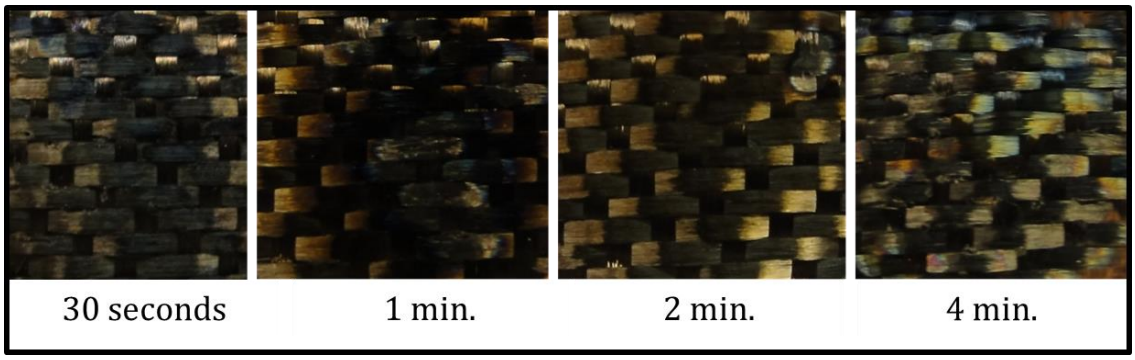

Figure 76: Photographs of the SiC coupon surface after a 60 W/cm^2 CO_2 plasma exposure for increasing durations

Photographs of the surface don't show the iridescence of a thin amorphous silica film that is typical after 1 minute in air plasmas, but rather a much darker taupe/black discoloration. Along with these visual differences, post CO_2 plasma samples were also much more flexible compared to the highly brittle air oxidized samples.

Silica layers too thick to display the surface iridescence and carbon deposits can both lead to near black surfaces therefore a SEM equipped with EDS was used to analyze the surface. The cross section of the fractured sample is presented in the following figure.

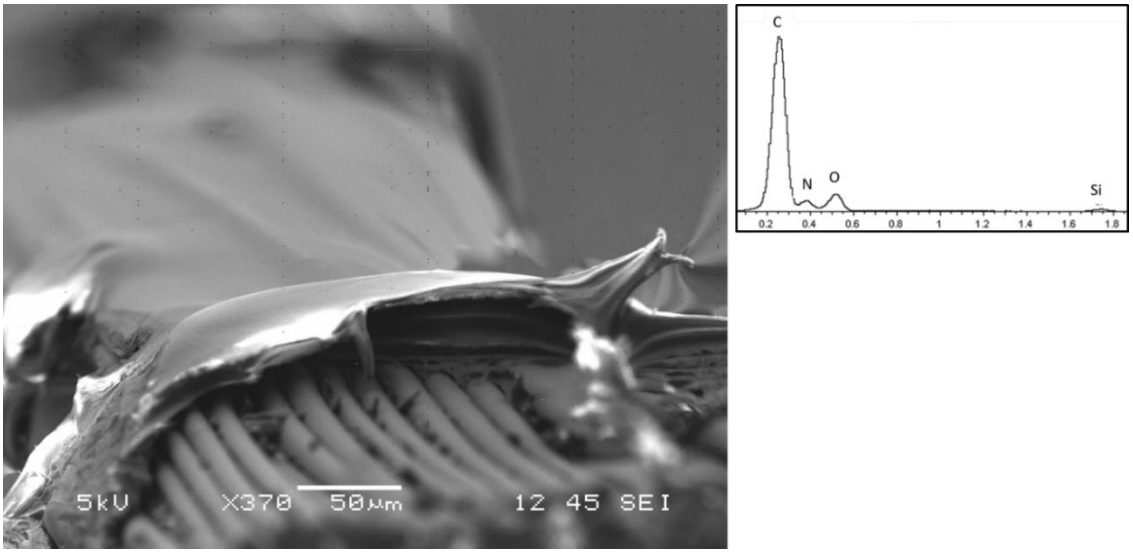

Figure 77: SEM image and EDS results of the SiC coupon after 60 W/cm^2 CO_2 plasma exposure for 4 minutes

It can be seen that the surface layer shows signs of ductile failure which is most likely the reason for the flexible nature of the samples that were oxidized at these CO_2 conditions. EDS results determined the oxide layer to be composed of a C, O, Si, and N. However, EDS can only tell us the chemical components of the surface layer and not the bond orientation. Therefore, it is uncertain if the integration of carbon into the molecular structure is in the form of a silicon-oxycarbide chain, free carbon, trapped CO or SiC within an SiO_2 oxide layer. A similar high carbon coating can be seen within the weave architecture in the following SEM image and EDS results.

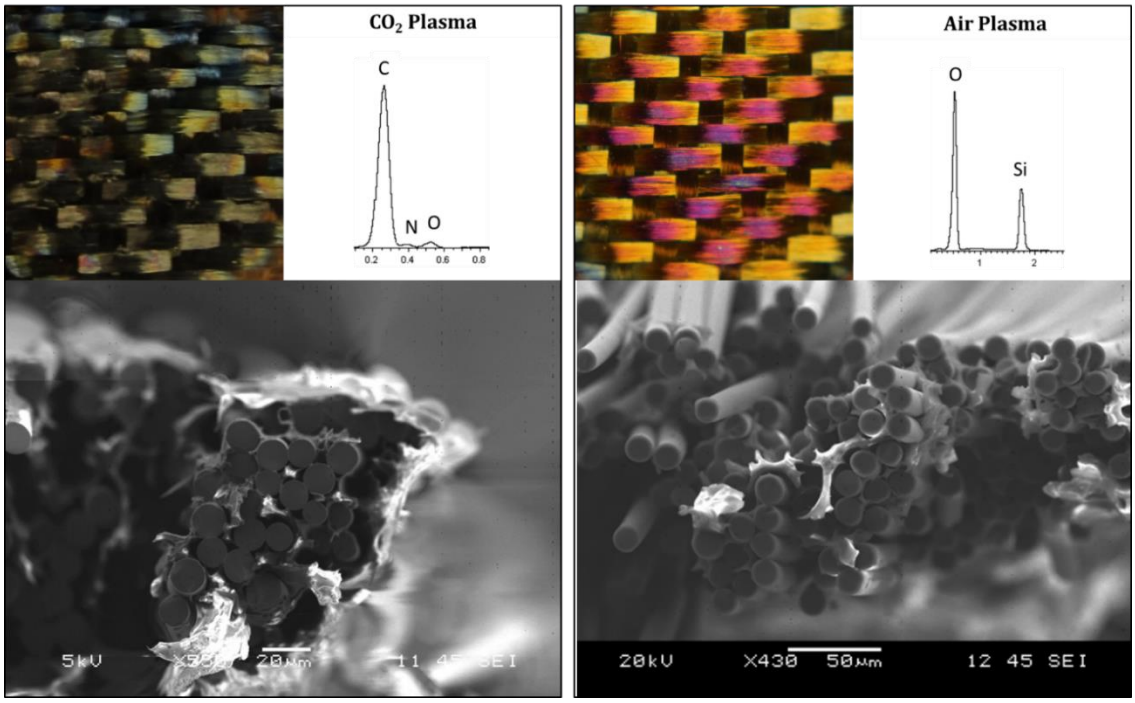

Figure 78: Surface photograph and SEM cross section image on a SiC coupon exposed to a 60 W/cm^2 CO_2 plasma for 4 minutes (left) and an air plasma (right). EDS results are also shown for each case

Substantial deposits fill the vacancies within the weave architecture with a clearly distinguishable separation between the individual fibers and the surface layers for both air and CO_2 tests. Although, the EDS analysis taken between the SiC fibers displays the typical Si-O elemental composition after air plasma exposure and a carbon rich layer after CO_2 plasma exposure.

The existence of the nitrogen could be the result of impurities within the compressed CO_2 tank, an undetected leak within the gas injection system, or due to the removal and storage of the sample post-test. Fortunately, a trace amount of nitrogen is present in the Mars atmosphere [112] and consistency between operating conditions was

maintained by using the same compressed gas tank and experimental configuration for all test cases. Although, it is interesting that nitrogen is not incorporated into the silica surface during air plasma testing but is observed during CO_2 testing.

9.3.3. Flares (>70 W/cm^2)

Sharp temperature spikes collected by the pyrometer were commonly seen at temperatures as low as 1250°C in CO_2 which is quite different than the low probabilities in air plasmas at similar temperatures. At lower heat fluxes these spikes appear to have little correlation with the strength of the fibers but at higher heat fluxes they can indicate the presence of a much more destructive phenomena. Exposure to heat fluxes above 80 W/cm^2 almost always led to a catastrophic failure for any test gas composition. The temperature profile of failed coupons for both air and CO_2 cases can be seen in the following plot.

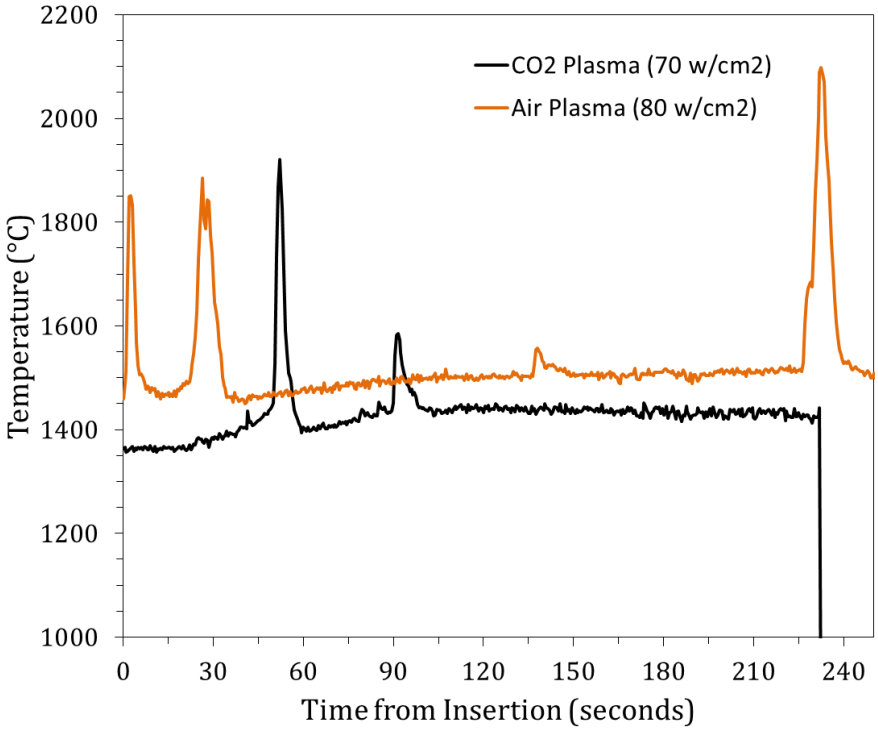

Figure 79: Temperature profiles of SiC samples that displayed destructive flares

It can be seen that spikes were observed at steady state temperatures around 1400°C for both air and CO_2 tests. At surface temperatures above 1400°C in CO_2 all samples had isolated regions of complete fiber consumption. Whereas only a few samples failed in air.

These temperature spikes are easily identifiable by a strong emission flare within the visible spectrum. For all oxidizing environments, these flares propagated along each tow. Video recording of the coupon surface allowed tracking of these flares. Snapshots of the surface during a flare can be seen in the following figure.

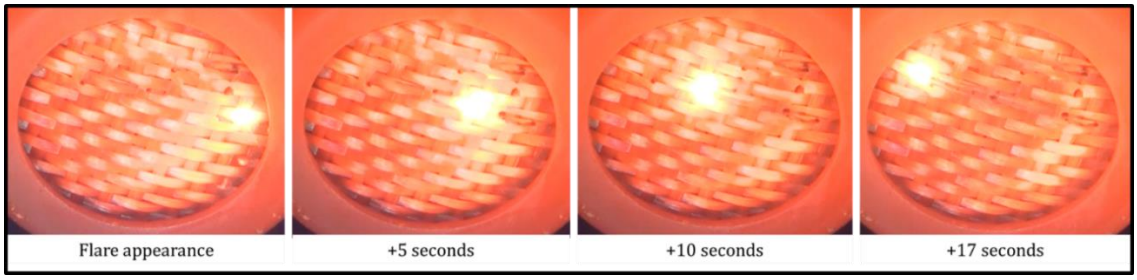

Figure 80: Surface images showing flare propagation with an average speed of 1mm/s

As the flare propagates, it completely consumes the tow and leaves behind a thick silica trail. A destroyed coupon can be seen in the following photo.

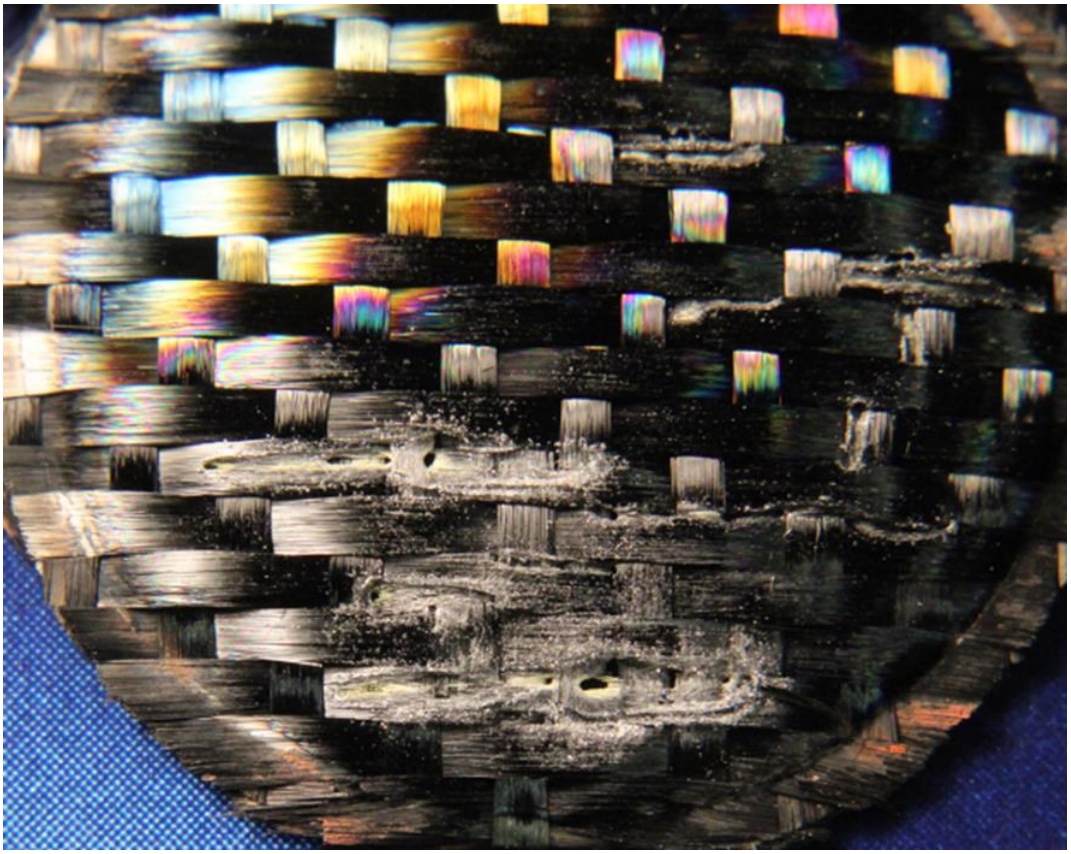

Figure 81: Photograph of the SiC coupon surface that failed after exposure to a CO_2 plasma

At relatively high CO_2 heat fluxes that led to destructive material flares, the morphology appears similar to other samples that were destroyed in air plasmas. The iridescence is due to the silica coating whereas the black areas around the destroyed locations have oxide layers too thick to provide the iridescence. Holes through the weave are also similar to those observed in air plasmas. SEM analysis of a coupon exposed to CO_2 displayed the worm holes through the weave typical in all oxidizing plasmas and can be seen in Figure 82.

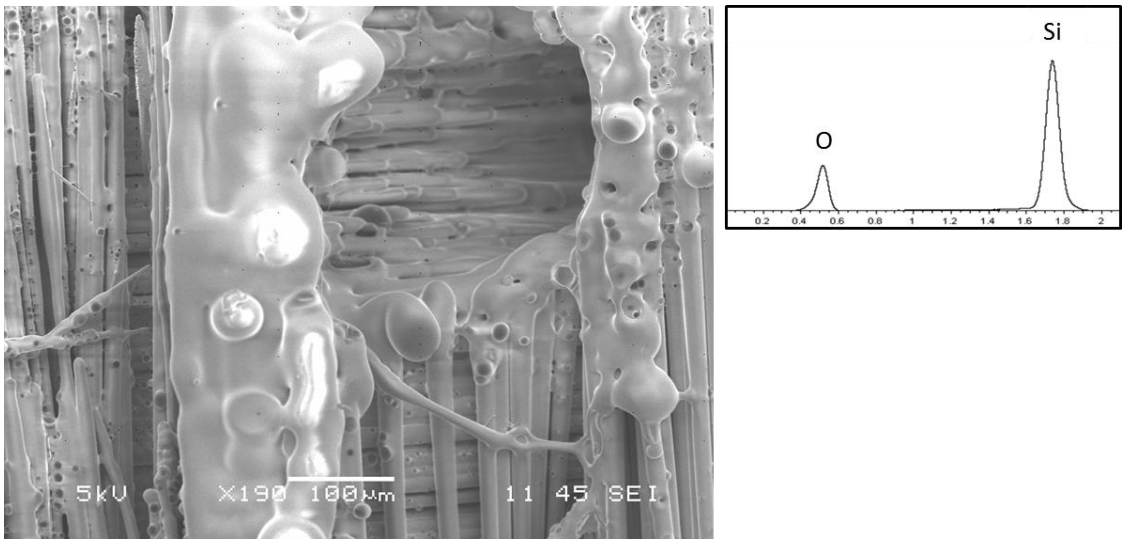

Figure 82: SEM image and EDS results of a coupon that failed in a CO_2 plasma

EDS was used to confirm the surface was also comprised of a silicon-oxygen layer. The SEM images of the surface shows the highly viscous nature of the silica layer around the flare. Bubbles protruding from the thick silica layer is due to the transport of trapped gaseous species.

SEM analysis was also performed on the back side of the failed coupon near the worm hole. The electrostatic charging on the image is due to the non-conductive silica surface.

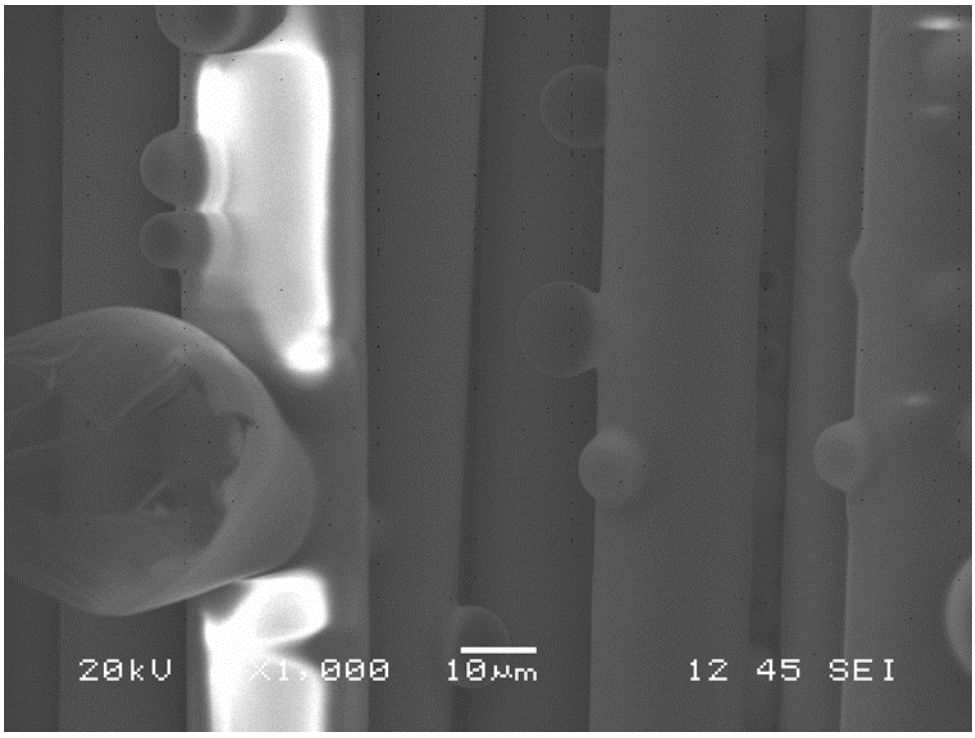

Figure 83: SEM image of the SiC coupon backside near a failed region that shows highly protruded bubbles

Fragile appearing bubbles were observed behind the holes through the weave. The thin walled highly protruded bubbles suggest that the location was semi protected from the shear of the plasma flow. Spherulitic structures on the backside of the coupon were also observed and is one feature that was not observed during air plasma testing, although they may still exist. These structures can be seen in the following SEM image.

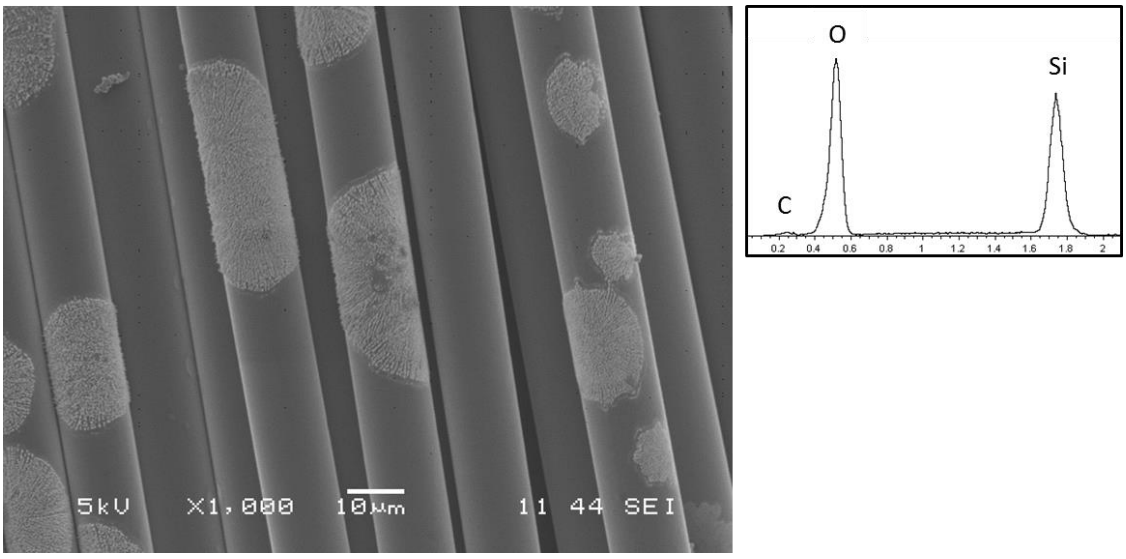

Figure 84: SEM image and EDS results taken on the back side of a failed coupon

These spherulitic structures are similar to those observed by Narushima in CO_2/CO atmospheres [114]. EDS was used to determine that these features were composed of mostly silicon and oxygen. Therefore, it is possible that cristobalite was formed during the flares due crystallization of the amorphous silica layer at the higher temperature locations.

9.4. Emission Tracking

Emission spectroscopy was performed within the boundary layer of the tested sample and shows similar results during a flare to those seen in air plasmas. Emission results using a 10 second integration time can be seen in the following plot.

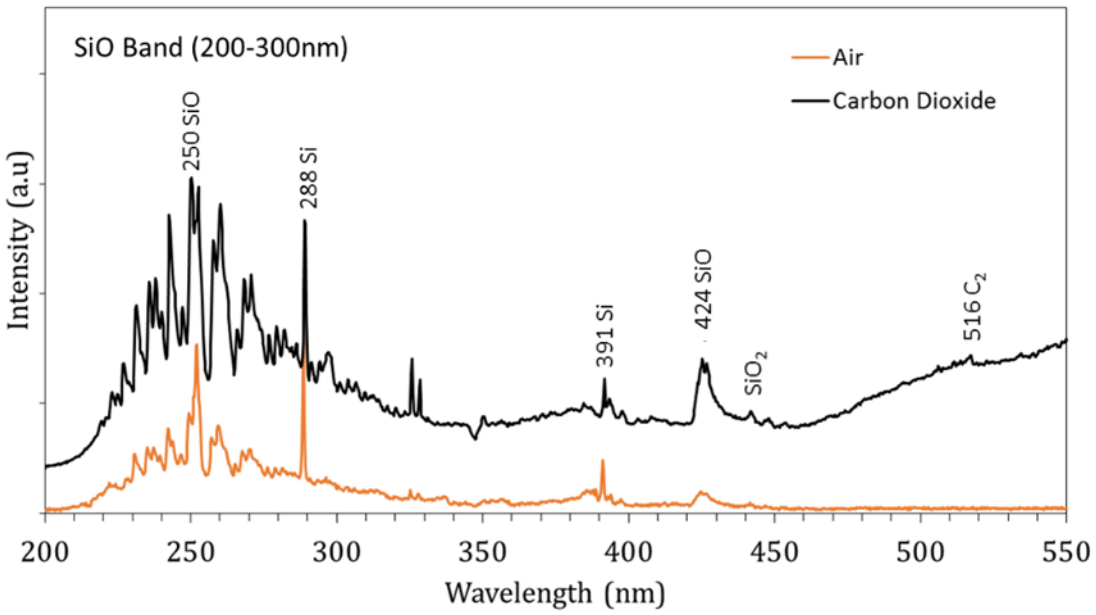

Figure 85: Emission captured in the thermal boundary layer above the sample during failure in an air and CO_2 plasma

Strong emission from Si and SiO was observable within the thermal boundary layer during flares in air and CO_2 plasmas. Weaker SiO_2 emission was also observable.

These emission features along with O-atom were tracked with time for 50 and 70 W/cm^2 heat flux conditions. The O-atom signal increased with increasing power suggesting the continued dissociation of molecular species. The plot of the scaled signal intensity vs time can be seen in the following figure.

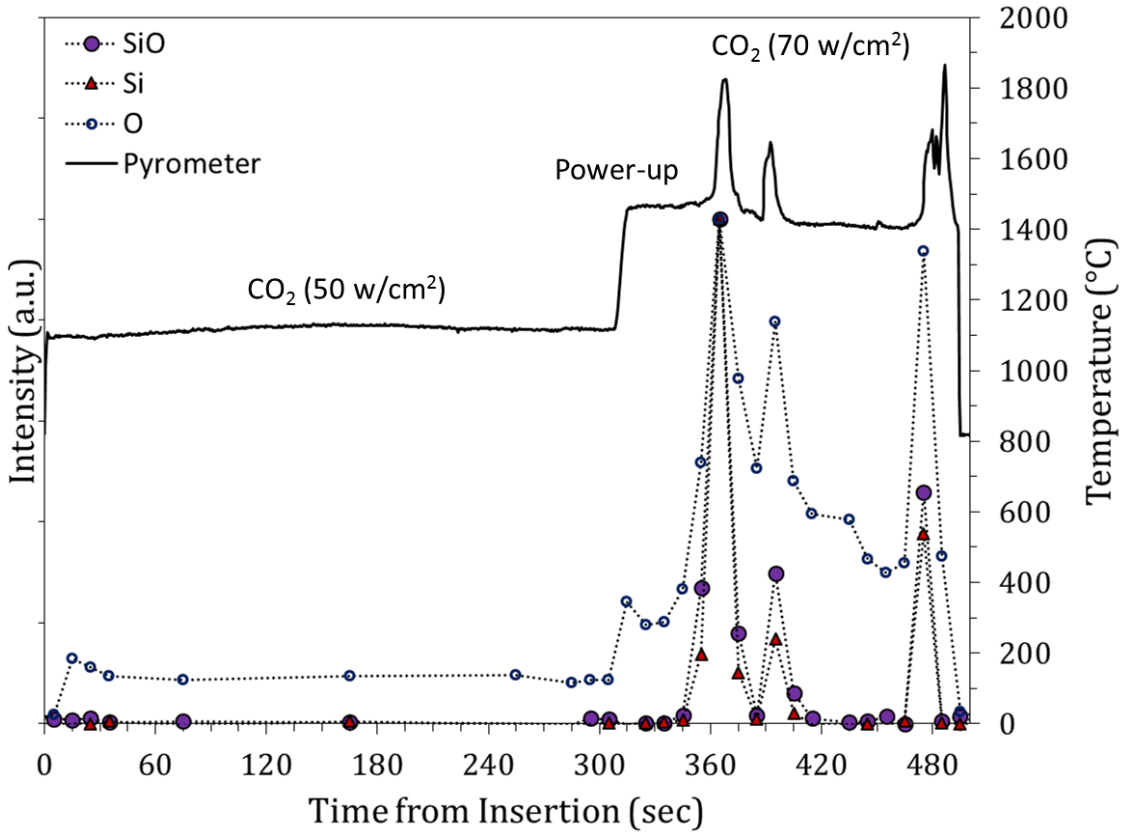

Figure 86: Emission feature tracking for a power-up test

Flares were quickly observed when the power was increased. Evidence of carbon was in the form of C_2 and CO_2 throughout the test but spikes in Si, SiO, and SiO_2 were only observable during the flares. Si and SiO were tracked at wavelengths of 288 and 250 respectively.

9.5. Discussion on CO_2 Plasma Results

9.5.1. Heterogeneous Surfaces

A complex mix of resulting surface morphologies have been reported by many different authors after oxidation of silica formers (Si and SiC) in CO_2 and CO using

different techniques. Silica detection has been reported on Hi-Nicalon fibers after oxidation experiments using CO_2 [115]. Whereas, carbon surfaces have been observed after oxidation experiments using CO [116]. A large transition between these two regimes leading to a highly porous silica layer has also been shown by varying the CO_2/CO gas ratio [114].

It is believed that the changing morphology observed in this investigation is not purely an artifact of the changing temperatures but is also dominated by the change in dissociation fraction at the different heating conditions. This is in agreement with the results obtained by Balat who observed morphological differences on the surface of rigid SiC samples when comparing results between molecular and microwave excited CO_2 gas [117].

It has been shown that at surface temperatures below 1250°C, CO does not react with SiC [107]. Therefore, at the low heat flux condition where the plasma is expected to be comprised of CO_2, CO and O, the major reacting species would be CO_2 and O. Whereas tests in both CO_2 and atomic oxygen have been shown to lead to a silica layer at these temperatures [115]. As seen in Figure 74, an increase in free stream temperature, causes CO and O-atom to be the dominant species. At these temperatures, CO could then react with SiC through the following equilibrium [65]:

$$SiC + CO \rightleftarrows SiO + 2C \qquad \text{eq. 30}$$

This equation shows carbon extraction from both the SiC material and the CO in the gas phase. Due to the lack of any reported silica layer during oxidation in pure CO, continued oxidation reactions between SiO and CO to form SiO_2 are unlikely.

It is expected that free carbon resulting from the previous equation will leave the surface through reactions with atomic oxygen to form CO. This reaction can be seen in the following equilibrium [65]:

$$C + O \rightleftarrows CO \qquad \text{eq. 31}$$

According to Le Chatelier's principle, an increase in the CO pressure will shift the equilibrium to favor the free carbon phase. Therefore, the mechanism to achieve the carbon incorporation into the resulting Si-O-C layer is thought to be due to the oxidation of SiC by CO or O-atom and the suppressing effect of high CO pressures on the C + O reaction. This goes to show that the resulting surface morphology is dependent on the individual partial pressures of the total system and not solely by the oxygen partial pressure [215].

9.5.2. Onset of Flares

Due to the fact that the trigger of the flares is still under debate, the cause for the lower temperature flares in CO_2 compared to air is much harder to determine. Also, direct

comparisons to air plasma test results must be carefully made due the additional differences that exist besides the chemical composition of the plasma. This includes the radiation spectral intensity from the excited species within the plasma. Whereas, the CO_2 plasma emits high energy ultra violet radiation, which can lead to significantly higher reaction rates without causing any diffusion limitations [54].

Despite these differences, it is believed that the high CO pressure is the reason for the higher probability of flares at lower temperatures in CO_2 plasmas. The high concentrations of carbon on the surface and in the reactive boundary layer can lead to carbothermal reduction of silica [118]. Whereas, CO gas as well as free carbon are expected to enhance the SiO_2 removal process. In turn, the higher permeability of a heterogeneous layer may not provide significant diffusion limitations to suppress the attack of oxygen [113]. In addition to silica reduction, carbon surface layers have been shown to be much more electrically conductive than silica layers [119]. Whereas, the CO_2 plasma can generate large electric fields across the SiC surface which can accelerate charge particle flow [54].

CHAPTER 10: SUMMARY AND FUTURE WORK

Flexible TPS materials are of interest due to their necessity for the success of Inflatable Aerodynamic Decelerators. Aerothermal screening of candidate outer fabric materials was performed in stagnation point configuration using the 30 kW Inductively Coupled Plasma Torch achieving surface temperatures in excess of 1400°C. Results show the superior performance of 2-D woven Hi-Nicalon SiC fibers compared to carbon fiber, Kevlar and Nextel BF-20 at heat fluxes between 50 and 80 w/cm^2. However, the overall performance of the fine diameter SiC fibers was limited by the presence of atomic oxygen. Whereas, oxidation progresses through a much different mechanism using dissociated gases compared to dry thermal oxidation typical of more conventional furnaces.

SEM images of the SiC post-test coupons display a rough porous surface due to significant bubble formation. EDS was used to confirm the existence of a newly formed amorphous silicon dioxide layer. The morphological changes that occurred during oxidation led to a time dependence of the emissivity, catalycity and reactivity. Optical pyrometry and emission spectroscopy were used to track these changes. An increase in atomic species consumption was detected during the rapid silica formation phase leading to higher surface temperatures. Subsequently, an emissivity increase with silica formation led to a net temperature decrease with time.

In order to help assess the viability of 2-D woven Hi-Nicalon fibers as an outer fabric material the fracture strength was quantified after aerothermal heating. Varying flow rates of nitrogen and oxygen were used to extract the influence of oxidation on the strength reduction of the Hi-Nicalon weave. Room temperature tensile test results have shown a steady 50% strength reduction in pure nitrogen plasmas with minimal effects on the surface morphology. Whereas coupon exposure to oxidizing environments led to extremely brittle fibers that were too fragile to test after durations of more than 240 seconds.

Above heat fluxes of 80 W/cm^2 almost all SiC coupons were destroyed. Si, SiO and SiO_2 were observed in the thermal boundary layer during failure in oxidizing environments. This in turn led to thick silica layers on the surface. Similar to oxidizing plasmas, catastrophic failure in nitrogen plasmas was accompanied by a large temperature spike but nitrogen incorporation into the surface lead to a jagged surface morphology.

Simulation of entry into the Mars atmosphere caused a material response that was vastly different than the predictable silica layer observed during re-entry simulation. Despite the fact that both entry conditions expose the SiC fabric to atomic oxygen, the high CO pressure during Mars entry led to carbon incorporation into the surface oxide layer and coupon failure at lower temperatures compared to air test results.

Due to the increased understanding of the aerothermal performance of SiC gained from this investigation in addition to the data collected at other ground test facilities, SiC fabrics have been deemed a promising candidate for future NASA missions. An in-flight experiment using an SiC fabric lay-up is scheduled for 2016 [120].

Most of this research was observationally based on a broad range of topics. It was the intent of the author to invoke questions that still need to be answered. Much more quantitative and/or application focused research is recommended for future tests. A few of these topics are mentioned below.

- Trajectory Relevant Tests: Even though the ICP torch provides the presence of flowing dissociated gases and heating due to exothermic reactions, significant aerothermal and aerodynamic differences between these tests and an actual flight trajectory still exist. These differences include; variations in surface pressure, shear, dissociation fraction and radiation intensity. In addition, the presence of hydrogen due to moisture in the atmosphere is also known to alter the oxidation phenomena compared to dry air but was not included in this study.

- Lay-up Uncertainties: The effect of impurities in the test environment can have a significant effect on the oxidation of the fibers and may arise from pyrolyzing insulators that outgas through the outer fabric at high temperatures. With this in

mind, it is recommended that future microscopic oxidation analysis is performed on outer fabric samples that were incorporated in the full flexible TPS lay-up.

- Hot Tensile Tests: Besides the many challenges that exist when extrapolating the aerothermochemistry of the ground test environment to flight conditions, it is also difficult to extrapolate the room temperature tensile test results to flight applications. Except for the case of aerocapture, where the surface may cool down between a first and second entry, thermal stresses during cool down may not be appreciable in hot conditions where the silica may be viscous. Also, the strength controlling flaws in the brittle silica layer may not exist. Moreover, the strength reduction is expected to be related to the mechanical state of the fibers. Therefore, an additional decrease in tensile strength may occur under combined heating and loading. Whereas creep onset, leading to increased tortuosity and oxygen permeation may enhance oxidation. Further hot tensile tests would be required to better determine application based strength loss.

- Coupon Comparisons: The different aerothermal tests performed on the circular SiC fabric coupons during this investigation were fairly unique, requiring large leaps to be made from the findings of other researchers. This strategy can rapidly advance the understanding of the SiC fabric performance but it also leaves large scientific knowledge gaps that should be filled in order to reaffirm the conclusions. It is recommended that quantitative oxidation analysis is performed on the rigid SiC

disks. It is also recommended that tensile tests are performed on circular coupons after oxidation in a conventional furnace at 1400°C due to the large difference between single fiber tensile tests and fabric tests.

REFERENCES

[1] Wright, Henry, Cutright, Amanda, Corliss, James, Bruce, Walter, Trombetta, Dominic, Mazaheri, Alireza, Coleman, Michael, Olds, Aaron, Hancock, Sean. "HEART Flight Test Overview." presented at the 9th International Planetary Probe Workshop, Toulouse, France. (2012).

[2] Del Corso, .J A., Cheatwood, F. M,. Bruce III, W. E, Hughes, S. J., Calomino, A M. "Advanced High-Temperature Flexible TPS for Inflatable Aerodynamic Decelerators." AIAA 2011-2510, 21st AIAA Aerodynamic Decelerator Systems Technology Conference and Seminar; Dublin Ireland, May 23-26, (2011).

[3] Del Corso, J. A., Bruce III, W. E., Hughes, S. J., Dec, J. A., Rezin, M. D., Meador, M. B., Hiaquan, G., Fletcher, D. G., Calomino, A. M., Cheatwood, F. M. "Flexible Thermal Protection System Development for Hypersonic Inflatable Aerodynamic Decelerators." 9th International Planetary Probe Workshop, Toulouse, France, 16-22 June (2012).

[4] Cassell, Alan M., Robin A.S. Beck, James O. Arnold, Helen Hwang, and Michael J. Wright, Christine E. Szalai, Max Blosser, Carl C. Poteet. "Development of Thermal Protection Materials for Future Mars Entry, Descent and Landing Systems." AIAA. Print

[5] Chollon, G., R. Pailler, R. Naslain, F. Laanani, M. Monthioux, P. Olry. "Thermal stability of a PCS-derived SiC fibre with a low oxygen content (Hi-Nicalon)." *J. Mater. Sci.* 32 (1997): 327–347.

[6] COI Ceramics, Hi-NicalonTM Ceramic Fiber, ATK Space Systems. www.coiceramics.com

[7] Rahaman, M. "Ceramic Processing and Sintering", Second Edition, 2003. ISBN: 978-0824709884

[8] DiCarlo, J.A., and Yun, H.M. "Non-oxide (Silicon Carbide) Fibers." *Handbook of Ceramic Composites,* ed. N. Bansal, Kluwer Academic Publishers, Boston, (2005): 33- 52.

[9] Zinn, S., and Semiatin, S. L. "Elements of Induction Heating: Design, Control, and Applications." Palo Alto, CA: Electric Power Research Institute, 1987. Print.

[10] Klayton, M. H. "Fundamental Electrical Technology." Reading, MA: Addison-Wesley Pub. 1977. Print.

[11] Lieberman, M. A., and Lichtenberg, A. J. "Principles of Plasma Discharges and Material Processing." John Wiley & Sons, New York, 1994. Chap. 12.

[12] Smith, S. "Investigation of a Subsonic and Supersonic Flow Characteristics of an Inductively Coupled Plasma Torch." The University of Vermont, Mechanical Engineering, Masters Thesis, 2013.

[13] ASTM. “Standard Test Method for Measuring Heat-Transfer Rate Using a Thermal Capacitance (Slug) Calorimeter.”

[14] Scott, C.D. “Catalytic Recombination of Nitrogen and Oxygen on High-Temperature Reusable Surface Insulation.” *Progress in Astronautics and Aeronautics* 77 (1981): 192-212.

[15] Dougherty, M., W. Owens, J. Meyers, D. Fletcher, D. "Investigations of Surface-Catalyzed Recombination Reactions in the Mars Atmosphere." AIAA 2011-1326, Paper presented at the 49th AIAA Aerospace Sciences Meeting, Orlando, Florida, (2011).

[16] Lutz, A., W. Owens, J. Meyers, D. Fletcher, and J. Marschall, "Investigations of Surface-Catalyzed Recombination Reactions in N2 Plasma." AIAA 2011-901, 49th AIAA Aerospace Sciences Meeting, Orlando, Florida, (2011).

[17] Magin, Thierry E., Degrez, Gérard. “Transport properties of partially ionized and unmagnetized plasmas.” *Journal of Computational Physics* 198.2 (2004): 424. MUTATION

[18] Owens, W. P., J. M. Meyers, A. J. Lutz, S. F. Smith and D. G. Fletcher. “Direct Assessment of Surface-Catalyzed Reaction Efficiency on SiC Materials.” NATO AVT-199 Specialists Meeting on Catalytic Gas Surface Interactions, Rhode-St-Genese, Belgium, Oct. 2012.

[19] 3M Ceramic Materials Department. “Ceramic Fiber For Outer Space Applications.” Technical Notebook (1996).

[20] Bose, D. M., et al. "The Hypersonic Inflatable Aerodynamic Decelerator (HIAD) Mission Applications Study," AIAA Aerodynamic Decelerator Systems Technology Conference and Seminar, Daytona Beach, FL, March (2013).

[21] Rosner, D. E., Allendorf, H. D. “High Temperature Kinetics of the Oxidation and Nitridation of Pyrolytic Silicon Carbide in Dissociated Gases.” *Journal of Physical Chemistry* 74.9 April, (1970): 1829–39.

[22] Beck, R. A. S., James O. Arnold, Susan White, Wenhong Fan, Mairead Stackpoole, Parul Agrawal, and Scott Coughlin. “Overview of Initial Development of Flexible Ablators for Hypersonic Inflatable Aerodynamic Decelerators.” 21st AIAA Aerodynamic Decelerator Systems Technology Conference and Seminar, 23 - 26 May Dublin, Ireland, (2011). AIAA 2011-2511.

[23] Raytek. "Marathon Series Operator's Manual." 2000. Print.

[24] Covington, M., Sawko, P. “Optical properties of woven ceramic fabrics for flexible heat shields.” AIAA, 4th Joint Thermophysics and Heat Transfer Conference, AIAA-86-1281 June (1986).

[25] Omega “Thermocouple Reference Guide.” www.Omega.com

[26] Savage, R. T., Love, W., Bloetscher, F. “High temperature performance of flexible thermal protection materials.” AIAA, 19th Thermophysics Conference, AIAA PAPER 84-1770, June, (1984).

[27] Sawko, P. M., and Tran, H. K., “Strength and Flexibility Properties of Advanced Ceramic Fabrics”, *SAMPE Quarterly* 17 (1985): 7-13. ISSN 0036-0821.

[28] Lacombe, A., and Lacoste, M. “Investigation of C/SiC “Breaking Point“ Under Arc Jet Environment at NASA—J. S. C.” *Journal of High Temperature Chemical Processes* 3 (1994): 285–296.

[29] Dabalà , P., Hilfer, G. and Auweter-Kurtz, M., “Investigation of the oxidation behaviour of thermal protection materials supported by mass spectrometry.” Proceedings of the 2nd European Symposium on Aerothermodynamics of Space Vehicles, ESTEC, Noordwijk, The Netherlands, Nov. 1994, ESA-SP-367, ESA Publications Division, Noordwijk, (1995): 237-246.

[30] Hilfer, G., and Auweter-Kurtz, M. “Experimental and theoretical investigation of the oxidation behavior of thermal protection materials under oxygen attack.” *High Temperatures - High Pressures* 27-28 (1995/1996): 435-448.

[31] Auweter-Kurtz, M., Hilfer, G., Habiger, H., Yamawaki, K., Yoshinaka, T., Speckmann, H.-D. “Investigation of oxidation protected C/C heat shield material in different plasma wind tunnels.” *Acta Astronautica* 45.2 Jan. (1999): 93-108. doi: 10.1016/S0094-5765(99)00114-9

[32] Hirsch, K., Roth, B., Altmann, I., Barth, K.-L., Jentschke, H., Lunk, A., Schumacher, U. "Plasma-induced silica-like protection layer formation on C/C - SiC heat-shield materials for re-entry vehicles." *High Temperatures - High Pressures* 31.4 (1999): 455 – 465.

[33] Altmann, I., Bauer, G., Hirsch, K., Jentschke, H., Stefan, K., Roth, B., Schinköth, D., and Schumacher, U., "In-Situ Diagnostics of the Interaction Region between a Nitrogen-Oxygen Plasma Jet and Hot C/C-SiC Ceramic Materials." *High Temperatures - High Pressures* 32 (2000): 573–579.

[34] Feigl, M., Auweter-Kurtz, M. "Investigation of SiO production in front of Si-based material surfaces to determine the transition from passive to active oxidation using planar laser-induced fluorescence." 35th AIAA Thermophysics Conference, AIAA-2001-3022, A01-31434, June (2001).

[35] Laux, T., Herdrich, G., and Auweter-Kurtz, M. "Oxidation Behavior of Sintered Silicon Carbide in Various Plasma Wind Tunnels." Hot Structures and Thermal Protection Systems for Space Vehicles, Proceedings of the 4th European Workshop held 26–29 November, 2002 in Palermo, Italy.; Vol. ESA SP-521, edited by A. Wilson, European Space Agency, Paris, (2003): 377–379.

[36] Morino, Y, T Yoshinaka, M Auweter-Kurtz, G Hilfer, H.-D Speckmann, A Sakai. "Erosion Characteristics Of SiC Coated C/C Materials In Arc-Heated High Enthalpy Air Flow." *Acta Astronautica* 50.3 February (2002): 149–158.

[37] Hald, H. “Operational Limits for Reusable Space Transportation Systems Due to Physical Boundaries of C/SiC Materials.” *Aerospace Science and Technology* 7.7 (2003): 551–559. doi:10.1016/S1270-9638(03)00054-3

[38] Gülhan, A., and Esser, B., Hannemann, K., and Karl, S. “Experimental and numerical approach for the qualification of TPS components in different planetary entry conditions.” Hot Structures and Thermal Protection Systems for Space Vehicles, Proceedings of the 4th European Workshop held 26-29 November, 2002 in Palermo, Italy. Edited by A. Wilson. ESA SP-521. Paris: European Space Agency, (2003): 177.

[39] Herdrich, G., M. Fertig, S. Löhle, S. Pidan, M. Auweter-Kurtz, and T. Laux. "Oxidation Behavior of Siliconcarbide-Based Materials by Using New Probe Techniques." *Journal of Spacecraft and Rockets* 42.5 (2005): 817-824. doi: 10.2514/1.12265

[40] Aldinger, F., Auweter-Kurtz, M., Fertig, M., Herdrich, G., Hirsch, K., Lindner, P., Matusch, D. Neuer, G., Schumacher, U. and Winter, M. “Behavior of reusable heat shield materials under re-entry conditions.” Basic Research and Technologies for Two Stage to Orbit Vehicles, Eds. Sachs, G., Wagner, S. and Jacob, D., Chapter 7., High-Temperature Materials and Hot Structures, Section 7.2, NOV, (2005). doi: 10.1002/3527605711.ch7

[41] Verant, J.-L., N. Perron, M. Balat-Pichelin, O. Chazot, A. Kolesnikov, V. Sakharov, O. Gerasimova, P. Omaly. “Microscopic and macroscopic analysis

for TPS SiC material under Earth and Mars re-entry conditions." *Int. J. Aerodynamics* 2.2-3-4 (2012).

[42] Alfano, Davide, Luigi Scatteia, Stefania Cantoni, and Marianne Balat-Pichelin. "Emissivity and catalycity measurements on SiC-coated carbon fibre reinforced silicon carbide composite." *Journal of the European Ceramic Society* 29 (2009): 2045–2051.

[43] Schussler, M., Auweter-Kurtz, M., Herdrich, G., and Lein, S. "Surface Characterization of Metallic and Ceramic TPS-Materials for Reusable Space Vehicles." *Acta Astronautica* 65.5-6 September-October (2006): 676–686.

[44] Panerai, F. and Chazot, O. "Characterization of Gas/Surface Interactions for Ceramic Matrix Composites in High Enthalpy, Low Pressure Air Flow." *Materials Chemistry and Physics* 134.2-3 (2012): 597-607.

[45] Sakraker, Isil, Asma C. O. "Experimental investigation of passive/active oxidation behavior of SiC based ceramic thermal protection materials exposed to high enthalpy plasma." *Journal of the European Ceramic Society* 33 (2013): 351–359.

[46] Helber, Bernd, Panerai, F., Chazot, Olivier, Magin, T.E. "Reusability Limits of Carbon/Silicon Carbide Heat Shield Materials Part 2: Volatilization Detection by Space-& Time-Resolved Emission Spectroscopy." RTO AVT-199, from Specialists Meeting on Catalytic Gas Surface Interactions, issue paper 20, published by von Karman Institute, (2013).

[47] Balat, M. J. H. “Determination of the Active-to-Passive Transition in the Oxidation of Silicon Carbide in Standard and Microwave-Excited Air.” *Journal of the European Ceramic Society* 16 (1996):. 55–62. doi:10.1016/0955-2219(95)00104-2

[48] Schneider, B., Guette, A., Naslain, R., Cataldi, M., and Costecalde, A. “A Theoretical and Experimental Approach to the Active-to-Passive Transition in the Oxidation of Silicon Carbide: Experiments at High Temperatures and Low Total Pressures.” *Journal of Materials Science* 33 (1998): 535–547. doi:10.1023/A:1004313022769

[49] Jorgensen, Paul J. “Effect of an Electric Field on Silicon Oxidation.” *J. Chem. Phys.* 37 (1962): 874. doi: 10.1063/1.1733177

[50] Kimura, Shinichiro, Eiichi Murakami, Terunori Warabisako, Eisuke Mitani, and Hideo Sunami, “An 18O study of oxygen exchange phenomena during microwave discharge plasma oxidation of silicon.” *J. Appl. Phys.* 63 (1988): 4655. doi: 10.1063/1.340119

[51] Balat, M., Flamant, G., Male, G., and Pichelin, G. “Active to Passive Transition in the Oxidation of Silicon Carbide at High Temperature and Low Pressure in Molecular and Atomic Oxygen.” *Journal of Materials Science* 27 (1992): 697–703. doi:10.1007/BF02403882

[52] Berton, B., Bacos, M. P., Demange, D., Lahaye, J. “High-temperature oxidation of silicon carbide in simulated atmospheric re-entry conditions” *Journal of Materials Science* 27.12 June (1992): 3206-3210.

[53] Hess, D. W. “Plasma-assisted oxidation, anodization, and nitridation of silicon.” *IBM Journal of Research and Development archive* 43.1-2 January (1999): 127-145. doi >10.1147/rd.431.0127

[54] Tatsumura, K., T. Shimura, E. Mishima, K. Kawamura, D. Yamasaki, H. Yamamoto, T. Watanabe, M. Umeno, and I. Ohdomari. “Reactions and diffusion of atomic and molecular oxygen in the SiO2 network.” Phys. Rev. B 72, 045205 – Published 13 July 2005.

[55] Vora, N. D. “High Temperature Oxidation of Silica Formers in Dissociated Oxygen.” PhD Dissertation, Vanderbilt University, Nashville, Tennessee, May, (2009).

[56] Wagner, C. “Passivity during the Oxidation of Silicon at Elevated Temperatures.” *Journal of Applied Physics* 29.9 September (1958): 1295-1297. doi:10.1063/1.1723429

[57] Jacobson, N. S., and Myers, D. L. “Active Oxidation of SiC.” *Oxidation of Metals* 75.1–2 (2011): 1–25. doi:10.1007/s11085-010-9216-4

[58] Balat-Pichelin, M., Charpentier, L., Panerai, F., Chazot, Olivier, Helber Bernd, Nickel, Klaus, “Passive/active oxidation transition for CMC structural materials

designed for the IXV vehicle re-entry phase." *Journal of the European Ceramic Society* 35.2 February (2015): 487–502.

[59] Hilfer, G. "The Impact of Environmental Conditions during Re-entry on the Re-usability of Si-based Ceramic TPS." Hot Structures and Thermal Protection Systems for Space Vehicles, Proceedings of the 4th European Workshop held 26-29 November, 2002 in Palermo, Italy. Edited by A. Wilson. ESA SP-521. Paris: European Space Agency, (2003): 363.

[60] Deal, B. E., and Grove, A. S. ''General Relationship for the Thermal Oxidation of Silicon,'' *J. Appl. Phys.* 36 (1965): 3770–78.

[61] Halbig, Michael C. "The Oxidation Kinetics of Continuous Carbon Fibers in a Cracked Ceramic Matrix Composite." NASA/TM--2001-210520, U.S. ARMY/ARL-TR-2296 (2001).

[62] Peeters, Jozef, and Li Li. "Oxidation of silicon in plasma afterglows: New model of oxide growth including recombination of diffusing O atoms." *J. Appl. Phys.* 73 (1993): 2477. doi: 10.1063/1.353107

[63] Blanc, Joseph. "A revised model for the oxidation of Si by oxygen." *Appl. Phys. Lett.* 33 (1978): 424-426. doi: 10.1063/1.90409

[64] Turkdogan, E.T., Grieveson, P. and Darken, L.S. "Enhancement of Diffusion-Limited Rates of Vaporization of Metals." *Journal of Physical Chemistry* 67.8 (1963): 1647-1654.

[65] Gulbransen, E. A., and Jansson, S. A. “The High-Temperature Oxidation, Reduction, and Volatilization Reactions of Silicon and Silicon Carbide.” *Oxid. Met.* 4.3 (1972): 181–201.

[66] Laux, C.O. “Radiation and Nonequilibrium Collisional-Radiative Models.” von Karman Institute Lecture Series 2002-07, Physico-Chemical Modeling of High Enthalpy and Plasma Flows, eds. D. Fletcher, J.-M. Charbonnier, G.S.R. Sarma, and T. Magin, Rhode-Saint-Genèse, Belgium, 2002. SPECAIR

[67] Gorskii, V. V., Gordeev, A. N., Dudkina, T. I. “Aerothermochemical destruction of silicon carbide washed by a high-temperature flow of air.” *High Temperature* 50.5 September (2012): 646-652.

[68] Pretorius, R., Strydom, W., and Mayer, J.W. “Si Tracer Studies of the Oxidation of Si, $CoSi^2$ and PtSi.” *Physical Review B* 22.4 August (1980): 1885-1891.

[69] Chiou, Y.L. “A note on the thicknesses of anodized niobium oxide films.” *Thin Solid Films* 8.4 October (1971): R37–R39. Short communication.

[70] Mieskowski, D. M., Mitchell, T. E. and Heuer, A. H., “Bubble Formation in Oxide Scales on SiC”, Communications of the American Ceramic Society, (1984), pg 17.

[71] Goto, T., and Homma, H., “High-Temperature Active/Passive Oxidation and Bubble Formation of CVD SiC in O2 and CO2 Atmospheres.” *Journal of the*

European Ceramic Society 22 (2002): 2749–2756. doi:10.1016/S0955-2219(02)00139-5

[72] Tedmon, Jr. C. S. "The Effect of Oxide Volatilization on the Oxidation Kinetics of Cr and Fe-Cr Alloys." *J. Electrochem. Soc.* 113.8 (1966): 766-768. doi: 10.1149/1.2424115

[73] Moene, R., Makkee, M., Moulijn, J. "High Surface Area Silicon Carbide as Catalyst Support Characterization and Stability." *Applied Catalysis A: General* 167 (1998): 321-330.

[74] Wooldridge, Margaret S., Stephen A. Danczyk, Jianfan Wu. "Quantitative evaluation of vibrational excitation of SiO $A^1\Pi$-$X^1\Sigma^+$ flame emission from a silane/hydrogen/oxygen/argon diffusion flame." *Journal of Quantitative Spectroscopy & Radiative Transfer* 64 (2000): 573-584.

[75] Marine, W., Tokarev, V., Gerri, M., Sentis, M., and Fogarassy, E. "Ablation Dynamics of Silicon Based Targets in Oxygen and Nitrogen Atomspheres." *Thin Solid Films* 214 (1994): 103–108.

[76] Kramida, A., Ralchenko, Yu., Reader, J., and NIST ASD Team (2012). NIST Atomic Spectra Database (ver. 5.0), [Online]. Available: http://physics.nist.gov/asd [2012, August 13]. National Institute of Standards and Technology, Gaithersburg, MD.

[77] Marschall, J., Pejaković, D. A, Fahrenholtz, W. G., Hilmas, G. E., Panerai, F., and Chazot, O. “Temperature Jump Phenomenon during Plasmatron Testing of ZrB2-SiC Ultrahigh-Temperature Ceramics.” *AIAA Journal of Thermophysics and Heat Transfer* 26.4 (2012): 559-572. doi: 10.2514/1.T3798

[78] Panerai, F., Helber, Bernd, Chazot, Olivier, Balat-Pichelin, M. “Surface temperature jump beyond active oxidation of carbon/silicon carbide composites in extreme aerothermal conditions.” *Carbon* 71 (2014): 102 – 119.

[79] Goulard, R. “On Catalytic Recombination Rates in Hypersonic Stagnation Heat Transfer.” *Jet Propulsion* 28 November (1958): 73 – 85.

[80] Thoemel J., Chazot O., Barbante P. “Aspects of advanced catalysis modeling for hypersonic flows.” Proceedings of the Summer Program 2008, Center for Turbulence Research, Stanford University, 29 (2008).

[81] Herdrich, G., M. Fertig, D. Petkow, A. Steinbeck, S. Fasoulas. “Experimental and numerical techniques to assess catalysis.” RTO AVT-199, from Specialists Meeting on Catalytic Gas Surface Interactions (2013).

[82] Pidan, S., Auweter-Kurtz, M., Herdrich, G. and Fertig, M. “Recombination Coefficients and Spectral Emissivity of Silicon Carbide-Based Thermal Protection Materials.” *Journal of Thermophysics and Heat Transfer* 19.4 October – December (2005): 566-571.

[83] Rosner, D. E., Allendorf, H. D. “Nitrogen as an Ablative Reactant in Dissociated Air.” *AIAA Journal* 8.1 (1970): 166-168.

[84] Breiland, W. G. “Reflectance-Correcting Pyrometry in Thin FIlm Deposition Applications.” Technical Report, SAND2003-1868, Sandia National Laboratories, Albuquerque, New Mexico 87185 and Livermore, California 94550, June (2003): Print.

[85] Bethe, Hans A., and Adams, Mac C. "A Theory for the Ablation of Glassy Materials." *Journal of the Aerospace Sciences* 26.6 (1959): 321-328.

[86] Nguyen-Xuan, F., Mallard, O., Cavadias, S., Amouroux, J., Le Bozec, A., Rapuc, M. “Catalycity Measurements on Metallic and SiC Material Surfaces, in a Pulsed Plasma Reactor.” Second European Symposium on Aerothermodynamics for Space Vehicles, Netherlands, November (1994).

[87] Kim, H. E., and Moorhead, A. J. “Strength of Nicalon Silicon Carbide Fibers Exposed to High-Temperature Gaseous Environments.” *J. Am. Ceram. Soc.* 74 (1991): 666–69.

[88] Tran, H. K., Sawko P. M. “Thermal Degradation Study of Silicon Carbide Threads Developed for Advanced Flexible Thermal Protection Systems.” NASA Technical Memorandum 103952, August (1992).

[89] Vahlas, C., P. Bocabois, and C. Bernard. “Thermal Degradation Mechanisms of Nicalon Fiber: A Thermodynamic Simulation.” *J. Mater. Sci.* 29 (1994): 5839–46.

[90] Emig, G., Wirth R. “Tensile Strength of Silicon Carbide Bundles at Elevated Temperatures.” *Journal of Materials Science* 30.22 (1995): 5813-5818.

[91] Bhatt, R. T., Garg, A., “Thermal Stability of Hi-Nicalon SiC Fiber in Nitrogen and Silicon Environments.” NASA Technical Memorandum 106987, Army Research Laboratory Technical Report ARL-TR-879, 10th International Conference on Composite Materials, August, (1995).

[92] Yun, H.M. and J.A. DiCarlo. “Thermomechanical Behavior of Advanced SiC Fiber Multifilament Tows.” *Cer. Eng. and Sci. Proceedings* 17A (1996): 61-67.

[93] Hochet, N., Berger, M. H., and Bunsell, A. R. “Microstructural Evolution of the Latest Generation of Small-Diameter SiC-Based Fibres Tested at High Temperatures.” *J. Microsc.* 185 (1997): 243–58.

[94] Zhu, Y. T., S. T. Taylor, M. G. Stout, D. P. Butt, and T. C. Lowe. “Kinetics of Thermal, Passive Oxidation of Nicalon Fibers.” *J. Am. Ceram. Soc.* 81 (1998): 655–60.

[95] Sacks, M. D. “Effect of Composition and Heat Treatment Conditions on the Tensile Strength and Creep Resistance of SiC-based Fibers.” *Journal of the European Ceramic Society* 19 (1999): 2305-2315.

[96] He, G., Shibayama, T., Takahashi, H. “Microstructural evolution of Hi-NicalonTM SiC fibers annealed and crept in various oxygen partial pressure atmospheres.” *J. Mater. Sci.* 35 (2000): 1153–1164.

[97] Takeda, M., Urano A., Sakamoto J.-I., Imai Y. “Microstructure and Oxidative Degradation Behavior of Silicon Carbide Fiber Derived from Polycarbosilane.” *J. American Ceramic Society* 83.5 (2000): 1171-76.

[98] Shimoo, T., F. Toyoda, and K. Okamura. “Thermal Stability of Low-Oxygen SiC Fiber (Hi-Nicalon) Subjected to Selected Oxidation Treatment.” *J. Am. Ceram. Soc.* 83.6 (2000): 1450–56.

[99] Youngblood, G.E., C. Lewinsohn, R.H. Jones, H. Kohyama. “Tensile strength and fracture surface characterization of Hi-Nicalon SiC fibres.” *J. Nucl. Mater.* 289 (2001): 1–9.

[100] Kister, G., Harris, B. “Tensile Properties of Heat Treated Nicalon and Hi-Nicalon Fibers.” *Composites: Part A*, Appl. Sci. Manuf., 33 (2002): 435-438.

[101] Sha, J.J., T. Nozawa, J.S. Park, Y. Katoh, A. Kohyama. “Effect of heat treatment on the tensile strength and creep resistance of advanced SiC fibers.” *J. Nucl. Mater.* 329–333 (2004): 592–596.

[102] Li, S.W., Z.D. Feng, H. Mei, L.T. Zhang. “Mechanical and microstructural evolution of Hi-Nicalon trade mark SiC fibers annealed in O2–H2O–Ar atmospheres.” *Mater. Sci. Eng. A* 487 (2008): 424–430.

[103] Yao, R., Feng Z., Chen L., Zhang Y., Zhang B. “Oxidation Behavior of Hi-Nicalon SiC Monofilament Fibers in Air and O2-H2O-Ar Atmospheres.” *Corrosion Science* 57 (2012): 182-191.

[104] Schiefer, H. F., Taft, D. H., Porter, J. W. “Effect of Number of Warp and Filling Yarns per Inch and some other Elements of Construction on the Properties of Cloth.” National Bureau of Stds. *Journal of Research of the National Bureau of Standards* 16, February, (1936).

[105] Shimoo, T., K. Okamura, M. Ito, M. Takeda. “High-temperature stability of low oxygen silicon carbide fiber heat-treated under different atmosphere.” *J. Mater. Sci.* 35 (2000): 3733–3739.

[106] Shimoo, T., K. Okamura, Y. Morisada. “Active-to-passive oxidation transition for polycarbosilane-derived silicon carbide fibers heated in Ar–O2 gas mixtures.” *J. Mater. Sci.* 37 (2002): 1793–1800.

[107] Ervin, Guy Jr. “Oxidation Behavior of Silicon Carbide.” *Journal of the American Ceramic Society* 41.9, September (1958): 347–352. doi: 10.1111/j.1151-2916.1958.tb12932.x

[108] Hinze, J.W., and Graham, H. C. “The Active Oxidation of Si and SiC in the Viscous Gas-Flow Regime.” *Journal of the Electrochemical Society* 123 (1976): 1066–1073. doi:10.1149/1.2132997

[109] Munir, Z., "Synthesis of High Temperature Materials by Self-Propagating Combustion Methods," *Ceramic Bulletin* 67.2 (1988): 342–349.

[110] Adler, Mark, Michael Wright, Charles Campbell, Ian Clark, Walt Engelund, and Tommaso Rivellini. "Entry, Descent, and Landing Roadmap: Technology Area 09." NASA. April (2012).

[111] Braun, R., Manning Robert. "Mars Exploration Entry, Descent and Landing Challenges." IEEE Aerospace Conference. Big Sky, MT, (2006).

[112] Mahaffy, Paul R., Christopher R. Webster, Sushil K. Atreya, Heather Franz, Michael Wong, Pamela G. Conrad, Dan Harpold, John J. Jones, Laurie A. Leshin, Heidi Manning, Tobias Owen, Robert O. Pepin, Steven Squyres, Melissa Trainer, and MSL Science Team, "Abundance and Isotopic Composition of Gases in the Martian Atmosphere from the Curiosity Rover." Science 341.6143, 19 July (2013): 263-266. doi:10.1126/science.1237966

[113] Balat, M., Berjoan, R., Pichelin, G., Rochman, D. "High-temperature oxidation of sintered silicon carbide under pure CO2 at low pressure: active–passive transition." *Applied Surface Science* 133 (1998): 115–123.

[114] Narushima, T., Goto, T., Yokoyama, Y., Takeuchi, M., Iguchi, Y. and Hirai, T. "Active-to-passive transition and bubble formation for high-temperature oxidation of chemically vapor-deposited silicon carbide in CO–CO2 atmosphere." *J. Am. Ceram. Soc.* 77 (1994): 1079.

[115] Shimoo, Toshio, Takehiro Morita and Kiyohito Okamura. “Oxidation of Low-Oxygen Silicon Carbide Fibers (Hi-Nicalon) in Carbon Dioxide.” *Journal of the American Ceramic Society* 84.12 December (2001): 2975–2980. doi: 10.1111/j.1151-2916.2001.tb01123.x

[116] Shimoo, T., K. Okamura, T. Morita. “Thermal stability of low-oxygen silicon carbide fibers (Hi-Nicalon) in carbon monoxide.” *Journal of Materials Science*, 38.14 (2003): 3089-3096.

[117] Balat, M, Berjoan, R. “Oxidation of sintered silicon carbide under microwave-induced CO_2 plasma at high temperature: active–passive transition.” *Applied Surface Science* 161.3–4, 2 July (2000): 434–442.

[118] Bibbo, G. S., Benson, P. M., Pantano, C. G. “Effect of carbon monoxide partial pressure on the high-temperature decomposition of Nicalon fibre.” *Journal of Materials Science* 26.18 September (1991): 5075-5080.

[119] Shimoo, T., T. Morita, K. Okamura. “Oxidation behavior and thermal stability of Si-C-O fibers (Nicalon) in carbon dioxide.” *Journal of Materials Science* 37.15 (2002): 3181-3188.3

[120] Dillman, Robert, Stephen Hughes, John DiNonno, Richard Bodkin, Joseph White, Joseph Del Corso, F. M. Cheatwood. “Planned Flight of the Terrestrial HIAD Orbital Reentry (THOR).” NASA publication

[121] Abeele, David V. "An Efficient Computational Model for Inductively Coupled Air Plasma Flows under Thermal and Chemical Non-Equilibrium." VKI Thesis (2000).

[122] Alfano, Davide. “Spectroscopic Properties of Carbon Fibre Reinforced Silicon Carbide Composites for Aerospace Applications.” Properties and Applications of Silicon Carbide, Prof. Rosario Gerhardt (Ed.), (2011). ISBN: 978-953-307-201-2, InTech, doi: 10.5772/15087

[123] Antill, J. E., and Warburton, J. B. “Active to Passive Transition in the Oxidation of SiC.” *Corros. Sci.* 11.6 (1971): 337–42.

[124] Antill, J.E., and Warburton, J.B. “Oxidation of Silicon and Silicon Carbide in Gaseous Atmospheres at 1000 - 1300°C.” 10-1 to 10-14 in Reactions between Solids and Gases, AGARD CP-52, Advisory Group for Aerospace Research and Development, Paris, France, (1970).

[125] Armani, Clint. “Creep performance of oxide ceramic fiber materials at elevated temperature in air and in steam.” PhD Dissertation, AFIT/DS/ENY/11-02. Graduate School of Engineering and Management, Air Force Institute of Technology (AU), Wright-Patterson AFB OH, March (2011).

[126] Aspinall, S. R. "Principles Governing the Behavior of Solid Materials in Severe High Temperature Environments." Union Carbide Research Institute (1965).

[127] Auweter-Kurtz, M., M. Fertig, G. Herdrich, S. Pidan, and M. Winter. "Advanced In-Flight Sensor Systems for Atmospheric Entry Maneuvres." Paper AIAA-2004- 2169, 37th AIAA Thermophysics Conference, Portland, Oregon, June (2004).

[128] Auweter-Kurtz, M., M. Fertig, G. Herdrich, T. Laux, U. Schöttle, Th. Wegmann, and M. Winter. "Entry Experiments at IRS In-Flight Measurement during Atmospheric Entries." *Space Technol*. 23.4 (2003): 217 – 234.

[129] Balat, M., Czerniak, M., Badie J.M. "Ceramics catalysis evaluation at high temperature using both thermal and chemical approaches." *J. Spacecrafts & Rockets* 36.2, (1999): 273-279.

[130] Balat-Pichelin, M. "Interaction of Reactive Gas Flows and Ceramics at High Temperature – Experimental Methods for the Measurement of Species Recombination during Planetary Entry." In Experiment, Modeling and Simulation of Gas-Surface Interactions for Reactive Flows in Hypersonic Flights. Educational Notes, RTO-EN-AVT-142, Paper 12, Neuilly-sur-Seine, France: RTO. (2007): 12-1 – 12-26. Available from: http://www.rto.nato.int/abstracts.asp.

[131] Balat-Pichelin, M. "Oxidation and Catalycity of Thermal Protection Materials at High Temperature." *High Temperature Material Processes* 8.1 Jan (2004): 161-171. doi: 10.1615/HighTempMatProc.v8.i1.100

[132] Balat-Pichelin, M., Badie, J. M., Berjoan, R., and Boubert, P., "Recombination Coefficient of Atomic Oxygen on Ceramic Materials Under Earth Reentry Conditions by Optical Emission Spectroscopy." *Chemical Physics* 291 (2003): 181-194.

[133] Balat-Pichelin, M., Duqueroie, F. "Heat transfer modelling at high temperature for the evaluation of atomic oxygen recombination on ceramic materials." *Int. J. Thermal Sciences* 40 (2001): 279-287.

[134] Barbante P. F., "Heat Flux Duplication Between Ground Facility and Hypersonic Flight." *J. Thermophysics and Heat Transfer* 23.4 October–December (2009). doi: 10.2514/1.35808

[135] Barbante, P, Chazot, O. "Flight extrapolation of plasma wind tunnel stagnation region flowfield." *J. Thermophysics and Heat Transfer* 20.3 (2006): 493–9.

[136] Barbante, P. F, "Accurate and Efficient Modeling of High Temperature Non-equilibrium Air Flows," PhD Thesis, Univ. Libre de Bruxelles, Bruxelles, (2001).

[137] Barbante, P. F., Degrez, G., and Sarma, G. S. R. "Computation of Nonequilibrium High Temperature Axisymmetric Boundary-Layer Flows," *Journal of Thermophysics and Heat Transfer* 16.4 (2002): 490–497.

[138] Barbante, P.F. "Reacting Flows Simulation with Applications to Ground to Flight Extrapolation." In Experiment, Modeling and Simulation of Gas-Surface

Interactions for Reactive Flows in Hypersonic Flights. Educational Notes RTO-EN-AVT-142, Paper 14. Neuilly-sur-Seine, France: RTO. (2007): 14-1 – 14-20.

[139] Bedra, L., and Balat-Pichelin, M. “Comparative Modeling Study and Experimental Results of Atomic Oxygen Recombination on Silica-Based Surfaces at High-Temperature.” *Aerospace Science and Technology* 9 (2005): 318–328. doi:10.1016/j.ast.2005.01.011

[140] Berger, M. H., Hochet, N., and Bunsell, A. R. “Microstructure and Thermomechanical Stability of a Low-Oxygen Nicalon Fibre.” *J. Microsc.* 177 (1994): 230–41.

[141] Biamino, S., Liedtke, V., Badini, C., Euchberger, G., Huertas Olivares, I., Pavese, M., Fino, P. “Multilayer SiC for thermal protection system of space vehicles: Manufacturing and testing under simulated re-entry conditions.” *Journal of the European Ceramic Society* 28 (2008): 2791–2800

[142] Bodet, R., J. Lamon, N. Jia, and R. E. Tressler. ‘‘Microstructural Stability and Creep Behavior of Si-C-O (Nicalon) Fibers in Carbon Monoxide and Argon Environments.’’ *J. Am. Ceram. Soc.* 79 (1996): 2673–86.

[143] Bodet, R., X. Bourrat, J. Lamon, and R. Naslain, "Tensile Creep Behavior of a Silicon Carbide-Based Fiber with a Low Oxygen Content." *J. of Materials Sci.* 30 (1995): 661-677.

[144] Borell, G. J., and Diller, T. E. "A Convection Calibration Method for Local Heat Flux Gages." *Journal of Heat Transfer* 109.83 (1987): 83-90. Print.

[145] Bottin, B, Carbonaro, M, Zemsch, S, Degrez, G. “Aerothermodynamic design of an inductively coupled plasma wind tunnel.” In: 32nd Thermophysics Conference, Atlanta, GA, USA (1997). AIAA 1997-2498.

[146] Bottin, B, Paris S, Van Der Haegen, V, Carbonaro, M, Novelli, A, Vennemann, D. “The VKI 1.2 MW Plasmatron facility for the thermal testing of TPS materials.” In: 3rd European Workshop on Thermal Protection Systems, Noordwijk, The Nerderlands, (1998).

[147] Bottin, B, Paris, S, Van Der Haegen, V, Carbonaro, M. “Experimental and computational determination of the VKI Plasmatron operating envelope.” In: 30th Plasmadynamic and Lasers Conference, Norfolk, VA, USA, (1999). AIAA 1999-3607.

[148] Bottin, B., Carbonaro, M., Zemsch, S., and Degrez, G., “Aerothermodynamic Design of an Inductively Coupled Plasma Wind Tunnel,” AIAA Paper 1997-2498, June (1997).

[149] Bottin, B., Chazot, O., Carbonaro, M., Van der Haegen, V., Paris, S., “The VKI Plasmatron Characteristics and Performance,” RTO AVT Course on Measurement Techniques for High Enthalpy and Plasma Flows, published in RTO EN-8, Belgium, (1999).

[150] Bottin, B., Vanden Abeele, D. P., Carbonaro, M., Degrez, G., and Sarma, G. S. R. “Thermodynamic and Transport Properties for Inductive Plasma Modeling,” *Journal of Thermophysics and Heat Transfer* 13.3 (1999): 343–350. doi:10.2514/2.6444

[151] Bouillon, E., F. Langlais, R. Pailler, R. Naslain, F. Cruege, P. V. Huong, J. C. Sarthou, A. Deppuech, C. Laffon, P. Lagarde, M. Monthioux, and A. Oberlin. “Conversion Mechanism of a Polycarbosilane Precursor into an SiC-Based Ceramic Material,” *J. Mater. Sci.* 26 (1991): 1333–45.

[152] Boulos, M. I. "The Inductively Coupled R.F. (radio Frequency) Plasma." *Pure & Appl. Chem.* 57.9 (1985): 1321-1352. Print.

[153] Bremen, W., A. Naomidis, and H. Nickel, “Oxidationsverhalten des Pyrolytisch Abgeschiedenen β-SiC unter einer Atmosphare aus CO-CO2-Gasgemischen (Oxidation Behavior of Pyrolytically Deposited β-SiC in an Atmosphere composed of CO-CO2 Gas Mixtures.” *J. Nucl. Mat.* 71 (1977): 56-64.

[154] Bruce III, W. E., Mesick, N. J., Ferlemann, P. G., Siemers III, P. M., Del Corso, J. A., Hughes, S. J., Tobin, S. A., Kardell, M. P. “Aerothermal Ground Testing of Flexible Thermal Protection Systems for Hypersonic Inflatable Aerodynamic Decelerators.” 9th International Planetary Probe Workshop, Toulouse France, June 18-22, (2012).

[155] Butt, Darryl P., Richard E. Tressler and Karl E. Spear. “Corrosion of Sic Materials in N2–H2–CO Gaseous Environments: I, Thermodynamics and

Kinetics of Reactions." *Journal of the American Ceramic Society* 75.12, December (1992): 3257–3267 doi: 10.1111/j.1151-2916.1992.tb04419.x.

[156] Carl, D. A., D. W. Hess, M. A. Lieberman, T. D. Nguyen, and R. Gronsky. "Effects of dc bias on the kinetics and electrical properties of silicon dioxide grown in an electron cyclotron resonance plasma." *J. Appl. Phys.* 70 (1991): 3301. doi: 10.1063/1.349264

[157] Cassell, Alan M., Gregory T. Swanson, R. Keith Johnson, Stephen J. Hughes, F. McNeil Cheatwood. "Overview of the Hypersonic Inflatable Aerodynamic Decelerator Large Article Ground Test Campaign." 21st AIAA Aerodynamic Decelerator Systems Technology Conference and Seminar, Dublin, Ireland, 23 - 26 May (2011). AIAA 2011-2569

[158] Charpentier, L., M. Balat-Pichelin, and F. Audubert, "High Temperature Oxidation of SiC Under Helium With Low-Pressure Oxygen-Part 1: Sintered Alpha-SiC." *J. Eur. Ceram. Soc.* 30.12 (2010): 2653–60.

[159] Charpentier, L., M. Balat-Pichelin, H. Glénat, E. Bêche, E. Laborde, and F. Audubert, "High Temperature Oxidation of SiC Under Helium With Low-Pressure Oxygen. Part 2: CVD Beta-SiC." *J. Eur. Ceram. Soc.* 30.12 (2010): 2661–70.

[160] Chawla, N., J.W. Holmes, and J.F. Mansfield, "Surface Roughness Characterization of Nicalon and Hi-Nicalon Ceramic Fibers by Atomic Force Microscopy." *Materials Characterization* 35 (1995): 199-206.

[161] Childs, P.E., and Wagner Jr., J.B. “Chemical Diffusion in Wustite and Chromium-Doped Manganese Oxide” *Heterogeneous Kinetics at Elevated Temperatures*, ed. G.R. Belton and W.L. Worrell, Plenum Press, New York, (1970): 269-342.

[162] Chollon, G., M. Czerniak, R. Pailler, X. Bourrat, R. Naslain, J. P. Pillot, and R. Cannet. “A Model SiC-Based Fibre with a Low Oxygen Content Prepared from a Polycarbosilane Precursor.” *J. Mater. Sci.* 32 (1997): 893–911.

[163] Chollon, G., Pailler, R., Naslain, R. and Olry, P. “Structure, composition, and mechanical behavior at high temperature of the oxygen-free Hi-Nicalon fiber.” In High-temperature Ceramic-Matrix Composites II: Manufacturing and Materials Development, Ceram. Trans., Vol. 59, ed. A. G. Evans and R. Naslain. American Ceramic Society, Westerville, OH, (1995): 299-302.

[164] Clark, T. J., Arons, R. M., Stamatoff, J. B., and Rabe, J. “Thermal degradation of Nicalon SiC fiber.” *Ceram. Eng. Sci. Proc.* 6.7-8 (1985): 576-578. doi: 10.1002/9780470320280.ch10

[165] Cojean, D., and Monthioux, M. “Unexpected Behaviour of Interfacial Carbon in SiC/SiC Composites during Oxidation,” *Br. Ceram. Trans. J.* 91, (1992): 188–95.

[166] Colin, C., Gélébart, L. “Behaviours of SiC fibers and SiC CVI matrix.” In: 13th European Congress on Composite Materials, Stockholm. (2008).

[167] Copeland, R. A., Pallix, J. B., and Stewart, D. A. “Surface-Catalyzed Production of NO from Recombination of N and O Atoms.” *J. Thermophysics and Heat Transfer* 12.4 (1998): 496 – 499.

[168] Costello, J. A., and Tressler, R. E. “Oxidation of Silicon Carbide Crystals and Ceramics: I, In Dry Oxygen.” *J. Am. Ceram. Soc.* 69 (1986): 674–81.

[169] Degrez, G., Vanden Abeele, D. P., Barbante, P. F., and Bottin, B., “Numerical Simulation of Inductively Coupled Plasma Flows under Chemical Non-equilibrium,” *International Journal of Numerical Methods for Heat and Fluid Flow* 14.4, (2004): 538–558.

[170] Del Corso, J. A., Bruce III, W. E., Liles, K. A., Hughes, S. J. “Thermal Analysis and Testing of Candidate Materials for PAIDAE Inflatable Aeroshell.” 20th AIAA Aerodynamic Decelerator Systems Technology Conference and Seminar, Seattle, May 4-7, (2009).

[171] Deneuve, A., et al, “Catalytic Growth of Silicon Carbide Composite with Nanoscopic Properties and Enhanced Oxidative Resistance as Catalyst Support.” *Applied Catalysis A: General* 385 (2010): 52-61.

[172] DiCarlo, J. A., “Creep limitations of current polycrystalline ceramic fibers.” *Composites Sci. Technol.* 51 (1994): 213-222.

[173] Dicarlo, J.A., Yun, H.M., Hurst, J.B. “Fracture mechanisms for SiC fibers and SiC/SiC composites under stress-rupture conditions at high temperatures.” *Appl. Math. Comput.* 152 (2004): 473–481.

[174] Dougherty, M., W. Owens, J. Meyers, D. Fletcher, “Investigations of Surface-Catalyzed Reactions in a Mars Mixture.” ESA 7th European Aerothermodynamics Symposium, Brugges, Belgium, May (2011).

[175] Eck, J., Balat-Pichelin, M., Charpentier, L., Bêche, E., Audubert, F., “Behavior of SiC at High Temperature Under Helium with Low Oxygen Partial Pressure.” *Journal of the European Ceramic Society* 28 (2008): 2995-3004.

[176] Eckert, H. U. "Analysis of Thermal Induction Plasmas Dominated by Radial Conduction Losses." *Journal of Applied Physics* 41.4 (1970): 1520-528. Print.

[177] Eriksson, G., and Hack, K. “ChemSage - A Corrputer Program for the Calculation of Complex Chemical Equilibria.” *Met. Trans. B* 21B (1990): 1013-23.

[178] Fay, J. A., and Riddell, F. R. “Theory of Stagnation Point Heat Transfer in Dissociated Air.” *Journal of the Aeronautical Sciences* 25.2, (1958): 73-85.

[179] Feng, A., Munir, Z. A. “Field assisted self propagating synthesis of SiC.” *Journal of Applied Physics* 76 (1994): 1927. doi: 10.1063/1.357677

[180] Fertig, M., Frühauf, H.-H. “Detailed Computation of the Aerothermodynamic Loads of the MIRKA Capsule.” Proceedings of the 3rd European Symposium

on Aerothermodynamics for space vehicles held at ESTEC, Noordwijk, The Netherlands, 24-26 November 1998, Publisher: Paris: European Space Agency, Edited by R. A. Harris, ESA SP, 426 (1999): 703. ISBN: 9290927046

[181] Fertig, M., Frühauf, H.-H., Auweter-Kurtz, M. "Modelling of Reactive Processes at SiC-Surfaces in Rarefied Nonequilibrium Airflows." AIAA-Paper 2002-3102, 8th AIAA Joint Thermophysics and Heat Transfer Conference, St. Louis, Missouri, USA, June 24-27, (2002).

[182] Filipuzzi, L., and Naslain, R. "Oxidation Kinetics of SiC-Based Ceramic Fibers." in Materials Science Monograph 68: Advanced Structural Inorganic Composites, Proceedings of the 7th CIMTEC. Edited by P. Vincenzini. Elsevier, Amsterdam, The Netherlands, (1991): 35–46

[183] Fitzer, E., and Ebi, R. "Kinetic Studies on the Oxidation of Silicon Carbide." in Silicon Carbide 1973, ed. R.C. Marshall, J.W. Faust, Jr., and C.E. Ryan, University of South Carolina Press, Columbia, SC, (1974): 320-28

[184] Fletcher, D. G. "Arcjet Flow Properties Determined from Laser-Induced Fluorescence of Atomic Nitrogen." *Appl. Opt. 38* (1999): 1850-1858.

[185] Fletcher, D. G., and Playez, M. "Characterization of Supersonic and Subsonic Plasma Flows." AIAA Paper No. 2006-3294, AIAA Thermophysics Conference, San Francisco, June, (2006): Von Karman Institute for Fluid Dynamics ed. Print.

[186] Fletcher, D. G., Bamford, D. J. “Arcjet flow characterization using laser-induced fluorescence of atomic species.” AIAA-98–2458, June (1998).

[187] Fletcher, D. G., Lutz, A. J., Meyers, J. M., Owens W. P., Dougherty M., “Species and Temperature Gradient Measurements in the Boundary Layer Over ICP Test Samples.” Paper No. 2139316, 7th ESA Symposium on the Aerothermodynamics of Space Vehicles, Brugges, May (2011).

[188] Fletcher, D. G., Thoemel, J., Chazot, O., and Marschall, J., “Realization of a Gas-Surface Interaction Test Case for Model Validation”, AIAA Paper No 2010-1249, 41st AIAA Aerospace Sciences Meeting, Orlando, January (2010).

[189] Forio, P., Lavaire, F., and Lamon, J. ‘‘Delayed Failure at Intermediate Temperatures (600°C–700°C) in Air in Silicon Carbide Multifilament Tows.’’ *J. Am. Ceram. Soc.* 87.5 (2004): 888–93.

[190] Freeman, M. P., and Chase, J. D. "Energy-Transfer Mechanism and Typical Operating Characteristics for the Thermal Rf Plasma Generator." *Journal of Applied Physics* 39.1 (1968): 180-90. Print.

[191] Gasch, M., Ellerby, D., Irby, E., Beckman, S., Gusman, M., Johnson, S. “Processing, properties and arc jet oxidation of hafnium diboride/silicon carbide ultra high temperature ceramics.” Journal of Material Science 39 (2004): 5925 – 5937

[192] Gauthier, W., and Lamon, J. ‘‘Delayed Failure of Hi-Nicalon and Hi-Nicalon S Multifilament Tows and Single Filaments at Intermediate Temperatures (500–800°C).’’ *J. Am. Ceram. Soc.* 92.3 (2009): 702–09.

[193] Gicquel, A., Pietre, S., Amouroux, J. “Ceramic surface evolution (SiC-SiC) during its interaction with a low pressure air plasma. Heat and mass transfer measurements and spectroscopy analysis in boundary-layer.” ISPC-8, Tokyo, paper: P-128 (1987).

[194] Gogotsi, Y., and Yoshimura, M. “Oxidation and Properties Degradation of SiC Fibers below 850°C.” *J. Mater. Sci. Lett.* 13 (1994): 680–83.

[195] Goto, T. “Oxidation resistance of silicon-based ceramics.” *Corr. Eng.* 48 (1999): 169.

[196] Greaves, J.C., and Linnett, J.W. “Recombination of Atoms at Surfaces – Part. 6 – Recombination of Oxygen Atoms on Silica from 20°C to 600°C.” *Transactions of the Faraday Society* 55 (1959): 1355 1361.

[197] Griffiths, David J. “Introduction to Electrodynamics.” 3rd ed. New Delhi: Prentice-Hall of India, (2009): Print.

[198] Grimaud, J. E., and Tillian, D. J., "Heat Transfer Rate Measurement Techniques in Arc-Heated Facilities." NASA. Print.

[199] Gudmundsson, J. T., and Lieberman, M. A. "Magnetic Induction and Plasma Impedance in a Cylindrical Inductive Discharge." *Plasma Sources Sci. Technol* 6 (1997): 540-50. Print.

[200] Gulbransen, F. A., Andrew, K. F., and Brassart, F. A. "The Oxidation of Silicon Carbide at 1150° to 1400°C and at $9x10^{-3}$ to $5x10^{-1}$ Torr Oxygen Pressure." *J. Electrochem. Soc.* 113 (1966): 1311–14.

[201] Gülhan, A., "Application of Pyrometry and IR-Thermography to High Surface Temperature Measurements." Defense Technical Information Center Compilation Part Notice ADPO10751, RTO AVT Course on Measurement Techniques for High Enthalpy and Plasma Flows, Belgium, 25-29 October (1999): published in RTO EN-8.

[202] Gülhan, A., Esser, B., Koch, U., & Hannemann, K. "Mars Entry Simulation in the Arc Heated Facility L2K." Fourth Symposium on Aerothermodynamics for Space Vehicles: co-sponsored by European Space Agency. October 15-18, 2001, Capua, Italy. Edited by R. A. Harris. European Space Agency, ESA SP-487, (2002): 665. ISBN: 92-9092-789-5.

[203] Hald, H., Ullmann, T. "Reentry Flight and Ground Testing Experience with Hot Structures of C/C-SiC Material." 44th AIAA/ASME/ASCE/AHS Structures, Structural Dynamics, and Materials Conference, Norfolk, Virginia, 7-10 April (2003): AIAA 2003-1667.

[204] Hald, H., Winkelmann, P. “Post Mission Analysis of the Heat Shield Experiment CETEX for the EXPRESS capsule.” 48th International Astronautical Congress, Turin, Italy, IAF-97-I.4.01, (1997).

[205] Harder, B. J., Jacobson, N.S., Myers, D.L. “Oxidation Transitions for SiC Part II. Passive-to-Active Transitions.” *J. Am. Ceram. Soc.* 96 (2013): 606-612.

[206] Hatta, Hiroshi, Takuya Aoki, Yasuo Kogo, Toshio Yarii, “High-temperature oxidation behavior of SiC-coated carbon fiber-reinforced carbon matrix composites.” *Composites: Part A* 30 (1999): 515–520.

[207] Helber, Bernd, Balat-Pichelin, M., Panerai, F., Charpentier, L., Chazot, Olivier. “Active/Passive Oxidation Transition and Active Oxidation Kinetics for C/SiC Composites in IXV Re-Entry Conditions.” 7th European Workshop on Thermal Protection Systems and Hot Structures, eds. ESA Communications, published by ESA Communications ESTEC, (2013).

[208] Herdrich, G., Auweter-Kurtz, M., & Endlich, P. “Mars Entry Simulation using the Inductively Heated Plasma Generator IPG4.” Engineering Note. *Journal of Spacecrafts and Rockets* 40.5 (2003): 690-694. http://dx.doi.org/10.2514/2.6894

[209] Herdrich, G., M. Auweter-Kurtz, H. L. Kurtz, T. Laux, M. Winter. “Operational Behavior of the Inductively Heated Plasma Source IPG3 for Re-entry Simulations.” *Journal of Thermophysics and Heat Transfer* 16.3, June-September (2002): 440-449.

[210] Herdrich, G., M. Auweter-Kurtz, M. Fertig, S. Löhle, S. Pidan, and T. Laux. "Oxidation Behavior of Siliconcarbide-Based Materials by Using New Probe Techniques." 37th AIAA Thermophysics Conference Portland, Oregon 28 June - 1 July (2004). AIAA-2004-2173

[211] Herdrich, G., M. Fertig, D. Petkow, A. Steinbeck, S. Fasoulas. "Experimental and numerical techniques to assess catalysis." Progress in Aerospace Sciences, Assessment of Aerothermodynamic Flight Prediction Tools, 48–49, January–February (2012): 27–41.

[212] Herdrich, G., S. Löhle, M. Auweter-Kurtz, P. Endlich, M. Fertig, S. Pidan, E. Schreiber. "IRS Ground-Testing Facilities: Thermal Protection System Development, Code Validation and Flight Experiment Development." AIAA Paper 2004-2596, 24th Aerodynamic Measurement Technology and Ground Testing Conference, OR, June 28 - July 1, (2004).

[213] Herdrich, Georg, Marynowski, Thomas, Dropmann, Michael, Fasoulas, Stefanos. "Mars and Venus Entry Simulation Capabilities of IRS Plasma Wind Tunnel PWK3." *Applied Physics Research* 4.1 (2012): 146.

[214] Hertl, W., and Pultz, W. W. ''SiO2 + SiC Reaction at Elevated Temperatures, Part 2. Effect of Added Gases.'' *Trans. Faraday Soc.* 62 (1966): 2499–504.

[215] Heuer, A. H., and Lou, V. L. K., "Volatility Diagrams for Silica, Silicon Nitride, and Silicon Carbide and Their Application to High-Temperature Decomposition and Oxidation*." J. Am. Ceram. Soc.* 73.10 (1990): 2789–803.

[216] Hightower, T. M., Olivares, R. A., and Philippidis, D. “Thermal Capacitance (Slug) Calorimeter Theory Including Heat Losses and Other Decaying Processes.” NASA Ames Research Center Sept. (2008): Print.

[217] Huger M., Souchard, S., and Gault, C. ‘‘Oxidation of Nicalon SiC Fibers.’’ *J. Mater. Sci. Lett.* 12 (1993): 414–16.

[218] Hughes. S. J, Cheatwood, F. M, Dillman, R. A, Wright, H. S, DelCorso, J. A, Calomino, A. M. “Hypersonic Inflatable Aerodynamic Decelerator (HIAD) Technology Development Overview.” AIAA 2011-2524, ADS Conference, NASA, May (2011).

[219] Hurley, D, Huston, D, Fletcher. D, and Owens, W, "Thermal protection system (TPS) monitoring acoustic emission." Proc. SPIE 7983, 79833P (2011). doi:10.1117/12.882144

[220] Iacono, J., M. Balat-Pichelin, A. Vesel, M. Mozetic. “Catalycity of Ceramics at High Temperature in a CO2 Non Equilibrium Plasma.” STO-MP-AVT-199

[221] Ichikawa, H., T. Hayase, Y. Nagata, H. Teranishi, and T. Ishikawa, “Strength and Structure of SiC Fiber after Exposure at High Temperatures.” *J. Soc. Mater. Sci., Jpn.* 36.407 (1987): 840–46.

[222] Incropera, F. P., and DeWitt, D. P. “Fundamentals of Heat and Mass Transfer.” 5th ed. New York: J. Wiley, (2002). Print.

[223] Irene, E. A., “Silicon oxidation studies: A revised model for thermal oxidation.” *J. Appl. Phys.* 54 (1983): 5416doi: 10.1063/1.332722

[224] Irene, E.A., Ghez, R. “Silicon oxidation studies: the role of H2O.” *J. Electrochem. Soc.* 124 (1977): 1757–1761.

[225] Ishikawa, T. “Recent developments of the SiC fiber nicalon and its composites, including properties of the SiC fiber Hi-Nicalon for ultra-high temperature.” *Composites Sci. Technol.* 51 (1994): 135-144.

[226] Ishikawa, T., S. Kajii, K. Matsunaga, T. Hogami, and Y. Kohtoku, “Microstructure and Properties of Si–Ti–C–O Fiber-Bonded Ceramics.” *J. Soc. Mater. Sci., Jpn*. 45 (1996): 593–98.

[227] Jacobson, N. S., “Carbothermal reduction of silica in high temperature materials.” in Applications of Thermodynamics in the Synthesis and Processing of Materials, P. Nash, B. Sundman (Eds.), The Minerals, Metals & Materials Society, Warrendale, PA, 1995. 19–27.

[228] Jacobson, N., Harder, B., Myers, D. “Oxidation Transitions for SiC Part I. Active-to-Passive Transitions.” *J. Am. Ceram. Soc.* 96 (2013): 838-844.

[229] Jacobson, N.S. “Corrosion of Silicon-Based Ceramics in Combustion Environments.” *J. Am. Ceram. Soc.* 76.1 (1993): 3-28.

[230] Jacobson, N.S., K.N. Lee, and D.S. Fox. “Reactions of Silicon Carbide and Silicon(IV) Oxide at Elevated Temperatures.” *J. Am. Ceram. Soc.* 75.6 (1992): 1603-11.

[231] Jaskowiak, M. H., and DiCarlo, J. A. “Pressure effects on the thermal stability of silicon carbide fibers.” *J. Am. Ceram. Soc.* 72.2 (1989): 192-197.

[232] Jentschke, H., Hirsch, K., Klenge, S., and Schumacher, U. “High Resolution Emission and Absorption Spectroscopy for Erosion Product Analysis in Boundary Plasmas.” *Review of Scientific Instruments* 70.1, January (1999): 336–339.

[233] Kakimoto, K., T. Shimoo, and K. Okamura. “Effect of Surface Oxide Layer on High-Temperature Pyrolysis of Si–Ti–C–O Fiber.” *J. Jpn. Inst. Met.* 57 (1993): 957–63.

[234] Kakimoto, K., T. Shimoo, and K. Okamura. “The Effect of Oxygen Content on Pyrolysis Suppression of Si–Ti–C–O Fibers Coated with Surface Oxide Layers.” *J. Ceram. Soc. Jpn.* 102 (1994): 482–87.

[235] Kakimoto, K., T. Shimoo, and K. Okamura. “The Oxidation Behavior of a Si–Ti–C–O Fiber with a Low Oxygen Content.” *J. Ceram. Soc. Jpn.* 103 (1995): 557–62.

[236] Kawai, Y., N. Konishi, J. Watanabe, and T. Ohmi. “Ultra low temperature growth of high integrity gate oxide films by low energy ion assisted oxidation.” *Appl. Phys. Lett.* 64 (1994): 2223. doi: 10.1063/1.111680

[237] Khachatryan, G. L., A. B. Arutyunyan, S. L. Kharatyan. “Activated Combustion of a Silicon–Carbon Mixture in Nitrogen and SHS of Si3N4–SiC Composite Ceramic Powders and Silicon Carbide.” *Combustion, Explosion, and Shock Waves* 42.5 (2006): 543–548. Translated from Fizika Goreniya i Vzryva.

[238] Kidd, C. T., and Adams Jr, J. C. “Development of a Heat-Flux Sensor for Commonality of Measurement in AEDC Hypersonic Wind Tunnels.” 21st AIAA Aerodynamic Measurement Technology and Ground Testing Conference (2000). Print.

[239] Kim, H. E., and Moorhead, A. J. “Effects of active oxidation on the flexural strength of a-Silicon Carbide.” *J. Am. Ceram. Soc.* 73 (1990): 1868.

[240] Kim, Y., Boudart, M. “Recombination of O, N, and H Atoms on Silica: Kinetics and Mechanism.” *American Chemical Society* Langmuir, 7.12 (1991): 2999-3005.

[241] Kolesnikov, A. F., Pershin, I. S., Vasil’evskii, S. A., and Yakushin, M. I., “Study of Quartz Surface Catalycity in Dissociated Carbon Dioxide Subsonic Flows.” *J. Spacecraft and Rockets* 37.5 (2000): 573 – 579.

[242] Kolesnikov, A. F., Pershin, I. S., Vasil'Evskii, S. A. “Predicting catalycity of Si-based coating and stagnation point heat transfer in high-enthalpy CO2 subsonic flows for the Mars entry conditions.” Proceedings of the International Workshop Planetary Probe Atmospheric Entry and Descent Trajectory Analysis and Science, 6-9 October 2003, Lisbon, Portugal. Edited by A. Wilson. ESA SP-544, Noordwijk, Netherlands: ESA Publications Division, (2004): 77 – 83. ISBN 92-9092-855-7

[243] Kolesnikov, A., Yakushin, M., Vasil'Evskii, S., Pershin, I., Gordeev, A. “Catalysis Effects on Quartz Surface in High-Enthalpy Subsonic Oxygen & Carbon Dioxide Flows.” Aerothermodynamics for space vehicles, Proceedings of the 3rd European Symposium on Aerothermodynamics for space vehicles held at ESTEC, Noordwijk, The Netherlands, 24-26 November 1998, Publisher: Paris: European Space Agency (ESA), Edited by R. A. Harris, ESA SP, 426 (1999). ISBN: 9290927046, p.537

[244] Kolodziej, P., and Stewart, D.A. “Nitrogen Recombination on High-Temperature Reusable Surface Insulation and the Analysis of its Effects on Surface Catalysis.” 22nd AIAA Thermophysics Conference, Honolulu, HI, USA, June (1987).

[245] Korzun, Ashley M., Gregory F. Dubos, Curtis K. Iwata, Benjamin A. Stahl, John J. Quicksall. “A concept for the entry, descent, and landing of high-mass

payloads at Mars." *Acta Astronautica* 66.7 (2010): 1146-1159. doi: 10.1016/j.actaastro.2009.10.003

[246] Krawiec, P., kaskel, S, "Thermal Stability of High Surface Area Silicon Carbide Materials." *Journal of Solid State Chemistry* 179 (2006): 2281-2289.

[247] Kubota, Y., H. Hatta, T. Yoshinaka, Y. Kogo, T. Goto, T. Rong, "Use of Volume Element Methods to Understand Experimental Differences in Active/Passive Transitions and Active Oxidation Rates for SiC." *J. Am. Ceram. Soc.* 96.4 (2013): 1317–1323. doi: 10.1111/jace.12141

[248] Laub, B., and Venkatapathy, E. "Thermal Protection System Technology and Facility Needs for Demanding Future Planetary Missions." International Workshop on Planetary Probe Atmospheric Entry and Descent Trajectory Analysis and Science, (2003).

[249] Laure, S., Auweter-Kurtz, M., Fasoulas, S., and Kurtz, H., "Reentry Simulation Within an Induction Heated Plasma Wind Tunnel." European Space Agency (1995). Print.

[250] Laux, T., Feigl, M., Auweter-Kurtz, M., and Stockle, T. "Estimation of the Surface Catalycity of PVD-Coatings by Simultaneous Heat Flux and LIF Measurements in High Enthalpy Air Flows." AIAA 2000-2364, 34th AIAA Thermophysics Conference, Denver, June (2000).

[251] Le Coustumer, P., M. Monthioux, and A. Oberlin, “Further Studies of the Stability of PCS-Derived Ceramic Fibers at High Temperatures: 1 Oxidation Behaviour.” *Br. Ceram. Trans.* 94 (1995): 177–84.

[252] Lea, A.C. “The Oxidation of Silicon-Carbide Refractory Materials.” *J. Soc. Glass Tech.* 33.150 (1949): 27-50T.

[253] Lees, L. “Laminar Heat Transfer Over Blunt-Nosed Bodies at Hypersonic Flight Speeds.” *Jet Propulsion* 26 February (1956): 259 – 269.

[254] Lepel High Frequency Laboratories. "Instruction Manual for Induction Heating Generator T-50-3-MC-TL." Print.

[255] Lipowitz, J., Barnard, T., Bujalski, D., Rabe, J. A., Zank, G. A., Xu, Y. and Zangvil, A. “Fine-diameter polycrystalline SiC fibers.” *Composites Sci. Technol.* 51 (1994): 167-171.

[256] Lipowitz, J., Rabe, J. A. and Zank, G. A. “Polycrystalline SiC fibers from organosilicon polymers.” *Ceram. Eng. Sci. Proc.* 12.9-10 (1991): 1819-1831.

[257] Liu, D.-M. “Oxidation of Polycrystalline α-Silicon Carbide Ceramic.” *Ceramics International* 23.5 (1997): 425–436. doi:10.1016/S0272-8842(96)00051-X

[258] Löhle, S., Lein, S., Eichhorn, Ch., Herdrich, G., & Winter, M. “Spectroscopic Investigation of an Inductively Heated CO2 Plasma for Mars entry simulation.” *Journal of Technical Physics*, Quarterly, 50.3 (2009): 233-246.

[259] Lu, W.-J., T.P. Chow, A.J. Steckl, W. Katz. “Thermal oxidation of sputtered silicon carbide thin films.” *J. Electrochem. Soc.* 131 (1984): 1907–1914.

[260] Luthra, K. L. ‘‘Some New Perspective on Oxidation of Silicon Carbide and Silicon Nitride.’’ *J. Am. Ceram. Soc.* 74 (1991): 1095–1103.

[261] Lutz, A., J. Meyers, W. Owens, S. Smith, and D. G. Fletcher, “Experimental Analysis of Carbon Nitridation and Oxidation Efficiency with Laser-Induced Fluorescence.” AIAA 2103-024, 51st AIAA Aerospace Sciences Meeting, Dallas (2013).

[262] Maeda, M., K. Nakamura, and T. Ohkubo. “Oxidation of Silicon Carbide in a Wet Atmosphere.” *J. Mater. Sci.* 23 (1988): 3933–38.

[263] Magin, T. E. “A Model for Inductive Plasma Wind Tunnels,” Ph.D. dissertation, Université Libre de Bruxelles, von Karman Institute for Fluid Dynamics, Rhode-Saint-Genèse, Belgium, 2004.

[264] Mah, T., Hecht, N. L., McCullum, D. E., Hoenigman, J. R., Kim, H. M., Katz, A. P. and Lipsitt, H. “Thermal stability of SiC fibres (Nicalon).” *J.Mater. Sci.* 19.4 (1984): 1191-1201.

[265] Maniette, Y., and Oberlin, A. ‘‘TEM Characterization of Some Crude or Air Heat-Treated SiC Nicalon Fibers.’’ *J. Mater. Sci.* 24 (1989): 3361–70.

[266] Marinelli, W.J., “Collisional quenching of atoms and molecules on spacecraft thermal protection surfaces.” AIAA-1988-2667 Thermophysics, Plasmadynamics and Lasers Conference, San Antonio, TX, USA, June (1988).

[267] Marschall, J. “Experimental Determination of Oxygen and Nitrogen Recombination Coefficients at Elevated Temperatures Using Laser-Induced Fluorescence.” AIAA 97-3879, August, (1997).

[268] Marschall, J. and MacLean, M. “Finite-Rate Surface Chemistry Model I: Formulation and Reaction System Examples.” AIAA 2011-3783, 42nd AIAA Thermophysics Conference, Honolulu, June (2011).

[269] Marschall, J., and Fletcher, D. G. “High-Enthalpy Test Environments, Flow Modeling and in situ Diagnostics for Characterizing Ultra-High Temperature Ceramics.” *Journal of the European Ceramic Society* 30.11 (2010): 2323–2336. doi:10.1016/j.jeurceramsoc.2010.01.010

[270] Marschall, J., Copeland, R.A., Hwang, H.H., and Wright, M.J. “Surface Catalysis Experiments on Metal Surfaces in Oxygen and Carbon Monoxide Mixtures.” AIAA-2006-181, January (2006).

[271] Marschall, J., Pejakovic, D. A., Fahrenholtz,W. G., Hilmas, G. E., Zhu, S. M., Ridge, J., Fletcher, D. G., Asma, C. O., and Thomel, J. “Oxidation of ZrB2-SiC Ultrahigh-Temperature Ceramic Composites in Dissociated Air.” *Journal of Thermophysics and Heat Transfer* 23.2 (2009). 267–278. doi:10.2514/1.39970

[272] Mazaheri, Alireza, “HEART Aerothermodynamic Analysis.” NASA TM-20120217568.

[273] Mensing, Arthur E., and Boedeker, L. R. "Theoretical Investigations of R-F Induction Heated Plasmas." NASA (1969). Print.

[274] Merkhouf, A., and Boulos, M. I. "Distributed Energy Analysis for an Integrated Radio Frequency Induction Plasma System." Journal of Applied Physics 33 (2000): 1581-587. Print.

[275] Merkhouf, A., and Boulos, M. I. "Mathematical Model for the Calculation of the Impedance of R.F. Inductively Coupled Plasmas." Plasma Technology Research Center. Print.

[276] Meyers, J. M. “Near Surface CO2 Detection in an Inductively Coupled Plasma Facility Using Diode Laser Absorption”, AIAA 2011-3788, AIAA 42nd Thermophysics Conference, Honolulu, Hawaii, June 2011.

[277] Meyers, J. M., W. P. Owens, and D. G. Fletcher, “Detection of Surface Catalyzed Reaction Products”, NATO AVT-199 Specialists Meeting on Catalytic Gas Surface Interactions, Rhode-St-Genese, Belgium, Oct. 2012.

[278] Meyers, J. M., W. P. Owens, M. Dougherty, A. Lutz, J. Uhl, and D. G. Fletcher, "Laser Spectroscopic Investigation of Surface-Catalyzed Reactions for Mars Exploration Vehicles." AIAA 2010-4915, 27th AIAA Aerodynamic

Measurement Technology and Ground Testing Conference, Chicago, IL, June (2010).

[279] Meyers, J., W. Owens, and D. G. Fletcher. “Detection of Surface Catalyzed Reaction Products in Air Plasmas,” AIAA 2103-3139, 44th AIAA Thermophysics Conference, San Diego, California, June 2013.

[280] Meyers, J., W. Owens, and D. G. Fletcher. “Investigation of Surface-Catalyzed Reaction Efficiencies,” AIAA 2103-3140, 44th AIAA Thermophysics Conference, San Diego, California, June 2013.

[281] Modlin Douglas N., and William A. Tiller, “Effects of Corona-Discharge-Induced Oxygen Ion Beams and Electric Fields on Silicon Oxidation Kinetics: II . Electric Field Effects”, J. Electrochem. Soc. 1985 132(7): 1659-1663

[282] Moeller, H. H. "Tensile testing of ceramic fiber tows." *Ceram. Eng. Sci. Proc.* 6 (1985): 558.

[283] Montaser, Akbar, Izumi Ishii, R. H. Clifford, S. A. Sinex, and S. G. Capar. "Versatile Impedance Matching Network for Inductively Coupled Plasma Spectrometry." *American Chemical Society* (1989): Print.

[284] Moore, Arthur W., and United States. National Aeronautics and Space Administration. “Pyrolytic boron nitride coatings on ceramic yarns and fabrication of insulations.” [microform] Arthur W. Moore Union Carbide Coatings Service Corp. ; National Aeronautics and Space Administration ;

National Technical Information Service, distributor Parma, Ohio, Washington, DC, Springfield, Va, 1992.

[285] Morgan Technical Ceramics. “Comparison of Silicon Carbide Manufacturing Methods.” www.morgantechnicalceramics.com

[286] Morimoto, T. “Potential strength of NicalonTM, Hi NicalonTM, and Hi Nicalon Type STM monofilaments of variable diameters.” *Composites: Part A* 37 (2006): 405-412.

[287] Morscher, G. N. and DiCarlo, J. A. “Creep resistance of advanced SiC fibers.” Proceedings of the NASA 6th Annual HITEMP Review, Cleveland, OH, (1993).

[288] Morscher, G.N., J.A. Dicarlo. “A simple test for thermomechanical evaluation of ceramic fibers” *J. Am. Ceram. Soc.* 75 (1992): 136–140.

[289] Munafò, A., Panesi, M., Jaffe, R., Lani, A., and Magin, T., “Vibrational State to State Kinetics in Expanding and Compressing Nitrogen Flows.” 10th AIAA/ASME Joint Thermophysics and Heat Transfer Conference, AIAA 2010-4335, Chicago, IL, USA, (2010).

[290] Munir, Z.A., “Field effects in self-propagating solid-state synthesis reactions.” *Solid State Ionics* 101-103 (1997): 991-1001.

[291] Munro, R. G., and Dapkunas, S. J. “Corrosion Characteristics of Silicon Carbide and Silicon Nitride.” *J. Res. Natl. Inst. Stand. Technol.* 98.607 (1993).

[292] Muranaka, T., et al. “Superconductivity in carrier-Doped Silicon Carbide.” *Sci Technol. Adv. Mater.* 9 (2008).

[293] Narushima, T., Goto, T. and Hirai, T. “Active to passive transition in the oxidation of CVD-SiC.” In Proceedings of the International Meeting on Advanced Materials. Materials Research Society, Pittsburgh, PA, Symp. G. 4 (1989): 205-300.

[294] Narushima, T., Goto, T. and Hirai, T. “High-temperature passive oxidation of chemically vapor deposited silicon carbide.” *Am. Ceram. Soc.* 72.8 (1989): 1386-1390.

[295] Narushima, T., Goto, T., Hirai, T., and Iguchi, Y. “High-temperature oxidation of silicon carbide and silicon nitride.” *Mater. Trans.* JIM, 38 (1997): 821.

[296] Narushima, T., Goto, T., Iguchi, Y., and Hirai, T. “High-Temperature Active Oxidation of Chemically Vapor-Deposited Silicon Carbide in an Ar-O2 Atmosphere.” *Journal of the American Ceramic Society* 74 (1991): 2583–2586. doi:10.1111/j.1151-2916.1991.tb06803.x

[297] Narushima, T., Goto, T., Yokoyama, Y., Hagiwara, J., Iguchi, Y., and Hirai, T., “High-Temperature Active Oxidation and Active-to-Passive Transition of Chemically Vapor-Deposited Silicon Nitride in N2-O2 and Ar-O2 Atmospheres.” *Journal of the American Ceramic Society* 77.9 (1994): 2369–2375. doi:10.1111/j.1151-2916.1994.tb04607.x

[298] Narushima, T., Goto, T., Yokoyama, Y., Iguchi, Y. and Hirai, T. “High-temperature active oxidation of chemically vapor deposited silicon carbide in CO–CO2 atmosphere.” *J. Am. Ceram. Soc.* 76 (1993): 2521.

[299] Narushima, T., T. Goto, Y. Iguchi, T. Hirai. “High-temperature oxidation of chemically vapor-deposited silicon carbide in wet oxygen at 1823–1923 K.” *J. Am. Ceram. Soc.* 73 (1990): 3580–3584.

[300] Nawaz, A., & Herdrich, G. “Impact of plasma tube wall thickness on power coupling in ICP. Plasma” *Sources Sci. Technol.* 18045018. (2009). http://dx.doi.org/10.1088/0963-0252/18/4/045018

[301] Neuer, G., and G. Jaroma-Weiland. “Spectral and Total Emissivity of High-Temperature Materials.” *International Journal of Thermophysics* 19.3 (1998).

[302] Nickel, K. G. “The Role of Condensed Silicon Monoxide in the Active-To-Passive Oxidation Transition of Silicon Carbide.” *J. Eur. Ceram. Soc.* 9.1 (1992): 3–8.

[303] Nickel, K.G. “Corrosion of non-oxide ceramics.” *Ceram. Int.* 23 (1997): 127–133.

[304] Ogasawara, K., K. Fujii, T. Morito. “Aerothermodynamic Flight Experience in OREX and HYFLEX.” 1st International Symposium on Atmospheric Reentry Vehicles and Systems, Arcachon, France, March, (1999).

[305] Ogbuji, L. U. “Development of Oxide Scale Microstructure on Single Crystal SiC.” *J. Mater. Sci.* 16 (1981): 2753-59.

[306] Ogbuji, L. U. J. T., and Opila, E. J. “A Comparison of the Oxidation Kinetics of SiC and Si3N4.” *J. Electrochem. Soc.* 142.3 (1995): 925-30.

[307] Ogura, Y., and T. Morimoto. “Mass Spectrometric Study of Oxidation of SiC in Low-Pressure Oxygen.” *J. Electrochem. Soc.* 149.4 (2002): J47–52.

[308] Oguraz, Yuzuru, and Morimoto, Tatsuo. “Mass Spectrometric Study of Oxidation of SiC in Low-Pressure Oxygen.” *Journal of The Electrochemical Society* 149.4 (2002): J47-J52. doi: 10.1149/1.1457991]

[309] Okamura, K., M. Sato, T. Seguchi, and S. Kawanishi. “High-Temperature Strength Improvement of Si–C–O Fiber by the Reduction of Oxygen Content.” Proc. 1st Jpn. Int. SAMPE Symp. (1989): 929–34.

[310] Opila, E. J., and Jacobson, N. S. “Oxidation and Corrosion of Ceramics.” in *Ceramics Science and Technology*, 4 (2013). Applications (eds R. Riedel and I.-W. Chen), Wiley-VCH Verlag GmbH & Co. KGaA, Weinheim, Germany. doi: 10.1002/9783527631971.ch01

[311] Opila, E., Serra, J. “Oxidation of Carbon Fiber-Reinforced Silicon Carbide Matrix Composites at Reduced Oxygen Partial Pressures.” *Journal of the American Ceramic Society* 94.7 (2011).

[312] Opila, E.J. “Influence of Alumina Reaction Tube Impurities on the Oxidation of Chemically-Vapor-Deposited Silicon Carbide.” *J. Am. Ceram. Soc.* 78.4 (1995): 1107-10.

[313] Opila, E.J. “Oxidation Kinetics of Chemically Vapor-Deposited Silicon Carbide in Wet Oxygen.” *J. Am. Ceram. Soc.* 77.3 (1994): 730-36.

[314] Opila, E.J. “Variation of the oxidation rate of SiC with water vapor pressure.” *J. Am. Ceram. Soc.* 82 (1999): 625–636.

[315] Opila, E.J., and N.S. Jacobson. “SiO(g) Formation from SiC in Mixed Oxidizing-Reducing Gases.” *Ox. Met.* 44.5-6 (1995): 527-44.

[316] Opila, E.J., and R.E. Hann. “Paralinear Oxidation of CVD SiC in Water Vapor.” *J. Am. Ceram. Soc.* 80.1 (1997): 197-205.

[317] Opila, E.J., D.S. Fox, and N.S. Jacobson. “Mass Spectrometric Identification of Si-O-H(g) Species from the Reaction of Silica with Water Vapor at Atmospheric Pressure.” *J. Am. Ceram. Soc.* 80.4 (1997): 1009-12.

[318] Opila, Elizabeth J., and QuynhGiao N. Nguyen. “Oxidation of Chemically-Vapor-Deposited Silicon Carbide in Carbon Dioxide.” *Journal of the American Ceramic Society* 81.7 July (1998): 1949–1952. doi: 10.1111/j.1151-2916.1998.tb02573.x

[319] Oren, Ruben, and Sorab K. Ghandhi, “Ultraviolet Enhanced Oxidation of Silicon.” *J. Appl. Phys*. 42 (1971): 752. doi: 10.1063/1.1660091

[320] Osawa, Hiroshi, Toshiyuki Suzuki, Hiroki Takayanagi, Masahito Mizuno, and Kazuhisa Fujita, Keisuke Sawada. “Characteristics of O2-Ar Inductively Coupled Plasma Test Flow During Catalytic Recombination Processes.” Journal of Thermophysics and Heat Transfer 27.1 January–March (2013). doi: 10.2514/1.T3722

[321] Owens, W. P., Meyers, J. M., and Fletcher, D. G. “Flexible TPS Surface Catalysis Testing in a 30 kW ICP Torch Facility.” AIAA 2012-3095, 43rd AIAA Thermophysics Conference, New Orleans, June (2012).

[322] Owens, W., J. Meyers, and D. G. Fletcher. “Surface Catalyzed Recombination Efficiencies for Flexible Thermal Protection Materials in Air Plasma.” AIAA 2103-3141, 44th AIAA Thermophysics Conference, San Diego, California, June (2013).

[323] Owens, W., Uhl, J., Dougherty M., Lutz A., Meyers J., Fletcher D. G. “Development of a 30 kW Inductively Coupled Plasma Torch Facility for Aerospace Material Testing.” AIAA Conference, University of Vermont, June (2010).

[324] Panerai, F., Chazot, O., and Helber, B. “Gas/Surface Interaction Study on Ceramic Matrix Composite Thermal Protection System in the VKI Plasmatron Facility.” AIAA Paper 2011-3642, June (2011).

[325] Panerai, F., Helber, B., Chazot, O., and Balat-Pichelin, M. “Reusability Limits of Carbon/Silicon Carbide Heat Shield Materials - Part 1: Surface Temperature

and Radiation Phenomenology." Educational Notes RTO-EN-AVT-199, Paper XX, Specialists Meeting on "Catalytic Gas Surface Interactions," Rhode-Saint-Genèse, Belgium, (2012).

[326] Panerai, F., Helber, Bernd, Chazot, Olivier, Nickel, Klaus, Balat-Pichelin, M. "Aerothermal response of ceramic matrix composites to nitrogen plasma at temperatures above 2000K." *Aerospace Science and Technology* 39 (2014): 1 – 5.

[327] Panerai, F., Helber, Bernd, Chazot, Olivier. "The Reusability Limits of Carbon/Silicon Carbide Heat Shield Materials Part 1: Surface Temperature and Radiation Phenomenology." STO-MP-AVT-199, from Specialists Meeting on Catalytic Gas Surface Interactions, issue 199, eds. RTO/NATO, published by RTO/NATO, (2013).

[328] Panesi, M. "Physical Models for Nonequilibrium Plasma Flow Simulations at High Speed Re-entry Conditions." Ph.D. dissertation, Aeronautics and Aerospace Dept., von Karman Institute for Fluid Dynamics, Rhode-Saint-Genèse, Belgium, 2009.

[329] Pejakovic, D., Marschall, J., Duan, L., and Martin, M. P. "Nitric Oxide Production from Surface Recombination of Oxygen and Nitrogen Atoms." *J. Thermophysics and Heat Transfer* 22.2 (2008): 178 – 186.

[330] Pejakovic, D., Marschall, J., Duan, L., and Martin, M. P., "Direct Detection of NO Produced by High-Temperature Surface-Catalyzed Atom Recombination." *J. Thermophysics and Heat Transfer* 24.3 (2010): 603 – 611.

[331] Peng, Jinhui, Jon Binner, and Steven Bradshaw. "Microwave Initiated Self-Propagating High-Temperature Synthesis of SiC." *Journal of Materials Synthesis and Processing* 9.6 November (2001).

[332] Pettibone, D. W., J. R. Suarez, and A. Gata. "The Effect of Thin Dielectric Films on the Accuracy of Pyrometric Temperature Measurement." MRS Proceedings, 1985 MRS Fall Meeting, Volume 52, 1985, Materials Research Society, (1986). doi:http://dx.doi.org/10.1557/PROC-52-209

[333] Pidan S., M. Auweter-Kurtz, G. Herdrich, M. Fertig. "Determination of Recombination Coefficients and Spectral Emissivities for Thermal Protection Materials." Paper AIAA Thermophysics Conference, USA, Portland, Oregon, (2004).

[334] Playez, M. "Titan Atmosphere Plasma Characterization Using Spectroscopic Measurement Techniques," Ph.D. Dissertation, Ecole Centrale. Paris, Laboratoire D'Energetique Moleculaire et Macroscopique Combustion, June (2006).

[335] Playez, M., Fletcher, D. G., Marschall, J., Fahrenholtz, W. G., Hilmas, G. E., and Zhu, S. M., "Optical Emission Spectroscopy During Plasmatron Testing of

ZrB2-SiC Ultrahigh-Temperature Ceramic Composites," *Journal of Thermophysics and Heat Transfer* 23.2 (2009): 279–285. doi:10.2514/1.39974

[336] Pope, R. B. "Stagnation-Point Convective Heat Transfer in Frozen Boundary Layers." *AIAA Journal* 6.4, April (1968): 619 – 626.

[337] Prewo, K. M., J. J. Brennan, and G. K. Layden. "Fiber-Reinforced Glasses and Glass-Ceramics for High-Performance Applications." *Am. Ceram. Soc. Bull.* 65.2 (1986): 305–14.

[338] Pultz, W. W., and Hertl, W. ''SiO2 + SiC Reaction at Elevated Temperatures, Part 1. Kinetics and Mechanism.'' *Trans. Faraday Soc.* 62 (1966): 2499–504.

[339] Raleigh, Douglas O. "Transport Processes in the Thermal Oxidation of Silicon." *Journal of the Electrochemical Society* August, (1966): 782.

[340] Ramberg, C. E., Cruciani, G., Spear, K. E., Tressler, R. E. and Ramberg, C. F. Jr. "Passive-Oxidation Kinetics of High-Purity Silicon Carbide between 800°C and 1100°C." *J. Am. Ceram. Soc.* 79 (1996): 2897–2911.

[341] Ramberg, C. Eric, Wayne L. Worrell. "Oxygen Transport in Silica at High Temperatures: Implications of Oxidation Kinetics." *J. Am. Ceram. Soc.* 84.11 (2001): 2607–16.

[342] Reed, T. B. "Induction-Coupled Plasma Torch." *Journal of Applied Physics* 32.5 (1961): 821-24. Print.

[343] Revesz, A. G., B. J. Mrstik, H. L. Hughes, and D. McCarthy. “Structure of SiO2 Films on Silicon as Revealed by Oxygen Transport.” *J. Electrochem. Soc.* 133.3 (1986): 586-592.

[344] Riley, Frank L. “Silicon Nitride and Related Materials.” *J. Am. Ceram. Soc.* 83.2 (2000): 245–65.

[345] Rogers, B. R., Z. Song, J. Marschall, N. Queraltó, and C. A. Zorman. “The Effect of Dissociated Oxygen on the Oxidation of Si, Polycrystalline SiC and LPCVD Si3N4.” B. R High Temperature Corrosion and Materials Chemistry V, edited by E. Opila et al., The Electrochemical Society Proceedings Series, PV 2004-16, Pennington, New Jersey, (2004): 268-278.

[346] Rond, C., Bultel, A., Boubert, P., and Cheron, B. G. “Spectroscopic measurements of nonequilibrium CO2 plasma in RF torch.” Chemical Physics 354 (2008): 16-26. http://dx.doi.org/10.1016/j.chemphys.2008.09.006

[347] Sacks, M. D., Scheiffele, G. W., Saleem, M., Staab, G., Williams, T. J., and Morrone, A. A. “Polymer-derived silicon carbide fibers with near-stoichiometric composition and low oxygen content.” In Ceramic Matrix Composites-Advanced High Temperature Structural Materials, Mat. Res. Soc. Symp. Proc., ed. R. A. Lowden,M.K. Ferber, J. R. DiPietro, S. G. DiPietro and K. K. Chawla. Materials Research Society, Pittsburgh, PA, 365 (1995): 3-10.

[348] Sacks, M. D., Scheiffele, G. W., Zhang, L., Yang, Y., and Brennan, J. J. "Polymer-derived SiC-based fibers with high tensile strength and improved creep resistance." *Ceram. Eng. Sci., Proc.* 19.3 (1998): 73-86.

[349] Sahin, P. "Simultaneous Pressure and Heat-Flux Measurement in High-Enthalpy Facilities For Aerospace Applications." Von Karman Institute For Fluid Dynamics [Rhode Saint Genese Belgium] Aug. (2002). Print.

[350] Saito Yoji, "Oxynitridation of silicon by remoteplasma excited nitrogen and oxygen", Appl. Phys. Lett. 68, 800 (1996); doi: 10.1063/1.116537

[351] Sarrette, J. P., Rouffet, B., and Ricard, A. "Determination of Nitrogen Atoms Loss Probabilities on Copper, Aluminium, Alumina, Brass, and Nylon Surfaces." *Plasma Processes and Polymers* 3, (2006): 120-126.

[352] Sata, T., and K. Fujii. "Oxidations of Silicon Nitride, Silicon Oxynitride and Sialon Powders in Atmospheres of O2–N2 System." *Yogyo Kyokaishi* 90 (1982): 110–17

[353] Schafer, S. A., and Lyon, S. A. "New model of the rapid initial oxidation of silicon." *Applied Physics Letters* 47 (1985): 154. doi: 10.1063/1.96246

[354] Schiroky, G. H., Mitchell, T. E. and Heuer, A. H. "Oxidation Behavior of Chemically Vapor-Deposited Silicon Carbide." *Advanced Ceramic Materials* 2.2 (1987): 137-41.

[355] Schiroky, G. H., R. J. Price, and J. E. Sheehan. “Oxidation Characteristics of CVD Silicon Carbide and Silicon Nitride.” GA Technologies Report, GA-A18696 (1986).

[356] Schleicher, R. G., and Barnes, R. M. "Remote Coupling Unit for Radiofrequency Inductively Coupled Plasma Discharges in Spectrochemical Analysis." Analytical Chemistry 47.4 (1975): Print.

[357] Schreck, Ph., C. Vix-Guterl, P. Ehrburger, and J. Lahaye. ‘‘Reactivity and Molecular Structure of Silicon Carbide Fibers Derived from Polycarbosilanes, Part I. Thermal Behavior and Reactivity.’’ *J. Mater. Sci.* 27 (1992): 4237–42.

[358] Scott, C. D. “Measured Catalycities of Various Candidate Space Shuttle Thermal Protection System Coatings at Low Temperatures.” NASA TN D-7113, Manned Spacecraft Center, Houston, Texas, March (1973).

[359] Sepka, S., Chen, Y.-K., Marschall, J., and Copeland, R.A. “Experimental Investigation of Surface Reactions in Carbon Monoxide and Oxygen Mixtures.” *J. Thermophysics and Heat Transfer* 14 (2000): 45-52.

[360] Sha, J.J. “Performance of SiC-based fibers under severe environments and its mechanistic analysis.” Doctoral Thesis, Kyoto Universiy, Kyoto, Japan, 2005.

[361] Sha, J.J., J.S. Park, T. Hinoki, A. Kohyama, J. Yu. “Tensile properties and creep behavior of SiC-based fibers under various oxygen partial pressures.” *Mater. Sci. Forum* 475–479 (2005): 1333–1336.

[362] Sha, J.J., J.S. Park, T. Hinoki, A. Kohyama. “Strength and fracture properties of advanced SiC-based fibers.” *Mech. Compos. Mater.* 42 (2006): 527–534.

[363] Sha, J.J., T. Hinoki, A. Kohyama. “Thermal and mechanical stabilities of Hi-Nicalon SiC fiber under annealing and creep in various oxygen partial pressures.” *Corros. Sci.* 50 (2008): 3132–3138.

[364] Shimoo T., K. Okamura, I. Tsukada, T. Seguchi, “Thermal stability of low-oxygen SiC fibers under different conditions.” *J. Mater. Sci.* 34 (1999): 5623–5631.

[365] Shimoo T., Y. Morisada, K. Okamura. “Oxidation behavior of Si–M–C–O fibers under wide range of oxygen partial pressures.” *J. Mater. Sci.* 37 (2002): 4361–4368.

[366] Shimoo, T., F. Toyoda, and K. Okamura. “Effect of Oxidation Condition on Thermal Stability of Si-C-O Fiber Coated with SiO2 Film.” *J. Ceram. Soc. Jpn.* 107 (1999): 263–69.

[367] Shimoo, T., F. Toyoda, and K. Okamura. “Effect of Oxygen Partial Pressure on Oxidation Rate of Si-C-O Fiber.” *J. Ceram. Soc. Jpn.* 106 (1998): 447–51.

[368] Shimoo, T., F. Toyoda, K. Okamura. “Oxidation kinetics of low-oxygen silicon carbide fiber.” *J. Mater. Sci.* 35 (2000): 3301–3306.

[369] Shimoo, T., H. Chen, and K. Okamura. ‘‘High-Temperature Stability of Nicalon under Ar or O2 Atmosphere.’’ *J. Mater. Sci.* 29 (1994). 456–63.

[370] Shimoo, T., H. Chen, and K. Okamura. “Effect of Thermal History on Pyrolysis of Si–C–O Amorphous Fiber Coated with Oxide Film.” *J. Jpn. Inst. Met.* 57 (1993) 652–58.

[371] Shimoo, T., H. Chen, and K. Okamura. “Mechanism of Oxidation of Si–C–O Fibers,” *J. Ceram. Soc. Jpn.* 100.7 (1992): 929–35.

[372] Shimoo, T., H. Chen, K. Kakimoto, and K. Okamura. “Suppression of Pyrolysis of Si–C–O Fiber with Oxide Film.” *J. Ceram. Soc. Jpn.* 101 (1993): 295–300.

[373] Shimoo, T., H. Takeuchi, K. Okamura. “Thermal stability of polycarbosilane derived silicon carbide fibers under reduced pressures.” *J. Am. Ceram. Soc.* 84 (2001): 566–570.

[374] Shimoo, T., I. Tsukada, M. Narisawa, T. Seguchi, and K. Okamura. “Change in Properties of Polycarbosilane-Derived SiC Fibers.” *J. Ceram. Soc. Jpn.* 105 (1997): 559–63.

[375] Shimoo, T., M. Sugimoto, and K. Okamura. “Effect of Crystallinity on Pyrolytic Rate of Silicon Carbide Fibre.” *Seramikkusu-Ronbun-shi* 98 (1990): 1324–29.

[376] Shimoo, T., M. Sugimoto, and K. Okamura. “Effect of Oxygen on Pyrolysis of SiC Fiber Synthesized from Polycarbosilane.” *J. Ceram. Soc. Jpn.* 100.2 (1992): 157–62.

[377] Shimoo, T., M. Sugimoto, and K. Okamura. “Mechanism of Pyrolysis of Amorphous Silicon Carbide Fibre Obtained from Polycarbosilane as Precursor.” *J. Jpn. Inst. Met.* 54 (1990): 802–808.

[378] Shimoo, T., T. Hayatsu, M. Narisawa, M. Takeda, H. Ichikawa, T. Seguchi, and K. Okamura. “Pyrolysis of Low Oxygen SiC Fiber Prepared by Electron-Irradiation Curing Method.” *J. Ceram. Soc. Jpn.* 101 (1993): 1379–83.

[379] Shimoo, T., T. Hayatsu, M. Takeda, H. Ichikawa, T. Segichi, and K. Okamura. “High-Temperature Decomposition of Low-Oxygen SiC Fiber under N2 Atmosphere.” *J. Ceram. Soc. Jpn.* 102 (1994): 1142–47.

[380] Shimoo, T., T. Hayatsu, M. Takeda, H. Ichikawa, T. Seguchi, and K. Okamura. “Mechanism of Oxidation of Low-Oxygen SiC Fiber Prepared by Electron Radiation Curing Method.” *J. Ceram. Soc. Jpn.* 102 (1994): 617–22.

[381] Shimoo, T., T. Maeda, and K. Okamura. “Pyrolysis of Si–C–O Fiber in Alumina Powder.” *J. Ceram. Soc. Jpn.* 101 (1993): 1274–80.

[382] Simon, G. and Bunsell, A. R. “Mechanical and structural characterization of the Nicalon silicon carbide fibre.” *J. Mater. Sci.* 19.11 (1984): 3649-3657.

[383] Singhal, S. C. “Thermodynamic Analysis of the High-Temperature Stability of Silicon Nitride and Silicon Carbide.” *Ceram. Int.* 2 (1976): 123–30.

[384] Smith, D. M., Moody, H., Wanstall, C., and Terrazas-Salinas, I. "The Design and Use of Calorimeters for Characterization of High Enthalpy Flows in Arc-

Heated Test Facilities." 11th AiAA/AAAF International Conference (2002). Print.

[385] Stackpoole, M., Sepka, and S., Cozmuta, I. “Post-Flight Evaluation of Stardust Sample Return Capsule Forebody Heatshield Material.” 46th AIAA Aerospace Sciences Meeting and Exhibit, AIAA 2008-1202, Reno, Nevada, January (2008).

[386] Starner, K. E. "Use of Thin-Skinned Calorimeters for High Heat Flux Arc-Jet Measurements." *ISA Transactions* 7.3 (1967): 181-86. Print.

[387] Stewart, D. A. “Surface Catalysis and Characterization of Proposed Candidate TPS for Access-to-Space Vehicles.” NASA TM 112206, July (1997).

[388] Stewart, D. A., Rakich, J. V., and Lanfranco, M. J. “Catalytic Surface Effects Experiment on the Space Shuttle.” AIAA 81-1143, June (1981).

[389] Stewart, D.A., “Determination of Surface Catalytic Efficiency for Thermal Protection Materials – Room Temperature to Their Upper Use Limit.” AIAA-Paper 96-1863, 31st AIAA Thermophysics Conference, New Orleans, LA, USA, (1996).

[390] Stewart, D.A., Chen, Y.-K. and Henline, W.D. “Effect of Non-Equilibrium Flow Chemistry and Surface Chemistry on Surface Heating to AFE.” 26th AIAA Thermophysics Conference, Honolulu, HI, USA, (1991).

[391] Strife, J. R., J. J. Brennan, and K. M. Prewo. “Status of Continuous Fiber-Reinforced Ceramic Matrix Composite Processing Technology.” *Ceram. Eng. Sci. Proc.* 11.7– 8 (1990): 871–919.

[392] Sun, Ming, and Isabel K. Lloyd. “Emissivity of Silicon Carbide Composites as a Function of Temperature and Microstructure.” MRS Proceedings, 410, 411 (1995). doi:10.1557/PROC-410-411.

[393] Sutton, G. W. “The Initial Development of Ablation Heat Protection: A Historical Perspective.” *Journal of Spacecraft and Rockets* 19.1 (1982): 3–11.

[394] TAFA Thermal Spray Equipment and Supplies. “Technical Data.” Concord, NH. 4 June 1985. Print.

[395] Takeda M., J. Sakamoto, Y. Imai, H. Ishikawa, and T. Ishikawa. “Properties of Stoichiometric Silicon Carbide Fiber Derived from Polycarbosilane.” *Cer. Eng. and Sci. Proceedings* 15 (1994): 133-141.

[396] Takeda, M., Imai, Y., Ichikawa, H. and Ishikawa, T. “Properties of the low oxygen content SiC fiber on high temperature heat treatment.” *Ceram. Eng. Sci. Proc.* 12.7-8 (1991): 1007-1018.

[397] Takeda, M., Imai, Y., Ichikawa, H., Ishikawa, T., Kasai, N., Suguchi, T. and Okamura, K. “Thermal stability of the low oxygen content silicon carbide fibers derived from polycarbosilane.” *Ceram. Eng. Sci. Proc.* 13.7-8 (1992): 209-217.

[398] Takeda, M., J. Sakamoto, A. Saeki, Y. Imai, and H. Ichikawa. “High Performance Silicon Carbide Fiber Hi-Nicalon for Ceramic Matrix Composites.” *Ceram. Eng. Sci. Proc.* 16.4 –5 (1995): 37–44.

[399] Takeda, M., J. Sakamoto, Y. Imai, H. Ichikawa. “Thermal stability of the low oxygen-content silicon carbide fiber, Hi-Nicalon™.” *Compos. Sci. Technol.* 59 (1999): 813–819.

[400] Takeda, M., Sakamoto, J., Saeki, A. and Ichikawa, H. “Mechanical and structural analysis of silicon carbide fiber Hi-Nicalon Type S.” *Ceram. Eng. Sci. Proc.* 17.4 (1996): 35-43.

[401] Takeda, M., Urano A., Sakamoto J.-I., Imai Y. “Microstructure and Oxidative Degradation Behavior of Silicon Carbide Fiber Hi-Nicalon Type S.” *J. Nuclear Materials* (1998): 1594-1599.

[402] Takeda, M., Y. Imai, H. Ichikawa, T. Ishikawa, N. Kasai, T. Seguchi, and K. Okamura. “Thermomechanical Analysis of the Low Oxygen Silicon Carbide Fibers Derived from Polycarbosilane.” *Ceram. Eng. Sci. Proc.* 14.9 –10 (1993): 540–47.

[403] Takeda, M., Y. Imai, H. Ichikawa, T. Seguchi, and K. Okamura. “Preparation and Properties of the Low Oxygen Silicon Carbide Fibers Derived from Polycarbosilane.” *Ceram. Eng. Sci. Proc.* 12 (1991): 1007–1012.

[404] Takeda. M., A. Urano, J. Sakamoto, Y. Imai. “Microstructure and oxidative degradation behavior of silicon carbide fiber Hi-Nicalon type S.” *J. Nucl. Mater.* 258–363 (1998): 1594–1599.

[405] Taylor, R E, D P. DeWitt, and P E. Johnson. “Spectral Emissivity at High Temperatures.” Ft. Belvoir: Defense Technical Information Center, (1980). Print.

[406] Taylor, S. T., Y. T. Zhu, W. R. Blumenthal, M. G. Stout, D. P. Butt, and T. C. Lowe. “Characterization of Nicalon Fibers with Varying Diameters. Part I: Strength and Fracture Studies.” *Journal of Materials Science* 33.6 (1998): 1465-1473.

[407] Thorpe, M. L., and Scammon, L. W. "Induction Plasma Heating." National Aeronautics and Space Administration (1969). Print.

[408] Tobin, C., and Uhl, J. “Hypersonic Plasma Probe.” The University of Vermont, Burlington, Vermont, 2009.

[409] Toreki, Wm., Batich, C. D., Sacks, M. D., Saleem, M., Choi, G. J. and Morrone, A. A. “Polymer-derived silicon carbide fibers with low oxygen content and improved thermomechanical stability.” *Composites Sci. Technol.* 51 (1994): 145-159.

[410] Toreki, Wm., Choi, G. J., Batich, C. D., Sacks, M. D. and Saleem, M. "Polymer-derived silicon carbide fibers with low oxygen content." Ceram. Eng. Sci. Proc. 13.7-8 (1992): 198-208.

[411] Tran, H. K. "Development of Lightweight Ceramic Ablators and Arc Jet Test Results." NASA TM- 108798, Jan. (1994).

[412] Tumino, G. "IXV: the Intermadiate eXperimental Vehicle." *ESA Bulletin* 128 November (2006).

[413] Turkdogan, E. T. "Selected Thermodynamic Functions." in Physical Chemistry of High-Temperature Technology. Academic Press, New York, 1980. 1–26.

[414] Uhl, J., W. P. Owens, M. J. Dougherty, A. J. Lutz, J .M. Meyers and D. G. Fletcher. "Pyrolysis Simulation in an ICP Torch Facility." AIAA 2011-3618, AIAA 42nd Thermophysics Conference, Honolulu, Hawaii, June (2011).

[415] Vahlas, C., and Laanani, F. "Thermodynamic Study of the Thermal Degradation of SiC-Based Fibers: Influence of SiC Grain Size." *J. Mater. Sci. Lett.* 14 (1995): 1558–61.

[416] Vahlas, C., F. Laanani, and M. Monthioux. "Thermodynamic Approach to the Oxidation of Hi-Nicalon Fiber." *J. Am. Ceram. Soc.* 82 (1999): 2514–16.

[417] Vancrayenest, B. "Heat Flux and Surface Temperature Measurements in High Enthalpy Plasma Flows." von Karmin Institute for Fluid Dynamics, Belgium, (2002).

[418] Vanswijgenhoven Eddy, Konstantza Lambrinou, Martine Wevers, Omer Van Der Biest. “Comparative study of the surface roughness of Nicalon and Tyranno silicon carbide fibres.” *Composites Part A* 29A (1998): 1417–1423.

[419] Vaughn, W. L., and Maahs, H. G., “Active-to-Passive Transition in the Oxidation of Silicon Carbide and Silicon Nitride in Air,” Journal of the American Ceramic Society, Vol. 73, No. 6, 1990, pp. 1540–1543. doi:10.1111/j.1151-2916.1990.tb09793.x

[420] Villegas, M., Sierra, T., Lucas, F., Fernandez, J., Caballero, A. “Oxidation Treatments for SiC Particles and its Compatibility with Glass.” *Journal of the European Ceramic Society* 27 (2007): 861-865.

[421] Walkup, R. E., and S. I. Raider. “In situ measurements of SiO(g) production during dry oxidation of crystalline silicon.” *Appl. Phys. Lett.* 53 (1988): 888-890. doi: 10.1063/1.100105

[422] Wang, J., Zhang, L., Zeng, Q., Vignoles, G. L., and Guette, A. “Theoretical Investigation for the Active-Passive Transition in the Oxidation of Silicon Carbide.” *Journal of the American Ceramic Society* 91.5 (2008): 1665–1673. doi:10.1111/j.1551-2916.2008.02353.x

[423] Wang, P. S., S. M. Hsu, and T. N. Wittberg. “Oxidation Kinetics of Silicon Carbide Whiskers Studied by X-Ray Photoelectron Spectroscopy.” *J. Mater. Sci.* 26 (1991): 1655.

[424] Willey, R.J. “Comparison of Kinetic Models for Atom Recombination on High-Temperature Reusable Surface Insulation.” *Journal of Thermophysics and Heat Transfer* 7.1 (1993): 55-62.

[425] Williams, S., Denny P. “Overview of the Production of Sintered SiC Optics and Sub-Assemblies.” Optical Materials and Structures Technologies II, SPIE Optics and Photonics, San Diego, CA, (2005).

[426] Wolfgang, Bauer, Alexander Moldenhauer, Freidbert Rogge. “Influence of a growing oxide layer on band-emissivities used for optical temperature measurements.” Proc. SPIE 7299, Thermosense XXXI, 72990P, April 22, (2009). doi:10.1117/12.828117

[427] Wolfgang, Bauer, Alexander Moldenhauer. “Emissivities of ceramics for temperature measurements.” Proc. SPIE 5405, Thermosense XXVI, 13 April 12, (2004). doi:10.1117/12.538739

[428] Wolters, D. R., and A. T. A. Zegersvan Duynhoven. “Kinetics of dry oxidation of silicon. I. Space charge limited growth.” *J. Appl. Phys.* 65 (1989): 5126. doi: 10.1063/1.343191

[429] Wright, M. J., Tang, C. Y., Edquist, K. T., Hollis, B. R., Krasa, P., and Campbell, C. A. “A Review of Aerothermal Modeling for Mars Entry Missions.” AIAA-2010-443, 48th AIAA Aerospace Sciences Meeting Including the New Horizons Forum and Aerospace Exposition, Orlando, Florida, Jan. 4-7, (2010).

[430] Wu, S.J., L.F. Cheng, L.T. Zhang, Y.D. Xu, J. Zhang, H. Mei. “Wet oxidation behaviors of Hi-Nicalon fibers.” *Appl. Surf. Sci.* 253 (2006): 1447–1450.

[431] Xu, Y., Zangvil, A., Lipowitz, J., Rabe, J. A. and Zank, G. A. “Microstructure and microchemistry of polymer-derived crystalline SiC fibers.” *J. Am. Ceram. Soc.* 76.12 (1993): 3034-3040.

[432] Yabuta, H., Miyahara, H, Watanabe, M, Hotta, E., and Okino, A. "Design and Evaluation of a Dual Inlet ICP Torch for Low Gas Consumption." *The Royal Society of Chemistry* (2002): 1090-095. Print.

[433] Yajima, S., J. Hayashi, M. Omori, and K. Okamura. “Development of a SiC Fiber with High Tensile Strength.” *Nature* (London), 261 (1976): 683–85.

[434] Yajima, S., K. Okamura, J. Hayashi. “Structural analysis in continuous silicon carbide fiber of high tensile strength.” *Chem. Lett.* 12 (1975): 1209–1212.

[435] Yajima, S., Okamura, K., Hayashi, J. and Omori, M. “Synthesis of continuous SiC fibers with high tensile strength.” *J. Am. Ceram. Soc.* 59 (1976): 324-327.

[436] Yao, R.Q., Y.Y. Wang, Z.D. Feng. “The effect of high-temperature annealing on tensile strength, its mechanism of Hi-Nicalon SiC fibres under inert atmosphere.” *Fatigue Fract. Eng. M* 31 (2008): 777–787.

[437] Yavorskii, I. A., V. I. Elchin, G. G. Gnesin, G. S. Oleinik. “Behavior of nonporous silicon carbide in various gaseous media at high temperatures.” *Soviet Powder Metallurgy and Metal Ceramics* 7.1 January (1968): 59-63.

[438] Young, R. A. “Measurements of the Diffusion Coefficient of Atomic Nitrogen in Molecular Nitrogen and the Catalytic Efficiency of Silver and Copper Oxide Surfaces.” *J. Chemical Physics* 34.4 April (1961): 1295 – 1301.

[439] Yun, H. M., Goldsby, J. C. and DiCarlo, J. A. “Environmental effects on creep and stress-rupture properties of advanced SiC fibers. In High-temperature Ceramic-Matrix Composites II: Manufacturing and Materials Development.” Ceram. Trans., ed. A. G. Evans and R. Naslain. American Ceramic Society, Westerville, OH, 58 (1995): 331-336.

[440] Yun, H.M. and J.A. DiCarlo. "High Temperature Contraction Behavior of Polymer-Derived SiC Fibers." Cer. Eng. and Sci. Proceedings 18A (1997): 135-146.

[441] Yun, H.M. and J.A. DiCarlo. “Comparison of the Tensile, Creep, and Rupture Strength Properties of Stoichiometric SiC Fibers.” (1999). NASA/TM-1999-209284

[442] Yun, H.M., and J.A. DiCarlo, “Thermomechanical Characterization of SiC Fiber Tows and Implications for CMC.” Proceedings of ICCM-12, Paris, France, (1999). NASA/TM – 1999-209283

[443] Zheng, Z., Tressler, R. E. and Spear, K. E. “Oxidation of singlecrystal silicon carbide part I. experimental studies.” *J. Electrochem. Soc.* 137 (1990): 854.

[444] Zoby, E. V, and Sullivan E. M. “Effects of Corner Radius on Stagnation-Point Velocity Gradients on Blunt Axisymmetric Bodies.” *J. Spacecraft and Rockets* 10.3 October (1966): 1567-1568.

APPENDIX A: Additional Information on the ICP Torch

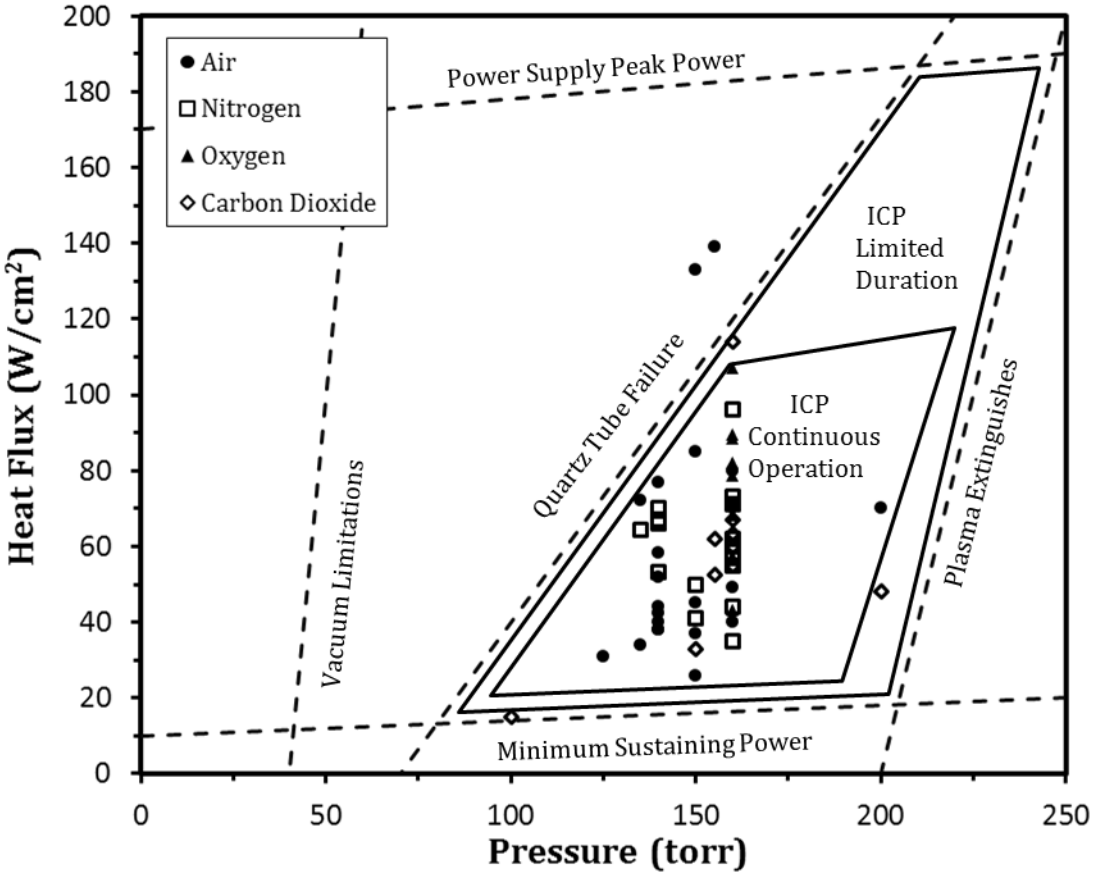

Appendix A.1: Graphical interpretation of the continually expanding ICP Torch operating envelope using slug calorimeter heat flux data at various powers, partial pressures and flow rates

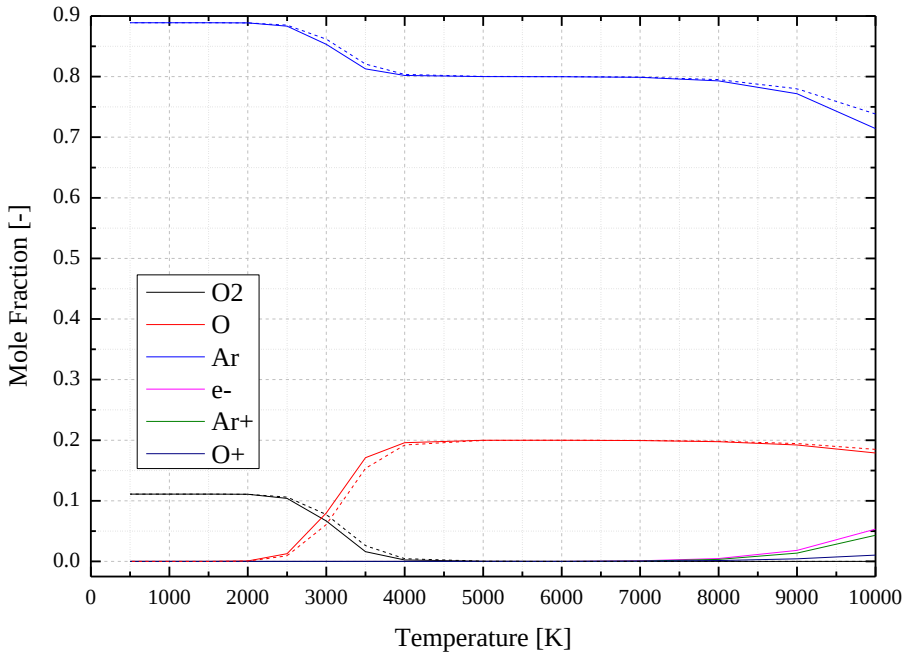

Appendix A.2: Equilibrium chemistry for oxygen/argon plasmas from the NASA CEA code showing complete dissociation of O_2 is possible for operational temperatures and pressures [courtesy J. Meyers]

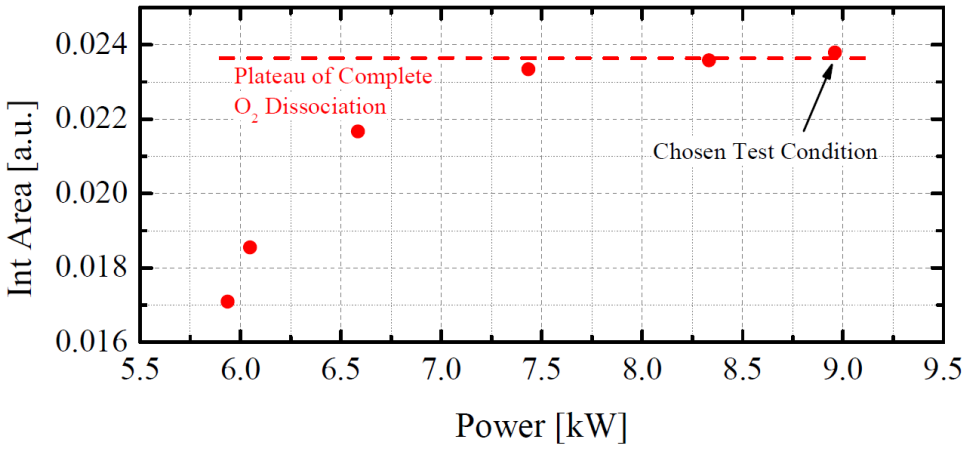

Appendix A.3: Plateau of the integrated O-atom LIF signal suggesting complete dissociation at operating powers above 7.5 kW in an O_2/Ar plasma

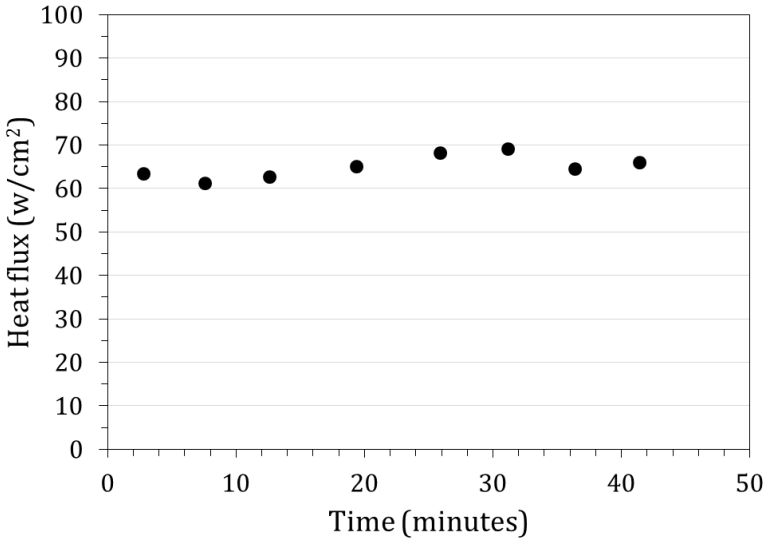

Appendix A.4: Plot of the heat flux vs time in a pure nitrogen plasma showing a heat flux variation of ±5 W/cm^2

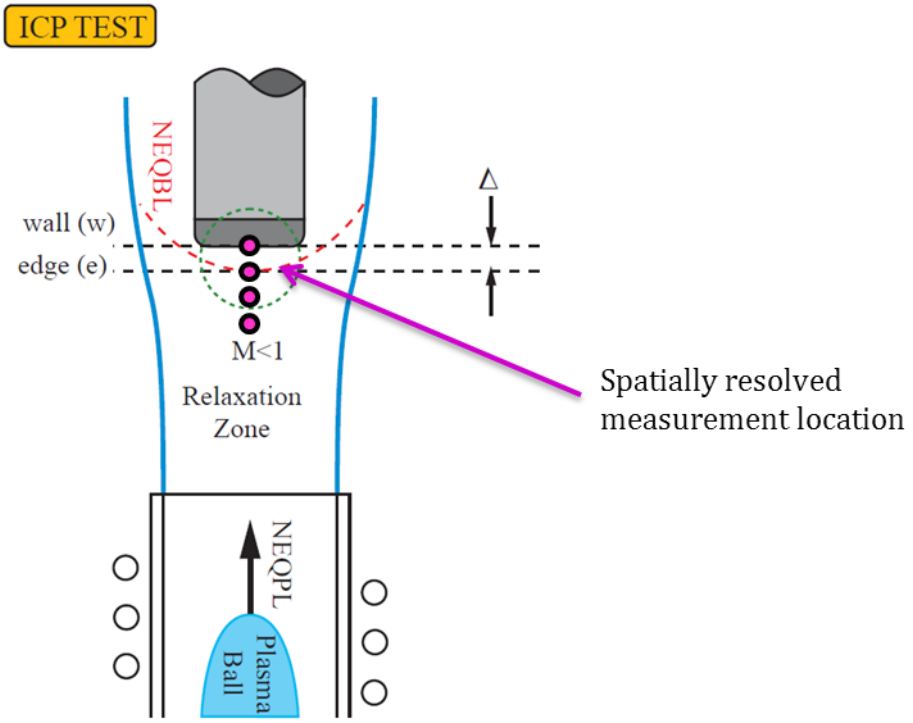

Appendix A.5: Illustration of the LIF measurement locations within the thermal boundary layer to determine catalytic efficiencies (not to scale) [Modified J. Meyers Image]

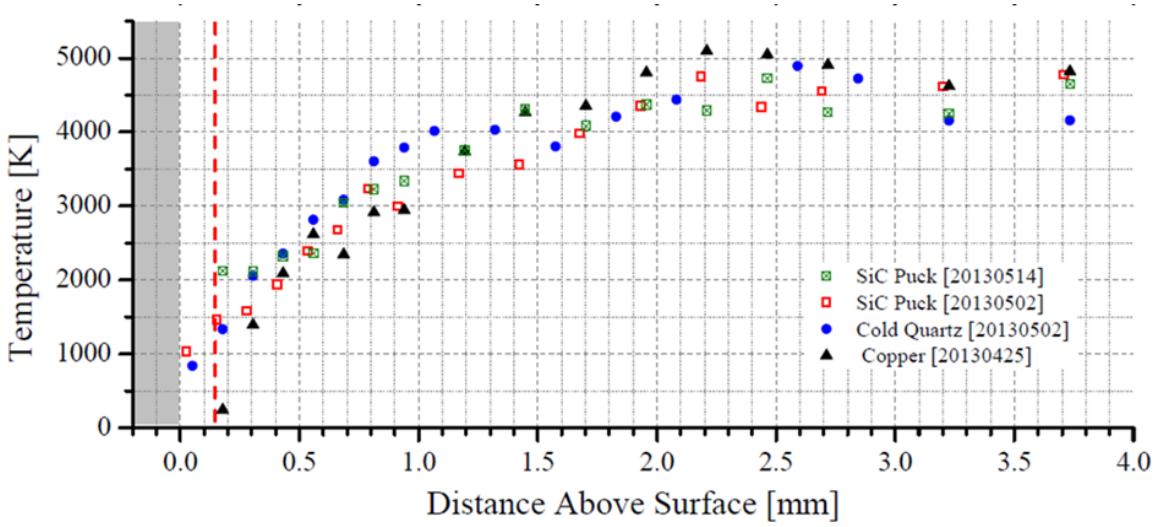

Appendix A.6: Plot of LIF measured temperatures vs distance from the sample surface for different materials showing the thermal boundary layer [Modified J. Meyers Image]

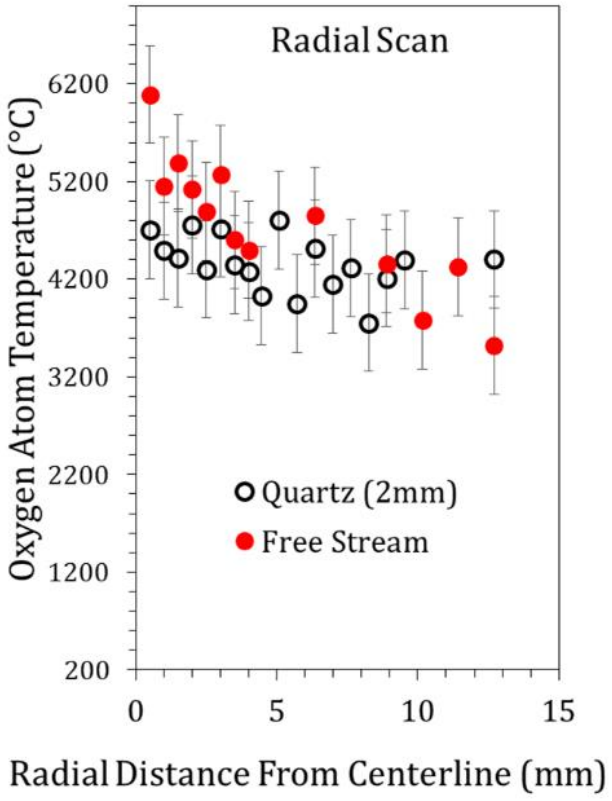

Appendix A.7: Plot of LIF measured O-atom temperatures vs axial distance from the plasma jet centerline taken 2 mm above a quartz sample in an O_2/Ar plasma. Results are compared to the plasma free stream at the same location

APPENDIX B: Additional Information on the Experimental Configuration

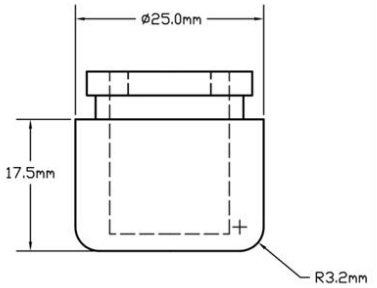

Hot / cold cup geometry.

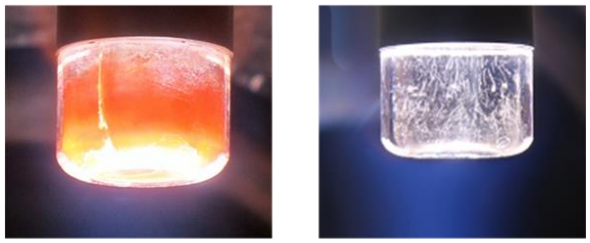

Hot (left) and cold (right) quartz Low γ surfaces

Appendix B.1: Dimensioned drawing of samples requiring water cooling and profile images of a quartz sample with and without water cooling

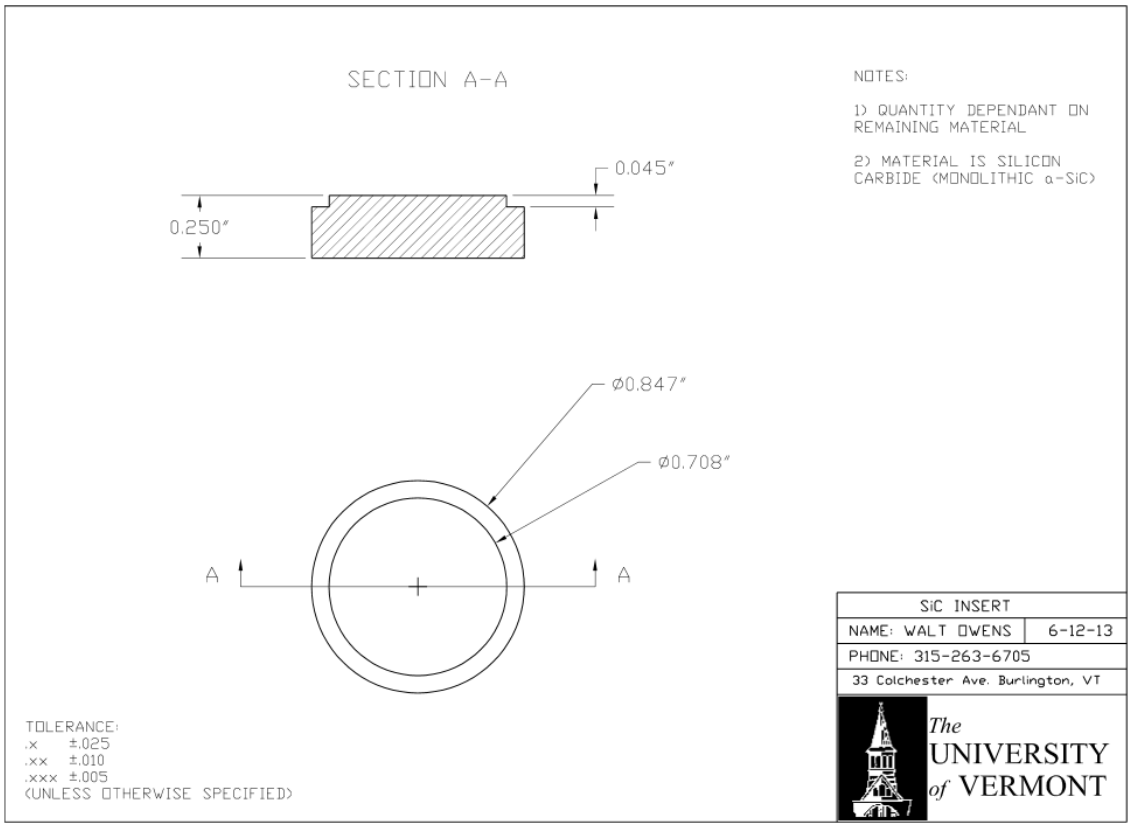

Appendix B.2: Technical drawing of the rigid SiC sample that can be mounted similarly to the SiC fabric coupons

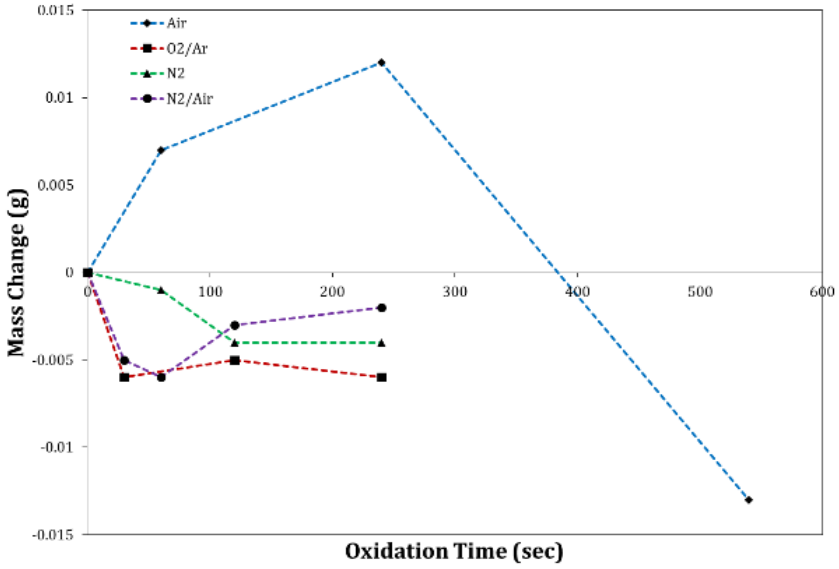

Appendix B.3: Mass change for combined SiC fabric and SiC sleeve after exposure to different plasma conditions

APPENDIX C: Additional Information on Silicon Removal

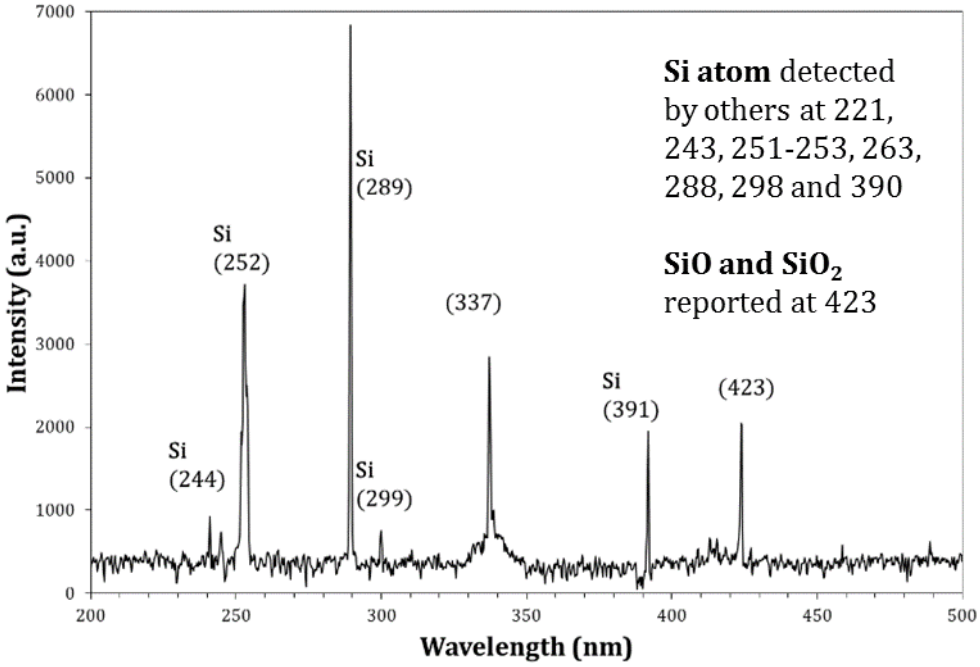

Appendix C.1: Emission data collected within the thermal boundary layer of a hot quartz sample in a nitrogen plasma at the lower detectable range of the spectrometer showing removal of silicon based gas species

APPENDIX D: Additional Information on the Transient Effects of Oxidation

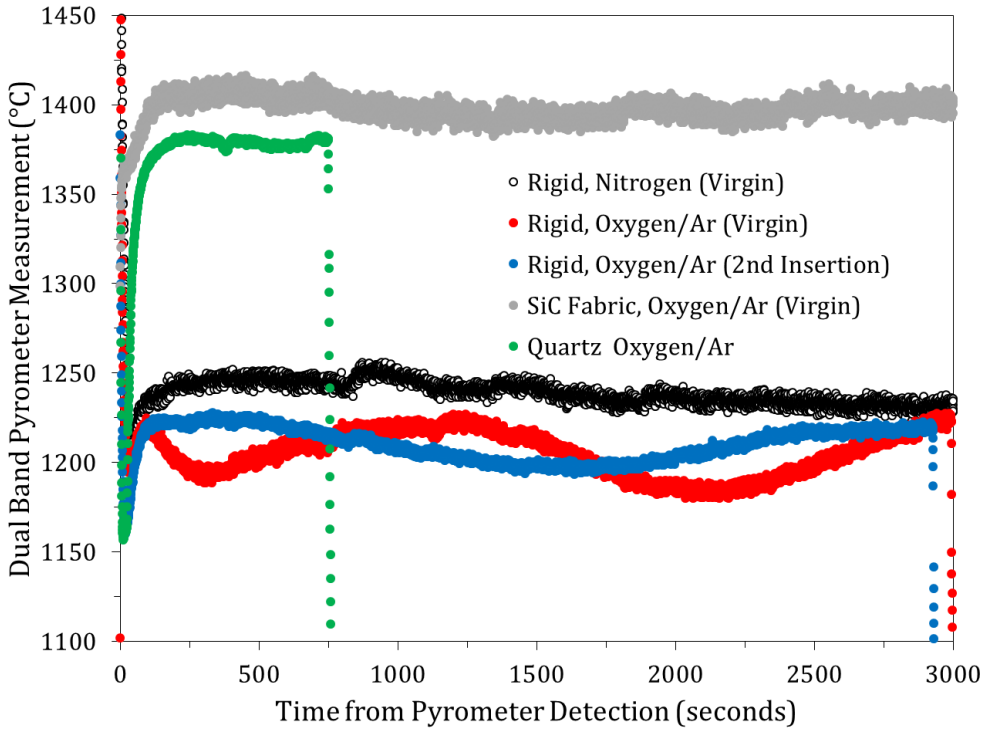

Appendix D.1: Pyrometer measurements showing oscillation at low temperature on the smooth SiC Mushroom samples compared to hot quartz and SiC fabric at the same operating conditions

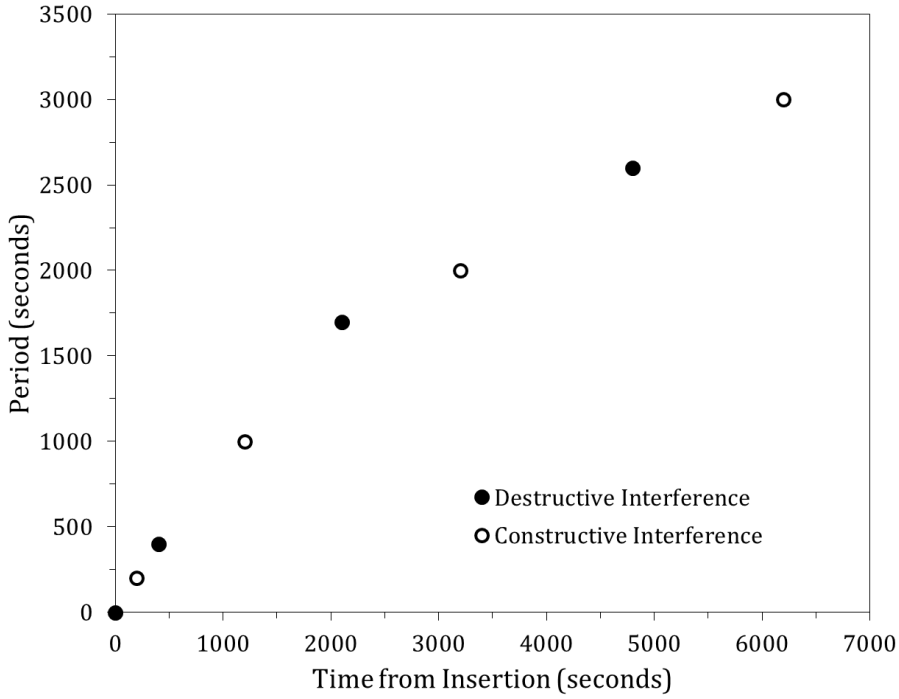

Appendix D.2: Plot showing the period of the peaks and troughs in the pyrometer oscillations on the rigid SiC sample compared to time as seen in Figure D.1. The curve suggests the SiO_2 thickness is continuing to increase at the low temperature tests

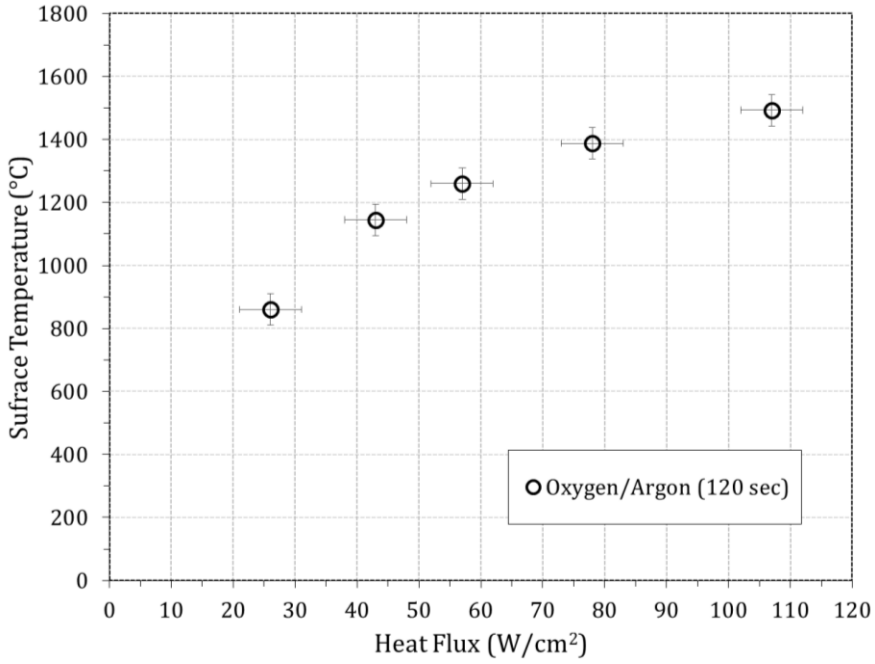

Appendix D.3: plot showing the dependence of SiC fabric coupon surface temperature on the plasma heat flux

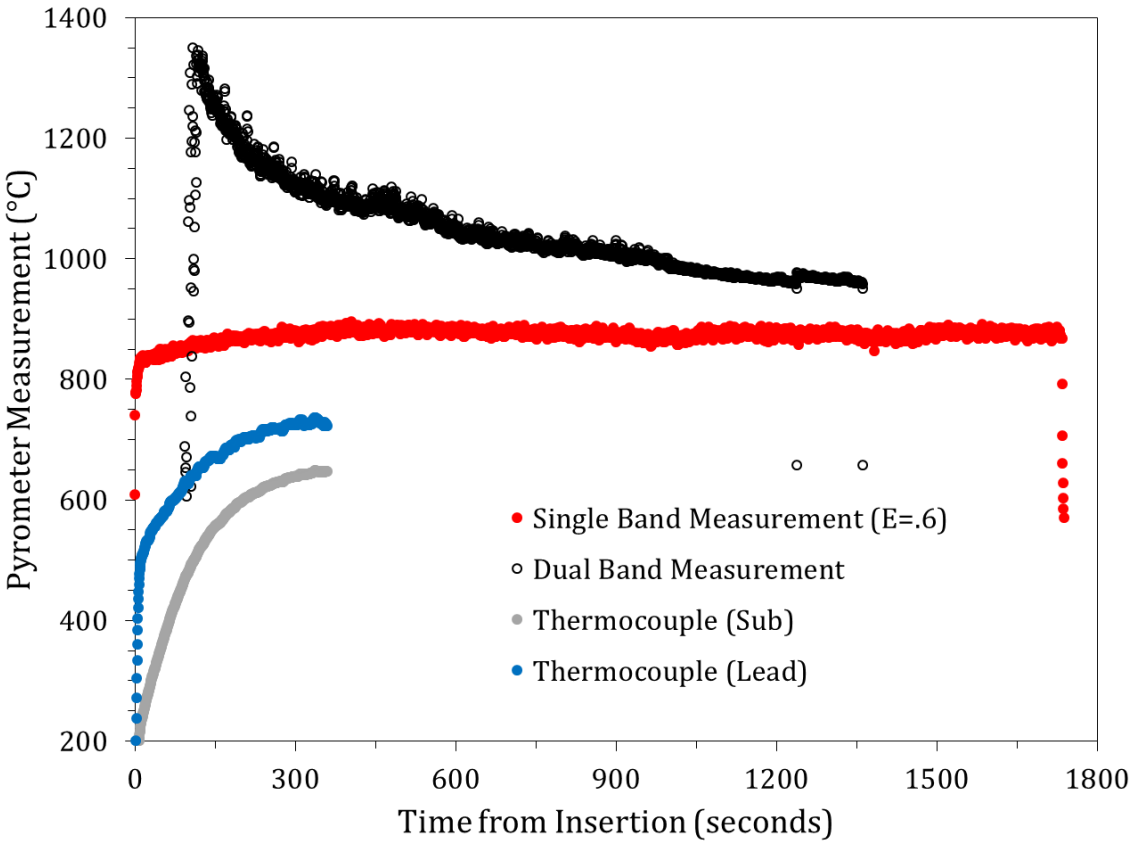

Appendix D.4: Plot showing measurements taken using 1 and 2 color mode on low temperature fabric coupons. Thermocouples were placed behind the lead and sub ply. The unrealistic temperature can be seen when using the 2 color mode at low temperatures

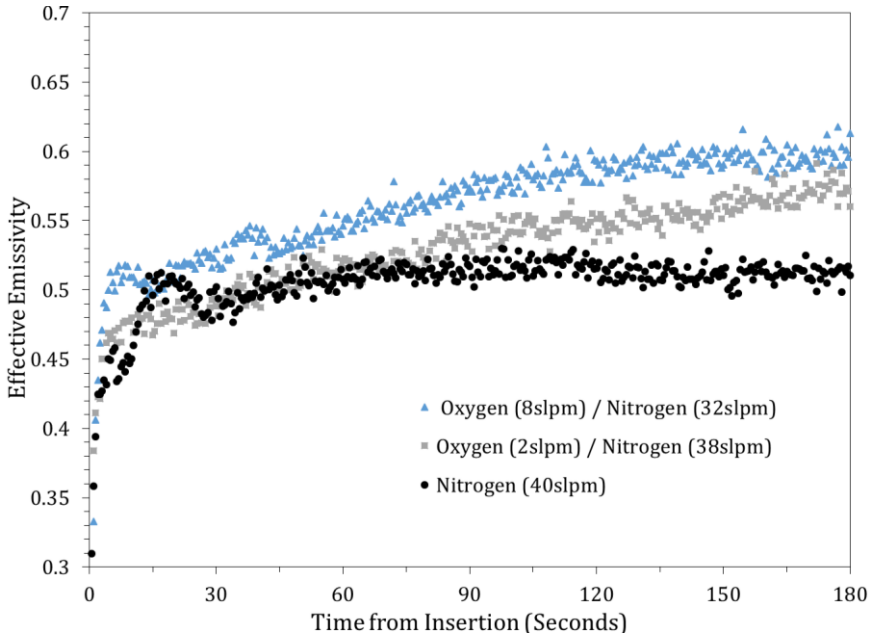

Appendix D.5: Plot showing emissivity vs time for different operating conditions

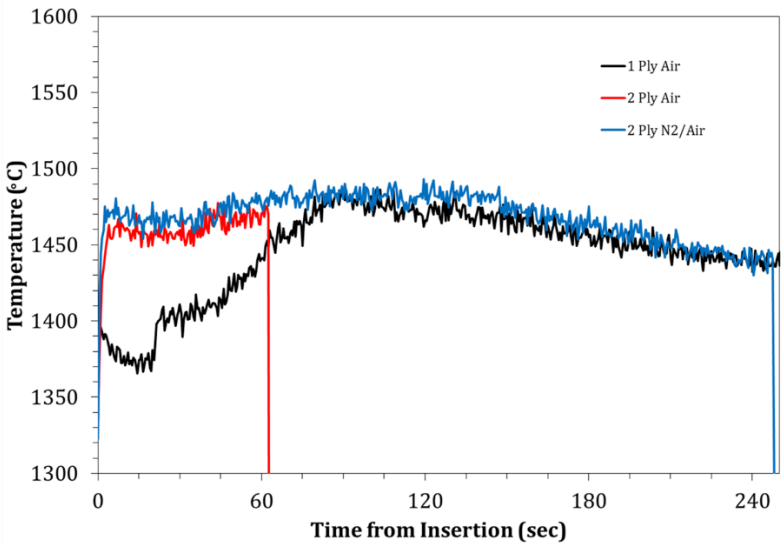

Appendix D.6: Plot comparing pyrometer data taken in 2 color mode for a 1 and 2 ply configuration. Results show the non-opaque nature of the virgin fabric and the strong influence of the sub ply on the pyrometer measurement during the first stages of oxidation.

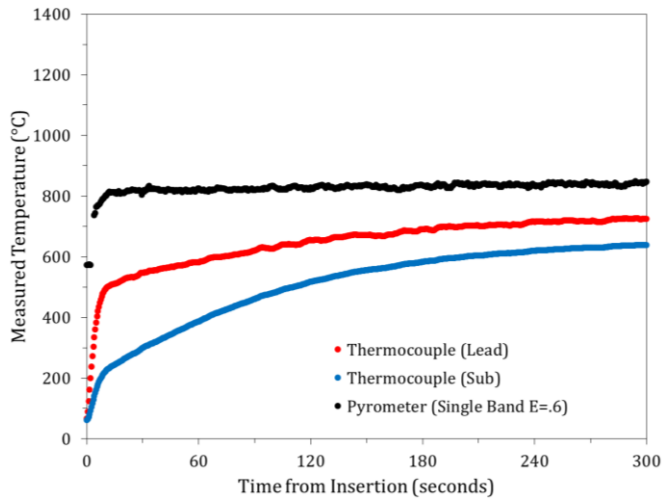

Appendix D.7: Pyrometer and thermocouple data for a low enthalpy plasma test showing the temperature drop through the SiC fabric

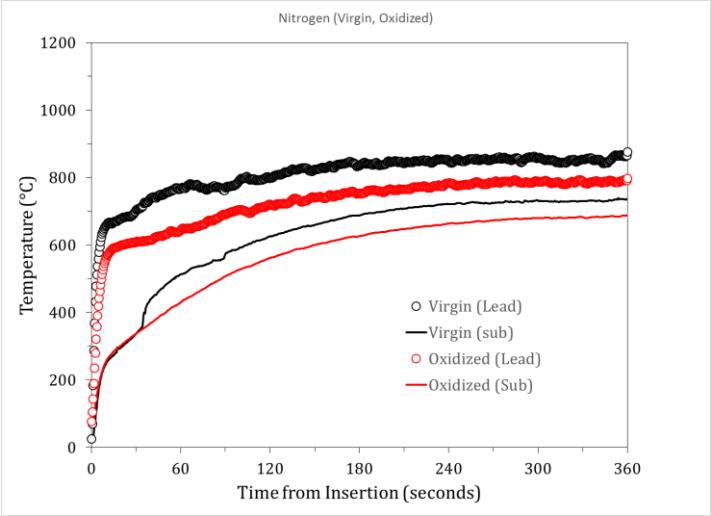

Appendix D.8: Lead and sub ply thermocouple measurements taken during exposure to an O_2/Ar plasma for a virgin and a reinserted coupon showing the typical lower back face temperature on the oxidized sample. The lack of thermal transport data on the contact loss between fibers in the weave architecture after oxidation makes quantitative conduction analysis difficult

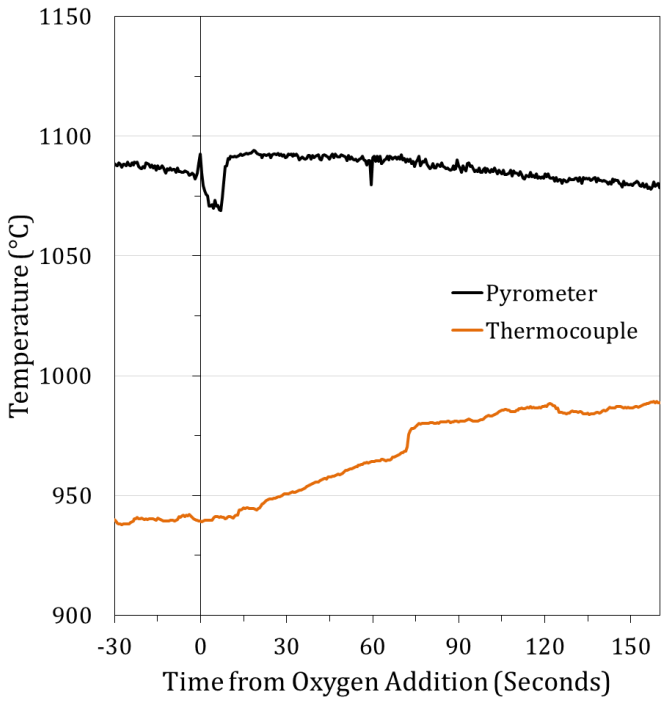

Appendix D.9: Air addition test using argon to achieve lower surface temperatures but no temperature hump was observed in the pyrometer measurement. Conditions were switched from an N_2/Ar to an Air/Ar

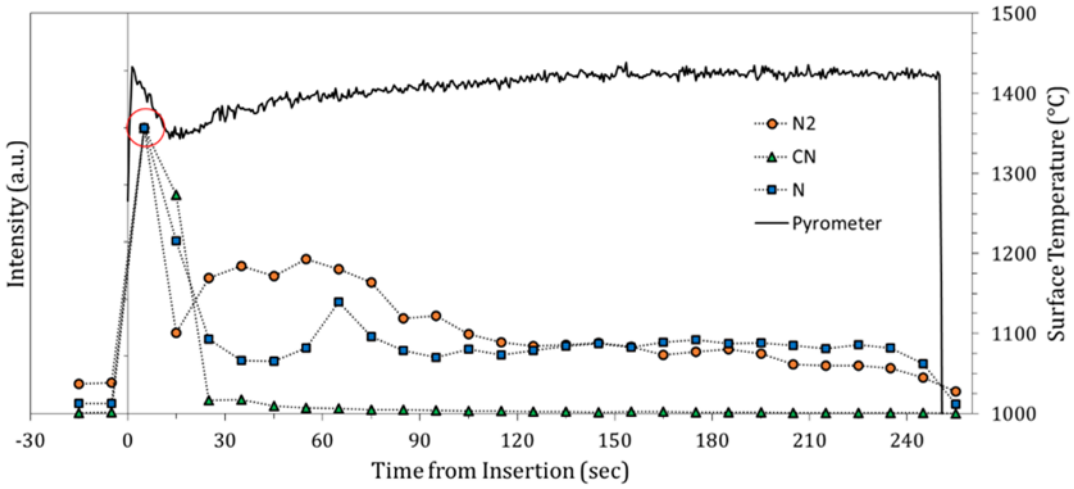

Appendix D.10: Emission tracking of gas species within the thermal boundary layer of a SiC fabric sample exposed to a pure nitrogen plasma showing a change with time

APPENDIX E: Additional Information on the Tensile Tests

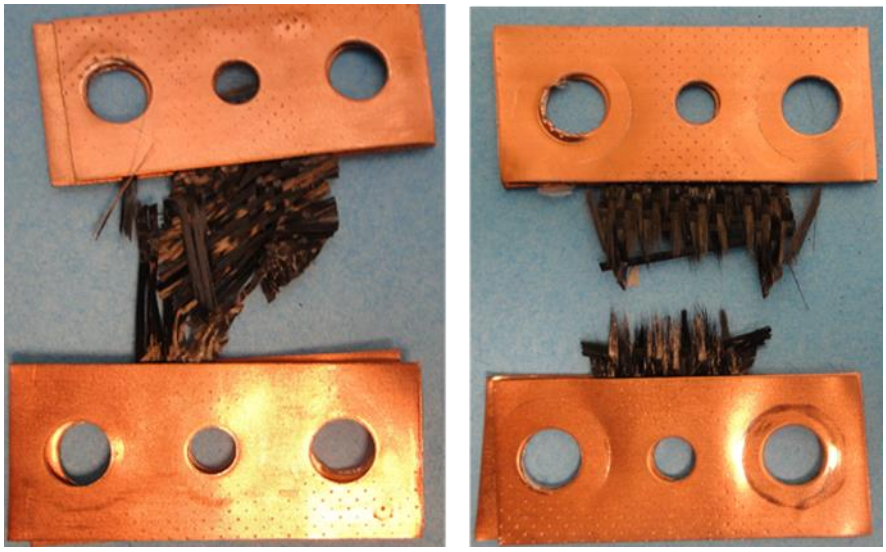

Appendix E.1: Photograph of post tensile test samples showing coupon slippage (left) and a clean break (right)

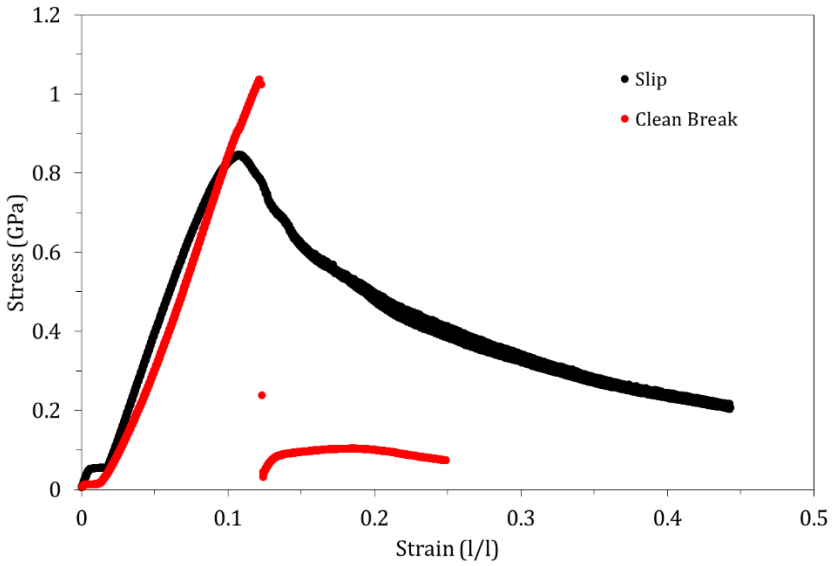

Appendix E.2: Stress vs strain plot of slip and clean break condition. The desired clean break is typical of the instantaneous drop in strength, whereas the slow decrease in strength is due to slippage of the coupon. The settling of the weave architecture can be identified by the initial jog in the stress-strain data. The rise in strength after the clean break is due to the unraveling of the broken fibers through the tightly crimped cross weave

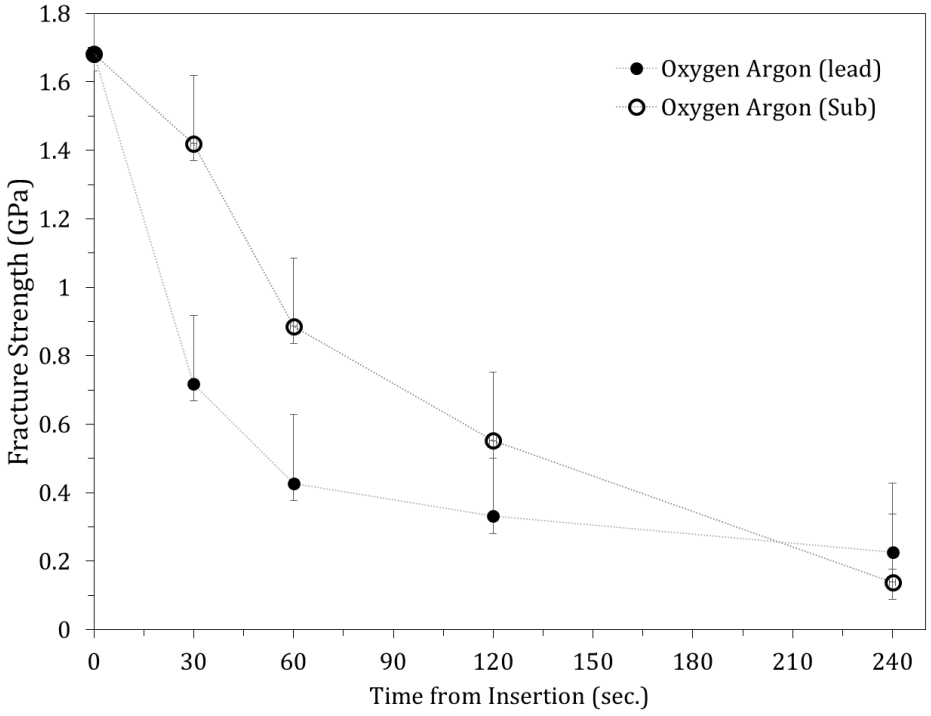

Appendix E.3: Fracture strength of SiC fabric coupons exposed an O_2/Ar plasma for the low power condition seen in Table 5

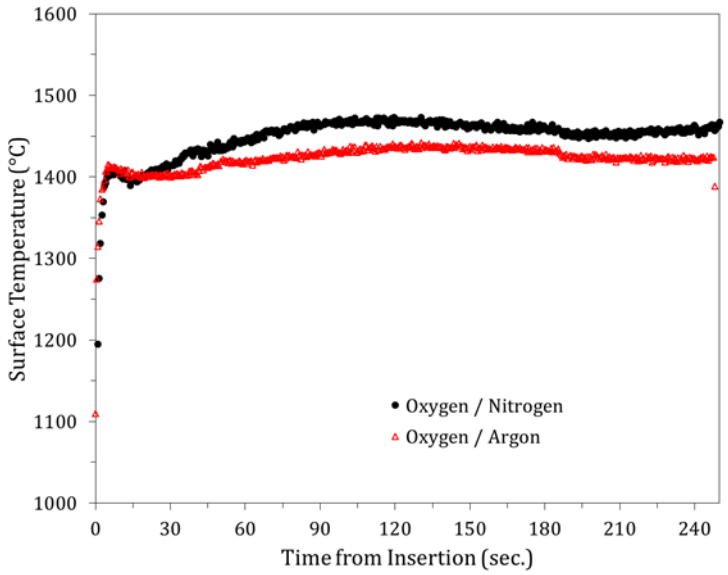

Appendix E.4: Air plasma temperature profile compared to the high power O_2/Ar condition seen in Table 5.

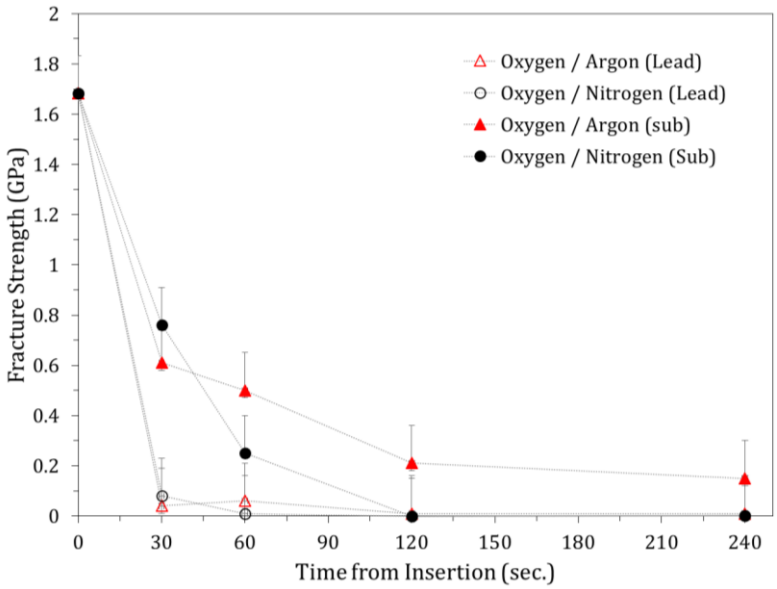

Appendix E.5: Plot of the fracture strength vs time for a high power O_2/Ar and Air test at conditions presented in Table 5 showing the stronger sub ply strength in an O_2/Ar plasma

Investigator	Material	Gas	Gas Flow	Pressure	Furnace Temperature
				torr	°C (±50)
Takeda	Fiber (Hi-Nicalon)	Dry Air	N/A	760	1400
Sha	Fiber (Hi-Nicalon)	Air	Flowing	760	1500
Yao	Fiber (Hi-Nicalon)	Air	N/A	760	1200
Kister	Fiber (Hi-Nicalon)	Air	Flowing	N/A	1200
Shimoo	Fiber (Hi-Nicalon)	Oxygen : Argon	N/A	190 O_2	1500

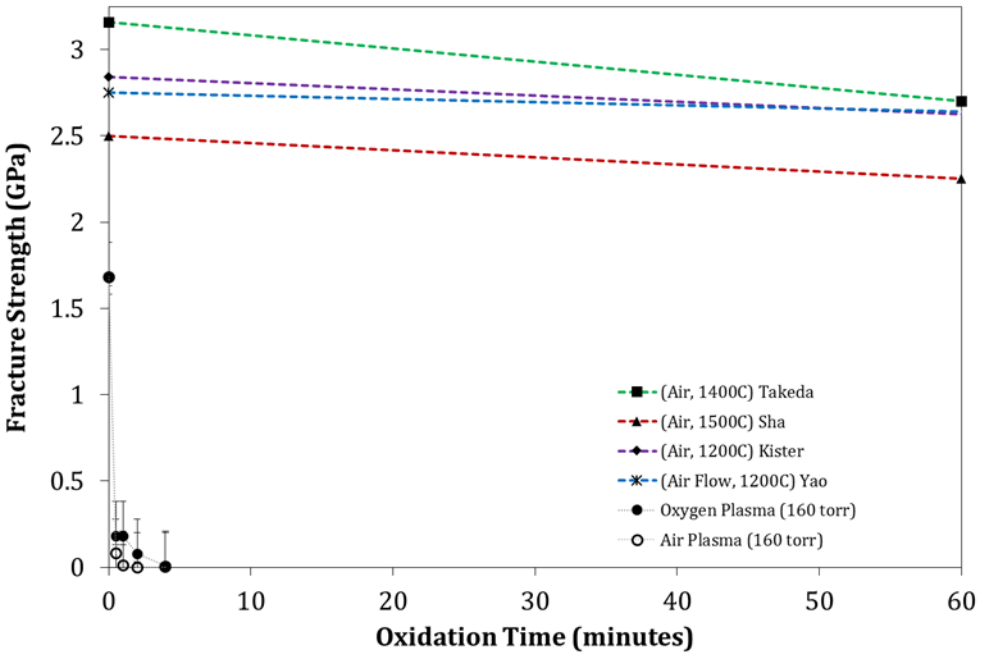

Appendix E.6: Operating conditions of others used to perform tensile tests on single oxidized SiC filaments (Top) and the strength of the single fiber tests strength compared to the SiC coupon results of this study (Bottom). Air plasma tests shows the strength comparison at O_2/N_2 ratios similar to those performed in atmospheric furnace tests on single fibers. The 100% oxygen case at 160 torr matches the oxygen partial pressure at standard atmospheric conditions.

It can be seen that by applying the SiC strength degradation results of typical furnace tests on individual fibers, for atmospheric entry trajectories, minimal strength reduction would be assumed for the relatively short duration of exposure. Therefore, over estimates of the performance might be expected if the influence of fabric weave, dissociation of oxygen and other significant phenomena of hypersonic flight are not accounted for. Unfortunately, the lab currently doesn't have the ability to perform tensile tests on single fibers. Also

separation of the fibers prior to plasma exposure would lead to an inaccurate representation of oxidation dependence on the weave architecture and manual post-test separation of the adhered fibers would be almost impossible.

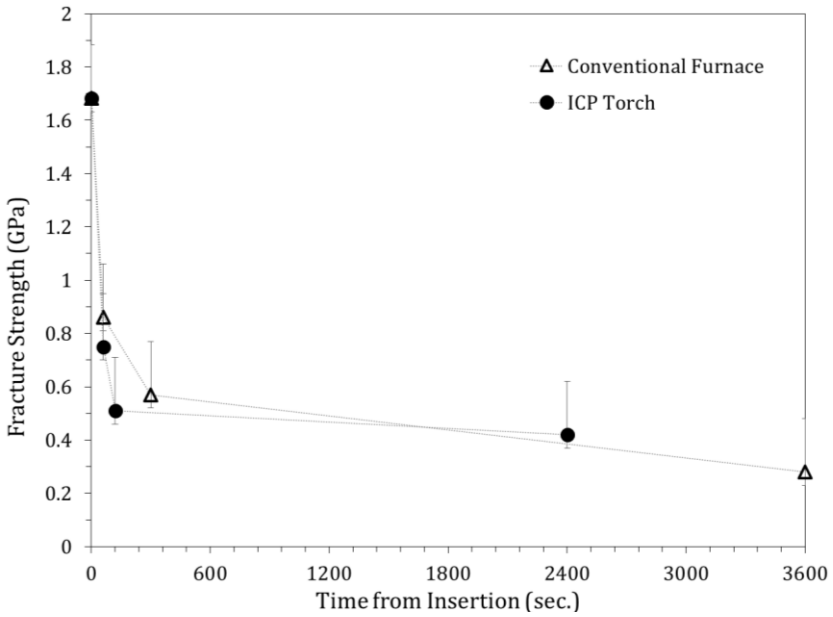

Appendix E.7: Plot showing tensile strength comparisons between samples oxidized in the box oven (oxygen partial pressure of 152 torr) compared to the ICP Torch (oxygen partial pressure to 40 torr) at the maximum box furnace temperature of 935°C. At these low power plasma conditions the dissociation of gases is expected to be extremely low and the predominant impinging species is most likely argon and O_2.

Within the margin of error no significant differences can be seen between the two fracture strength reduction profiles. Surprisingly, at these temperatures the strength reduction appears to be heavily dependent on the surface temperature and not the heating source. Although many other non-negligible variables also exist, therefore a direct comparison cannot lead to any confident conclusions. It is interesting that at similar temperatures and fiber strengths distinctly different morphological features were observed.

Even though there was a much lower oxygen concentration during the ICP air test, the post-tests samples were significantly stiffer compared to the post furnace test samples and displayed the typical iridescence pattern of an oxidized coupon. Whereas the box furnace test remained flexible and had no visual signs of oxidation. The lower temperature tests samples are also expected to have minimal bubble formation or other strength controlling defects in the fibers.

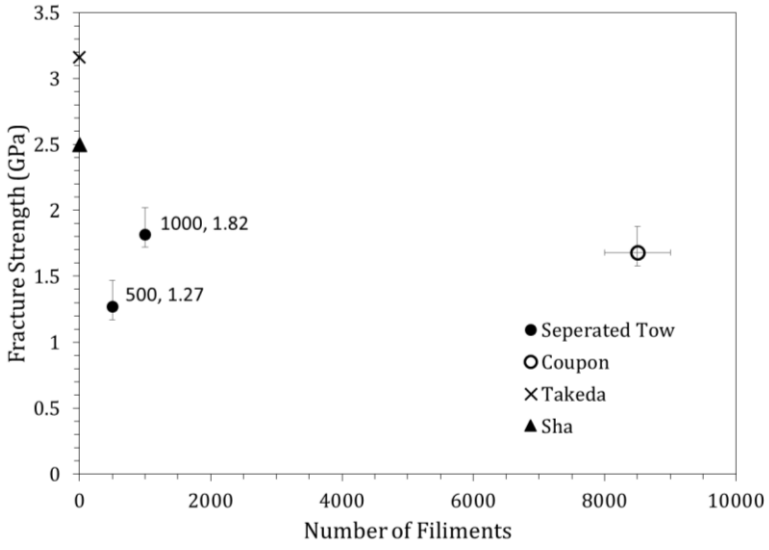

Appendix E.8: Published virgin material strength data of single filaments compared a virgin coupon. Virgin single and multi-tow tensile tests results are also presented

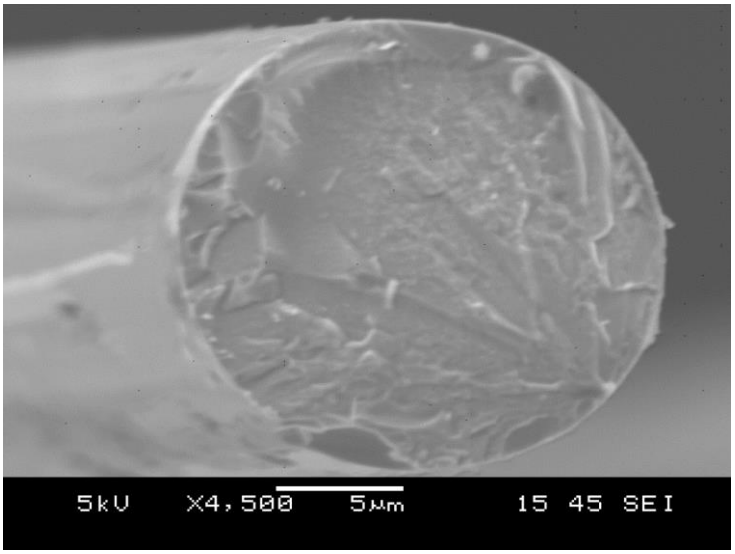

Appendix E.9: SEM image of a fractured virgin fiber end

APPENDIX F: Additional Information on Coupon Failure

Appendix F.1: Profile image of the pre-gashed SiC fabric sample taken during exposure to an air plasma

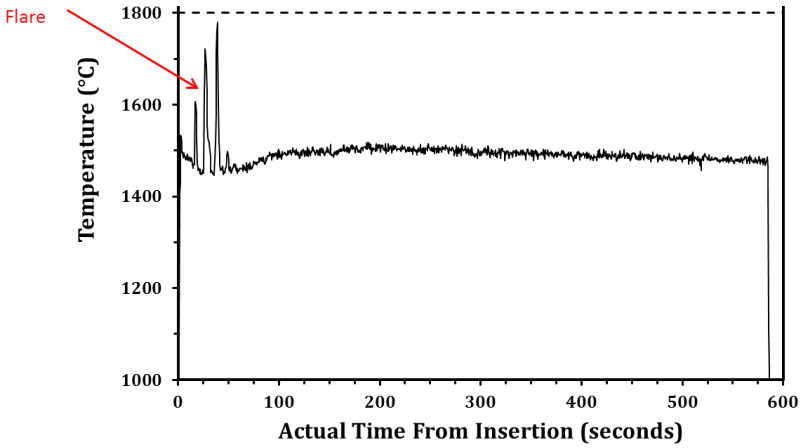

Appendix F.2: Temperature profile taken during the gash test

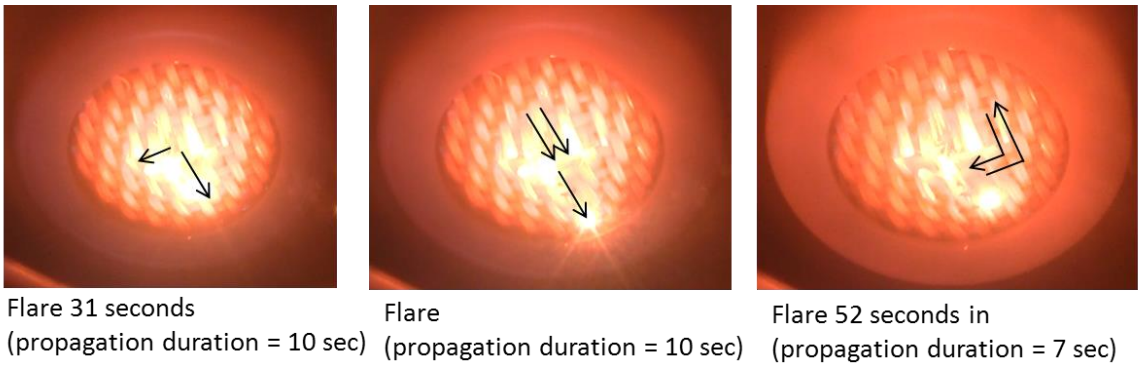

Appendix F.3: Surface image taken during air plasma exposure showing the propagation of flares that were initiated by the gash

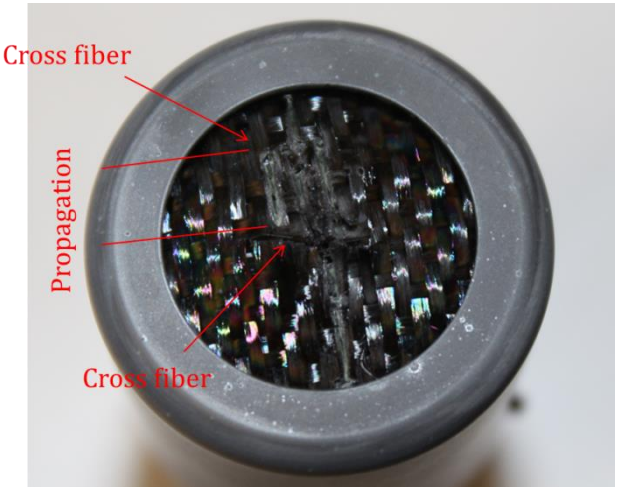

Appendix F.4: Post-test image of the gashed sample showing initiation of flares at the gash

APPENDIX G: Additional Information on CO_2 Plasma Tests

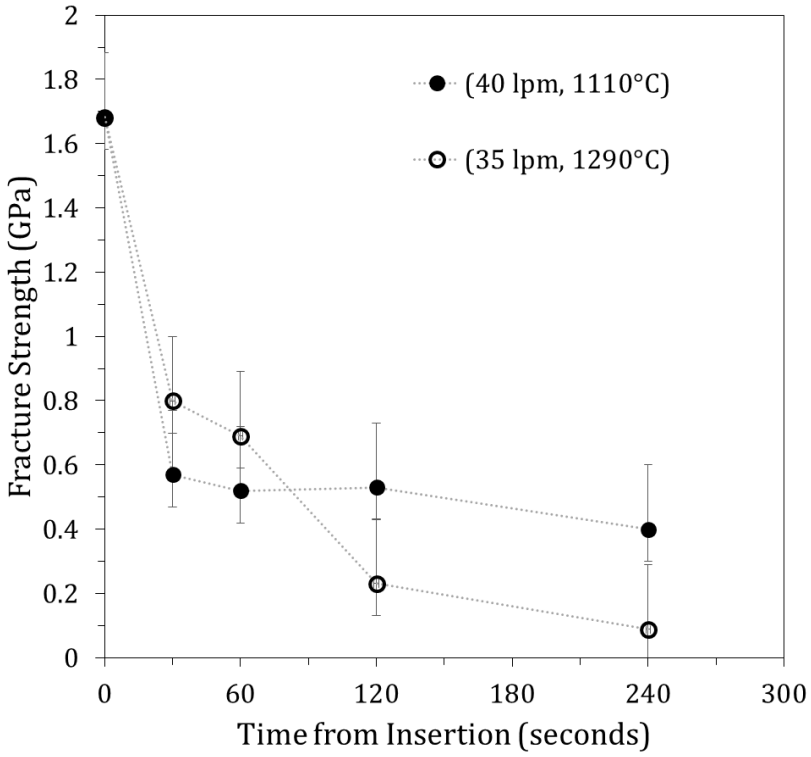

Appendix G.1: Plot showing the tensile strength of SiC fibers after exposure to two different CO_2 conditions. Strength loss was similar to air tests although samples at 1290°C were flexible and had minor flares

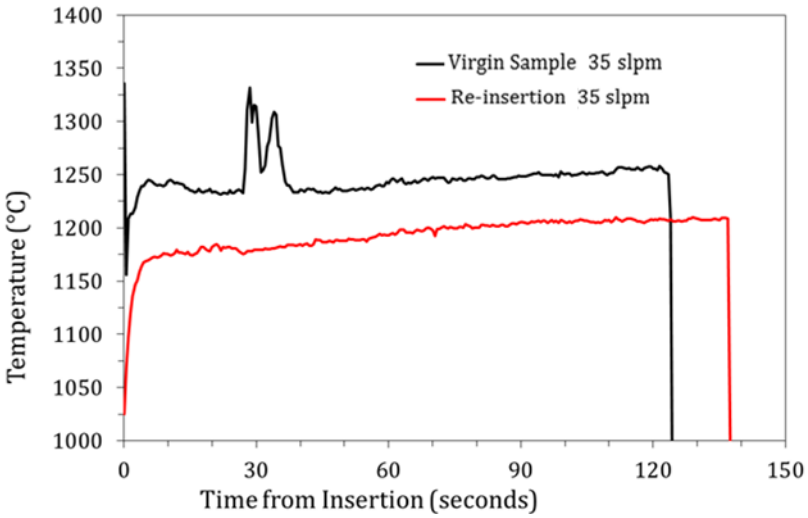

Appendix G.2: Temperature profile for a first and second insertion into a CO_2 plasma at 60 W/cm^2 showing a parallel temperature offset

APPENDIX H: Additional Information on Nextel BF-20

Power Supply		Test Chamber			Sample	
Plate Amperage amps (±.1)	Power kW (±2)	Gas Flow lpm (±1)	Pressure torr (±5)	Heat Flux W/cm^2 (±10)	SiC Fabric Peak Temperature ºC (±50)	**Nextel Performance** Condition
2	6.7	**10 N_2, 30 Ar**	160	**44**	**1283**	**Long Exposure Failure**
2.5	9.6	**10 N_2, 30 Ar**	160	**60**	**1421**	**Catastophic Failure**
2.5	14.1	**40 N_2**	160	**62**	**1397**	**Catastophic Failure**
2	6.9	**10 Air, 30 Ar**	160	**49**	**1287**	**Long Exposure Failure**
2.5	10.1	**10 Air, 30 Ar**	160	**71**	**1459**	**Catastophic Failure**
2.5	14	**40 Air**	160	**80**	**1539**	**Catastophic Failure**
2	6	**10 O_2, 30 Ar**	160	**43**	**1234**	**Long Exposure Failure**
2.5	9.1	**10 O_2, 30 Ar**	160	**68**	**1417**	**Catastophic Failure**

Appendix H.1: Operating conditions where Nextel samples failed and SiC samples survived

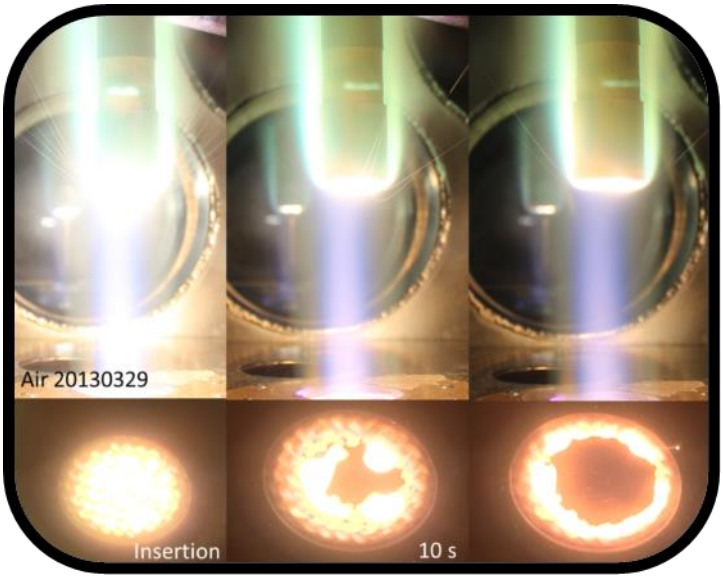

Appendix H.2: Profile and surface images of a Nextel sample taken during air plasma exposure. Even on non-failed samples, the coral sizing is removed exposing the white fibers. After failure, visual traces of metallic boron or aluminum can be seen inside the SiC sleeve. Balls and streaks of flowing silica were much more prevalent during the SiC/Nextel layups and it is believed that this thick viscous layer is the reason for the interesting temperature response.

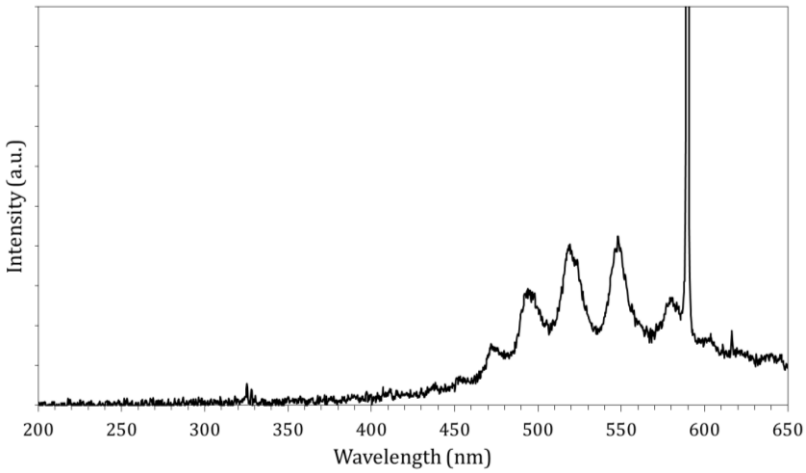

Appendix H.3: Emission spectra captured within the thermal boundary layer of a Nextel sample during O_2/Ar exposure showing overlapping boron oxides which is visually distinguishable as the intense green emission. When oxygen is not present, strong silicon features can be seen at 252, and 288. Traces of boron atom are also observable at 250nm

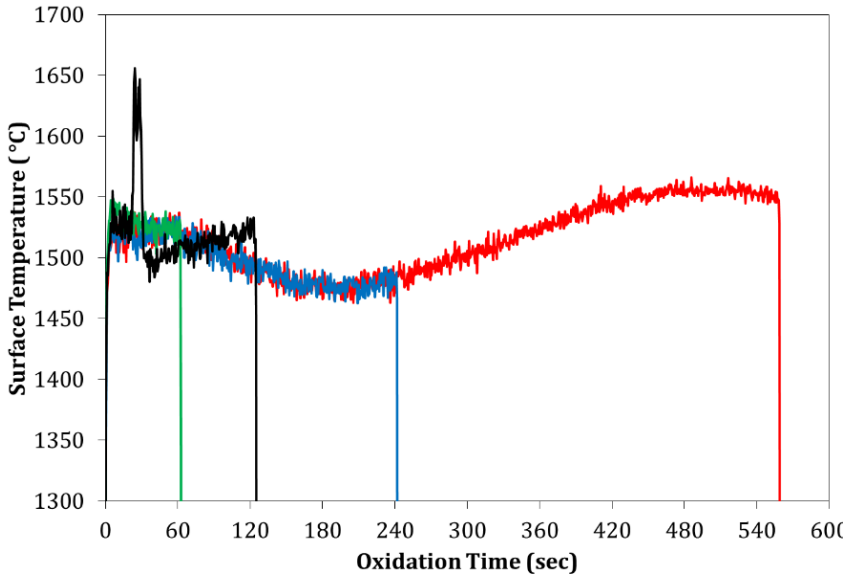

Appendix H.4: Temperature profile of the SiC/Nextel lay-up exposed to an air plasma. The plot shows a higher achieved surface temperature and larger temperature fluctuations

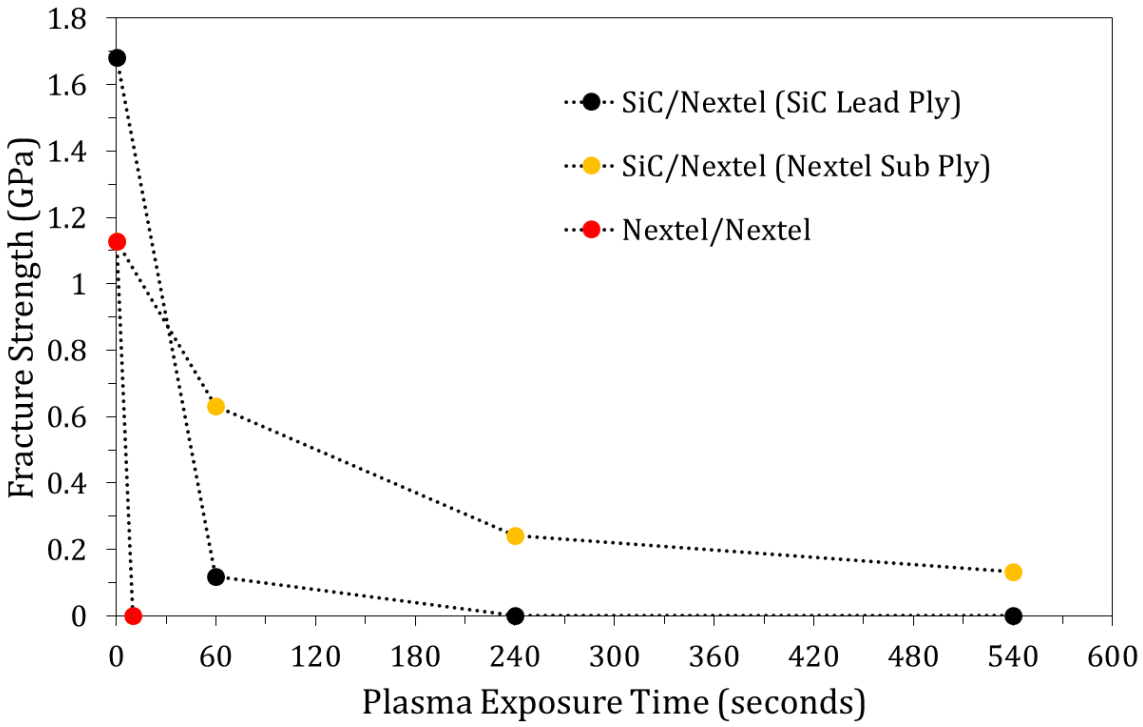

Appendix H.5: Strength of the fabric coupons with a SiC lead ply and a Nextel sub ply after exposure to the air plasma showing the survival of the Nextel fabric when it is protected behind the lead SiC ply. Interestingly, the Nextel sub ply is stronger after 240 seconds compared to the SiC sub ply as shown in Chapter 7.